DEVELOPMENT AND CHARACTERIZATION OF ADVANCED MATERIALS FOR ENERGY CONVERSION AND STORAGE

by

RAINA A. KRIVINA

A DISSERTATION

Presented to the Department of Chemistry and Biochemistry
and the Division of Graduate Studies of the University of Oregon
in partial fulfillment of the requirements
for the degree of
Doctor of Philosophy

June 2022

DISSERTATION APPROVAL PAGE

Student: Raina A. Krivina

Title: Development and Characterization of Advanced Materials for Energy Conversion and Storage

This dissertation has been accepted and approved in partial fulfillment of the requirements for the Doctor of Philosophy degree in the Department of Chemistry and Biochemistry by:

Catherine Page	Chairperson
Shannon Boettcher	Advisor
James Hutchison	Advisor
Amanda Cook	Core Member
Andrew Nelson	Institutional Representative

and

Krista Chronister	Vice Provost for Graduate Studies

Original approval signatures are on file with the University of Oregon Division of Graduate Studies.

Degree awarded June 2022

DISSERTATION ABSTRACT

Raina A. Krivina

Doctor of Philosophy

Department of Chemistry and Biochemistry

June 2022

Title: Development and Characterization of Advanced Materials for Energy Conversion and Storage

Climate change dilemma forces researchers from all over the world to focus on developing solutions for reducing fossil fuel consumption and overall energy use. In this dissertation, several advanced materials for energy consumption reduction and renewable energy storage are explored. Chapter I introduces the materials and studies completed. One promising material that can reduce the heating and cooling energy demands in buildings is tin-doped indium oxide (ITO). ITO can block incoming heat radiation. The ITO coatings are currently produced by wasteful sputter deposition methods. Chapter II describes solution processing of ITO nanomaterial. Solution processing of these materials allows to reduce waste during deposition while using nanomaterial instead of bulk enables to combine the optical properties of ITO with different dopant levels in a single thin film.

The bottleneck of large-scale implementation of renewable energy is the lack of storage technologies. A key technology that has potential to connect renewable energy production and end user is water electrolysis. Water electrolysis allows to direct the energy produced by wind turbines or solar panels to split water and produce H_2 that can be stored and transported safely. Chapter III introduces a novel catalyst for the anodic half-reaction in acid synthesized from a molecular precursor that aims to maximize the intrinsic activity of every active site while minimizing the overall catalyst loading. In Chapter IV, the degradation routes for complex polymers used in water splitting devices are investigated. The potential-induced polymer oxidation in the presence of several widely-used supporting electrolytes is discussed. The final two chapters give an overview of the challenges of using non-platinum-group-metal catalysts in water electrolyzers and unveils the numerous degradation modes possible for these catalysts in a zero-gap system. This work benefits the electrolysis field by providing new insight into the complex processes occurring during electrolyzer operation understanding of which is essential for designing robust stable materials for water electrolyzers.

This dissertation contains previously published and unpublished co-authored materials.

CURRICULUM VITAE

NAME OF AUTHOR: Raina A. Krivina

GRADUATE AND UNDERGRADUATE SCHOOLS ATTENDED:

University of Oregon, Eugene, OR
Richard Stockton University of New Jersey, Galloway, NJ
Russian International Academy for Tourism, Krasnoyarsk, Russia

DEGREES AWARDED:

Doctor of Philosophy, Chemistry, 2022, University of Oregon
Bachelor of Science, Chemistry, 2017, Richard Stockton University of New Jersey
Bachelor of Science, Management, 2010, Russian International Academy for Tourism

AREAS OF SPECIAL INTEREST:

Electrochemistry; Materials Chemistry; Water Electrolysis

PROFESSIONAL EXPERIENCE:

Research Assistant, Boettcher and Hutchison Laboratories, University of Oregon, 2018-2022

Research and Development Intern, Proton OnSite, Wallingford, CT, January 2020 to March 2020

Teaching Assistant, University of Oregon, 2017-2018

PUBLICATIONS:

Krivina, R. A. and Lindquist, G. A.; Beaudoin, S. R.; Stovall, T. N.; Thompson, W. L.; Fabrizio, K.; Hutchison, J. E.; Boettcher, S. W. Anode Catalysts in Anion-Exchange-Membrane Electrolysis Without Supporting Electrolyte: Conductivity, Dynamics, and Ionomer Degradation. *Submitted to Advanced Materials.*

Krivina, R. A.; Lindquist, G. A.; Yang, M. C.; Cook, A. K.; Hendon, C. H.; Motz, A. R.; Capuano, C.; Ayers, K. E.; Hutchison, J. E.; Boettcher, S. W. Three-Electrode Study of Electrochemical Ionomer Degradation Relevant to Anion-Exchange-Membrane Water Electrolyzers. *ACS Appl. Mater. Interfaces* **2022, DOI:** 10.1021/acsami.1c22472.

Kaufman, A. J.; Krivina, R. A.; Shen, M.; Boettcher, S. W. Controlling Catalyst-Semiconductor Contacts Interfacial Charge Separation in p-InP Photocathodes. *ACS Energy Lett.* **2022**, *7* (1), 541-549.

Krivina, R. A.; Ou, Y.; Xu, Q.; Twight, L. P.; Stovall, T. N.; Boettcher, S. W. Oxygen Electrocatalysis on Mixed-Metal Oxides/Oxyhydroxides: From Fundamentals to Membrane Electrolyzer Technology. *Acc. Mater. Res*. **2021**, *2* (7), 548–558.

Lindquist, G. A.; Oener, S. Z.; Krivina, R. A.; Motz, A. R.; Keane, A.; Capuano, C.; Ayers, K. E.; Boettcher, S. W. Performance and Durability of Pure-Water-Fed Anion Exchange Membrane Electrolyzers Using Baseline Materials and Operation. *ACS Appl. Mater. Interfaces* **2021**, *13* (44), 51917–51924.

Krivina, R. A.; Knecht, T. A.; Crockett, B. M.; Boettcher, S. W.; Hutchison, J. E. Sculpting Optical Properties of Thin Film IR Filters through Nanocrystal Synthesis and Additive, Solution Processing. *Chem. Mater*. **2020**, *32* (19) 8683–8693.

ACKNOWLEDGMENTS

This work was funded by the U.S. Department of Energy's Office of Energy Efficiency and Renewable Energy (EERE) under the Fuel Cell Technologies Office (FCTO) under award DE-EE0008841 and the National Science Foundation GOALI grant CHE-1955106. This work made use of the UO CAMCOR Facility, supported by grants from the W.M. Keck Foundation, the M.J. Murdock Charitable Trust, ONAMI, the Air Force Research Laboratory (agreement number FA8650-05-1-5041), NSF (award numbers 0923577, 0421086) and the University of Oregon. I am grateful to the CAMCOR stuff, especially to Stephen Golledge, Julie Chouinard, Adam Clairmont, Kurt Langworthy, Valerie Brogden, and Joshua Razink for maintaining the instruments in excellent conditions, assisting in data collection and interpretation. I thank the UO Administrative stuff, especially Janet Kneller, Kathy Noakes, Jim Rasmussen, Leah O'Brien, and Christi Mabinuori, for their help and support throughout my graduate career. I am grateful to my collaborators in Germany, Serhiy Cherevko and Matej Zlatar, for making exciting investigations possible.

To my advisor Shannon Boettcher, I am grateful for pushing me to be a competent scientist and to never stop learning, to be excited about my work and to think outside of the box. To my advisor Jim Hutchison, I am thankful for probing the depth of my knowledge, for always asking for more understanding, and for making me a better writer. If I went back five years, I would still pick you two as my advisors. I as a scientist am a product of your hard work.

To my committee, Amanda, Cathy, and Andrew, thank you for always showing up, being enthusiastic, and having my back. I enjoyed our every interaction. Thank you for caring about me.

To my undergraduate mentor Prof. Louise Sowers, I am ever so grateful for encouraging me to go to graduate school and for believing that I could succeed when I thought I could not.

My Boettcher and Hutchison lab mates, especially Jessica Fehrs, Tawney Knecht, Grace Lindquist, Lisa Enman, Sebastian Oener, and Brandon Crockett, you made this hard period of my life bearable and fun. Thank you for always being ready to help and share every hardship.

I thank my amazing friends Natalia Niebuhr, Galina Vigul, Anastasia Kirillova, Diana Bashirova, Iskander Bayanov, Anastasia Davidova, Natalia Romanenko, Ildar Baygeldin, Tatiana Zaikova, and Alexi Rukavishnikov for being an incredibly important part of my life, making me happy, making me feel at home, and always wanting to see me.

To my boyfriend Lance, thank you for making my stay in Oregon so pleasant. Thank you for taking me on amazing trips, for making me a part of your life, helping me not to feel alone, and for continuous support.

To my family, thank you all for thinking that I am an outstanding person capable of anything. Thank you for loving me and missing me and keeping me in your hearts. Grandma and Dad, I wish you were still here to see me defend. I miss you all and love you tremendously.

To my grandmother

TABLE OF CONTENTS

Chapter Page

Chapter Page

LIST OF FIGURES

Figure Page

Figure Page

Figure Page

LIST OF TABLES

Table Page

CHAPTER I

INTRODUCTION

Section “Tunable Optical Properties in Doped Semiconductor Nanomaterials” contains co-authored material previously published as *Chem. Mater*. **2020**, 32 (*19*) 8683–8693 reproduced with permission. Copyright 2020 American Chemical Society. Prof. Hutchison, Prof. Boettcher, and I conceived of the project. Tawney Knecht and I performed the experiments and analyzed data with assistance from Brandon Crockett. Tawney Knecht and I wrote the paper with editorial help of Brandon Crockett, Prof. Hutchison, and Prof. Boettcher.

Section “Oxygen Evolution Electrocatalysts from Molecular Precursors” contains co-authored unpublished material. Prof. Boettcher and I conceived of the project. Matej Zlatar and I performed the experiments and analyzed data with assistance from Nathan Stovall, Grace Lindquist, Daniel Escalera-Lopez, Amanda Cook. Matej Zlatar and I wrote the paper with editorial assistance from all the authors. It is prepared in the format of the ACS Catalysis.

Section “Anion-Exchange Polymer Degradation due to Anion Effect” contains co-authored material previously published as *ACS Appl. Mater. Interfaces* **2022, DOI**: 10.1021/acsami.1c22472 and is reproduced with permission. Copyright 2022 American Chemical Society. Prof. Bottcher and I conceived of the project. I performed the experiments, collected and analyzed data. Prof. Hutchison assisted with data interpretation. Prof. Hendon and Min Chieh Yang performed computational work. I wrote the paper with editorial assistance of Amanda Cook, Katherine Ayers, Chistopher Capuano, Andrew Motz, Grace Lindquist, Prof. Hutchison, and Prof. Boettcher.

Section “Non-Platinum-Group-Metal Catalysis: Fundamentals and Outlook” contains co-authored materials previously published as *Acc. Mater. Res*. **2021**, 2 (*7*), 548–558 reproduced with permission. Copyright 2021 Accounts of Materials Research. Prof. Boettcher and I conceived of the project. I wrote the paper with assistance from

Yingqing Ou, Quicheng Xu, Liam Twight, and Nathan Stovall. Prof. Boettcher provided editorial assistance.

Section “Non-Platinum-Group-Metal Catalysts Stability for Membrane Electrolysis” contains co-authored unpublished material recently submitted to *Advanced Materials*. Prof. Boettcher, Grace Lindquist, and I conceived of the project. Grace Lindquist and I collected experimental data with assistance from Nathan Stovall, Sarah Beaudoin, Willow Thompson, and Kevin Fabrizio. Prof. Hutchison and Prof. Boettcher assisted with data interpretation. Grace Lindquist and I wrote the manuscript with editorial assistance from Prof. Hutchison and Prof. Boettcher. It is prepared in the format of the journal Advanced Materials.

Tunable Optical Properties in Doped Semiconductor Nanomaterials

Plasmonic band-stop filters with tunable optical absorbance in the near- and mid-IR are important for wireless communications, bioimaging, and filtering applications. However, their design is constrained by the limited tunability of individual components and complex fabrication techniques. In Chapter II, we demonstrate a method to overcome these limitations that employs mixtures of nanocrystals to predictably sculpt the combined localized surface plasmon resonance (LSPR) for band-stop filters. The additive nature of the LSPR optical absorbances of tin-doped In_2O_3 (ITO) nanocrystals was used to control the combined absorbance in a nanocrystal thin film. The optical properties of the nanocrystals were modulated via a low-temperature esterification synthesis and an inexpensive solution-processing fabrication method, spin-coating, was used to produce the films. Because of the additive nature of the LSPR absorbance of the nanocrystals, the absorption of the films can be easily predicted and designed by summing the spectra of the individual components over the range of 6,000 – 1,000 cm^{-1}. By design and synthesis of individual nanocrystals with tailored optical properties, and selecting the right combinations of nanocrystals to incorporate into films, both wide and narrow band-stop filters were easily constructed (the schematic illustration of the approach is depicted in Figure 1.1).

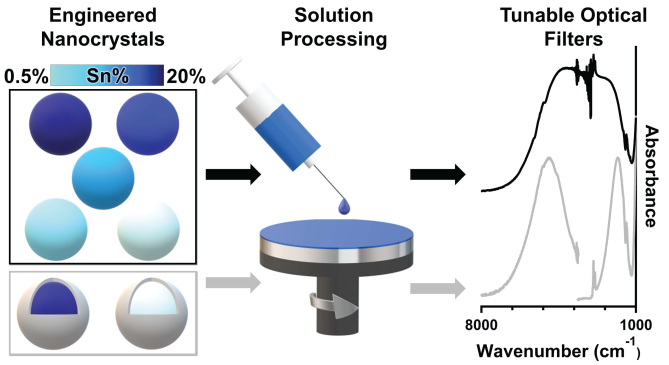

Figure 1.1. Schematic illustration of the solution-processing approach to obtaining ITO thin films with additive optical properties.

Chapter II contains co-authored materials previously published as *Chem. Mater*. **2020**, 32 (*19*) 8683–8693 reproduced with permission. Copyright 2020 American Chemical Society. Prof. Hutchison, Prof. Boettcher, and I conceived of the project. Tawney Knecht and I performed the experiments and analyzed data with assistance from Brandon Crockett. Tawney Knecht and I wrote the paper with editorial help of Brandon Crockett, Prof. Hutchison, and Prof. Boettcher.

Oxygen Evolution Electrocatalysts from Molecular Precursors

Water electrolysis is a leading route for renewable energy storage on a large scale. One of the most-successful water-electrolyzer technologies, proton-exchange-membrane water electrolyzers (PEMWEs), produces high purity H_2, can withstand fluctuations in applied load, and operates with a pure-water feed. However, the acidic environment within the electrolyzer requires the use of platinum-group-metal catalysts for durability, such as IrO_2 and Pt. At the anode, the slow oxygen evolution reaction (OER) requires high overpotential to achieve industry-relevant current densities even with a high loading of IrO_2. Efforts have been devoted to improving the intrinsic activity of IrO_2 to decrease the loading without sacrificing activity. Using simple commercially-available precursors we synthesized sub-monolayer-thick IrO_x on the surfaces of conductive metal oxides, in attempt to make every Ir atom available for catalysis. In Chapter III, we demonstrate that the catalyst loading can be controlled on several key metal-oxide surfaces through a surface-limited reaction. Using this system, we further study the catalyst/protective layer interactions of IrO_x with TiO_2, an acid-stable metal oxide that that is also known to improve OER activity (schematic of synthesis approach is shown in Figure 1.2). Addition of TiO_2 by two atomic layer deposition cycles indeed enhances Ir activity but triggered high catalyst dissolution in strong acid. The effects of TiO_2 on the catalyst's performance were assessed by ICP-MS coupled *in situ* with an electrochemical flow cell and X-ray photoelectron spectroscopy. We show the interplay between the support/catalyst/protective layer dissolution and investigate the effects of annealing on the stability of our catalysts. These ultrathin Ir-based catalysts may be of utility for advanced spectroscopic investigations of the OER mechanism and be employed in PEMWEs in a nanopowder form with further development.

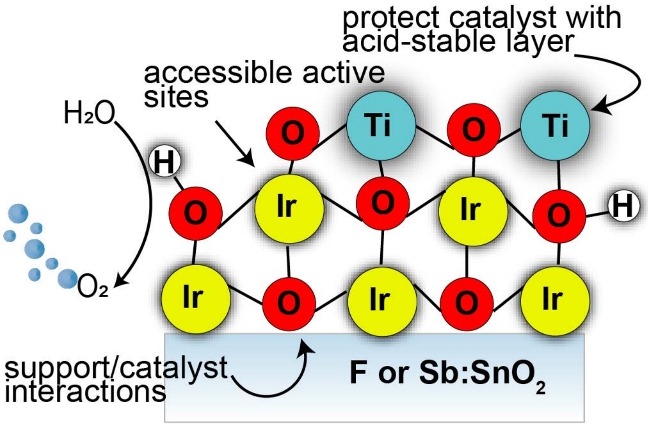

Figure 1.2. Schematic of creating an ultrathin IrO_x catalyst layer on a conductive support and protecting it with TiO_2.

Chapter III contains co-authored unpublished material. Prof. Boettcher and I conceived of the project. Matej Zlatar and I performed the experiments and analyzed data with assistance from Nathan Stovall, Grace Lindquist, Daniel Escalera-Lopez, Amanda Cook. Matej Zlatar and I wrote the paper with editorial assistance from all the authors. It is prepared in the format of the ACS Catalysis.

Anion-Exchange Polymer Degradation due to Anion Effect

Among existing water electrolysis (WE) technologies, anion-exchange-membrane water electrolyzers (AEMWEs) show promise for low-cost operation enabled by the basic solid-polymer electrolyte used to conduct hydroxide ions. The basic environment within the electrolyzer in principle allows the use of non-platinum-group metal catalysts and less-expensive cell components compared to acidic-membrane systems. Nevertheless, AEMWEs are still underdeveloped, and the degradation and failure modes are not well understood. To improve performance and durability, supporting electrolytes such as KOH and K_2CO_3 are often added to the water feed. The effect of the anion interactions with the ionomer membrane (particularly other than OH^-), however, remains poorly understood. In Chapter IV, we studied three commercial anion-exchange ionomers (Aemion, Sustainion and PiperION) during oxygen evolution (OER) at oxidizing potentials in several supporting electrolytes and characterized their chemical stability with surface-sensitive techniques. We analyzed factors including the ionomer conductivity, redox potential, and pH tolerance to determine what governs ionomer stability during OER. Specifically, we discovered that oxidation of Aemion at the electrode surface is favored in the presence of CO_3^{2-}/HCO_3^- anions perhaps due to the poor conductivity of that ionomer in the carbonate/bicarbonate form. Sustainion tends to lose its charge-carrying groups as a result of electrochemical degradation favored in basic electrolytes. PiperION seems to be similarly negatively affected by a pH drop and low carbonate/bicarbonate conductivity under the applied oxidizing potential. The insight into the interactions of the supporting electrolyte anions with the ionomer/membrane helps shed light on some of the degradation pathways possible inside of the AEMWE and enable informed design of materials for water electrolysis.

Chapter IV contains co-authored material previously published as *ACS Appl. Mater. Interfaces* **2022, DOI**: 10.1021/acsami.1c22472 and is reproduced with permission. Copyright 2022 American Chemical Society. Prof. Bottcher and I conceived of the project. I performed the experiments, collected and analyzed data. Prof. Hutchison assisted with data interpretation. Prof. Hendon and Min Chieh Yang performed computational work. I wrote the paper with editorial assistance of Amanda Cook, Katherine Ayers, Chistopher Capuano, Andrew Motz, Grace Lindquist, Prof. Hutchison, and Prof. Boettcher.

Non-Platinum-Group Metal Catalysis: Fundamentals and Outlook

Catalyzing the oxygen evolution reaction (OER) is important for key energy storage technologies, particularly water electrolysis and photoelectrolysis for hydrogen fuel production. In neutral-to-alkaline conditions, first-row transition-metal oxides/(oxy)hydroxides are the fastest-known OER catalysts and have been the subject of intense study for the past decade. Critical to their high performance is the intentional or accidental addition of Fe to Ni/Co oxides that convert to layered (oxy)hydroxide structures during the OER. Unraveling the role Fe plays in the catalysis and the molecular identity of the true "active site" has proved challenging, however, due to the dynamics of the host structure and absorbed Fe sites, as well as the diversity of local structures in these disordered active phases. In Chapter V, we highlight our work to understand the role of Fe in Ni/Co (oxy)hydroxide OER catalysts. We first discuss how we characterize the intrinsic activity of the first-row transition-metal (oxy)hydroxide catalysts as thin films by accurately accounting for the contributions of the catalyst-layer thickness (mass loading), electrical conductivity, the underlying substrate's chemical interactions with the catalyst, and the presence of Fe species in the electrolyte. We show how Fe-doped Ni/Co (oxy)hydroxides restructure during catalysis, absorb/desorb Fe, and in some cases degrade or regenerate their activity during electrochemical testing. Along the way, we highlight the relevant techniques and procedures that allowed us to better understand the role of Fe in activating other first-row transition metals for OER. We find several modes of Fe incorporation in Ni/Co (oxy)hydroxides and show how those modes correlate with activity and durability. We summarize the evidence for the identity of the active site in single-metal and mixed-metal catalysts (Figure 1.3). We also discuss how this understanding informs the incorporation of earth-abundant transition-metal OER catalysts in anion-exchange-membrane water electrolyzers (AEMWE) that provide a locally basic anode environment but run on pure water and have advantages over the more-developed proton-exchange-membrane water electrolyzers (PEMWE) that require platinum-group-metal (PGM) catalysts. We outline the key issues of introducing Fe-doped Ni/Co (oxy)hydroxide catalysts at the anode of the AEMWE, such as the oxidative processes triggered by Fe species traveling through the polymer membrane, pH gradient effects on the catalyst stability, and potentially limited catalyst utilization in the compressed stack configuration. We also suggest possible mitigation strategies for these issues. Finally, we summarize remaining challenges including long-term stability of Fe-doped Ni/Co (oxy)hydroxides under OER conditions and the lack of accurate models to visualize the dynamic active surface that hinder our understanding of, and thus ability to design, these catalysts.

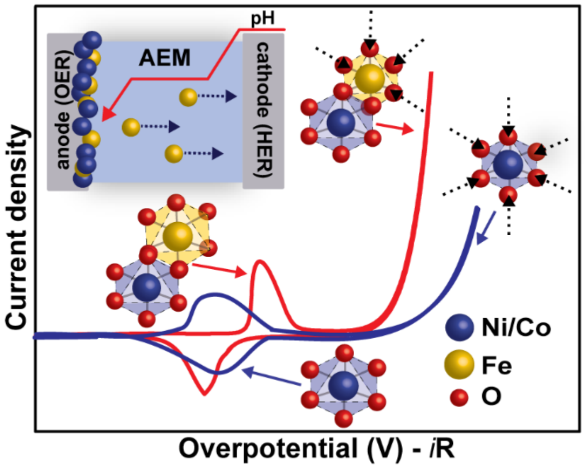

Figure 1.3. The change in metal-oxygen bond length during OER suggests that in mixed-metal catalysts such as Ni/Fe and Co/Fe oxides, the active site is Fe.

Chapter V contains co-authored materials previously published as *Acc. Mater. Res*. **2021**, 2 (*7*), 548–558 reproduced with permission. Copyright 2021 Accounts of Materials Research. Prof, Boettcher and I conceived of the project. I wrote the paper with assistance from Yingqing Ou, Quicheng Xu, Liam Twight, and Nathan Stovall. Prof. Boettcher provided editorial assistance.

Non-Platinum-Group Metal Catalysts Stability for Membrane Electrolysis

Anion-exchange-membrane water electrolyzers (AEMWEs) in principle operate without soluble electrolyte using earth-abundant catalysts and cell materials and thus lower the cost of green H_2. Current systems lack competitive performance and durability needed for commercialization. One critical issue is a poor understanding of catalyst-specific degradation processes in the electrolyzer. While non-platinum-group-metal (PGM) oxygen-evolution catalysts show excellent performance and durability in strongly alkaline electrolyte, such performance has not transferred directly to pure-water AEMWEs. In Chapter VI, the AEMWEs with five common non-PGM anode catalysts are built and the catalysts' structural stability and interactions with the alkaline ionomer are characterized during electrolyzer operation and post-mortem. The results show catalyst electrical conductivity is key to obtaining high-performing systems and many non-PGM catalysts restructure and leach during operation. Dynamic Fe sites correlate with enhanced degradation rates, as does the addition of soluble Fe impurities. In contrast, electronically conductive and Fe-free Co_3O_4 nanoparticles yield AEMWEs from simple, industry-standard preparation methods, with performance and stability comparable to IrO_2. These results reveal the fundamental dynamic catalytic processes resulting in AEMWE device failure under relevant conditions, demonstrate a viable non-PGM catalysts for AEMWE, and illustrate underlying design rules for engineering anode catalyst/ionomer layers with higher performance and durability.

Chapter VI contains co-authored unpublished material that was submitted to *Advanced Materials*. Prof. Boettcher, Grace Lindquist, and I conceived of the project. Grace Lindquist and I collected experimental data with assistance from Nathan Stovall, Sarah Beaudoin, Willow Thompson, and Kevin Fabrizio. Prof. Hutchison and Prof. Boettcher assisted with data interpretation. Grace Lindquist and I wrote the manuscript with editorial assistance from Prof. Hutchison and Prof. Boettcher. It is prepared in the format of the journal Advanced Materials.

Bridge

All projects discussed in this Dissertation are dedicated to investigation of ways to reduce energy consumption and develop energy storage solutions applicable to intermittent renewable energy. Chapter I introduced all the topics covered in this Dissertation. Chapter II discusses the use of nanoparticle thin films with additive plasmonic properties for blocking specific energy ranges of light. Chapter III introduces a new catalyst for water electrolysis in acid that allows to significantly reduce the loading making the process more cost-efficient. Chapter IV focuses on anion-exchange-membrane electrolysis that uses a solid polymer electrolyte. The stability of the polymer in contact with various anions under applied potential is discussed. Chapter V summarizes our understanding of the oxygen evolution reaction in basic conditions with non-platinum-group-metal catalysts and predicts the challenges of translating that knowledge into zero-gap electrolyzer systems. Chapter VI discusses the performance of a range of non-platinum-group-metal catalysts in a zero-gap electrolyzer. This dissertation concludes by discussing the importance of enhancing our understanding of the failure modes during water electrolysis and provides insight into the current state of low-temperature electrolysis.

CHAPTER II

SCULPTING OPTICAL PROPERTIES OF THIN FILM IR FILTERS THROUGH NANOCRYSTAL SYNTHESIS AND ADDITIVE, SOLUTION PROCESSING

Chapter II contains co-authored materials previously published as *Chem. Mater*. **2020**, 32 (*19*) 8683–8693 reproduced with permission. Copyright 2020 American Chemical Society. Prof. Hutchison, Prof. Boettcher, and I conceived of the project. Tawney Knecht and I performed the experiments and analyzed data with assistance from Brandon Crockett. Tawney Knecht and I wrote the paper with editorial help of Brandon Crockett, Prof. Hutchison, and Prof. Boettcher.

Introduction

Band-pass/band-stop filters with tunable wavelengths and compact structures are desirable for manipulating the optical properties of light sources used in wireless communication, biological imaging, and sensors.[1–4] Traditionally, band-stop filters are composed of several dielectric layers with alternating low and high refractive indices in order to control light absorption in the region of interest.[3,5-15] The materials comprising the filter stack are chosen based on their optical characteristics in the energy range of interest. Such filters typically operate under the multiplication rule of probability, where the amount of light that passes through the filter is determined by the intersection of the passbands.[8] The incident light is absorbed in the regions with no passband overlap and transmitted in the region of an overlap. Thus, resulting spectra are not the sum, but rather the product, of the spectra resulting from each individual layer in the stack. This renders it challenging to create multi-pass band filters with predictable optical spectra from the preexisting single-pass band filters.[8] Additionally, the stacking of different materials to achieve the desired performance leads to the total thickness of the stack being greater than the target wavelengths.[8] Furthermore, fabrication of the filter geometries often requires processing techniques such as photolithography, sputtering, and pulsed laser ablation, which places practical limits on the scale of application.[16]

Plasmonic nanomaterials can block certain wavelengths of light making them attractive for use in electrochromic windows[17–22] and optical band-pass and band-stop filters.[3,5-15] Optical filters that are based upon plasmonic materials operate under the addition, as opposed to multiplication, rule of probability where the final transmission through the stack is a sum of the individual probabilities and is determined by the bandwidth of each layer.[8] For the localized surface plasmon resonance (LSPR)-facilitated absorbance to be additive, the filter stack must consist of materials with linear optical properties and have a thickness below the target wavelength similar to the traditional filter stacks. In addition, such configurations typically need to be paired with a complex grating composed of plasmonic noble metals such as Au, and require lithographic fabrication techniques.[23,24]

The ability to tune the plasmonic response is an important attribute that, despite much effort to improve, still suffers from several limitations. The most widely studied plasmonic materials are noble metals (e.g. Au, Ag, Cu). The high concentration of the free carriers set by the identity of those metals places the LSPR in the UV and visible range. [25–28] The inability to change the number of free carriers places limits on the potential to tune the LSPR energy and peak shape in metal nanomaterials. Successful strategies include changing the shape and size, or adding “shells” of materials with complementary properties, however, these structures are not always easy to access through synthesis.[25–28] Even when these structural parameters can be controlled to shift the LSPR, optical absorption typically occurs only from the UV-vis to the onset of the near-infrared (near-IR). Thus, the LSPR energies accessible using noble metals are insufficient for the applications that require tunable optical properties in the near-IR and mid-infrared (mid-IR) ranges of the electromagnetic spectrum, such as electrochromic windows, optical band-stop filters necessary for biological sensing and imaging, and free-space communication.[8,29–31]

Doped metal-oxide nanomaterials are a promising class of materials that have also demonstrated LSPR.[32–34] These materials are more earth-abundant and offer a variety of advantages that complement the attributes of plasmonic noble metals. The LSPR energy of doped metal-oxides is significantly lower than that of the noble metals due to a lower concentration of the charge carriers, which makes it possible to access the energy range from the near-IR into the mid-IR. Given that the carrier concentration is tuned through the dopant concentration, the optical properties of doped metal-oxides can be more easily tuned than the metals. Varying the doping concentration[17,20,32] and distribution[21] in these materials shifts the LSPR maximum to higher or lower energies and can be used to adjust the LSPR peak width and intensity. The doped metal-oxides are thus promising materials for plasmonic band-stop filters.

In Chapter II, we present a simple fabrication process to make tunable filters for the energy range between 6,000 and 1,000 cm^{-1} that takes advantage of the additive nature of the absorbance response when employing precisely constructed tin-doped indium oxide (ITO) nanocrystals synthesized through a slow-injection route.[35,36] The LSPR energy of ITO nanocrystals can be shifted from the near-IR to mid-IR range of the spectrum by controlling the size, doping level and dopant placement using the slow-injection synthesis, producing ITO nanocrystals desirable for designing near- or mid-IR filters. Because no single composition of ITO nanocrystal is capable of blocking a wide region (Figure 2.1a) or multiple distinct narrow regions (Figure 2.1b) of the electromagnetic spectrum, construction of a tunable band-stop filter requires a combination of individual optical responses from several nanocrystals. We report the optical properties of layered and homogeneously mixed films of ITO nanocrystals prepared by quick and simple solution processing (see Appendix A for all figures). We show that the additive nature of the absorbance allows us to sculpt the resulting absorbance spectra to produce wide and narrow band-stop filters in nanocrystal films without the necessity of a thick filter stack, complex grating, and/or restricting processing techniques.

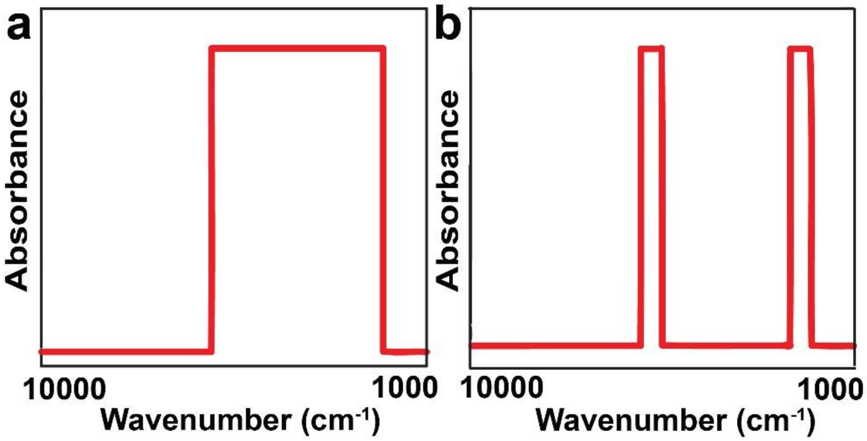

Figure 2.1. Schematic of targeted LSPR responses. (a) A wide band-stop filter that blocks a wide range of wavelengths in the near- and mid-IR regions and (b) a narrow band-stop filter that selectively blocks narrow regions of the near- and mid-IR regions.

Experimental

Materials and Methods. Indium(III) acetate, tin(IV) acetate, and oleic acid (90% technical grade) were used as received from Sigma-Aldrich. Oleyl alcohol (85% technical grade) was used as received from Alfa Aesar.

Synthesis of ITO and ITO/In_2O_3 Core/Shell Nanocrystals. Syntheses were performed in accordance with previously published results.[34,35] For homogeneously-doped ITO nanocrystals, indium(III) acetate and tin(IV) acetate were mixed in a 20-mL scintillation vial with 4 mL of oleic acid in the desired In/Sn molar ratio to add up to 2 mmol total metal acetate (1.99:0.01, 1.98:0.02, 1.95:0.05, 1.90:0.10, and 1.80:0.20 mmol In:Sn for the 0.6, 1.2, 3.3, 6.8, and 16% doped ITO, respectively). Each precursor solution was heated to 150°C under N_2 flow with constant stirring for several hours. ITO nanocrystals were then formed by injecting the mixed In/Sn-oleate precursor into 13 mL of oleyl alcohol at 290°C under flowing N_2 via a syringe pump at a rate of 18 mL hr^{-1}. Nanocrystals were washed in acetone and redispersed in toluene.

ITO/In_2O_3 core/shell nanocrystals were synthesized following a similar procedure as described above. The core and shell precursor solutions were prepared separately. The core precursor solution containing the mixed In/Sn-oleate in the ratios desired for the core doping (0.66:0.01, 0.65:0.02, 0.95:0.05, 0.59:0.07, and 1.67:0.20 mmol In:Sn for the cores of 1.5%, 3%, 5%, 10%, and 16% Sn, respectively) was injected first at a rate of 18 mL hr^{-1} via a syringe pump into 13 mL of oleyl alcohol at 290°C under flowing N_2. An aliquot of this solution was taken in order to determine the core size and doping concentration. Then In-oleate solution was injected at the same rate in the quantity necessary to bring the total amount of metal-oleate in the flask to 2 mmol. For the ITO samples used for the narrow band-stop filter we synthesized a 2 mmol doped core (1.80:0.20 and 1.99:0.01 mmol In:Sn for the 12% ITO core and 0.4% ITO core with thin In_2O_3 shells, respectively) and injected 0.3 mmol In-oleate to obtain an ultra-thin shell.

Characterization of ITO and ITO/In_2O_3 Core/Shell Nanocrystals. Elemental compositions of ITO nanocrystals with doping levels above 2% were determined using a Thermo Scientific ESCALAB 250 X-ray photoelectron spectrometer (XPS). Tin:indium content was determined by integrating the tin $3d_{5/2}$ peak and comparing the intensity to that of the indium $3d_{5/2}$ peak. Peak binding energies were referenced to the C1s hydrocarbon peak at 284.8 eV. Samples were prepared by drop-casting solutions of nanocrystals dispersed in toluene onto silicon wafers and allowing them to dry.

Elemental compositions of ITO nanocrystals with doping levels below 2% were determined by inductively coupled plasma optical emission spectrometry (ICP-OES). A Teledyne Leeman Laboratories (Hudson, NH) Prodigy High Dispersion ICP-OES system was used. Samples were prepared by digesting dried nanocrystals in concentrated HCl for 48 h before being diluted with 2% v/v HNO_3 for analysis.

Transmission electron microscopy (TEM) micrographs were acquired on a FEI Tecnai Spirit TEM (Hillsboro, OR) operating at 120 kV. Lacey carbon grids supported on copper from Ted Pella (Redding, CA) were used to image the nanocrystals. TEM grids were prepared by submerging in ~0.5 mg/ml solutions of nanocrystals in toluene.

Size and polydispersity of the nanocrystals were determined using a lab-scale small-angle X-ray scattering (SAXS) instrument (SAXSess, Anton Paar, Austria). The system is equipped with a Cu $k\alpha$ ($\lambda = 0.154$ nm) X-ray source that was operated at 40 kV and 50 mA. A charge-coupled device detector (Roper Scientific, Germany) was used to detect scattered X-rays. An average of 50 individual scattering curves was acquired for various acquisition times (0.1-3 s) to maximize signal to noise. Raw data was processed with SAXSquant software (version 2.0) and curve fitting was done using Irena macros for IGOR (V. 6.3.7.2).[37] A spherical form factor was used for curve fitting, supported by morphology visualized by TEM.

Preparation and Characterization of Thin Films. Thin films of ITO nanocrystals were prepared by spin-coating solutions of ~50 mg/mL nanocrystals in toluene onto UV-grade CaF_2 substrates (2.54 cm diameter x 1 mm thick, UQG Optics, Cambridge, England). Substrates were first cleaned by sonication in toluene for 10 min then isopropanol for 10 min. A Laurell WS-400-6NPP-LITE Manual Spin Processor was used at a rotation rate of 3000 RPM for 30 s. Solvent was allowed to evaporate in air before characterization. For multilayered samples, each layer was annealed in air at 150°C for 10 minutes prior to the deposition of the next layer.

UV-vis spectra of thin films were collected on a PerkinElmer (Waltham, MA) Lambda 1050 spectrometer from wavelengths of 250 – 3,300 nm (40,000 – 3,030 cm^{-1}) with a scan resolution of 1 nm. Fourier Transform Infrared (FTIR) spectra were collected on a Thermo Fisher Nicolet 6700 spectrometer from wavelengths of 2,500 – 25,000 nm (4,000 – 400 cm^{-1}). To visualize the LSPR of the thin films with different doping levels in the same plot, we joined the spectra obtained from UV-vis and IR spectrometers at 3,500 cm^{-1}. FWHM was calculated by manually finding the middle of the LSPR peak in OriginPro 9 software.

Scanning electron microscopy (SEM) was performed to characterize the homogeneously-mixed and multilayered films of the homogeneously-doped ITO nanocrystals using an FEI Helios Nanolab 600i FIB-SEM with a Through-Lens detector. The homogeneously mixed film was prepared by first diluting the solutions of 0.7, 1, 3, 7, and 16% Sn-doped indium oxide nanocrystals such that their optical absorbance when spin-coated into a film would be ~0.1. These solutions were then mixed together such that the final concentration was 50 mg/mL, and this solution was then spin-coated onto a silicon substrate. For the multilayered films, the diluted solutions were spin-coated onto a silicon substrate from lowest to highest doping and vice versa, as illustrated in Figure 4a and S1, annealing the substrate at 150°C for 10 minutes in between the layer additions. Oleate ligands in these samples were removed in order to reduce charging during image acquisition. To remove the oleate ligands, the substrates with the films were soaked in a solution of 1 M formic acid in acetonitrile for one hour, and then annealed at 300^{o}C under air for one hour, following a previously established procedure.[40] Top-down images were acquired using an accelerating voltage of 5 kV and a beam current between 86 – 1,400 pA. To obtain cross section images of the ITO nanocrystal films, a layer of carbon was first deposited. The sample was then milled using a commercial gallium focused ion beam operating at 30 kV using an ion current of 2.5 nA for the initial milling, and then an ion current of 0.79 nA to polish the edge for subsequent imaging. Cross-section images were then acquired using an accelerating voltage of 2 kV and a beam current of 86 pA. SEM images are shown in Figure A.1.

Results and Discussion

To investigate tunable optical filters based upon thin films of plasmonic nanocrystals we need access to a variety of nanocrystals with defined optical features from which we can form uniform films. Further, we need to understand how the optical properties of these films depend upon the type and spatial distribution (layered vs. mixed, for example) of the nanocrystal building blocks. Here we describe the synthesis of 12 different compositions of ITO nanocrystals that allow the systematic variation of optical absorption from ~ 6,000 – 1,000 cm^{-1}, report the optical properties of films formed from mixtures of these nanocrystals, and describe how specific mixtures can be used to produce optical filters with desired characteristics.

Synthesis of a Library of Materials. The LSPR response of metal-oxide nanocrystals can be tuned by altering nanocrystal size, the identity and concentration of the dopant(s), where those dopants are localized in the nanocrystal, and defect concentration.[21,34,38] To have a predictable effect on the optical properties of the designed material, each these parameters must be controlled during synthesis. Unfortunately, these parameters have been historically difficult to manage through synthesis. A number of nanocrystal syntheses exist for ITO, but it was difficult to systematically adjust the structural features that influence their properties. The resulting nanocrystals often exhibit significant size dispersity and poorly controlled dopant placement and doping levels. Because of differences in defect levels and radial dopant placement, the properties of ITO nanocrystals of the same size and doping level made by different syntheses differ substantially.[21] The energy, shape, and intensity of the LSPR in plasmonic nanoparticles are highly sensitive to doping concentration and radial distribution, as well as to the presence of crystal defects, and thus precise control over these properties is necessary in order to predictably shape the optical response.[16,38]

A low-temperature esterification synthesis previously developed by our group enables unprecedented control over the properties of ITO nanocrystals.[34–36,39] It allows layer-by-layer growth of metal-oxide nanocrystals that leads to superior control of nanocrystal size and dopant concentration and placement. The synthesis grants access to a large library of materials with a wide range of LSPR energies and shapes and has been shown to work for a variety of binary oxides.[34-35] The desired modifications of the optical properties can be easily accomplished by varying parameters such as the amount of precursor added (size), ratio of the metals in the precursor (dopant identity and amount), order of addition of metal precursors (radial dopant distribution), and dopant activation and damping control (core/shell structuring) (Figure 2.2). Ligand-stabilized ITO nanocrystals form dispersions that can be solution-processed to obtain nanocrystal thin films with desired optical and electronic properties.[40]

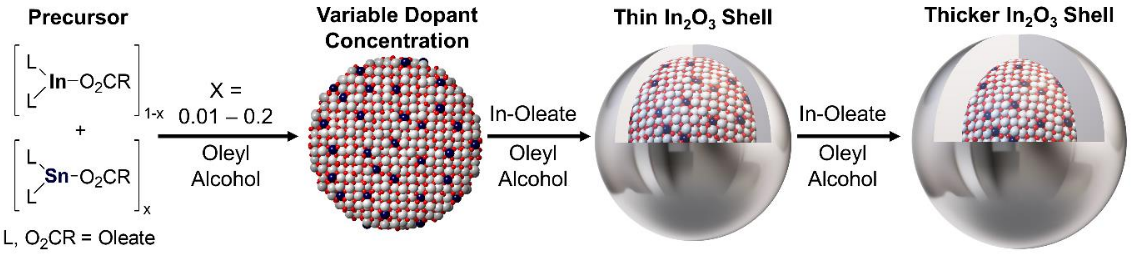

Figure 2.2. Slow-injection synthesis of ITO nanoparticles. Controlled addition of metal oleate precursors into hot oleyl alcohol allows precise control over nanocrystal size, dopant concentration and placement, and construction of core/shell structures needed to sculpt the optical properties of ITO nanocrystals and resulting thin films.

We started by synthesizing 10 nm ITO nanocrystals with different tin doping levels (0.7, 1, 3, 7, and 16 metal %). Because the nanocrystal size can influence their optical properties,[40] all nanocrystal samples were prepared with the same core diameter so that the effect of size would not need to be considered when comparing optical properties between samples. A predictable shift in the LSPR energy of fabricated ITO thin films towards higher energies was observed as the dopant concentration was increased (Figure 2.3a). Nanocrystal size was kept constant by using the same amount (2 mmol) of metal-oleate precursor for each synthesis. Doping levels were varied by changing the tin/indium oleate ratio in the precursor. Nanocrystals were first characterized in solution. Small-angle X-ray scattering (SAXS) was performed to characterize size and dispersity (Figures A.2-A.3); transmission electron microscopy (TEM) was used to examine the morphology (Figure A.4); and X-ray photoelectron spectroscopy (XPS) and inductively coupled plasma optical emission spectroscopy (ICP-OES) were performed to quantify the Sn content (Figure A.5). Nanoparticles were then spin-coated to form thin films before their optical properties were characterized by UV/Vis and Fourier transform infrared spectroscopy (FTIR) (Figure A.6).

The optical spectrum of the sample containing 0.7 Sn metal % (0.7% ITO) was almost indistinguishable from the undoped indium oxide, thus it formed the lower limit for the doping level. We chose 16% as an upper doping limit because the LSPR-facilitated absorbance of films produced from more heavily doped nanocrystals begins to broaden and red-shift due to increased scattering from the added dopants.[34] The continuous growth of the nanocrystals facilitated by a slow addition of the precursors makes it possible to increase the doping level up to 20% without phase segregation, but the shift in the LSPR peak induced by the additional dopants is counteracted by increasing scattering.[34]

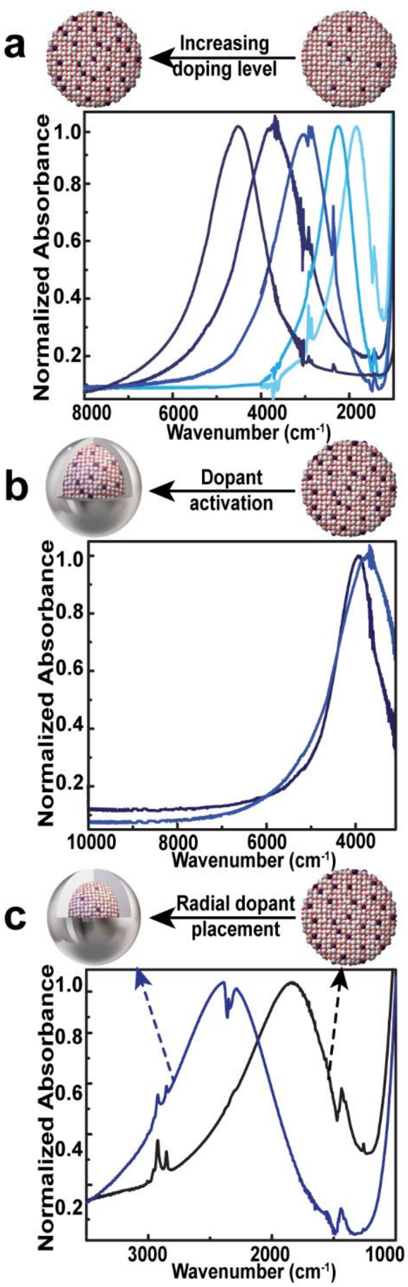

Figure 2.3. The influence of tin dopant concentration and spatial distribution on the energy and shape of the LSPR signal in indium oxide nanocrystal films. (a) Increasing the concentration of dopant, and thus free carriers, shifts the LSPR toward higher energy in homogeneously-doped ITO nanocrystal thin films. Spectra for nanocrystals containing 16%, 7%, 3%, 1%, and 0.7% Sn are displayed from left to right. (b) Adding an undoped shell increases dopant activation and decreases damping, resulting in narrower LSPR peaks (blue: 7% homogeneously-doped ITO; dark blue: 5% ITO core with an In_2O_3 shell). (c) Manipulating the radial dopant distribution influences the energy of the LSPR peak for nanocrystals.

In addition to the overall doping level, the placement of dopant atoms provides an alternative approach to modify the shape and energy of the optical spectrum across the near- and mid-IR ranges.[41] To demonstrate how dopant placement influences the optical properties, we synthesized core/shell ITO/In_2O_3 nanocrystals over the same range of overall dopant concentrations as the homogeneously-doped nanocrystals, but with the tin atoms localized in the core. These core/shell structures have been shown to exhibit narrower LSPR linewidths due to increased surface dopant activation and decreased damping (Figure 2.3b).[34] The core/shell approach can also be utilized to shift the LSPR to higher energy without increasing the overall doping concentration (Figure 2.3c). By manipulating the doping levels and radial placement we obtained a library of ~10 nm ITO nanocrystals (Table 2.1) that could be easily fabricated into thin films with the absorbance covering a wide range of energies (6,000-1,000 cm^{-1}) and a variety of shapes.

Multilayered ITO Films. We next investigated whether we could tap the properties of these nanocrystals to fabricate band-stop filters with tunable absorption across the mid-IR and near-IR. A common practice in the field involves the layering of materials possessing different properties to tune the optical response of a filter.[8] Thus, our first approach was to study the optical properties of filters produced by depositing layers of different doped nanocrystals from the library in Table 2.1.

The size of the nanocrystals was intentionally kept constant to avoid size-related property changes. ITO nanocrystals are known to have size-dependent properties. The LSPR can change the energy and shape for the nanocrystals of the same composition but different size. The size-dependent properties are not discussed in this work.

Table 2.1. Library of ITO nanocrystals synthesized through a slow-injection esterification synthesis.

Samples	Diameter[a] (nm, by SAXS)	Doping[b] (by XPS[c] or ICP-OES[d])	LSPR Max (cm^{-1})	FWHM (cm^{-1})
0.7% ITO	10.7 ± 1.3	0.65 ± 0.01[d]	1,844	816
1% ITO	11.3 ± 1.5	1.24 ± 0.01[d]	2,249	895
3% ITO	9.3 ± 0.7	3.3 ± 0.1[c]	2,978	1,375
7% ITO	10.3 ± 1.0	6.8 ± 0.2[c]	3,737	1,793
16% ITO	10.5 ± 1.3	16.0 ± 0.3[c]	4,509	1,534
1.5% ITO core with In_2O_3 shell	Core only: 7.2 ± 1.0 Core/shell: 10.3 ± 1.2	0.58 ± 0.01[d]	2,389	978
3% ITO core with In_2O_3 shell	Core only: 9.0 ± 1.2 Core/shell: 10.3 ± 1.4	1.31 ± 0.01[d]	3,001	1,074
5% ITO core with In_2O_3 shell	10.0 ± 1.1	2.9 ± 0.1[c]	3,937	1,125
10% ITO core with In_2O_3 shell	9.7 ± 0.7	3.8 ± 0.2[c]	4,080	1,140
16% ITO core with In_2O_3 shell	9.9 ± 1.3	13.0 ± 0.1[c]	4,411	1,876
0.4% ITO core with In_2O_3 shell	Core only: 9.7 ± 1.4 Core/shell: 10.3 ± 1.3	0.35 ± 0.01[d]	1,740	872
12% ITO core with In_2O_3 shell	Core only: 9.4 ± 1.1 Core/shell: 9.8 ± 1.2	10.6 ± 0.2[c]	4,509	1,512

[a] SAXS sizes for core/shell nanoparticles were measured twice: after addition of the doped core (“core only” in the table), and after the undoped shell was added (“core/shell” in the table).
[b] Each doping percentage is represented as the Sn-to-In metal percent.
[c] Samples where Sn content was measured by XPS
[d] Samples where Sn content was measured by ICP-OES

For these studies, we utilized several of the homogeneously-doped ITO nanocrystals described in Table 1 with the LSPR energies covering a wide energy range starting in the mid-IR (1000 cm^{-1}) and ending in the near-IR (6,000 cm^{-1}). Each sample was dissolved in toluene and diluted so that a spin-coated layer of that individual nanocrystal had a measured maximum absorbance intensity of approximately 0.1. Solutions of different nanocrystal types were sequentially spin-coated on a CaF_2 substrate starting with the lowest doped sample (0.7% ITO) and increasing the doping level in each consecutive layer, ending with 16% ITO (Figure 2.4a). After each layer was deposited, the substrate was annealed in air at 150°C for 10 minutes. Annealing at 150°C removes solvent and prevents the ITO nanocrystal films from being removed by contact with the organic solvent used in subsequent deposition steps. We also made a film wherein the order of deposition was reversed, starting with the highest doped sample, and finishing with the lowest (Figure 2.4b) to determine if the order of the layers mattered. The changes in the absorbance of the multilayered films were monitored with UV/Vis-NIR (Figure 2.4c and d) after each subsequent layer was deposited.

The spectra in Figure 2.4 (c and d) suggest that the order of deposition of the layers significantly influences the shape and intensities of the optical response of the layered films. The spectra of the film demonstrated in Figure 2.4a show the absorbance maximum shifting to higher energy with each layer along with an increase in the intensity of the absorbance (Figure 2.4c). As layers containing nanocrystals with higher doping levels are added, the contributions to the absorption due to the initially deposited layers containing lower doped nanocrystals seem to diminish completely by the time the 16% ITO layer is deposited. With the addition of the last layer, the shape and energy of the overall absorbance spectrum closely resembles the optical response of a film made of only 16% ITO nanocrystals. For the second film structure (Figure 2.4b) that has the reversed order of layers, the intensity of the combined spectrum (Figure 2.4d) also increases upon the addition of each layer but the absorbance maximum does not shift significantly. Instead, the width of the absorbance increases upon the addition of subsequent layers. Although the spectra reveal contributions from each of the individual spectra, the higher doped layers appear to dominate the spectral response. Still, the second layering approach does produce a filter that absorbs over a broader spectral range, even though the response is not additive.

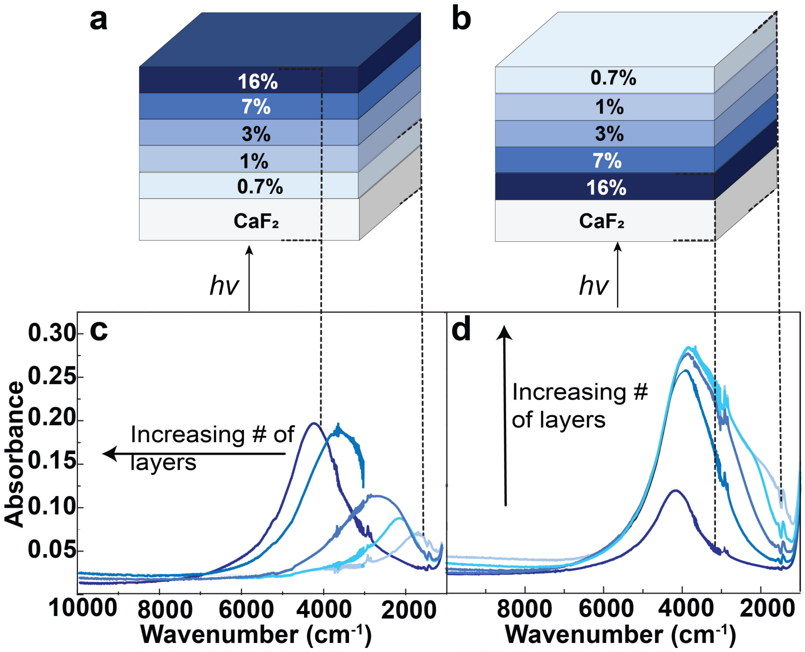

Figure 2.4. Absorbance spectra of multilayered ITO films. Multilayered films fabricated by spin-coating ITO nanocrystal solutions that were diluted to produce films with an absorbance of approximately 0.1. The solutions were spin-coated starting with the lowest doping concentration and proceeding to the highest in (a) and from the highest to lowest in (b). The changes in the optical absorbance were monitored with the UV/Vis-NIR after deposition of each consecutive layer and are shown in the bottom panel. Plot (c) corresponds to the structure in (a). Plot (d) corresponds to the structure shown in (b). The direction of the beam is shown by the arrows. The absorbance spectra were obtained by measuring the transmittance of the films deposited on CaF_2 and converting transmission to absorbance (2-log(%T)). The collected absorbance was not corrected for the absorbance of the substrate (See Figure A.7 for the absorbance of CaF_2), because the substrate did not absorb a significant amount of light in the LSPR region.

We were curious about why the ordering of the layers had such an influence on the optical properties of the films given that composition and the interfaces between the layers within the film are the same. Given the previously stated finding that all the layers remain intact during the deposition process, we reasoned that the two samples in Figure 4 might produce a different combined optical spectrum due to differences in reflectivity that arise from the order in which the beam encounters each layer. To test this hypothesis, we took the UV-vis/NIR spectra of the samples in Figure 2.4, arranging the samples so that the beam entered the sample from the opposite direction. The resulting spectra were identical regardless of the incident beam direction (Figure A.8) apart from a small change in the intensity of the signal likely caused by the inhomogeneity of the film thickness. We concluded that the loss of absorbance due to reflectance at each interface cannot be the major cause of the observed differences in the absorbance of the different film structures.

The main difference between the samples with the opposite ordering of the layers is the proximity of the highest and lowest-doped materials to either the substrate or air interfaces. The layer directly in contact with CaF_2 is exposed to a much higher dielectric environment than that provided by the interface with air.[42-43] The shape and energy of LSPR peaks are strongly influenced by the dielectric environment,[16,44-47] shifting to lower energy and broadening when placed in a high dielectric environment. Further, the ITO nanoparticles with higher doping level have been shown to be less affected by the change in the dielectric medium then the lower doped nanoparticles.[16,48-52] Thus, the absorbance contribution of the 0.7% ITO layer in the film shown in Figure 2.4a might be underrepresented in the multilayered films because it is sandwiched between materials with higher dielectric constants than air: the substrate and another ITO film. In the sample shown in Figure 2.4b, the 16% ITO layer is sandwiched between the substrate and the 7% ITO layer that both have relatively high dielectric constants. As more layers are deposited, the environment surrounding the 16% ITO layer remains constant and its contribution is not diminished from being in contact with a high dielectric medium.

To test our hypothesis that the dielectric environment strongly affects the combined optical spectrum of multilayered films, we designed a simpler system that consisted of only two layers comprised of the 16% and 0.7% ITO nanocrystals. Two films were constructed wherein we changed the order in which we spin-coated the ITO solutions and the optical properties for each were analyzed (Figure 2.5a).

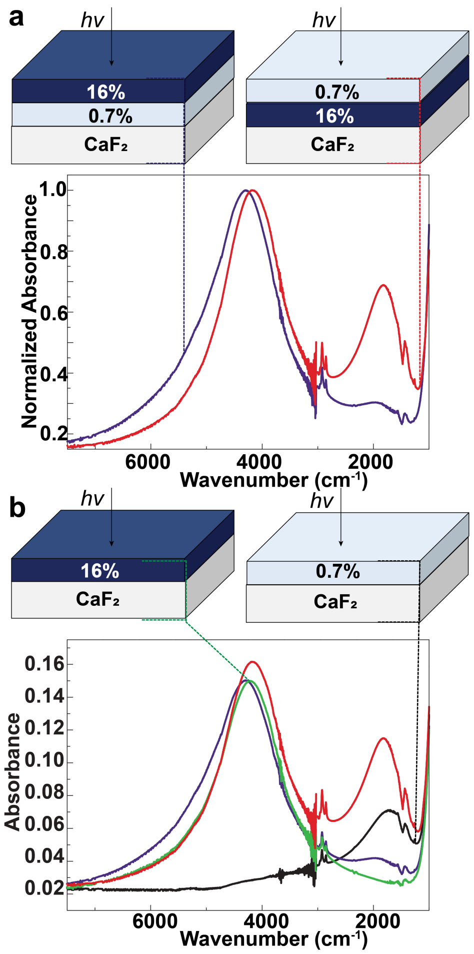

Figure 2.5. The order of ITO layers determines the absorbance. (a) Bilayer films fabricated to evaluate the influence of the surrounding dielectric medium on the combined optical responses. The diagrams show the order in which the ITO solutions were spin-coated. The solutions were diluted so that the measured absorbance was approximately equal in intensity. The spectra were normalized to the intensity of the optical absorbance peak at 4,509 cm^{-1} contributed by the 16% Sn-doped film. (b) Raw (non-normalized) absorbance of the two-layer films (same colors as in (a)) plotted with the individual spectra of the 16% (green) and 0.7% (black) ITO films. The direction of the beam is shown by the arrows.

When 16% ITO is layered over the 0.7% ITO layer on CaF_2, the spectrum (Figure 2.5a) resembles that of the higher doped film alone. The contribution of the lower-doped layer is underrepresented. The absorbance due to the 0.7% ITO film (at 1,822 cm^{-1}) has lower intensity than was recorded for the lower-doped film alone (Figure 2.5b). When the layering is reversed, absorption due to the 0.7% Sn-doped layer can be clearly identified.

The intensities of the layers are not equal but are clearly discernable in the combined optical spectrum. The raw optical spectra of the lower and higher-doped films by themselves compared with the spectra of the two-layer films (Figure 2.5b) clearly show the changes in the absorbance maxima positions and intensities. Layering the 0.7% Sn-doped nanocrystals over the 16% Sn-doped layer intensifies the absorbance of the individual contributions (red trace in Figure 2.5a and b) and red-shifts the 16% Sn-doped layer contribution while blue-shifting the optical contribution of the lower doped layer.

The energy shifts observed in the combined spectra of the two-layer films are consistent with the effects expected from changing the dielectric environment in the vicinity of the film. Further, the attenuation and intensity enhancement of the optical properties in the two-layer films follow the same trend as we found in the multilayered films. The contribution of the 0.7% ITO layer sandwiched between the substrate and the higher doped layer is diminished significantly from being in contact with a high dielectric environment, whereas the reverse ordering does not lessen the optical contribution of the 16% ITO layer to the combined absorbance.

In both the two-layer and multilayered films, the changes in the spectral response appear to be strongly influenced by the local dielectric environment of the layer. Films with a lower doping concentration appear to be affected to a higher extent than the samples with a higher doping level. As a consequence of these effects, spin-coating consecutive layers of ITO films does not result in easily predictable combined absorbance. Given our interests in developing a convenient approach to constructing optical filters from nanocrystal building blocks, we did not investigate other possible reasons for the observed phenomena in the multilayered films, but instead moved on to evaluate the optical properties of homogeneously mixed nanocrystal films. We reasoned that, if the sensitivity of the LSPR to the dielectric environment of the substrate and neighboring layers has a strong influence on the combined optical response, we should be able to fabricate films where the different nanocrystals are homogeneously distributed throughout the film producing a uniform dielectric environment. This approach could potentially lead to a more predictable optical response.

Homogeneously Mixed ITO for Wide Band-Stop Filters. Provided that the ITO nanocrystal films can be solution-processed, a uniform dielectric environment should be achievable through simply combining the nanocrystal solutions of different doping concentrations to attain a combined absorbance that is the sum of the absorbances of the individual nanocrystals. Creating a homogeneous dielectric environment should then allow us to predictably engineer a wide band-stop optical filter covering a range of wavelengths from the mid-IR to the near-IR. Thus, we set out to investigate if mixing the nanocrystal solutions and processing them into a thin film would enable us to absorb light covering the range of 1,000 and 6,000 cm^{-1} and avoid the unpredictable optical properties observed for the multilayered films.

From the library of nanomaterials in Table 2.1, we selected the same homogeneously-doped ITO nanocrystals that we used to design the multilayered films and that had individual LSPR absorbance peaks in the range from the mid-IR (1,000 cm^{-1}) to the near-IR (6,000 cm^{-1}). The absorbance spectra of the selected nanocrystals are shown in Figure 2.6a (dashed blue lines). Figure 6a shows the predicted absorbance spectrum (solid red line) we obtained by summing the normalized absorbance data for the five homogeneously-doped ITO nanocrystal components. The calculated spectrum predicts a wide band absorbing light between 1,000-6,000 cm^{-1}, encompassing the range of wavelengths covered by the absorbances of the individual nanocrystal components. Note that in the summed spectrum the intensity near 2,000 cm^{-1} is lower than one might intuitively predict from the component spectra. We attribute the decreased absorbance intensity to decreased overlap between neighboring spectra. If mixing the component ITO nanocrystals results in additive absorbance properties, then we would expect a spectrum similar to the predicted spectrum where the absorbance intensity across 1,000 – 6,000 cm^{-1} is equal.

To test the hypothesis that mixing nanocrystals would result in predictable additive optical properties, we mixed the ITO nanocrystal solutions (0.7, 1, 3, 7, and 16% ITO) in concentrations such that the measured absorbance intensity of each nanocrystal doping level would be equal when processed into a thin film. We spin-coated the resulting mixture onto a CaF_2 substrate and measured the optical absorbance by FTIR and

UV/Vis spectroscopy. Figure 2.6b depicts the summed spectrum (red) from Figure 2.6a overlaid with the experimentally measured absorbance spectrum resulting from a mix of nanocrystals of different doping levels processed into a thin film (blue).

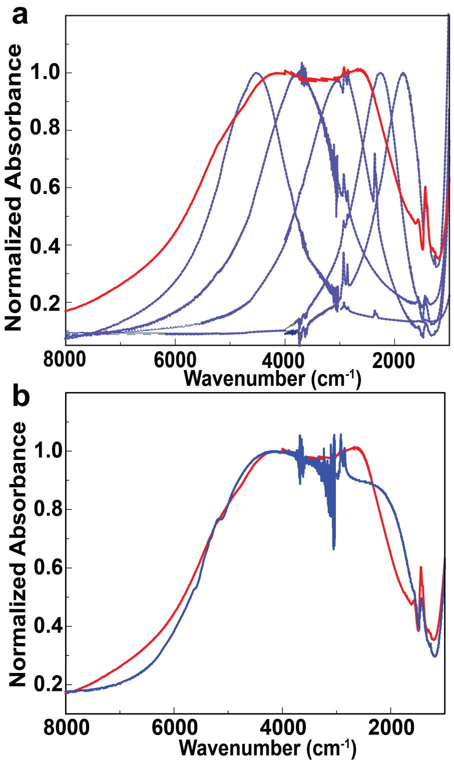

Figure 2.6. Formulation and evaluation of a wide band-pass filter produced by homogeneously mixing nanocrystals in a thin film. (a) Individual spectra (dashed lines) of homogeneously-doped nanocrystals (0.7, 1, 3, 7, and 16% ITO) were summed to obtain the combined normalized spectrum (red) that establishes the predicted optical response of the filter; (b) Comparison of the predicted (red) and measured (blue) absorbance of homogeneously mixed ITO nanocrystal thin film. The interference in the wavelength range of 4,500 to 3,000 cm^{-1} is due to CH stretches and instrumental noise at the end of the detector ranges where the traces from the UV/Vis and FTIR spectrometers were combined.

The experimentally measured spectrum looks remarkably similar to the predicted optical response. The absorbance onset starts at about 7,000 cm^{-1} for both spectra. The combined absorbance extends far into the mid-IR (~1,000 cm^{-1}) accounting for the individual contributions of each nanocrystal component. Based on the measured experimental spectrum, the optical properties of ITO used in the mixed film are not experiencing an unequal intensity enhancement or attenuation. Given that the same ITO solutions were used to prepare the films with the optical responses shown in Figures 2.4c, 2.4d and Figure 2.6b, the exceptional match between the experimental spectrum and the predicted spectrum in the homogeneously mixed solution films and the loss of the contributions of individual components in the multilayered films clearly demonstrates the superiority of using a solution processing method that renders a uniform dielectric environment.

The close agreement between the measured and predicted spectra supports our hypothesis that a predictable combined optical response is achievable by mixing nanocrystals of different Sn doping concentrations in solution and subsequently spin-coating the mixed solution into a film. The equal contributions of the individual components in the experimental spectrum suggest that ITO nanoparticles of each doping concentration are experiencing a dielectric medium created by a uniform mixture of the other ITO nanocrystals which results in diminishing the effects of the dielectric medium gradient at the air/film and film/substrate interfaces. The absorbance of the film covers a wide energy range desired for a wide band-stop filter or as a coating for low-emissivity windows.[5-15,29–34,57] These results indicate that both the range of absorbance as well as the absorbance intensity are predictable and tunable through selection of different ITO nanocrystals from the library of synthesized materials. The additive nature of the absorbance demonstrated by the solution-processed films, combined with the tunability of the ITO nanocrystal synthesis, enables a superior level of control over the optical properties of the band-stop filters for the near-IR to the mid-IR region. The final absorbance spectrum is easily predicted by looking at the LSPR energies and shapes of the ITO solutions prior to mixing. This level of tunability is important for a facile design of band-stop filters and has not yet been demonstrated in solution-processed films.[2,8,49-51]

Homogeneously Mixed Core/Shell ITO/In_2O_3 Nanocrystals. Having successfully engineered a wide band-stop filter, we turned our attention to the construction of a narrow band-stop filter to emphasize that we can selectively block wavelength ranges while allowing some light to pass in the mid-IR. Our goal was to engineer a band-stop filter schematically illustrated in Figure 2.1b, where two distinct energies of light are blocked, but all other energies of light are allowed to pass. To construct a narrow band-stop filter, we wanted to produce a film from a mixture of two types of nanocrystals that have widely separated peaks and narrow line widths. To do this, we adjusted both dopant level and core/shell architectures to tune the peak positions and widths.

For the narrow band-stop filter, it is desirable to have a set of clearly separated peaks which can be achieved via using a distinctly different doping concentrations and decreased line widths. As a starting point, we considered the nanocrystals that led to the highest and lowest energy peaks shown in Figure 2.3a (16% and 0.7% homogeneously-doped ITO). The two films have a slight overlap in their optical spectra at around 3,000 cm^{-1}. In an attempt to separate the spectra even further, we used the synthesis modification discussed above that leads to the LSPR energy shifts and narrowing of the line width: the core/shell approach. We synthesized ITO nanoparticles with 12% Sn doping concentration in the core and a thin 0.3 nm In_2O_3 shell so that the overall doping level decreased to 11%. Although these core/shell nanocrystals have a lower doping level (11 %) than the 16% ITO, the dopant activation introduced by an undoped shell shifts the LSPR of the film to the same wavelength (4,509 cm^{-1}). The shell also reduces scattering, thus decreasing the line width from 1,534 to 1,512 cm^{-1} (Figure 2.7a).[34] As we previously mentioned, the lowest doping concentration at which we observed the LSPR in homogeneously-doped nanoparticles was 0.7% (LSPR max at 1,844 cm^{-1}). In order to shift the LSPR to an even lower energy to increase the peak separation from the higher doped peak we aimed to further decrease the doping concentration, but through a core/shell strategy. Using an undoped shell to activate surface dopants and decrease scattering, we synthesized ITO nanoparticles with only 0.4% Sn doping at the core and added an ultrathin 0.2 nm shell of In_2O_3, lowering the overall doping to 0.35% Sn while still supporting the LSPR in the sample. The resulting optical spectrum is shown in Figure 2.7b. An ultrathin shell allowed for a distinguishable LSPR peak at incredibly low doping concentration along with shifting the LSPR energy maximum to 1,740 cm^{-1}.

The top trace in Figure 2.7c shows the sum of the individual, normalized spectra from each of the two individual nanocrystal components. This is the spectrum that one would predict if the absorbances are additive and it shows two energetically separated peaks with absorbance maxima at approximately 4,400 cm^{-1} and 1,800 cm^{-1} of equal absorbance intensity. To construct the filter, we mixed the two nanocrystal solutions in concentrations such that the resulting absorbance intensity from the nanocrystal films would equal approximately 0.1. After having mixed the solutions of the 12% Sn-doped ITO and 0.4% ITO nanocrystals covered with thin In_2O_3 shells in the appropriate concentrations, the nanocrystals were spin-coated into a thin film. The absorbance was measured using FTIR and UV/Vis spectroscopy. The resulting spectrum is shown in Figure 2.7c (bottom) (Figure A.9 for non-normalized data).

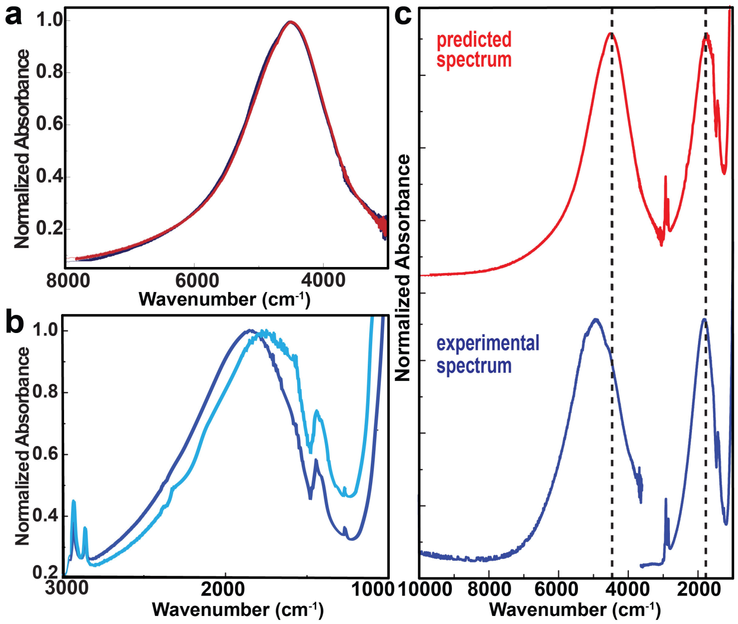

Figure 2.7. **Optical properties of ITO nanocrystal building blocks and formulation/evaluation of a narrow band-pass filter.** (a) Comparison of the optical spectra for nanocrystals containing 16% homogeneously-doped ITO (dark blue) and ITO core/In_2O_3 shell containing 12% Sn (red trace). The spectra are normalized at the absorption maximum. The ultrathin indium oxide shell (0.3 nm) activates the surface dopants and decreases scattering. The two films have an identical LSPR energy max at 4,509 cm^{-1} but the LSPR line width of the core/shell film is narrower (1,512 compared to 1,534 cm^{-1}); (b) Comparison of the absorbance spectra for 0.7% homogeneously-doped ITO (darker blue) and 0.4% ITO with a thin In_2O_3 shell (light blue). Addition of an ultrathin 0.2 nm undoped shell facilitated surface dopant activation and decreased scattering which resulted in a distinguishable LSPR peak at only 0.4% Sn doping concentration; (c) Predicted (top) and experimental (bottom) spectra of the homogeneously mixed thin film produced from 0.4% and 12% Sn-doped ITO cores with thin In_2O_3 shells, illustrating the properties of a narrow band-stop filter.

The predicted spectrum, which is the sum of the individual spectra, and the measured absorbance spectra are nearly identical. Both the predicted and measured optical spectra show two distinct absorbance peaks of approximately equal intensity, with one appearing at high energy and one appearing at low energy. Given that using the ITO solutions of similar doping concentrations in the two-layer films (Figure 2.5a) resulted in the attenuation of one of the components, the predictability of the optical response of the narrow band-stop filter shown in Figure 2.7c is truly remarkable. This further supports our hypothesis that homogeneously mixing nanocrystals in solution prior to spin-coating leads to a more homogeneous dielectric environment.

Compared to the predicted absorbance spectrum (Figure 2.7c, top), the high energy band peak is slightly blue-shifted and wider in the measured absorbance spectrum (Figure 2.7c, bottom). We attribute the blue-shift of the high energy LSPR peak to the higher dielectric environment that the 12% ITO with an In_2O_3 shell are embedded in compared to air. ITO with any doping concentration has a higher dielectric constant than air. ITO nanocrystals with high doping concentrations have higher LSPR peak intensities compared to the nanocrystals with low doping level at the same film thicknesses. In order to achieve similar absorbances for the two solutions we chose, we used a larger fraction of the 0.4 % ITO with a thin In_2O_3 shell than of the 12% ITO with an undoped shell (80% of the lower doped nanoparticles and 20% of the higher doped ones). Thus, the highly doped component of the film is affected by the changes in the dielectric medium more than the lower doped ITO given the film composition. The broadening of the high energy band is attributed to the decreased ability of the 12% ITO with an undoped shell to couple effectively, resulting in increased damping. Thus, when designing a filter consisting of significantly unequal ratios of the components, we must take into consideration the overall dielectric environment in the film and how it affects those components. The combined optical response modulations produced by the created dielectric medium can also be used as a lever to sculp the desired optical filter. These results clearly demonstrate that homogeneously mixed films of specifically tailored ITO nanocrystals can be used to produce a narrow band-stop filter.

Conclusion

A library of 12 ITO nanocrystals with tin doping concentrations ranging from 0.4% to 16% and core/shell architectures with various degrees of dopant activation was constructed using a slow-injection, esterification synthetic strategy. The synthetic method allows one to tune the concentration and spatial distribution of dopant atoms in order to sculpt the LSPR peak shape and energy in the near-IR and mid-IR. We used the library of nanomaterials to produce layered and homogeneously mixed nanocrystal films and studied how the film architecture influenced the optical properties of the films. Wide and narrow band-stop filters were fabricated to evaluate the utility of this approach for applications involving plasmonic band-stop filters.

For nanocrystal films comprised of layers of different nanocrystals, we found that the combined optical properties were not easily predictable. The response was not additive and depended upon the order of deposition of the layers. We attributed the difference between the layered and the experimental LSPR spectra to the influence of interfaces between the layers of nanocrystals that create dielectric gradients within the final film. The optical response of the ITO nanocrystal layers within the film was either attenuated or enhanced depending on the dielectric environment, which led to unpredictable shifts in energy and broadening of individual absorbances. On the other hand, homogenous mixing of ITO nanocrystals with different doping concentrations in a single film produced optical responses that matched predictions from simple addition of the component optical absorption spectra. These mixed nanocrystal films possess a homogeneous dielectric environment and lack interlayer boundaries that may reflect or scatter light in ways that are not simple to predict. Based upon these findings, it was possible to design and produce nanocrystal ITO films from solution mixtures of precisely doped nanoparticles that function as both wide and narrow band-pass filters in the near- and mid-IR, enabling the use of tunable ITO nanocrystals for band-pass filter applications. To our knowledge, this is the first demonstration of plasmonic wide and narrow band-stop filters that rely on simple solution-processing fabrication scalable to large areas and have predictable properties.

The results suggest that the combination of nanocrystal synthesis, to control the optical properties of the building blocks, and solution processing is a powerful approach to designing thin film optical filters. Although demonstrated here only for ITO nanocrystals, this strategy could also be applied to tuning the LSPR response of other doped metal-oxides, such as cerium- and molybdenum-doped indium oxide,[31,52] In-doped cadmium oxide, or aluminum-doped zinc oxide[31] for a variety of applications beyond optical filters, including electrochromic windows and sensing.[30,31,53]

Bridge

Chapter II summarized my work with ITO nanocrystal films and showed that their optical properties are highly tunable and additive. These materials have potential for being implemented to reduce our energy consumption. The thin-film processing techniques described in this chapter were used for the work described in Chapters III, IV, and VI. The next chapters focus on water electrolysis technologies and failure modes analysis of the electrolyzer systems.

CHAPTER III

OXYGEN EVOLUTION ELECTROCATALYSIS IN ACID: ATOMIC TUNING OF STABILITY NUMBER FOR SUBMONOLAYER IRIDIUM OXIDE ON CONDUCTIVE OXIDES FROM MOLECULAR PRECURSORS

Chapter III contains co-authored unpublished material. Prof. Boettcher and I conceived of the project. Matej Zlatar and I performed the experiments and analyzed data with assistance from Nathan Stovall, Grace Lindquist, Daniel Escalera-Lopez, and Amanda Cook. Matej Zlatar and I wrote the paper with editorial assistance from all the authors. It is prepared in the format of the *ACS Catalysis*.

Introduction

Water electrolysis is a key source of clean, renewable H_2.[1-2] Powered by low-carbon or renewable energy, water electrolysis enables decarbonization of many economic sectors if capital costs are sufficiently low. H_2 production by electrolysis is rapidly becoming more cost-competitive with an 80% decrease in renewable electricity prices since 2010.[2] Alkaline and proton-exchange-membrane water electrolysis (PEMWE) are the most-mature electrolysis technologies on the market today.[3] PEMWE offers many benefits over alkaline electrolysis due to the use of a solid polymer membrane (Nafion) instead of a liquid electrolyte which enables operation at high current densities (> 2 $A \cdot cm^{-2}$ at 1.7 V), load following, reduced product crossover, and the collection of compressed H_2.[3-5] The acidic nature of Nafion, however, limits the catalyst choice for PEM stacks to the platinum group metals (PGM) (mainly Ir and Pt) and restricts the materials choice for the stack components to acid-stable titanium coated with PGMs.[3, 6-7] Alternatives to the PEMWE that use ionomer membranes with basic character are currently under development, but are still at an early stage.[8-10]

While Pt at the cathode operates at a low overpotential, the oxygen evolution reaction (OER) at the anode requires higher overpotentials even with the current benchmark catalyst, IrO_2.[11] Currently catalyst cost is not the driving factor of the electrolysis costs, but it will play a significant role once the reduction of other costs is achieved and demand for precious metals increases.[12] Decreasing the Ir loading at the anode from 2-3 $mg \cdot cm^{-2}$ to 0.4 $mg \cdot cm^{-2}$ would make the PEMWE more sustainable and cost-effective.[12] Many non-PGM materials have been studied as a replacement for IrO_2, but reaching the activity of IrO_2 requires high loadings and long-term stability remains an issue.[13-16] OER catalyst cost reduction is possible through increasing its lifetime or maintaining high activity while decreasing the loading. The latter is usually accomplished by dispersing IrO_2 onto a conductive acid-stable support maximizing the exposed active sites while taking advantage of the favorable metal-support interactions.[17-19]

Regrettably, there are only a few known nominally stable support materials that can withstand harsh OER conditions in an acidic environment. Among the most studied are TiO_2, fluorine-doped tin oxide (FTO), and antimony-doped tin oxide (ATO).[17-20] Crystalline forms of TiO_2 are acid-stable but this compound is a semiconductor. Thus, when a mixed IrO_2/TiO_2 catalyst is used, a sufficient amount of Ir must be incorporated to create a conductive network.[18] However, experimental reports along with computational work suggest activity and stability improvements with the addition of TiO_2 to or on top of IrO_2.[18, 21-22] The enhancement is attributed to tuning the surface charge density through favorable metal-support interactions.[21] The addition of TiO_2 has been probed by dispersing IrO_2 nanoparticles on TiO_2 support, covering a layer of IrO_2 with TiO_2, synthesizing core/shell IrO_2/TiO_2, and other methods.[18, 21, 23] Thin layers of TiO_2 on Pt or IrO_2 has also been demonstrated to accelerate water dissociation for HER in acid and base.[24] Unlike TiO_2, FTO and ATO are conductive, although their electrical properties strongly depend on the synthesis method and dopant concentration/distribution.[25-28] In a stability study under OER-relevant conditions FTO showed higher stability than ATO, exhibiting no measurable dissolution -0.34 to 2.7 V vs. RHE in acid. ATO degrades due to Sb^{5+} solubility which leads to formation of an SnO_2-rich surface layer that impedes electron transport.[29] Decorating ATO or FTO high-surface-area supports with IrO_2 nanoparticles facilitates better catalyst dispersion, favorable metal-support interactions, and purportedly leads to reduction in loading in three-electrode tests with liquid electrolytes.[17, 30] The three-electrode cell test conditions, however, differ from the stability/activity tests in a membrane-electrode assembly (MEA).[3] Compressed cell stacks suffer from limited catalyst utilization due to ion, electron, or mass transfer effects; the catalyst at the interface with the membrane is the major contributor to the observed current density.[31] IrO_2 dispersed on an inert support in an MEA has even less catalyst in direct contact with the membrane. Thus, the field lacks the knowledge of how to prepare systems where every Ir atom is electrochemically active for catalysis and how to maximize the performance of such a catalyst.

The exposure of every Ir atom seems possible only through having a monolayer-thick catalyst layer on a support. During OER, the catalyst can undergo dissolution/redeposition processes that ultimately lead to the loss of the catalyst in a three-electrode cell setup with a liquid electrolyte but might be mitigated by the presence of a solid membrane impeding the migration of the Ir species away from the anode.[32] Another strategy to improve the stability of an ultrathin catalyst would be an addition of a protective layer that can prevent Ir dissolution. An attempt to create a sub-monolayer-thick catalyst has been made using a molecular catalyst $[Ir(pyalc)(H_2O)_2(\mu\text{-}O)]_2^{2+}$ that binds to metal-oxide surfaces and remains stable for OER at pH 2.6 on *nano*ITO electrode for several hours.[33] The proposed molecular catalyst, however, did not withstand stronger acids and transformed into an amorphous IrO_x.[34] To improve performance, the metal-oxide supports with $[Ir(pyalc)(H_2O)_2(\mu\text{-}O)]_2^{2+}$ bound to their surface were annealed to remove the ligands and form an ultrathin layer of IrO_2 on the surface.[34] The supports were soaked in the precursor solution multiple times between the annealing steps to grow thicker IrO_2 layers. This type of solution-based atomic layer deposition (ALD) improved stability compared to the initial molecular Ir complex, but long-term durability was not achieved. In addition, $[Ir(pyalc)(H_2O)_2(\mu\text{-}O)]_2^{2+}$ is not commercially available which complicates further study and scaling.

Inspired by the reported influence of the nature of the metal oxide and the amount of bound Ir on activity, we report in Chapter III an approach to create, and fundamentally study, oxide-supported Ir leveraging a simple and commercial 1,5-cyclooctadiene iridium chloride dimer, $[(COD)IrCl]_2$. We show that $[(COD)IrCl]_2$ adheres to the surface of metal oxides in a simple soaking procedure and upon annealing forms a sub-monolayer-thick IrO_x catalyst. We study the OER performance of the sub-monolayer-thick IrO_x of different loadings in acid on ATO nanoparticles and planar FTO substrates, discovering that the increase of Ir loading not only improves activity but also enhances stability of these catalyst. By adding an ultrathin protective TiO_2 layer by ALD, we further increase IrO_x intrinsic activity but trigger high dissolution, as demonstrated by changes to the stability number (the number of O_2 molecules evolved per atom of iridium lost)[35] measured via *in situ* electrochemical measurements coupled with inductively-coupled plasma mass spectrometry (ICP-MS). The changes to the catalyst chemical structure are tracked with X-ray photoelectron spectroscopy (XPS) that shows downshifts in Ir 4f binding energy upon TiO_2 addition. We hypothesize that in this new system most iridium atoms are active during OER, and the surface characterization results are not obscured by the contribution from the bulk of the catalyst. This approach allows us to access the impact of the binding environment on the intrinsic activity of iridium atoms and develop strategies for engineering better OER catalysts.

Experimental

Materials. Chloro(1,5-cyclooctadiene)iridium(I) dimer ($[(COD)IrCl]_2$) was purchased from TCI. Antimony-doped tin-oxide (ATO) nanoparticles (~50 nm) were ordered from Sigma Aldrich. HPLC grade solvents used in synthesis (acetonitrile and toluene) were purchased from Fisher Chemical. Isopropanol (IPA) and toluene used in washing the synthesized material and electrode ink preparation were purchased from Sigma Aldrich and used as received. Fluorine-doped tin oxide (FTO) coated glass slides (surface resistivity ~ 13 Ω/sq) were obtained from Sigma Aldrich.

Synthesis of Ir-Functionalized Metal-Oxides. ATO nanoparticles were vacuum dried at 80 °C overnight on the Schlenk line before bringing them into the glovebox under N_2. Acetonitrile and toluene used in synthesis (Fisher Chemical, HPLC grade) were dispensed under N_2 from an LC Technology SP-1 solvent system and transferred to the glovebox in an air-free flask. The 3.9 mM solutions of $[(COD)IrCl]_2$ in toluene and acetonitrile were prepared in the glovebox. Sixty milligrams of dried ATO nanoparticles were added to 4 vials: two with 3 mL of $[(COD)IrCl]_2$ in toluene; and two with 3 mL of

$[(COD)IrCl]_2$ in acetonitrile. Each vial was capped with a Teflon-lined lid. The mixtures were left to stir overnight; one reaction for each solvent was kept at 100℃, the other at room temperature. Then the particles were transferred to a centrifuge vial and washed with toluene or acetonitrile (depending on the solvent used in synthesis) twice to remove the remaining unreacted $[(COD)IrCl]_2$.

Planar 1 cm × 1 cm FTO substrates were sonicated in IPA, cleaned with O_2 plasma, and heated on a hot plate to 100 ℃ before being transferred to the glovebox. The substrates were placed into glass vials with Teflon-lined lids. A small amount of the 3.9 mM solution of $[(COD)IrCl]_2$ in toluene (just sufficient to cover the surfaces of the FTO substrates) was added into each vial with a small stir bar. The substrates were left to react overnight at 100 ℃. Then the substrates were taken out of the glovebox and sonicated in toluene to remove any unreacted Ir dimer.

Characterization of Ir-Functionalized Nanoparticles and Planar Substrates. Elemental compositions of Ir-functionalized ATO nanoparticles and FTO substrates were determined with a Thermo Scientific ESCALAB 250 X-ray photoelectron spectrometer (XPS) using an Al Kα monochromated (20 eV pass energy, 500 μm spot size) source. The samples were charge-neutralized using an in-lens electron source. Spectra were analyzed using ThermoScientific Avantage 4.88 software. Peak binding energies were referenced to the C1s hydrocarbon peak at 284.8 eV. Powder samples were prepared by drop-casting solutions of nanoparticles dispersed in IPA onto silicon wafers and allowing them to dry.

The amount of Ir on Ir-functionalized ATO nanoparticles was determined by inductively coupled plasma optical emission spectrometry (ICP-OES). A Teledyne Leeman Laboratories (Hudson, NH) Prodigy High Dispersion ICP-OES system was used. We were unable to remove Ir off the ATO nanoparticles once they were annealed, which is a crucial step to grow a thicker layer of IrO_x on the surface. Instead, we analyzed the precursor solution of $[(COD)IrCl]_2$ before and after reacting it with a known amount of ATO nanoparticles. A 0.1 mL aliquot was taken from the precursor solution before and after the reaction with the nanoparticles. The solvent was allowed to evaporate and the precipitated $[(COD)IrCl]_2$ was digested in concentrated HCl overnight at room temperature. The resulting solution was passed through a 0.1μm syringe filter and diluted with 2% v/v HNO_3 for analysis. This procedure was repeated after each consecutive soak.

To track the dimer attachment to the surface of ATO nanoparticles in each solvent, optical measurements were collected on Perkin Elmer Lambda-1050 UV/Vis/NIR spectrophotometer. Small aliquots (0.25 mL) of the $[(COD)IrCl]_2$ solutions were taken before adding ATO nanoparticles and at different time intervals during synthesis, diluted to 2.5 mL and analyzed from 250 to 800 nm with a scan resolution of 1 nm.

NMR spectra were collected on Bruker Avance III-HD 600 MHz NMR spectrometer. The 3.9 mM $[(COD)IrCl]_2$ solutions were prepared with toluene-d_8 and acetonitrile-d_3 (Cambridge Isotope Labs) and were analyzed before and after reacting with ATO nanoparticles for 5 h without further dilutions.

Triphenyl silanol (TPS) and tris(*tert*-butoxy) silanol (TBS) were dissolved separately in toluene-d_8 in the glovebox under inert atmosphere. ^1H NMR spectra of the initial solutions were recorded. To the 1mL solutions of TBS and TPS, 2 mL of 3.9 mM $[(COD)IrCl]_2$ solution in toluene-d_8 was added. The mixed solutions were set on a hot plate at 100 ℃ with stirring for 1 h. ^1H NMR spectra of the solutions after 1 h of mixing were recorded.

The electron microscopy and chemical composition images of Ir-functionalized nanoparticles were collected on a Titan 80-200 TEM equipped with an EDX detector (accelerating voltage of 200 kV). The samples for analysis were prepared by drop-casting dilute solutions of ATO and Ir-functionalized ATO nanoparticles in IPA on Cu grids and allowing them to dry.

Iridium Layer Growth on Metal-Oxide Substrates. $[(COD)IrCl]_2$ (~60 mg, 0.09 mmol) was dissolved in 20 mL of anhydrous toluene in the glovebox. The solution was filtered through a syringe filter and 400 mg of ATO were added. The nanopowder was allowed to react in the Ir-containing solution overnight at 100 ℃. The reacted powder was washed in toluene twice via centrifugation and annealed in the box furnace at 350 ℃ for 3 h. The annealed powder was ground, then dried in the oven overnight at 100 ℃ before being transferred to the glovebox. The powder was reacted with $[(COD)IrCl]_2$ solution in toluene for a second time. At the end of the second overnight reaction the powder was again washed, annealed, and placed back in the glovebox to react with $[(COD)IrCl]_2$ a third time. After the third soak the nanopowder was again washed in toluene and annealed at 350 ℃ before being used for electrochemical testing. The catalyst shell growth on a planar FTO substrate was accomplished in the same manner. The powder samples and the planar substrates were analyzed with XPS after each soak.

Thermogravimetric Analysis of $[(COD)IrCl]_2$. A 10 mg sample of $[(COD)IrCl]_2$ was placed in an Al pan and loaded into TA Instruments Thermogravimetric Analyzer (TGA Q500). The sample was heated from room temperature to 600 ℃ at 5 ℃/min in air (Figure B.3).

Atomic-Layer Deposition (ALD) of TiO_2. ATO nanopowder after one and three soaks in Ir dimer precursor solution in toluene annealed at 350 ℃ for 3 h was placed in the ALD vacuum chamber on a piece of Al foil with raised edges. A fine metal mesh was placed over the foil to prevent the powder loss during the deposition process. The powder was decorated with TiO_2 via 5 ALD cycles. The deposition was carried out at 250 ℃ using tetrakis(dimethylamido)titanium (TDMAT) and water as TiO_2 precursors. The precursors were alternating with a 0.05 s pulse of water and a 0.5 s pulse for TDMAT allowing a 60 s purge between each precursor.

Ir-functionalized FTO substrates (1 cm × 1 cm) after one and three soaks in the Ir dimer solution in toluene and a 3-hour anneal at 350 ℃ were placed in the ALD vacuum chamber and reacted with the same precursors as the nanopowder but at 150 ℃ with a 1 s water pulse, 0.25 second TDMAT pulse, and a 15 s purge between the precursors. After deposition some of the substrates were additionally annealed at 400 ℃ for 1 h.

The thickness of the resulting TiO_2 protective layers was measured on a Si witness wafer with a Woollam M44 Spectroscopic Ellipsometer. Measurements were collected at the incident angles of 45°, 50°, 55°, 60°, 65°, 70°, 75° in the range 240 - 1688 nm. The analysis is based on least-squares regression analysis. The deviation is represented by the mean square error (MSE).

Electrochemical Measurements in a Three-Electrode Cell. The annealed Ir-functionalized nanopowder was mixed with IPA to prepare a 60 mg/mL catalyst ink. IPA and O_2 plasma cleaned FTO substrates (1 cm × 1 cm) were spin-coated with the ink at 3000 rpm (Laurell WS-400-6NPP-LITE) and annealed at 350 ℃ for 1 h. Ir-functionalized planar FTO substrates were used after the 3-h 350 °C annealing. The substrates were fabricated into electrodes by making an ohmic contact to the FTO surface with a Sn/Cu coil wire and Ag paint. The coil was then fixed in a five-inch glass tube. The contact and the tube were insulated by epoxy (Loctite 9460) and cured in the oven. A BioLogic SP300 potentiostat was used in three-electrode mode for electrochemical measurements. The electrodes were tested in 0.1 M $HClO_4$ with a Pt wire as the counter electrode and a saturated calomel electrode (SCE; 0.241 V vs SHE in saturated KCl) as a reference electrode. To determine the catalyst activity towards OER, three CVs (0.5 V – 1.5 V vs SCE) were collected. Electrochemical data were corrected for uncompensated series resistance R_u, which was determined by equating R_u to the minimum total impedance in the frequency regime between 100 mHz to 1 MHz where the capacitive and inductive impedances are negligible, and the phase angle was near zero.

Preparation of Electrodes for SFC-ICP-MS Measurements. Working electrodes used in coupled electrochemical measurements were prepared by drop-casting catalyst spots from previously prepared inks. To achieve a predefined ink concentration of 6.6 mg/mL, the corresponding amount of powder sample was weighed and dissolved in ultrapure H_2O (Merck Milli-Q, 18 MΩ, total organic carbon <3 ppb) and isopropanol in a 7:1 ratio. After dissolving the samples, perfluorinated Nafion ionomer solution (Sigma Aldrich, 5 wt %) was added as a binder in a 4:1 catalyst-to-ionomer weight ratio. Inks were then sonicated for 10 min with 4-s/2-s on/off pulses using a probe sonicator (Branson Ultrasonics SFX150) to achieve homogenous dispersion. The pH of the prepared inks was adjusted to ~11 with 1 M aq. KOH, followed by drop-casting of 0.2 µL aliquots on Au foil plates (25 × 25 mm, 99.95 %, Alfa Aesar) mirror polished with alumina suspensions (sequentially from 1 to 0.5 and finally 0.03 µm particle diameter). Each catalyst spot had a diameter of approximately 1.3 mm, measured on the Keyence VK-X250 profilometer.

SFC-ICP-MS Electrochemical Experiments. To estimate the corrosion stability of Ir on planar FTO substrates and ATO nanoparticles, an inductively coupled plasma mass spectrometer (ICP-MS, Perkin Elmer, NexION 300x and 350x) was connected to custom electrochemical scanning flow cell (SFC). The setup enabled the downstream detection of dissolved species during electrochemical measurements. The SFC setup approaches the samples from above by an XYZ-translation stage (Physik Instrumente) with a force of ~850 mN (measured by force sensor, ME-Meßsysteme). In one case, the working electrode consisted of Ir-functionalized ATO, drop-casted on Au foil, while in the other case, of Ir-FTO substrates. On the inlet tube of the SFC, a graphite rod (Sigma Aldrich, 99.995% trace metal basis) encased in a glass compartment was connected as a counter electrode, while on the outlet side of the cell, the capillary channel was connected to a reference Ag/AgCl electrode (Metrohm, 3 M KCl). This channel ends close to the surface of the working electrode, thus minimizing the uncompensated ohmic resistance. All electrodes were connected to a Gamry Reference 600 potentiostat, and the whole setup was controlled by a custom-developed LabVIEW software. The Ar-purged 0.1 M $HClO_4$ used as an electrolyte was prepared by diluting $HClO_4$ (Suprapur 70%, Merck) with ultrapure water. Electrode potentials are referenced to the reversible hydrogen electrode (RHE) scale, calibrated daily against H^+/H_2 on polycrystalline Pt foil. The catalyst dissolution rate was measured at an electrolyte flow rate of ~3.2 µL s^{-1}, determined by the ICP-MS peristaltic pump. To ensure optimal working conditions, ICP-MS was optimized daily using NexION Setup Solution (PerkinElmer) and calibrated for all investigated metals by three-point calibration. Calibration solutions of 0.5, 1, and 5 ppb concentrations (Certipur ICP-MS Standard, Merck) were prepared daily. The drift and performance of the system throughout the measurements were monitored by several internal standard solutions (Re, Rh, Te, Sc, conc. 10 µg L^{-1}), chosen based on similar first ionization potential and mass (Certipur ICP-MS Standard, Merck).

To assess activity-stability properties, the electrodes were held at 0 mA cm^{-2} for 180 s, followed by 0.5 mA cm^{-2} for 300 s, and again at 0 mA cm^{-2} for 180 s. Obtained analyte signal was recalculated to concentration using the calibration curve and normalized by the flow rate and geometric area of the working electrode. For a full description of the whole setup, please refer to our previous publications.[36-38] Lastly, all measurements were replicated three times to ensure reproducibility. The working electrodes prepared for the three-electrode cell testing were subjected to the same potential holds, rinsed, dried, and analyzed with XPS.

Results and Discussion

Synthesis and Characterization of Ir-Functionalized Metal Oxides.

Determining Conditions for Metal-Oxide Surface Functionalization. The synthesis described in this work was developed using only simple commercial precursors. $[(COD)IrCl]_2$ was chosen as the Ir precursor for its commercial availability, low cost, and solubility in several common organic solvents. Due to the presence of COD and Cl ligands, $[(COD)IrCl]_2$ dissolves well in polar and non-polar solvents. The solution of $[(COD)IrCl]_2$ is, however, unstable in air and upon contact with water, so the synthesis was carried out in the glovebox under N_2.

FTO films on glass and ATO nanoparticles, both conductive and acid-stable, were selected to test whether $[(COD)IrCl]_2$ would adhere to metal oxide surfaces. [20, 29, 39] To determine the optimal conditions for the reaction, polar and nonpolar solvents, acetonitrile and toluene, were tested. The stability of $[(COD)IrCl]_2$ in toluene and acetonitrile (ACN) at room temperature and at 100 °C was confirmed by analyzing the UV-vis spectra of the dimer solutions after 25 h in the glovebox. No changes to the spectra were observed. Then ATO nanoparticles were added to the Ir precursor solutions. The nanoparticles were chosen for the high surface area (47 m^2/g) to make the concentration change in the precursor solution noticeable. The nanoparticles were stirred in the $[(COD)IrCl]_2$ solutions for 25 h with aliquots taken every few hours for UV-vis analysis. One reaction for each solvent was kept at room temperature, one at 100 °C.

Figure 3.1a shows the UV-visible spectra of freshly made $[(COD)IrCl]_2$ solutions in toluene and ACN (see Appendix B for all figures). The spectra in the two solvents look different with the λ_{max} in toluene at 454 nm and in ACN at 413 nm. The difference might be due to interactions of strongly coordinating ACN ligands with the metal centers of the dimer compared to the lack of thereof in weak interaction with toluene.

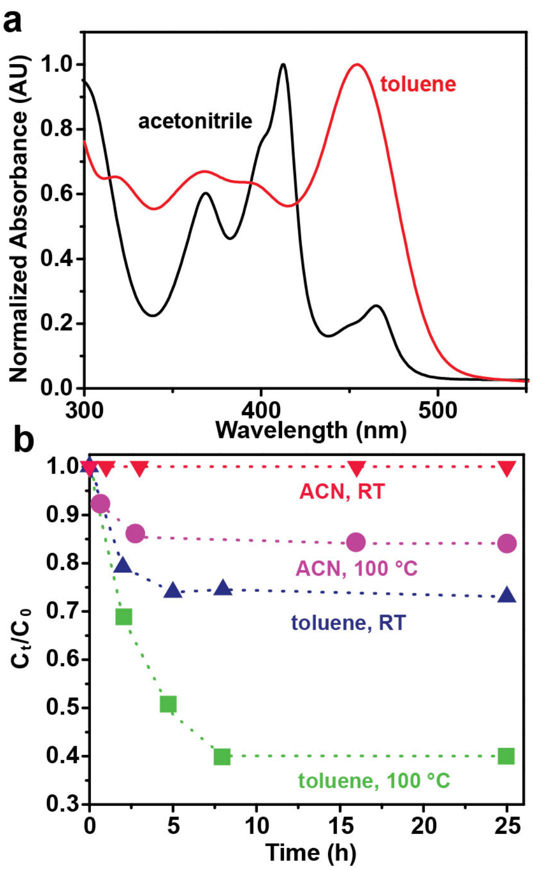

Figure 3.1. UV-vis analysis suggests more $[(COD)IrCl]_2$ adhesion in toluene. a) Normalized UV-vis spectra of $[(COD)IrCl]_2$ taken in acetonitrile (black) and toluene (red). b) The change in concentration of the $[(COD)IrCl]_2$ stock solutions in acetonitrile and toluene during the reaction with ATO nanoparticles at room temperature and at 100 °C.

The absorbance at λ_{max} was used to calculate the change in concentration over time (C_t/C_0; Figure 3.1b). Notably, the spectra of $[(COD)IrCl]_2$ in toluene and ACN do not change their shapes as the reactions progress, just the intensity, suggesting that the dimer preserves its initial structure in the solutions (Figure B.1). No change in $[(COD)IrCl]_2$ concentration was observed for the reaction carried out in ACN at room temperature. However, when the solution was heated to 100 °C, ~15% of $[(COD)IrCl]_2$ attached to the nanoparticles. In toluene, the change in concentration was observed for the reaction carried out at room temperature and at 100 °C. At room temperature, ~25% of $[(COD)IrCl]_2$ attached to ATO; at 100 °C, 60%. The nanoparticles reacted with $[(COD)IrCl]_2$ in ACN and the toluene solution changed color from light blue to dark green (Figure B.2). The attachment of $[(COD)IrCl]_2$ to ATO nanoparticles happens during the first 5-7 h of the reaction. Afterwards the concentration of $[(COD)IrCl]_2$ in the solutions remains unchanged. The lack of continuous dimer loss from the solution up until the end of the reaction suggests that the adhesion reaction is surface-limited.

The difference in the amount of the dimer adhered to ATO in ACN and toluene is likely due to the difference in the interactions between $[(COD)IrCl]_2$ and the solvent molecules. Polar ACN might arrange itself at the surface of the metal-oxide nanoparticles preventing the dimer from interacting with the surface. ACN might also replace the ligands on the Ir centers modifying the affinity of the new structure for the metal oxide surface. Toluene being nonpolar and non-coordinating should not introduce substantial activation barriers for $[(COD)IrCl]_2$ to access the surface of ATO. The surface adsorption/reaction rate increases with temperature as with any other kinetically-controlled process. The significant difference in the amount of $[(COD)IrCl]_2$ adhered to ATO in toluene and ACN also suggests a different mechanism of attachment.

The reactions of ATO nanoparticles and $[(COD)IrCl]_2$ at 100 °C were repeated in deuterated toluene (toluene-d_8) and ACN (ACN-d_3) and monitored with ^{1}H NMR. No substantial changes to the Ir dimer structure were observed during the reactions consistent with $[(COD)IrCl]_2$ adhesion to ATO without the loss of ligands (Figure B.3).

Iridium Functionalization of ATO and FTO Supports. Using the established reaction conditions, we soaked ATO nanoparticles and FTO planar substrate in the 3.9 mM solution of $[(COD)IrCl]_2$ overnight, then analyzed them with XPS, TEM-EDX, and ICP-OES.

XPS analysis of the unreacted $[(COD)IrCl]_2$ powder confirms the 1:1 Ir:Cl ratio. The Ir 4f peak was fitted with two doublets (Ir 4f7 at 61.2 and 62.8 eV) (Figure 3.2a). The binding energies of the 4f7 peaks matched literature values for $[(COD)IrCl]_2$.[40] The peak at 61.2 eV is attributed to Ir(1+) while the peak at higher binding energy was assigned to the hydroxylated Ir surface species.[40] The Ir 4f peak of $[(COD)IrCl]_2$ attached to ATO nanopowder was fit with one set of Ir 4f7 peaks centered at 62.0 eV (Figure 3.2a). The Ir:Cl ratio remained 1:1 suggesting that the dimer attaches or absorbs to the metal oxide intact and is also consistent with monolayer limited growth and all Ir species in the same chemical environment. The Ir 4f peak of the dimer adhered to a FTO substrate was also fit with one set of peaks at 62.1 eV (Figure 3.2a). The Ir:Cl ratio was also 1:1.

The Ir loading on ATO nanoparticles of 0.2 ± 0.03 ng_{Ir}/cm^2_{ATO} was determined by taking aliquots of the precursor solution before and after reacting it with a known amount of ATO and digesting the aliquots for ICP-OES. The distribution of Ir on ATO was mapped with TEM-EDX (Figure 3.2b) and was similarly dispersed before and after heating to IrO_x.

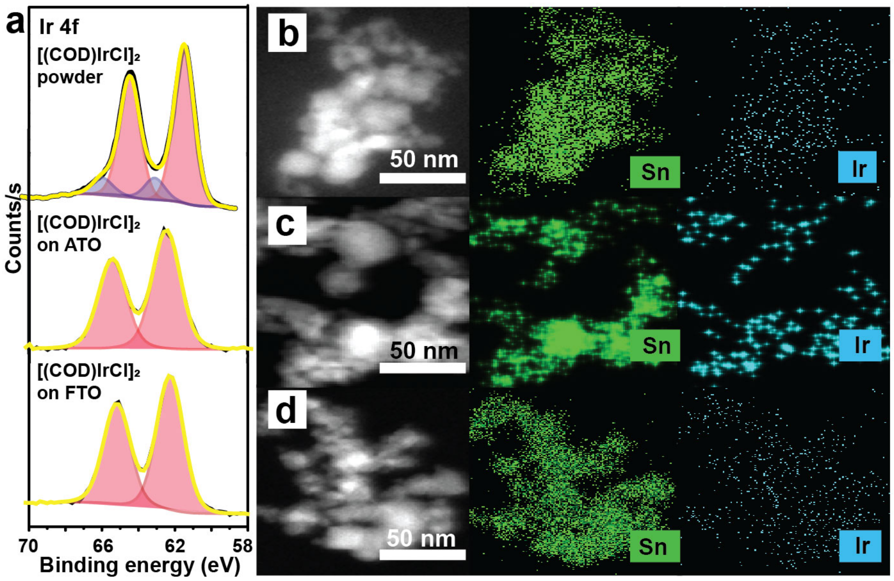

Figure 3.2. **Surface characterization confirms Ir on ATO.** a) XPS of Ir 4f in $[(COD)IrCl]_2$ powder and after the dimer attached to ATO nanoparticles and FTO substrate. TEM-EDX images of Ir-functionalized ATO nanoparticles (b) after one soak in the precursor solution; (c) after 350 °C annealing; and (d) after 600 °C annealing.

To access the mechanism of $[(COD)IrCl]_2$ attachment to metal-oxide surfaces, an experiment was conducted with soluble metal hydroxide species: triphenyl silanol (TPS) and tris(*tert*-butoxy) silanol (TBS). The Ir dimer was mixed with the metal hydroxides in tolune-d_8, allowed to react for 1 h, and the mixtures were analyzed with ^1H NMR (Figure B.4). No evidence of $[(COD)IrCl]_2$ binding to the terminal OH of TPS or TBS was observed suggesting the dimer likely adheres to ATO and FTO through electrostatic interactions.

Iridium-Oxide Film Growth on the Surface of Conductive Supports. Practical applications such as PEMWE might require increasing Ir loading to achieve industry-relevant current densities. Since the dimer can adhere to the surface of a metal-oxide support through a simple soak, more dimers should attach to the Ir species already on the surface if the ligands are removed, and an Ir-O network is formed. By TGA (Figure B.5), most of the mass loss occurs between 200 and 310 ℃ (~43%). COD ligands comprise ~53% of $[(COD)IrCl]_2$ by mass, Cl ~8 %. Chloride ligands are known to require higher temperatures for removal.[41] A 5% mass loss was observed between 310 and 600 ℃.

We annealed Ir-ATO powder at 350 and 600 ℃ to confirm the loss of ligands. At 350 ℃, half of Cl is lost and the surface Ir:Sn ratio stays unchanged (~7 %). Ir 4f peak changes from one to two doublets (Ir 4f7 at 62.4 and 63.5 eV), likely due to the dimer breaking and bonding to the surface while some Ir remains bound to Cl. After 600 ℃, all Cl is lost, the surface Ir:Sn ratio decreases by 50%, and only one state of Ir present (Ir 4f7 centered at 62.4 eV). The change in the surface Ir:Sn ratio likely comes from agglomeration and/or mixing of the Ir with the ATO so the XPS signal of Ir decreases. TEM-EDX maps of atom distribution (Figure 3.2b, c, d) do not show any clear changes after annealing. The 350 ℃ anneal was chosen for Ir-shell growth to avoid mixing/agglomeration.

ATO nanoparticles and the FTO substrate were soaked three times in $[(COD)IrCl]_2$ solution in toluene overnight at 100 ℃ with a three-hour 350 ℃ anneal between soaks. The surface Ir:Sn ratio increases with every soak (Figure 3.3a) illustrating controlled Ir-O coating thicknesses. After three soaks ATO nanoparticles (3S-ATO) had a surface Ir/Sn ratio of 25% (2.3 ± 0.2 ng_{Ir}/cm^2_{ATO} by ICP-OES). The Ir 4f peak has three doublets (4f7 peaks at 62.1, 63.2, and 64.6 eV), indicating multiple binding environments.

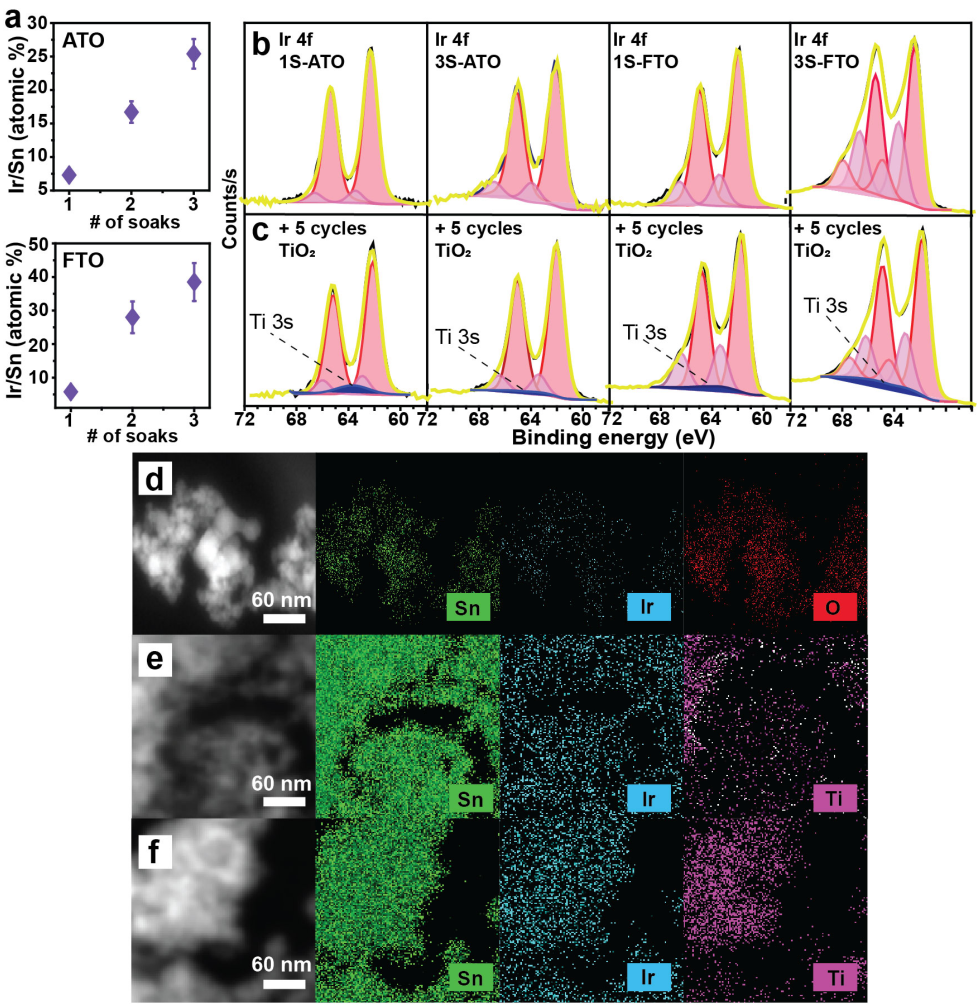

Figure 3.3. **Ir shell growth and TiO_2 deposition on metal-oxide substrates.** a) The Ir:Sn ratio increases with every consecutive soak of ATO nanoparticles or FTO planar substrate in the Ir precursor solution. b) XP spectra of Ir 4f peaks collected on metal-oxide substrates that were soaked in the Ir precursor solution once or three times. c) XP spectra of Ir 4f peaks collected on the metal-oxide substrates soaked in the Ir precursor solution once or three times and prior to TiO_2 deposition by ALD. Elemental mapping by TEM-EDX of Sn, Ir, and Ti on (d) 3S-ATO; (e) 1S-ATO-5-TiO_2 and (f) 3S-ATO-5-TiO_2.

FTO substrate soaked once (1S-FTO) gains the second Ir 4f doublet at 63.5 eV; the surface Ir:Sn ratio is 6% and after three soaks increases to 38%. A higher Ir:Sn ratio for the planar metal oxide support compared to the nanopowder might result from more favorable interactions of $[(COD)IrCl]_2$ with the F-doped vs the Sb-doped surface. Like

3S-ATO, 3S-FTO sample has three Ir 4f doublets at 62.4, 63.6, and 64.8 eV (Table B.1) (see Appendix B for all tables).

TiO_2 Protective Layer. ALD enables the growth of conformal metal oxide films of desired thickness at low temperatures on planar as well as porous or powder substrates.[42] The addition of TiO_2 via 10 cycles of ALD to planar IrO_2 was reported to increase the OER specific activity in 1 M H_2SO_4 by 9-fold.[21] The improvement was attributed to tuning the surface electronic properties and optimizing the point of zero charge.[21] Aside from enhancing the intrinsic activity of IrO_x, an overlayer of TiO_2 might support better catalyst stability toward deleterious dissolution side reactions given its inertness in acidic conditions. The Ir-functionalized ATO nanoparticles and FTO substrates were decorated with five cycles of TiO_2 via ALD at 150 ℃ (for FTO) and 250 ℃ (for ATO) using tetrakis(dimethylamido)titanium (TDMAT) precursor (Table B.3 for thicknesses). Higher deposition temperature was used on the nanoparticles to facilitate binding to less exposed surfaces, along with longer purge time to allow more time to remove the unreacted precursor trapped in the powder. The XPS analysis of 1S-FTO and 3S-FTO shows Ir 4f shifting to lower binding energy upon TiO_2 addition (~ 0.2 eV for 1S-FTO; ~ 0.7 eV for 3S-FTO) (Figure 3.3b, c). No shifts in Ir 4f binding energy were observed for 1S-ATO and 3S-ATO. The shift in binding energy might indicate electron donation from Ti to Ir or to the underlying support. The absence of the energy shift in the nanopowder samples might results from less TiO_2 bound to the surface or absence of charge density changes at the surface of ATO. These samples were tested for OER activity and durability as discussed below.

Electrochemical Performance of Ir-Functionalized Metal-Oxide Supports. Although electrochemical measurements provide insight into catalyst activity, any conclusions regarding electrocatalyst stability are incomplete and sometimes misleading without understanding the dissolution of the catalyst and the underlying support. To tackle this, we used a scanning electrochemical flow cell (SFC) coupled with downstream ICP-MS to track the potential-dependent dissolution and activity of tested catalysts and complement traditional three-electrode cell measurements. Catalyst stability was estimated by the so-called stability number (S-number). The S-number is a dimensionless metric, independent of the number of active sites, surface area, or loading. It represents the amount of oxygen molecules evolved per one iridium atom dissolved in the electrolyte, detected by ICP-MS. The S-number is calculated by dividing the total integrated charge over time (when assuming 100 % faradaic efficiency, total charge corresponds to the amount of evolved O_2 during OER) with the amount of catalyst dissolved. In short, high S-number values indicate a stable catalyst, and small S-numbers unstable catalysts.[35]

Influence of Ir Loading on Ir-FTO Activity-Stability Relationship. 3S-FTO has a lower OER onset and achieves higher current density than 1S-FTO (Figure 3.4a) including a ~150 mV decrease in overpotential at 0.5 $mA \cdot cm^{-2}$ (Figure 3.4c). Ledendecker *et al.* reported a similar increase in OER activity as a result of varying the number of the liquid ALD cycles of IrO_x on FTO substrates.[34] Here we discover that the increase in OER activity is also accompanied by a substantial increase in stability (Figure 3.4d). The stability number of 3S-FTO is ~3× higher than the 1S-FTO sample (1.2×10^4 compared to 4×10^3). However, S-numbers of both samples are much lower compared to metallic Ir and hydrous IrO_x films ($S \sim 10^4 – 10^5$) crystalline IrO_2 films ($S \sim 10^6 – 10^7$).[35, 43] The stability improvement might also originate from the higher Ir loading of 3S-FTO and thus lower mass normalized currents applied during the galvanostatic hold, or that the anchoring strength of IrO_x onto FTO is weaker than on IrO_x.[44] The activity improvement of 3S-FTO compared to 1S-FTO is likely related to the need for significant Ir-O-Ir type connectivity in the catalyst as opposed to more isolated IrO_x sites that may be present in 1S-FTO.

XPS analysis of the Ir 4f peak in the pristine 1S-FTO and 3S-FTO samples suggests a thicker Ir coverage on 3S-FTO as evidenced by an increase in the Ir:Sn ratio from 5.7 to 38.5%. The post-operation XPS analysis of 1S-FTO shows no shifts in the binding energy for the main Ir 4f peak but the second doublet at higher binding energy disappears (Figure B.9b). The Ir:Sn ratio decreases from 5.7 to 3.9% supporting the dissolution observed by ICP-MS (Table B.2). Post-operation 3S-FTO Ir 4f peak was fit with three doublets similarly to the pristine sample (Figure B.9b). The peak, however, shifts to a lower binding energy which might result from the loss of remaining Cl ligands and the formation of a more stable network on the surface of FTO. The Ir:Sn ratio, however, increases after the current hold from 38.5 to 56.3 % despite the observed dissolution. The dissolution profiles (Figure B.6) for 1S-FTO show spikes of dissolved Ir during the initial 0 mA·cm^{-2} hold and at 0.5 mA·cm^{2}. Sn dissolution is very high for this sample while no current is passing but decreases to the level of Sn loss in 3S-FTO during the 0.5 mA·cm^{2} hold. The 3S-FTO primarily loses Ir while the current is passing. Thus, the same amount of Sn is lost during OER (at 0.5 mA·cm^{2}) in both 1S and 3 S samples, but Ir dissolution occurs at a faster rate for 1S-FTO. The difference in rates of Ir dissolution might explain the decrease in Ir:Sn ratio in 1S-FTO and its increase in post-operation 3S-FTO.

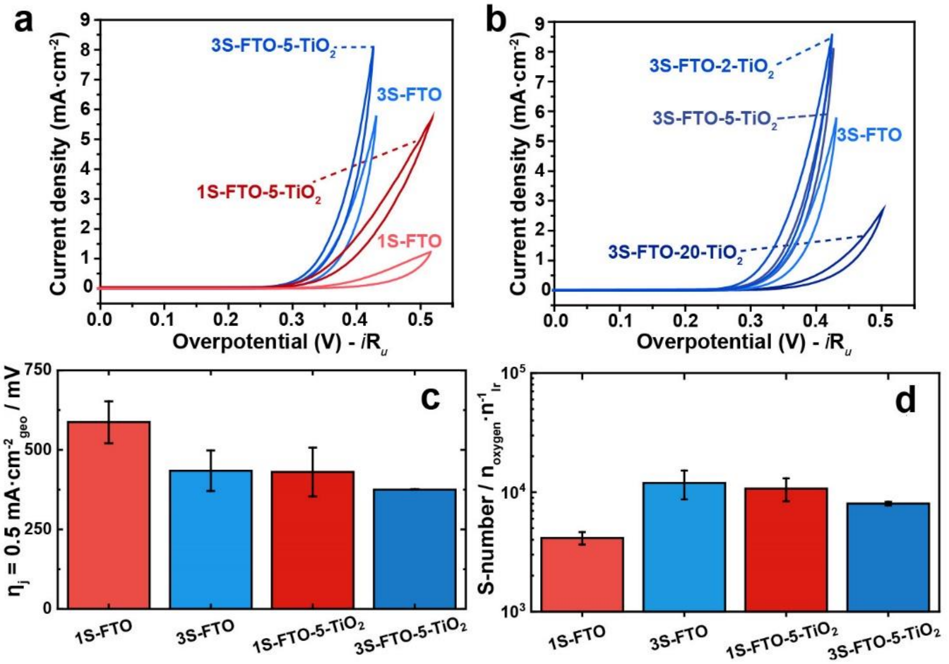

Figure 3.4. A thin layer of TiO$_2$ on Ir-FTO enhances activity. a, b) Cyclic voltammetry plots for Ir-functionalized FTO substrates collected in 0.1 M HClO$_4$ at pH ~1. c) Compilation of OER overpotentials (η) for the different Ir-based catalysts measured at geometric current densities of 0.5 mA cm^{-2}. Overpotential values presented on the figure were taken at the end of the chronopotentiometry measurements, where samples reached steady-state operation. d) S-numbers of different Ir-based catalysts prepared in this work. S-numbers values are calculated from a galvanostatic hold at 0.5 mA cm^{-2}. For representative dissolution profiles, we refer to Figures B.6-B.8.

TiO$_2$ Coated Ir-FTO Thin Films and Activity-Stability Relationships. Addition of 5 cycles of TiO$_2$ by ALD resulted in improved OER activities regardless of the Ir loading in the samples (Figure 3.4a). For 1S-FTO, the OER overpotential drops by ca. 150 mV and for 3S-FTO it drops by ca. 60 mV (Figure 3.4c). In the case of 1S-FTO, adding TiO_2 on top increased its stability to values comparable to the pristine 3S-FTO sample (S-number ≈ 1.0×10^4). For 3S-FTO, Ir stability worsens contrary to 1S-FTO (S-number decreases to 8.0×10^3). Considering the same amount of TiO_2 ALD cycles added to both samples, 3S-FTO-5-TiO_2 shows twice as much Ti dissolved, accompanied by almost two times higher Sn dissolution (Figure B.11). If the surface coverage of IrO_x on FTO was not complete after just one soak in $[(COD)IrCl]_2$, TiO_2 could bind to FTO as well which could suppress Sn dissolution, which in its turn minimizes Ir dissolution during OER. After three soaks in $[(COD)IrCl]_2$ FTO surface has much higher IrO_x coverage allowing less TiO_2 to bind to the support which might lead to significant losses of Ir, Sn, and Ti in the 3S-FTO-5-TiO_2 sample during OER. This may be in part due to the dynamic nature of the IrO_x structure during OER.

XPS analysis of the 1S-FTO and 3S-FTO samples with 5 cycles of TiO_2 before and after electrochemical testing is shown in Figure B.9. The Ir and Ti dissolution observed by ICP-MS is confirmed by the decrease of Ir:Sn and Ti:Sn ratios in the samples after electrochemical testing (Table B.2). The binding energy of the Ir 4f peak in the 3S-FTO sample shifts down by ~0.7 eV upon TiO_2 deposition. The Ir 4f peak in 1S-FTO-5-TiO_2 shifts only by 0.2 eV which is within the experimental error of XPS. The observed shift to lower binding energy for Ir 4f upon TiO_2 addition is not consistent with the literature instances. Finke *et al.* describes a downshift in binding energy of Ti 2p upon TiO_2 addition to a layer of IrO_2 with no energy shifts observed for Ir 4f.[21] Kasian *et al.* also observed a downshift in Ti 2p binding energy when Ir content was increased for Ir-Ti alloys.[22] The shift in the binding energy of Ti 2p is attributed to the charge transfer from Ir surface to TiO_2. A reversed trend observed in our experimental model suggests that the deposited protective layer interacts with the catalyst and the support in a different way than in the catalyst systems reported in the literature. In our system, an ultrathin layer of IrO_x is interacting with an n-type metal oxide that can transfer charge density to the catalyst layer resulting in a downshift of the Ir 4f peak. For the sample with higher Ir loading (3S-FTO) not all layers of Ir might be affected by the charge density transfer.

Indeed, Ir 4f in 3S-FTO is at a higher binding energy than in 1S-FTO (Table B.1). Addition of TiO_2 seems to enhance the charge density transfer to the Ir layer.

Influence of TiO_2 ALD Number of Cycles on Ir-FTO Thin Films. To evaluate how the number of TiO_2 cycles affects the interplay between OER activity and stability, we prepared 3S-FTO with 2 ,5, and 20 cycles of TiO_2 by ALD. 1S-FTO was not chosen due to the high overpotentials required to drive OER at 0.5 mA cm^{-2}. The thickness of the TiO_2 layers was measured on a witness Si wafer by ellipsometry (Table B.3). The addition of only 2 cycles of TiO_2 to 3S-FTO improves the activity of the sample to the level of 3S-FTO-5-TiO_2 (Figure 3.4b). The addition of 20 cycles decreases the activity significantly. Unfortunately, the S-numbers and the overpotentials at 0.5 $mA\cdot cm^{-2}$ for the unprotected sample cannot be compared to the TiO_2-covered samples due to a large range of experimental values for 3S-FTO (Figure B.7). But when compared to each other, the samples with 2 and 5 cycles of TiO_2 are more active but less stable than 3S-FTO-20-TiO_2. According to the dissolution profiles, 3S-FTO sample protected by 2 cycles of TiO_2 loses as much Sn as 3S-FTO-5-TiO_2, but Sn dissolution goes down for 3S-FTO-20-TiO_2 (Figure B.11). It appears that 20 cycles of TiO_2 results in less Sn, Ir, and Ti loss (Figure B.8 and B.11).

All TiO_2 was lost from 3S-FTO-2-TiO_2 during the current hold according to XPS (Table B.2). The ratio of Ir:Sn decreases. The sample protected by 20 cycles of TiO_2 exhibited Ti:Sn ratio decrease but an increase in Ir:Sn after testing. This is likely due to a thicker layer of TiO_2 at the topmost layer in the pristine samples decreasing the Ir counts. Once some of the TiO_2 is removed during testing, Ir becomes more accessible for analysis (Figure B.12 for TiO_2 XPS spectra). Interestingly, despite having more Ti, 3S-FTO-20-TiO_2 exhibits the same amount of Ti dissolution as 3S-FTO-5-TiO_2 (Figure B.11b).

Thus, only 2 cycles of TiO_2 (~0.14 nm) cause the activity improvement compared to unprotected 3S-FTO but also trigger high Ir, Ti, and Sn loss observed for 3S-FTO-5-TiO_2 as well. The decrease in activity for 3S-FTO-20-TiO_2 likely results from blocking the Ir active sites by TiO_2. But lower activity facilitates higher stability: less Ir, Ti, and Sn loss. The tradeoff between having the active sites accessible while protected must be balanced to achieve stable long-term performance.[45-46] Markovic *et al*. found that a stable oxide is inactive during OER connecting the catalyst's transition to higher oxidation state to dissolution and surface defect formation resulting in a higher activity.[45]

Influence of Post-ALD Annealing on TiO_2-Ir-FTO Thin Films. To further the Ir stability, we annealed the samples at 400 °C after the ALD of TiO_2. The activity of all the annealed samples is now lower than of 3S-FTO with 3S-FTO-20-TiO_2 (400 ℃) being the worst (Figure 3.5a). The overpotential at 0.5 $mA\cdot cm^{-2}$ for the samples with 2 and 5 cycles of TiO_2 is indistinguishable from 3S-FTO (Figure 3.5b); for 3S-FTO-20-TiO_2 (400 ℃) it is higher. However, after the additional anneal, the samples exhibit higher stabilities. All post-ALD annealed samples show 3-4 times higher S-number than 3S-FTO and the samples that were not annealed after ALD (Figure 3.5c). The trends might originate from changes in Ir and Ti crystallinity and oxidation states after heating at 400 °C. With regards to Ir, Geiger *et al.* previously reported that a significant amount of IrO_2 is formed by increasing the annealing temperature from 300 to 400 °C. Its characteristic rutile-type phase is less active than amorphous and metallic Ir, but more stable due its compact crystalline structure.[47] In the case of Ti, Lin *et al.* reported that an increase in surface roughness was obtained by heating TiO_2 films at 400 °C, followed by slight densification. This was also accompanied by changes in film crystallinity; films heated at 300 °C were amorphous, while those heated at 400 °C showed the formation of a crystalline anatase phase.[48] The anatase phase is reported to be more stable in acidic (low pH) conditions compared to the amorphous phase by Kriegel *et al*.[49] This is in agreement with the 3-4 times lower Ti dissolution observed for the post-ALD annealed samples (Figure B.11c). Additional annealing likely causes surface reconstruction leading to Ir and Ti atoms mixing, which we observe through the drop of Ti:Sn ratio in all post-ALD annealed sample compared to TiO_2-protectd samples that were not annealed (Table B.2). The mixing should further stabilize Ir providing an acid-stable matrix but would likely make it less accessible for catalysis.

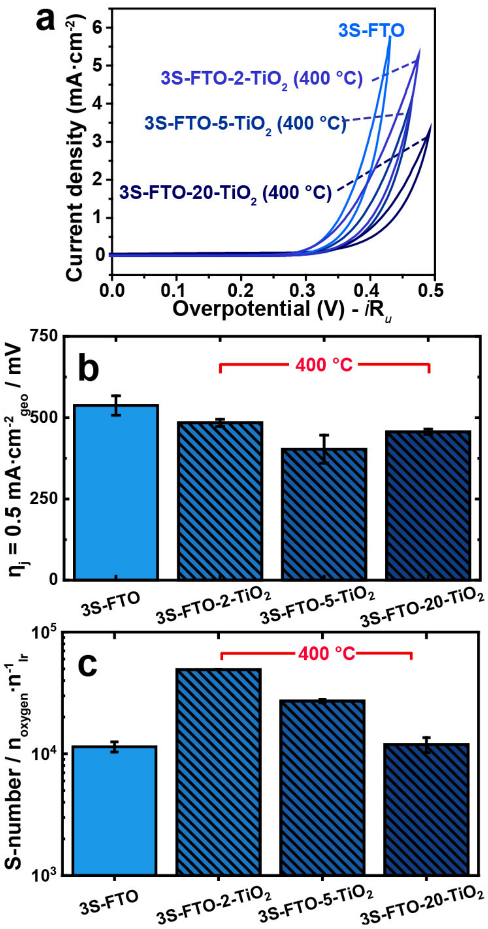

Figure 3.5. Post-ALD annealing improves stability but lowers activity. a) CVs collected in 0.1 M $HClO_4$ on the TiO_2-protected samples annealed at 400 °C after ALD. The OER activity decreased compared to 3S-FTO. b) Overpotential at 0.5 mA·cm^{-2} and c) S-number for the post-ALD annealed samples. Though the overpotential values did not improve, the stability of the annealed samples increased.

After electrochemical testing, the Ir 4f peak in 3S-FTO-2-TiO_2 (400 °C) shifts to lower binding energy (Figure B.13b). Most of TiO_2 is gone and the Ir:Sn ratio decreases consistent with the ICP-MS results (Table B.2). The XP spectra of Ir 4f for the samples with 5 and 20 cycles of TiO_2 do not shift in energy after electrochemical testing. The ratios of Ti:Sn remain almost unchanged, while Ir:Sn ratios increase. The increase in the Ir:Sn ratios is likely prompted by a partial loss of TiO_2 observed by ICP-MS making Ir more exposed to XPS analysis. Sn dissolution is observed as well but is substantially lower than for the samples not annealed after ALD or for the 3S-FTO sample.

Additional annealing of TiO_2-protected Ir is a viable strategy to increase the catalyst's stability. Though there is partial loss of activity, the stability improvement can lead to longer-term operation for water electrolyzers.

Influence of TiO_2 ALD Decoration on Ir-ATO Nanopowders. After studying the planar model system, we switched to a more industrially-relevant nanopowder Ir-ATO system. The nanopowders were dispersed onto FTO electrodes for testing. Similarly to Ir-functionalized FTO, the activity of Ir-decorated ATO nanoparticles improved with the increase of Ir loading (Figure 3.6a). The improvement might arise from more active sites available for catalysis and favorable Ir-O-Ir interactions in the denser catalyst network. Addition of 5 cycles of TiO_2 to 1S-ATO resulted in an earlier OER onset. Like the FTO systems, TiO_2 on 3S-ATO did not cause a comparable activity enhancement, but higher current density was achieved (Figure 3.6a).

We could not reliably study the dissolution profile of 1S-ATO and 1S-ATO-5-TiO_2 with the flow cell because they were not active enough. The OER activity of 3S-ATO is comparable to the 3S-FTO model system (475 and 434 mV) (Figure 3.6b). Comparing our 3S-ATO catalyst to the previously published IrO_x-ATO catalyst, its activity is much lower (475 mV overpotential compared to 270 mV), which can be explained by the 500x times lower Ir loadings used in this study (~ 10 $\mu g \cdot cm^{-2}$ compared to ~ 2 $ng \cdot cm^{-2}_{ATO}$ here).[19] Similarly with the 3S-FTO, the addition of 5 ALD cycles of TiO_2 to ATO decreased the OER overpotential ca. 60 mV but also decreased the stability compared to 3S-ATO. The S-number of 3S-ATO after TiO_2 decoration was 3 times lower than for Ir-FTO, ascribed to the less-stable ATO support. Even though ATO is less stable than FTO (due to Sb leaching), the S-number without TiO_2 is approximately the same. Interestingly, Sn dissolution was 8 times lower, while Sb dissolution increased by 2.5 times in 3S-ATO-5-TiO_2 compared to the 3S-ATO sample. Geiger *et al*. showed that Sb leaches from ATO during OER in acid leading to a formation of a SnO_2-rich surface.[29] Similarly to the case of Ir, we hypothesize that TiO_2 incorporation could also affect the relative stability of ATO and its dissolution pathways.

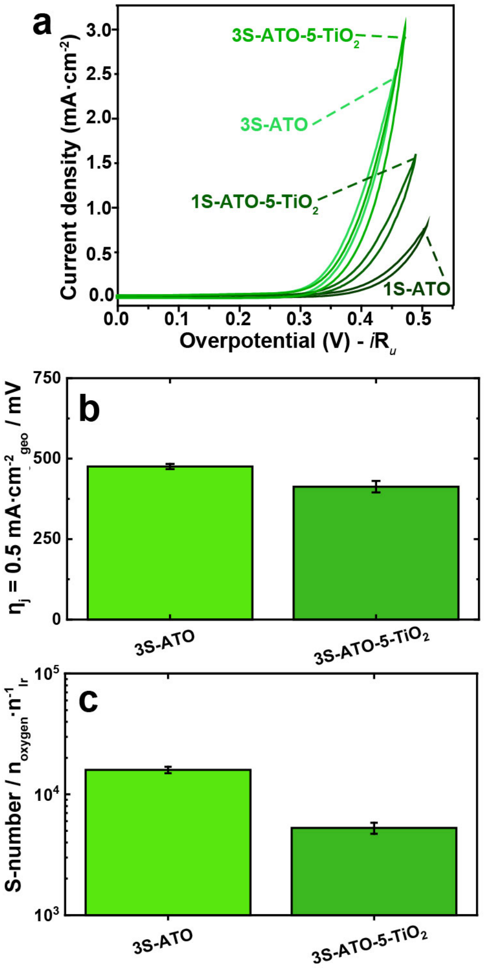

Figure 3.6. Activity enhancement is accompanied by stability decrease for Ir-ATO. a) CV plots for Ir-functionalized ATO nanopowder dispersed on FTO electrodes collected in 0.1 M $HClO_4$. b) Overpotential values at 0.5 mA·cm^{-2} and c) S-numbers calculated for 3S-ATO and 3S-ATO-5-TiO_2.

3S-ATO analyzed by XPS shows increased Ir:Sn ratio compared to 1S-ATO (Table B.2). The binding energy of Ir 4f in 1S-ATO and 3S-ATO samples did not shift to lower values after TiO_2 addition (Figure B.14). The absence of the shift when using a different support might be indicative of TiO_2 influencing IrO_x/support interactions instead of having a direct effect on Ir 4f binding energy by electron donation or withdrawal. As mentioned above, the Ir loss in the TiO_2-protected sample is accompanied by Sb dissolution whereas Sn dissolution is suppressed compared to the 3S-ATO sample. The stability loss upon TiO_2 addition in 3S FTO and FTO samples (compared to the improved stability for 1S-FTO-5-TiO_2) might indicate different degree of interactions between TiO_2 and the conductive support. We would expect more TiO_2 is able to bind to the support as well as IrO_x in 1S samples vs 3S samples in which the surface is more covered by IrO_x. TiO_2 bound to the support might results in high support stability during OER.

In summary, similar activity-stability relationships are observed for both model systems: planar and nanopowders confirming the applicability of the ALD TiO_2 decoration method in real applications. However, it is important to mention that there is a higher decrease of stability by adding TiO_2 in sample 3S-ATO compared to planar sample 3S-FTO, which indicates that additional support interactions cannot be ruled out.

Conclusion

In Chapter III, we report a novel synthesis of an ultrathin IrO_x catalyst from a molecular precursor that can be accomplished on F-doped (planar) or Sb-doped (nanopowdered) SnO_2. This synthesis uses only commercially available precursors and can be easily controlled and scaled. We investigated the effects of varying the loading of Ir and the addition of TiO_2 on the OER activity and stability of Ir-functionalized supports by combining in operando ICM-MS and post-mortem XPS analyses. We observed a stability improvement (3x) for the higher-loading samples demonstrating the need for significant Ir-O-Ir network. We demonstrated that the addition of a very small amount of TiO_2 (2-5 ALD cycles) can significantly improve the OER activity while triggering higher dissolution supporting the high activity/low stability trend reported by Markovic *et al.*[45] Stability enhancement for TiO_2-protected samples was only observed when the thickness of the protective layer was increased likely providing structural support to Ir or after post-ALD annealing leading to Ti/Ir mixing. The ability of TiO_2 to trigger dissolution was not previously reported.

Further, our results showed that TiO_2 can alter the stability of the support when deposited on a catalyst layer thin enough to allow TiO_2/support interaction. TiO_2 increased Sn dissolution during OER on FTO supports but suppressed Sn dissolution while increasing Sb dissolution on ATO nanoparticles leading to different dissolution modes.

Previously published works showed OER activity enhancement for TiO_2-protected Ir but in those cases a thicker TiO_2 or IrO_2 layer was used preventing any TiO_2/support interactions and minimizing IrO_2/support interactions which would be the strongest only at the interface.[21-22] In our model system we can observe several interactions that have an effect on the catalyst's performance: the catalyst/support (observed by the shifts in Ir 4f energy); TiO_2/IrO_x; and TiO_2/support. The ultra-thin TiO_2-protected catalyst on different conductive metal-oxide supports can be used for *in situ* X-ray absorption experiments. It was reported that during OER higher oxidation states are reached which leads to high activity but low stability.[45] Determining how TiO_2 affects the oxidation state of Ir during OER (and the oxidation states of the metals in the support) could be key to designing a high-performing stable catalyst for OER in acid.

Bridge

Chapter III summarized the developed synthesis of a novel catalyst for the anodic reaction in acid and described ways to tune the intrinsic stability and activity of Ir active sites. This work sheds light on the true interactions of TiO_2 with the catalyst and the support and provides a model system for further investigations. Surface characterization analysis described in this chapter was used in the following chapters. The next chapters focus on alkaline-membrane water electrolysis.

CHAPTER IV

THREE-ELECTRODE STUDY OF ELECTROCHEMICAL IONOMER DEGRADATION RELEVANT TO ANION-EXCHANGE-MEMBRANE WATER ELECTROLYZERS

Chapter IV contains co-authored material previously published as *ACS Appl. Mater. Interfaces* **2022, DOI**: 10.1021/acsami.1c22472 and is reproduced with permission. Copyright 2022 American Chemical Society. Prof. Bottcher and I conceived of the project. I performed the experiments, collected and analyzed data. Prof. Hutchison assisted with data interpretation. Prof. Hendon and Min Chieh Yang performed computational work. I wrote the paper with editorial assistance of Amanda Cook, Katherine Ayers, Chistopher Capuano, Andrew Motz, Grace Lindquist, Prof. Hutchison, and Prof. Boettcher.

Introduction

Water electrolysis has the potential to provide clean H_2 from renewable electricity for heating, powering transport, chemical production, and metal refining.[1] To compete with fossil fuels, H_2 must be low cost (probably <2 $/kg) and produced at scale.[2-3] Improving efficiency and durability while dramatically lowering capital cost of electrolyzers is key to implementing sustainable H_2 production on a scale commensurate with energy needs.

Anion-exchange-membrane water electrolyzers (AEMWEs) are a newer technology that has potential to overcome the weaknesses of more-mature electrolyzer technologies, such as proton-exchange-membrane water electrolyzers (PEMWEs) and alkaline water electrolyzers (AWEs).[4-5] AEMWEs adapt the compressed stack design of PEMWEs to produce pressurized H_2, but uses a solid OH^--conducting anion-exchange polymer membrane that creates a locally basic environment for the cathode and anode catalysts.[2, 6] A sheet of the solid AEM (typically 20-80 μm in thickness) is placed between the anode and cathode electrodes, while a soluble or dispersed form of the AEM polymer, the ionomer, is mixed in the catalyst ink to improve ionic and physical contact between the membrane and the catalyst-covered electrodes. Such membranes/ionomers, in principle, allow the use of non-platinum-group (non-PGM) catalysts that are superior to IrO_2 in alkaline pH for water oxidation and avoid using concentrated KOH, ideally pumping pure water though the system instead for lower balance of plant costs.[7-9]

AEMWEs are still under development and their durability is inferior to PEMWEs and AWEs.[2] The existing AEMs are generally not as physically and chemically robust as Nafion used in PEMWEs and suffer from insufficient ionic conductivity during operation.[2, 10] To mitigate ohmic losses, particularly in the catalyst/ionomer reaction layer, supporting electrolytes such as 0.1 to 1.0 M KOH or K_2CO_3 have been added to the AEMWE feed. Addition of electrolyte improves performance but introduces other issues.[6, 11-13] Performance loss pathways remain difficult to identify and, thus, an informed design of the cell components is challenging.

The interface between the catalyst and ionomer binder comprises the reactive zone at the anode and is likely the weakest point in the system due to the highly oxidizing potential.[14-15] Being in direct contact with the anode catalyst surface, the ionomer would be the first to sustain any chemical changes due to oxidation.[16] The oxidation of the ionomers under applied potential has been shown to lead to the formation of new chemical structures, a change in local pH at the catalyst surface, and consequent catalyst loss.[16-19]

In the presence of supporting electrolyte containing carbonate, the degradation modes may be more complicated. The presence of carbonate anions instead of OH^- might lead to a steeper pH gradient within the membrane. The understanding of the anion interactions and their effect on the stability of the ionomer/membrane during operation in a supporting electrolyte containing anions other than OH^- is limited.[12, 16, 20]

Here our results suggest that the identity of the anions that transport through the ionomer binder during electrolysis and their interactions with the charged groups within the polymer can facilitate ionomer degradation. We illustrate possible degradation modes of ionomers in supporting electrolytes to understand interactions of anions with the ionomers possessing different chemical structures. We focus on three high-performance commercial ionomers: Aemion by Ionomr,[21] Sustainion by Dioxide Materials,[22] and PiperION by Versogen,[23] (Figure 4.1) with common supporting electrolytes under oxidizing applied potentials (see Appendix C for all figures and tables). Because different catalyst surfaces have been observed to promote ionomer degradation,[16] we do not add catalyst to the ionomers but instead test them on planar metal electrodes across all experimental degradation measurements. We analyze the effects of the anions' identity on their transport through the ionomers and track the changes to the chemical structures of the ionomers as the potential increases. We use density functional theory (DFT) calculations to estimate trends in redox potentials and visualize predicted HOMO orbitals located on the conjugated components of each ionomer. This work thus provides insight into the nature of the interactions of the various anions with the ionomers/membranes, helps to assess its effects, and illustrates the structure-stability relationship for the different supporting electrolytes. Particularly, this work is relevant for designing more chemically stable ionomers and identifying the best ionomer for an AEMWE given the supporting electrolyte used.

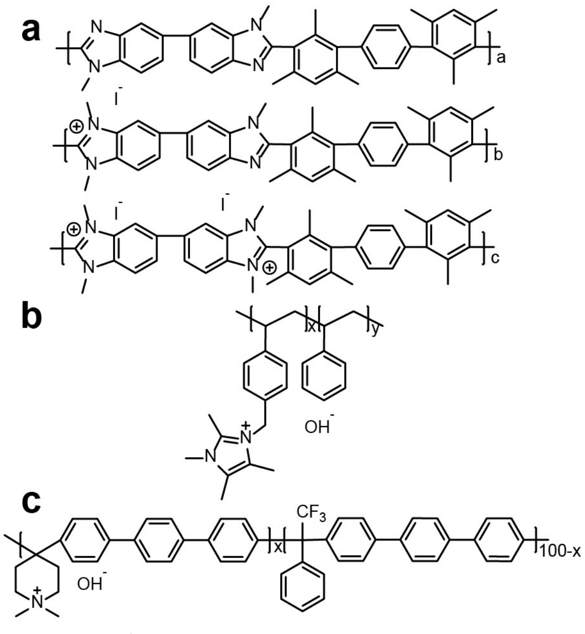

Figure 4.1. Chemical structures of (a) Aemion by Ionomr; (b) Sustainion by Dioxide Materials; and (c) PiperION by Versogen.

Experimental

Materials. Sustainion-XA9 and PiperION (PAP-TP-85) ionomer solutions in ethanol (5 wt. %) were used as received from Dioxide Materials and Versogen, respectively. Aemion (AP1-HNN8-00-X) by Ionomr dry powder was received and dissolved in ethanol to obtain 5 wt. % solution. Supporting electrolytes were prepared using KOH pellets (Fischer Chemical, ≥ 85.0%), K_2CO_3 (Fischer Chemical, ≥ 99.0%), $KHCO_3$ (Fischer Chemical, ≥ 99.7%), NaOH (Fischer Chemical, ≥ 97.0%), H_3BO_3 (Mallinckrodt, ≥ 99.5%), and perchloric acid (60-62%, J. T. Baker Chemical, ACS grade) dissolved in 18.2 MΩ·cm H_2O.

Electrochemical Measurements with a Quartz Crystal Microbalance. Ionomer solutions at 5 wt. % were spin-coated at 3000 rpm onto 5 MHz Au/Ti quartz crystals (QCs, Fil-Tech) and annealed at 80 °C for 15 min. Aemion films were then soaked in 1 M NaCl for 1 h to ion-exchange the I^- counter-ion for Cl^-. Sustainion films were soaked in 1 M KOH for 1 h after annealing. PiperION films were soaked in 1 M HCl for 5 min immediately after spin-coating, then rinsed with 18.2 MΩ·cm H_2O and annealed at 80 °C. Prior to electrochemical testing, the PiperION films were also soaked in 0.5 M NaOH for 15 min (see discussion on the preconditioning of the selected ionomers in Appendix C). A BioLogic SP300 potentiostat was used operating in three-electrode mode. A Pt coil was used as the counter electrode, while the Au/Ti QC with ionomer films on top served as the working electrode connected to the QCM controller (Stanford Research Systems QCM200) for monitoring mass changes during electrochemical testing. Potentials in three-electrode modes were measured versus a 1 M KOH Hg/HgO reference electrode (CH Instruments). The cell was degassed with N_2 prior to electrochemical testing. High-purity N_2 was bubbled in the electrolyte during the experiment.

The ionomer films were tested in three electrolytes: 1 M KOH (pH 14), 1 M carbonate/bicarbonate buffer (pH 10), and 1 M borate buffer (pH 8). In each supporting electrolyte, the films were first held at the open circuit voltage (OCV) for 2 h, then a series of overpotentials (relative to the reversible oxygen potential in that electrolyte) was applied (η = 400 mV, 500 mV, 600 mV, and 700 mV) for 1 h each. The films were then held at the OCV again for 1 h. The changes to the QCM resonance frequency during the chronoamperometry were converted to percent mass loss relative to the initial masses of the fresh films in each supporting electrolyte. The films' thicknesses were calculated using the ionomers' densities provided by the manufacturers, the known area of the Au/Ti electrode, and the film's mass calculated from changes in resonance frequency using the Sauerbrey equation:[24] $\Delta f = -C_f \times \Delta m$, where Δf is the observed frequency change (Hz), C_f is the sensitivity factor of the 5 MHz AT-cut quartz crystals (56.6 ± 3.7 Hz·μg^{-1}·cm^{2}), and Δm is the change in mass per unit area (μg·cm^{-2}). A Dektak 6M stylus profilometer was used to confirm the calculated film thickness (see Table C.1 for the summary of the thicknesses) (see Appendix C for all figures).

Thin Films Characterization by X-ray Photoelectron Spectroscopy (XPS). Pt/Ti-coated glass slides (1 cm × 1 cm) were cleaned by O_2 plasma and rinsed with ethanol at 3000 rpm. The 5 wt. % ionomer solutions were diluted to 0.16 wt. % with ethanol and spin-coated on the Pt/Ti-coated glass substrates at 3000 rpm and annealed at 80 °C for 15 min. Aemion films were soaked in 1 M NaCl for 1 h after drying on the hot plate. Sustainion films were soaked in 1 M KOH for 1 h after annealing. PiperION films were soaked in 1 M HCl for 3 min immediately after spin-coating, then rinsed with 18.2 MΩ·cm H_2O and dried. The ionomer-covered substrates were fabricated into electrodes by making an ohmic contact to the Pt surface with a Cu-wire coil and Ag paint. The coil was then fixed in a five-inch glass tube. The contact and the tube were insulated by epoxy (Loctite 9460) and cured in the oven. The electrodes were tested in a similar three-electrode cell as the Au/Ti quartz-crystal electrode, but a new electrode was used for each overpotential. The cell was degassed with N_2 prior to electrochemical testing. High-purity N_2 was bubbled in the electrolyte during the experiment. The films were held at the OCV for 20 min before the potential was applied for 1 h in each of the three supporting electrolytes. The working electrode was then taken out, the film rinsed with copious amounts of water, and dried at 80 °C for 1 h. PiperION substrates were soaked in 1 M HCl for 3 min after electrochemical testing before they were dried. Each film was analyzed with X-ray photoelectron spectroscopy (XPS) on an ESCALAB 250 (ThermoScientific) using an Al Kα monochromated (20 eV pass energy, 500 μm spot size) source. The samples were charge-neutralized using an in-lens electron source. Spectra were analyzed using ThermoScientific Avantage 4.88 software. The C 1s signal at 284.8 eV was used to calibrate the binding energy scale (see Table C.2 for the summary of peak fitting). A similar test was carried out with the three ionomer films using 0.1 M $HClO_4$ as electrolyte at η = 400 and 600 mV. The films tested in acid were also analyzed with XPS.

Attenuated Total Reflectance Measurements. Au/Ti-coated glass slides (3 cm × 3 cm) were cleaned by O_2 plasma and rinsed with ethanol at 3000 rpm. The 5 wt. % ionomer solutions were spin-coated on the Au/Ti-coated glass substrates at 3000 rpm and annealed at 80 °C for 15 min. Aemion films were soaked in 1 NaCl for 1 h after annealing. Sustainion films were soaked in 1 M KOH for 1 h after annealing. PiperION films were soaked in 1 M HCl for 5 min immediately after spin-coating, then rinsed with 18.2 MΩ·cm H_2O and annealed. Prior to electrochemical testing, the PiperION films were also soaked in 0.5 M NaOH for 15 min. The ionomer-covered substrates were fabricated into electrodes as described previously. The electrodes were tested in a similar three-electrode cell as above, but after applying each overpotential for 1 h the electrode was taken out, rinsed with copious amounts of water, dried at 80 °C for 30 min (the PiperION film was soaked in 1 M HCl for 5 min prior to drying to remove OH^- that would damage the film in the dry state), and analyzed by collecting an attenuated total reflectance (ATR) spectrum (200 scans) using Smart *i*TR accessory equipped with a diamond crystal on a Thermo Fischer Nicolet 6700 spectrometer (4,000 – 400 cm^{-1}) with a resolution of 6 cm^{-1}. The same substrate was then fabricated into an electrode again to be tested at the next highest overpotential in the same supporting electrolyte.

Computations. Density functional theory (DFT) was used to assess both the oxidation potentials and vibration properties of representative portions of Sustainion, PiperION, and Aemion. To do so, a hybrid-GGA method was used, PBE1PBE/6-31+G*. The redox potential was computed using a previously reported method,[25] with the computational Standard Hydrogen Electrode value of -4.44 eV. The truncated portions of the polymers were created by passivating cleaved sp^3-carbon bonds with charge compensatory protons. Both *cis* and *trans* conformations of Sustainion were examined. For the larger polymers, PiperION and Aemion, the polymer was truncated to exclude cationic portions of the polymer (*i.e.* the portion with very large oxidation potentials). A pseudo-solvent was included in the computations using the Self Consistent Reaction Field approach, with the polarizable continuum model (solvent = water), simulated at 293 K. Frequencies were used to confirm that truncated geometries are at least metastable, and the computed vibrations were scaled by 0.981 to account for the DFT approach used herein.

Results and Discussion

The ionic radius and hydration energy of ions have been shown to govern ion transport through anion-exchange membranes.[26] The anions with lower hydration energy adsorb onto the membrane more easily but diffuse slower.[26] Adsorption refers to the process of anion partial dehydration and formation of an electrostatic bond to the charged groups on the membrane surface. The overall size of the anion and its geometry also influence the adsorption of anions and the rate of diffusion through the membrane. Given these findings, anions strongly interacting with the cationic ionomer groups might accumulate in the membrane, lowering OH^- concentration and thus conductivity, which can negatively affect the ionomer/membrane stability.

To gain insight specifically into the ionomer/supporting anions interactions under anodic applied potentials, we studied simplified thin-film model systems of commercial ionomers (Aemion by Ionomr, Sustainion by Dioxide Materials, and PiperION by Versogen) on Au/Ti and Pt/Ti electrodes in three supporting electrolytes (~ pH 14, 1 M KOH; ~ pH 10, 1 M $K_2CO_3/KHCO_3$ buffer; and ~ pH 8, 1 M borate buffer) under a range of applied potentials. The specific versions of the ionomer were chosen because they appear frequently in the literature and their structure and properties are well-known. We recognize that newer materials might be available from Ionomr, Dioxide Materials, and Versogen (for instance, Aemion$^+$)[18, 27] that we did not include into our study due to their unavailability during the initial stages of the work. No catalyst powder was added to avoid catalyst-surface-specific degradation. Borate buffer (pH 8) was selected as the third supporting electrolyte because at this pH and concentration, the aqueous species in the buffer exist mostly as a triborate cluster ($3B(OH)_3 \leftrightarrow B_3O_3(OH)_4^- + H^+ + 2H_2O$).[28] While this electrolyte provides a less basic pH, the bulky triborate clusters are unlikely to adsorb and diffuse through the ionomer films and affect the internal pH.[29] The anions' ionic radii, geometries, and hydration energies are summarized in Table C.2.

Tracking Ionomers' Dissolution under Applied Potential. To assess the ionomers' stability in the selected electrolytes under increasing oxidizing potentials, thin ionomer films (see Table C.1 for thicknesses) were spin-coated from the 5 wt. % ionomer solutions on Au/Ti quartz-crystal electrodes. Figure 4.2 shows the changes in the films' mass under increasing overpotential (overpotential η is the excess potential beyond the thermodynamic potential required for the water oxidation reaction to occur; reported in mV vs E_{OER} at a given pH).

Initially at the open circuit voltage when no current flows (OCV), the films were observed to gain mass (Figure 4.2). This is likely due to the hydration of the films as well as counter-ion exchange that further leads to water entering the polymer. In borate buffer, this mass increase was smallest for all ionomer films. This result supports the initial hypothesis that the triborate clusters[28] have difficulty diffusing through the film compared to OH^- and CO_3^{2-}/HCO_3^-.

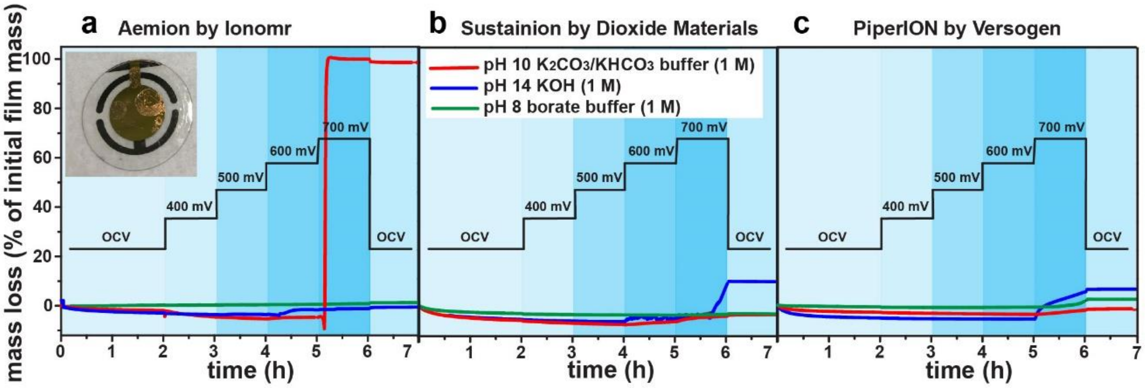

Figure 4.2. Dissolution of ionomer films under applied potential. The mass changes were monitored for 7 h in 1 M KOH (blue traces), 1 M carbonate/bicarbonate buffer (red traces), and 1 M borate buffer (green traces) for a) Aemion by Ionomr, b) Sustainion by Dioxide Materials, and c) PiperION by Versogen. The data is plotted as the percentage of mass loss relative to the initial mass of an ionomer film immersed in the electrolyte. The overpotentials are referenced to E_{OER} at the pH of the electrolytes. The open circuit voltage (E_{ocv}) ranges measured for each electrolyte are E_{ocv} = -0.5 to -0.6 V vs E_{OER} at pH 10, E_{ocv} = -0.4 to -0.2 V vs E_{OER} at pH 14, and E_{ocv} = -0.6 to -0.1 V vs E_{OER} at pH 8 (these values are ranges because the electrolyte is devoid of redox species capable of setting the electrode potential). Inset: Aemion film flaking off a quartz crystal after electrochemical testing in carbonate.

Films tested in the borate buffer also did not yield any mass losses under applied oxidizing potentials, even at the highest overpotential. In KOH electrolyte, the ionomer films took up water and increased in mass at the OCV. At η = 700 mV, Sustainion and PiperION lost ~5-10% of their mass. Aemion appeared to lose some of the mass gained during hydration and initial ion exchange at η = 600 mV. These mass changes might be indicative of the ionomer dehydration or the initiation of a degradation process. In K_2CO_3/$KHCO_3$ buffer, the difference between the mass losses observed for Aemion, Sustainion, and PiperION was significant. Neither Sustainion nor PiperION lost mass. The Aemion film was completely lost at η = 700 mV after just a few minutes (Figure C.2 for the Aemion film that was preconditioned differently in attempt to improve stability). Ionomer films are known to de-adhere from a surface during ion-exchange,[30] but this is unlikely the cause given the time at OCV allowing for ion-exchange into the HCO_3^-/CO_3^{2-} form. It is possible that the origin of the film loss is a chemical change to the structure of the ionomer that caused the portion of the film directly in contact with the electrode to become soluble. Inset in Figure 4.2 shows Aemion film starting to flake off at η = 600 mV. Based on this observation we conclude that the interface of the ionomer film directly in contact with the electrode surface oxidizes, increasing solubility and decreasing adhesion to the surface, while the rest of the film is intact. The solubility of the fragment directly in contact with the electrode causes the films to flake off.

The information that can be obtained from the QCM is limited to the mass changes. Thus, to investigate chemical degradation occurring in the system additional characterization techniques were employed. We could not gain the information we needed from the common techniques used to access the stability of thick solid membranes, e. g. tensile strength or ion-exchange capacity measurements. The films are only degraded at the interface with the electrode while the rest of the polymer remains intact. The degraded fraction of the film is likely very small and is not expected to affect bulk physical and chemical properties. Instead, we analyzed the ultrathin polymer films with surface-sensitive characterization techniques.

Tracking Structural Changes in Thin Ionomer Films with XPS. XPS was used to track changes to the structures of the three studied ionomers in the different supporting electrolytes. To obtain thinner ionomer films the ionomer solution were diluted to 0.16 wt. %. The resulting film thicknesses were 18, 9, and 12 (± 1 nm) for Aemion, Sustainion, and PiperION, respectively. Using such thin polymer films allows to gain the information about structural changes happening at the interface of the electrode surface with ionomer and would not be possible on thicker membranes. However, this approach eliminates the ability to easily measure the films' ion-exchange capacity and conductivity, which are common and useful descriptors of the ionomer stability. These descriptors require measurements of mass and volume along with typically measuring the ionomer in a two-probe station, which is difficult with very thin films due to lack of mechanical strength.

We also tested our hypothesis that the triborate clusters ($B_3O_3(OH)_4^-$) present in the pH 8 borate buffer would not interact within the ionomer films. Boron has a low XPS sensitivity factor (0.49; for comparison, the sensitivity factor of C is 1.0, and N is 1.8).[31] To determine if any boron-containing species diffused in the films, we used thicker ionomer films spin-coated from a 5 wt. % solution and tested at η = 600 mV in borate buffer. The B 1s peak was collected with a 75 eV pass energy and the B/C ratio in the film was calculated. For Aemion, Sustainion, and PiperION the B/C ratio was 0.3, 0.3, and 0.1%, respectively. That same nominal amount of B, however, was also found in the ionomer films tested in KOH. We infer that the B observed by XPS in the ionomer films is due to the presence of the contaminants in the supporting electrolyte, not additional B species entering the films.

The summary of the peak fitting and binding energies for Aemion, Sustainion, and PiperION is in Table C.3. Complex polymer matrices such as ionomer films are challenging to analyze by XPS given that the peak positions are influenced by the bonding as well as surrounding environment, which in an ionomer includes charged counterions. Using the published chemical structures we tentatively identified the peaks composing C 1s and N 1s spectra (see below). Figure 4.3 shows the predicted chemical degradation routes for Aemion [21, 32-33], Sustainion [3, 5, 34], and PiperION [32] polymers. A possible electrochemical route is shown for PiperION. However, all the three polymers can degrade under applied potential through a variety of mechanisms.[15-16, 19, 35]

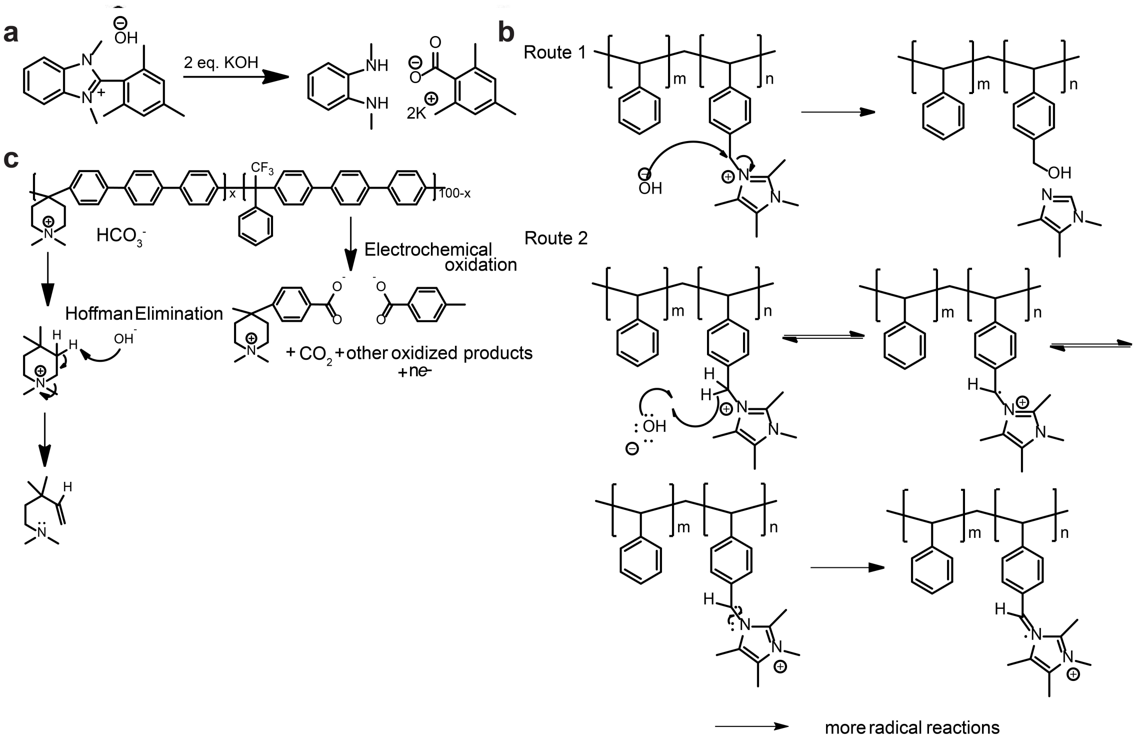

Figure 4.3. Chemical and electrochemical degradation routes for the studied ionomers. (a) Aemion is hypothesized to undergo degradation through nucleophilic displacement or a nucleophilic OH- attack on the benzimidazolium C_2-position that leads to the ring-opening. (b) Sustainion can also be subject to the imidazolium ring-opening or undergo an OH^- attack at the α-carbon joining the imidazole and the phenyl group. (c) PiperION likely suffers from Hoffman β-elimination and S_N2-methyl substitution in the piperidinium ring. Electrochemical degradation (shown only for PiperION) is possible for all three polymers through the attack of reactive oxygen species ($HO\cdot$, $HO_2\cdot$, O_2^-) that are produced as OER intermediates or as a consequence of other electrochemical reactions under applied oxidative potential**.**

Aemion Structural Changes. Aemion is composed of substituted phenyl and benzimidazole fragments (Figure 4.1a) and analyzed as a pristine thin film has three peaks contributing to its C 1s spectrum (Figure 4.4, bottom panel). We assigned the peak at 284.8 eV to the C=C and C-H bonds that are dominant in that structure. The two smaller peaks at higher binding energies amount to about 20% of the total carbon in the structure and were assigned to C bound to N^+ and N. The N/C ratio based on the chemical structure and XPS data is ~10 atomic %. The N 1s spectrum of the pristine film was also fitted with three peaks. The peak at 401.4 eV was assigned to the N carrying the positive charge. The smaller peaks at 398.3 and 400 eV likely originate from other nitrogen atoms in the polymer structure that do not carry the positive charge.

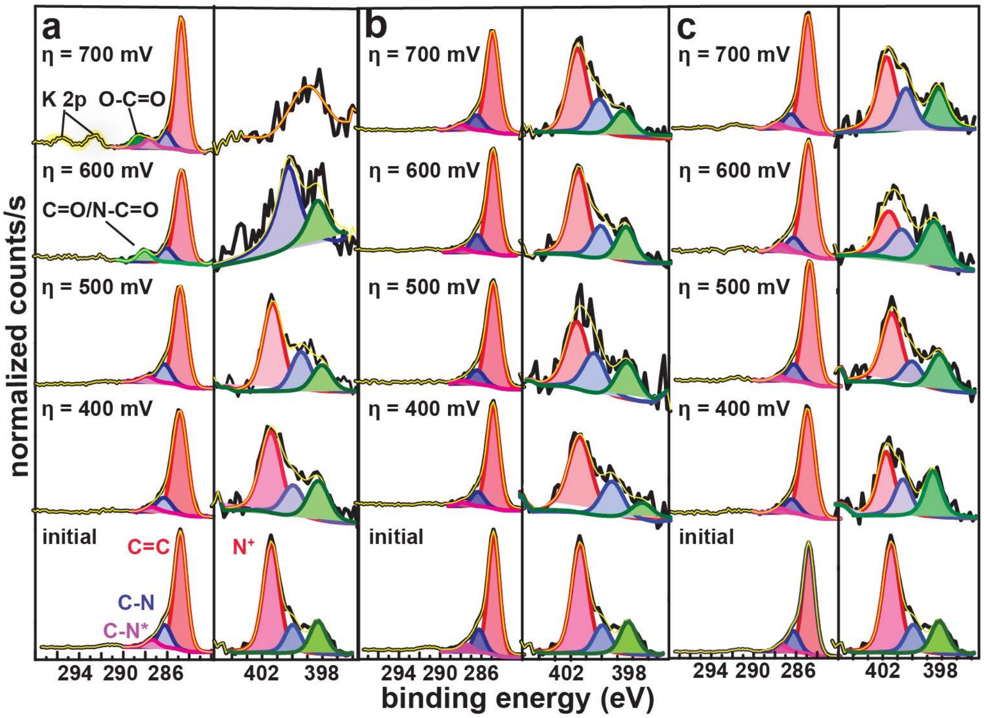

Figure 4.4. **Structural changes to the Aemion film in three supporting electrolytes.** XP spectra of C 1s and N1s of Aemion thin films as Aemion changes under increasing applied potential in (a) pH 10, 1 M K_2CO_3/$KHCO_3$ buffer; (b) 1 M KOH; and (c) pH 8, 1 M borate buffer. Because the thin polymer films might sustain beam damage during prolonged XPS analysis, we tested if the C 1s spectra of the ionomers changed as we increase the number of scans on the same spot (Figure C.1). We did not observe any changes caused by the increase of the number of scans for the three ionomer films. Thus, peaks observed by XPS in the thin film samples tested under applied potentials are unlikely to be the result of beam damage.

The structural changes of the Aemion film after polarization in 1 M K_2CO_3/$KHCO_3$ buffer are shown in Figure 4.4a. At η = 400 mV the film maintained its initial composition. At η = 500 mV the Pt/C ratio, which allows us to track dissolution, increased from ~ 0.11 to 0.28, though no new peaks appear in the XP spectra. At η = 600 mV the film dissolution became more significant (Pt/C > 1.0). A new peak at 288.2 eV appeared in the C 1s spectrum. The N 1s spectrum changes along with C 1s. The loss of the peak assigned to N^+ at 401.4 eV was observed. The N/C ratio increased from ~ 0.10 - 0.11 to 0.17. The unchanged N/C ratio in the XP spectra prior to η = 600 mV suggests that during film degradation and consequent dissolution both N and C are lost together. As the overpotential increases to 700 mV (the overpotential at which the film falls off the electrode), another carbon peak appears at 288.8 V while N 1s completely lost its initial shape and settled at ~399.1 eV. Thus, the hypothesis that the Aemion film suffers degradation in $K_2CO_3/KHCO_3$ buffer and is lost from the electrode due to dissolution in the electrolyte appears supported by the XPS data.

Aemion exhibited a slight mass loss in 1 M KOH starting at η = 500 mV (Pt/C gradually increased from 0.11 to 0.26 between η = 500 and 700 mV). The N/C ratio remained constant as did the C-N/total-C ratio. The shape of N 1s peak, however, changed; the contribution of the N^+ becomes smaller while the other two N 1s peaks increase in relative intensity (Figure 4.4b). The changes of N 1s peak in the absence of observed loss of nitrogen might indicate that some benzimidazole groups are demethylated or the N^+ is quenched through another mechanism. We do not see the appearance of any C 1 s or N 1s peaks at higher binding energies than the original peaks as we observe in $K_2CO_3/KHCO_3$ buffer. Thus, we did not observe any signs of the polymer oxidation in KOH. The film loss during electrochemical testing in KOH is not as pronounced as in $K_2CO_3/KHCO_3$ suggesting that the ionomer is more stable in KOH.

In pH 8, 1 M borate buffer (Figure 4.4c) Aemion films demonstrated fewer changes to the film composition than in KOH. The N/C and C-N/total-C ratios remained constant throughout the electrochemical testing. The Pt/C counts slightly increased at η = 700 mV which is likely due to ionomer instability at that overpotential independent of the electrolyte. However, the shape of N 1s peak changed; diminished contribution from N^+ and increased contributions of the N 1s peaks at lower binding energies were observed.

The Aemion ionomer appears to undergo some structural changes along with dissolution in all three electrolytes, but it appears to severely degrade only in $K_2CO_3/KHCO_3$ buffer. The chemical degradation route predicted for Aemion through the OH^- nucleophilic attack is shown in Figure 4.3a.[21] The benzimidazolium ring opening and the formation of a carboxylate from the original polymer would lead to the film dissolution. Stabilized by high degree of methylation, Aemion degrades through this mechanism only when OH^- becomes strongly nucleophilic, which might be induced by proximity to a charged electrode withdrawing electron density. Another possible degradation route is oxidation of the polymer structure by the OER intermediates or phenyl oxidation at the metal surface. Interestingly, the presence of carbonate/bicarbonate anions that are expected to interact with the ionomer strongly affect the stability of the film. The absence of the same degree of degradation in borate buffer (pH 8) compared to carbonate/bicarbonate buffer (pH 10) suggest that the pH of the bulk electrolyte alone does not dictate the stability. The complete loss of the film during the QCM experiment and the new higher energy peaks in the C 1s spectrum point to the polymer backbone fracturing into soluble fragments leading to the film dissolution. Conductivity of Aemion in carbonate and bicarbonate solutions is significantly lower than in KOH (in 1 M $KHCO_3$, $\sigma = 3.8\ mS\cdot cm^{-1}$; in 1 M K_2CO_3, $\sigma = 2.0\ mS\cdot cm^{-1}$; in 1 M KOH, $\sigma = 10.0\ mS\cdot cm^{-1}$ at room temperature).[21] Kiessling *et al.* demonstrated that membrane conductivity is especially important at high current densities.[36] We achieve higher current densities at higher overpotentials where Aemion shows signs of degradation. A concentration gradient along with a pH gradient might develop at the ionomer/bulk electrolyte interface making the polymer more prone to oxidation either due to the local pH drop or the absence of OH^- to participate in OER.

Sustainion Structural Changes. The spectrum of C 1s for the pristine Sustainion film was fitted with three component peaks; the peak at 284.8 V originating from the C-C, C-H, and C=C in the structure, and two peaks at 285.9 and 286.9 eV which we again assigned to C bonded to N and N^+ (C bonded to N was ~ 20% of the total carbon content) (Figure 4.5). The N 1s spectrum of the pristine film has two peaks; the dominant peak at 401.6 eV that corresponds to the N carrying the positive charge (the N in the imidazolium ring are chemically equivalent due to resonance), and a much smaller peak at 399.7 eV that was assigned to the N in the imidazolium ring that was insufficiently methylated. The N/C ratio for Sustainion thin film before testing was ~ 6%.

Figure 4.5 shows similar changes happening to the structure of Sustainion in pH 14 KOH and $K_2CO_3/KHCO_3$ buffer. The peaks in the C 1s spectrum assigned to C bonded to N diminished in both electrolytes (C-N/total-C ratio went down from 20% to 5-9% in both electrolytes as early in the testing as at $\eta = 400$ mV) and shifted by ~ 0.5

eV. The N/C ratio went from 6% to 3% indicating N loss. The N 1s peak shape changed under applied potential in a similar way in both supporting electrolytes. The peak at 401.5 eV assigned to N^+ no longer dominates. Even at the lowest overpotential (η = 400 mV) in both supporting electrolytes, we now observed a set of three peaks more comparable in size at 401.6, 399.9, and 398.1 eV. However, the N^+ peak is not completely lost. The Pt/C ratio increases slightly by η = 600 mV in both electrolytes pointing at a small portion of the film dissolving.

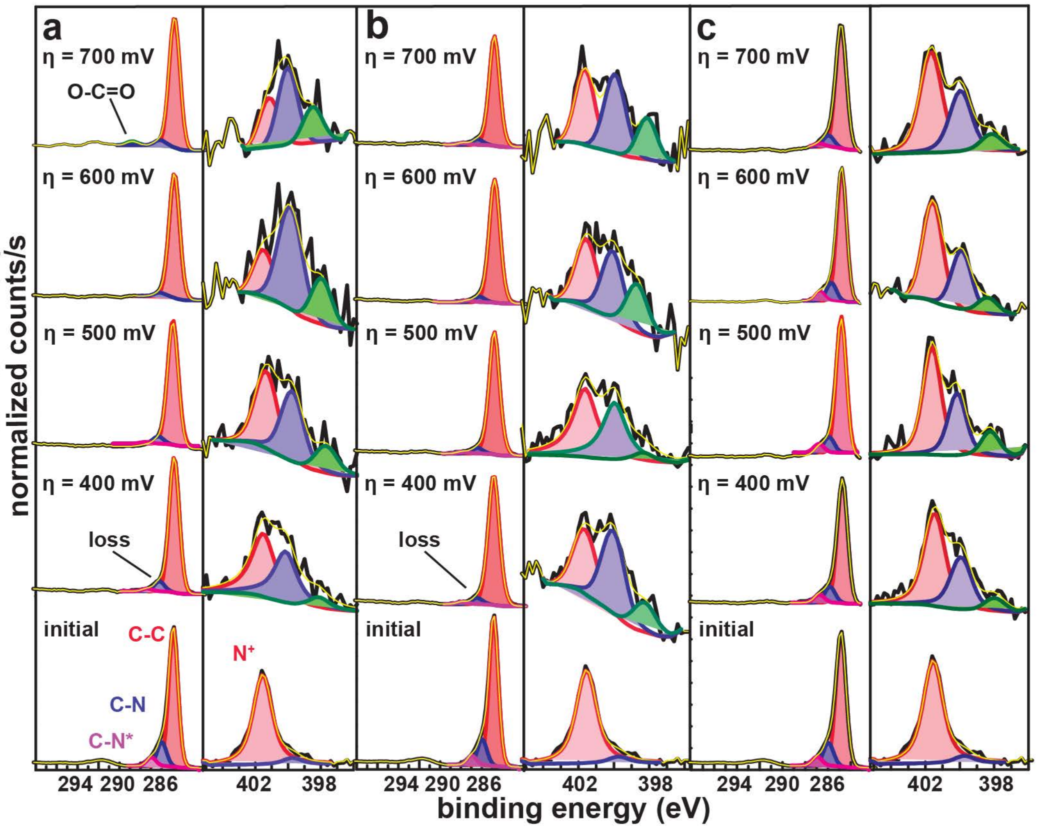

Figure 4.5. **Changes to the chemical structure of Sustainion under applied potential.** C 1s and N 1s XP spectra of Sustainion thin films tested at increasing overpotential in (a) pH 10, 1 M K_2CO_3/$KHCO_3$ buffer, (b) pH 14, 1 M KOH; and (c) pH 8, 1 M borate buffer.

Figure 4.5c shows the changes to the C 1s and N 1s XP spectra of Sustainion tested in 1 M borate buffer at pH 8. The C-N/total-C ratio decreased from 20 to 16% which is a smaller change than in KOH or K_2CO_3/$KHCO_3$ where the C-N/total-C ratio decreased by >50%. The N/C and Pt/C ratios remained unchanged. The N 1s peak underwent changes similar to the changes we observed in KOH and $K_2CO_3/KHCO_3$ but in this electrolyte the N^+ peak remained dominant.

Two of the possible chemical degradation routes for Sustainion are shown in Figure 4.3b. Imidazolium ring opening can be promoted by a nucleophilic attack.[37] The decrease in C-N/total-C ratio along with the material dissolution seen in the XPS results appears consistent with the loss of the imidazolium sidechains. The loss of sidechains, but not the backbone, is consistent with the ionomer film remaining on the electrode during QCM testing. However, N is still present in the film and, based on the new N 1s peaks at lower binding energy, is experiencing changes to its oxidation state or bonding environment. This would be possible if the imidazolium was undergoing structural changes prior to the complete degradation and separation from the backbone. Thus, ring-opening might be an intermediate to the removal of the imidazole group, or Routes 1 and 2 might happen concurrently in the case of chemical degradation by nucleophilic attack. However, Sustainion does not obviously degrade in the supporting electrolytes chosen for this study without applied potential. Thus, if a nucleophilic attack is happening, it appears facilitated in some way by the oxidizing potential.

Electrochemical degradation pathways are also possible. For instance, the phenyl connecting the imidazole ring to the backbone might be oxidized by OER intermediates or at the metal surface leading to the loss of the charge-carrying group. Unlike Aemion, Sustainion degraded the least in the electrolyte with the lowest pH while having almost identical degree of structural changes in KOH and carbonate/bicarbonate buffer. Sustainion does not seem to be affected specifically by the interactions with CO_3^{2-}/HCO_3^- anions as it degrades to the same extent in KOH. Perhaps the origin of Sustainion's tolerance of CO_3^{2-}/HCO_3^- anions is its ability to conduct these anions more efficiently than Aemion. The conductivity reported for Sustainion-X24 membrane in 1 M $KHCO_3$ is 24 $mS\cdot cm^{-1}$ at room temperature which is considerably lower than its conductivity in 1 M KOH (64 $mS\cdot cm^{-1}$)[38] but still much higher than the conductivity of Aemion in CO_3^{2-}/HCO_3^- forms (in 1 M $KHCO_3$, $\sigma = 3.8\ mS\cdot cm^{-1}$; in 1M K_2CO_3, $\sigma = 2.0\ mS\cdot cm^{-1}$). The least degradation in the lowest pH might be indicative of Sustainion being more affected by the concentration of OH^- in the electrolytes and undergoing the loss of sidechains as a result of nucleophilic attack or an oxidation reaction involving OH^- attack and electron transfer.

PiperION Structural Changes. We then examined if PiperION thin films show signs of oxidative damage in the supporting electrolytes under applied potential. In addition to looking at C 1s and N 1s spectra, we also collected F 1s spectra to monitor the trifluoromethyl group stability during operation (the F/C ratio in the pristine film was calculated to be ~ 1-2%). The C 1s spectrum was fitted with three peaks: the dominant peak at 284.8 eV assigned to C-C, C-H, and C=C and two smaller peaks at 285.9 and 286.7 eV for $C\text{-}N^+$ bonds (Figure 4.6, bottom panel). The N 1s peak for PiperION was fitted with only one peak at 402.7 eV and was assigned to the N^+ present in the structure in the piperidinium ring (N/C is about 3-4% in the pristine film and ~ 18% of C is bonded to N out of the total carbon content).

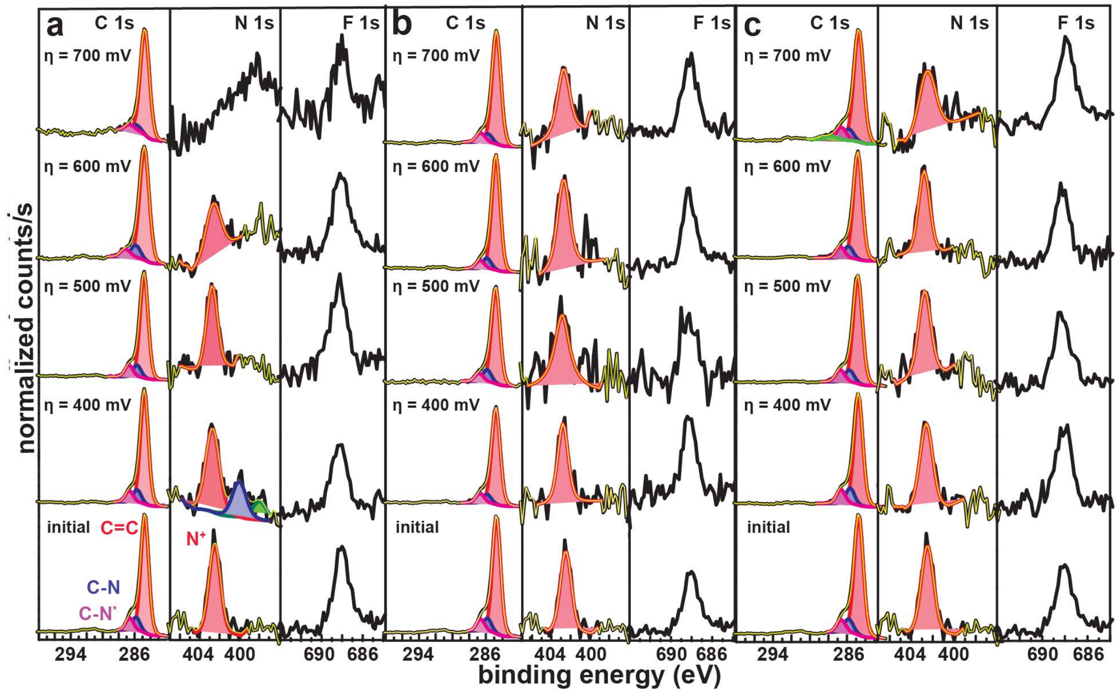

Figure 4.6. **Changes to chemical structure of PiperION under applied potential.** C 1s, N 1s, and F 1s spectra for PiperION thin ionomer films tested in (a) pH 10, 1 M $K_2CO_3/KHCO_3$ buffer; (b) 1M KOH; and (c) pH 8, 1M borate buffer.

In $K_2CO_3/KHCO_3$ the film dissolution was observed at lower overpotentials (Figure 4.6a). At η = 400 mV, N 1s spectrum changes to include several peaks at lower binding energy but the new N 1s peaks disappear by η = 500 mV. The observed changes to the shape of N 1s peak might originate from the intermediates of the degradation process. By η = 600 mV, the Pt/C ratio went from 11% to 41% along with a small decrease in the N/C and C-N/total-C ratios. As the overpotential of 700 mV was reached, the dissolution became more significant (Pt/C = 150%) with N 1s peak shifting to lower binding energy and decreasing in intensity. The amount of C bonded to N also decreased by a half. The F/C ratio for η = 600 mV and η = 700 mV was 4 and 3%, respectively (compared to 1-2% in the pristine ionomer film) suggesting that while the trifluoromethyl group remains, other carbon-containing fragments are lost. However, we do not see any sign of carbon forming new bonds characteristic of degradation products. The decrease in the N content and the absence of a more pronounced mass loss during the QCM test are suggestive of the chemical changes happening to the charge-carrying sidechains. It is, nonetheless, difficult to pinpoint the mechanism of degradation. The degradation products could dissolve in the supporting electrolyte and thus not be picked up by the XPS analysis.

During the electrochemical testing in 1.0 M KOH, PiperION film was not observed to dissolve/detach until η = 700 mV (Figure 4.6b). At η = 700 mV, the Pt/C ratio increased but not significantly: from 11 to 16%. The C-N/total-C ratio decreased, and F/C ratio increased.

In borate buffer (Figure 4.6c), despite a lower pH, no changes to the film structure were observed until η = 700 mV. We suspect that PiperION is not stable at this overpotential, and this degradation is independent of electrolyte identity. By the end of the electrochemical testing the Pt/C ratio went from 11 to 30%.

PiperION was not observed to dissolve or sustain chemical changes in 1.0 M KOH and pH 8 borate buffer until η = 700 mV. Thus, it does not seem to be affected by a high or low concentration of OH^- in the supporting electrolyte. However, in $K_2CO_3/KHCO_3$ buffer, the polymer underwent chemical changes and dissolved. One of the possible electrochemical degradation routes for this polymer is the oxidation of the phenyl ring in the backbone (Figure 4.3c). However, we were not able to observe any degradation products consistent with that mechanism. Another mechanism might take place, or the degradation products may dissolve into the electrolyte making it difficult to track them. To try and pinpoint the possible reasons for the instability of PiperION in carbonate/bicarbonate buffer specifically, we considered the conductivity of PiperION in carbonate and bicarbonate electrolytes. The conductivity of PiperION solid membrane in water at room temperature when it is ion-exchanged to the carbonate form is 6 mS·cm^{-1}, and 5 mS·cm^{-1} when it is ion-exchanged to bicarbonate form.[39] These values are higher than the conductivity of Aemion in carbonate/bicarbonate electrolytes but significantly lower than the carbonate/bicarbonate conductivity reported for Sustainion. However, the conductivities reported in the literature are affected by the measurement method. For example, in the recent work by Endrödi *et al.* the conductivities of PiperION and Sustainion in carbonate and bicarbonate electrolytes were measured for a range of elevated temperatures and were found comparable.[40] PiperION might be affected by a lower local pH due to the concentration and pH gradients forming at the interface of the thin film and bulk electrolyte or be subjected to oxidation by the electrode surface in the absence of OH$^-$ due to the low conductivity of CO_3^{2-}/HCO_3^- anions.

Attenuated Total Reflectance (ATR) FTIR Spectroscopy Analysis. To further investigate the film degradation processes in the presence of the electrolytes under applied potential, we employed ATR-FTIR on 5 wt. % ionomer films.

Aemion ATR-FTIR Analysis. The summary of the changes to the Aemion spectrum under each applied potential in the three electrolytes is shown in Figure 4.7. In the pristine film (black traces in Figure 4.7) the vibrational mode at 1630 cm^{-1} was assigned to the C=N bond in the imidazole fragment. We find a similar mode in the spectrum of an imidazole compound in the literature.[41-42] The most noticeable changes to the spectrum happened in $K_2CO_3/KHCO_3$ buffer. The mode at 1630 cm^{-1} transformed into two vibrational modes with maxima at 1640 and 1610 cm^{-1}. At η = 500 mV two new modes appeared at 1250 and 1220 cm^{-1}; the mode at 1400 cm^{-1} transformed into multiple modes; and a small vibrational mode appeared at 753 cm^{-1}. The transformation of the C=N mode into multiple modes can be interpreted as the loss of the imidazole ring and possible formation of N-H and other C=C bonds in the changed structure. The new modes at 1250 and 1220 cm^{-1} can originate from a C-N or a C-O bond formation.

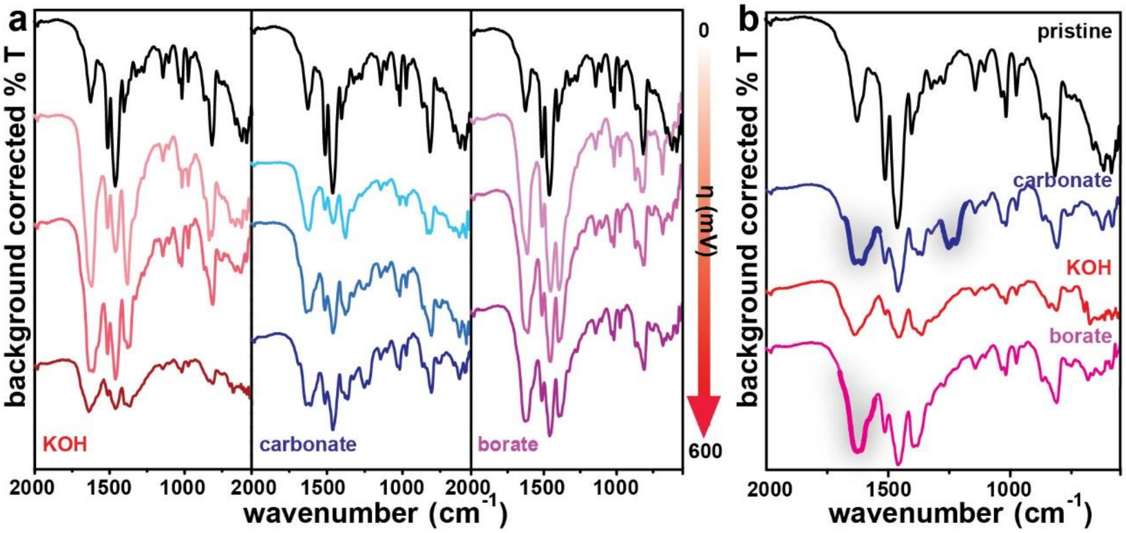

Figure 4.7. **Chemical changes to the structure of Aemion probed by ATR-FTIR.** (a) ATR-FTIR spectra of Aemion films collected after testing the films in 1.0 M KOH (red traces), 1 M K_2CO_3/$KHCO_3$ buffer pH 10 (blue traces), and 1 M borate buffer pH 8 (purple traces). Top to bottom: black trace is of pristine Aemion film, then in order of increasing overpotential (η = 400, 500, and 600 mV). (b) ATR-FTIR spectra collected on Aemion films tested at η = 600 mV in the three supporting electrolytes.

The changes observed by ATR-FTIR for Aemion tested in KOH are not as pronounced (Figure 4.7, red traces). The vibrational mode at 1400 cm^{-1} converts into multiple modes similarly to the changes we observe in K_2CO_3/$KHCO_3$ buffer. The small modes in the 1300-1250 cm^{-1} range disappear but do not convert into new modes that appeared in K_2CO_3/$KHCO_3$. A small mode appears at 753 cm^{-1} at η = 500 mV, which is the region that describes changes in substitution in aromatic compounds. This may indicate a demethylation of the nitrogen in the imidazole as a result of OH^- attack or a different mechanism. The 500 mV is the same overpotential at which we start observing film loss and diminishing C-N/total-C ratio by XPS.

Figure 4.7 also shows the gradual changes to the film structure in 1 M borate buffer. The vibrational mode at 1630 cm^{-1} deforms slightly compared to its initial shape and the region between 1400 and 1250 cm^{-1} changes. The mode at 1390 cm^{-1} turns into two modes and the small modes at ~ 1320 cm^{-1} disappear. The observed changes might be indicative of changes to the N bonding environment. However, the changes are not significant enough to cause film loss that would be apparent by QCM and XPS.

ATR-FTIR data for Aemion is consistent with the XPS results: it shows that the film undergoes some structural changes in every supporting electrolyte with the changes in carbonate/bicarbonate buffer being the most significant. The XPS analysis of the film tested in carbonate/bicarbonate buffer shows the formation of C=O species along with N^+ loss and film dissolution. ATR-FTIR confirms these changes showing the loss of the C=N mode intensity and several other new modes growing.

Sustainion ATR-FTIR Analysis. Sustainion ATR-FTIR spectra at different overpotentials were collected in a similar manner (Figure 4.8). Like Aemion, Sustainion possesses an imidazole group. We assigned the vibrational mode at 1650 cm^{-1} to the C=N in imidazole. The spectrum of Sustainion undergoes similar transformations after electrochemistry in KOH and $K_2CO_3/KHCO_3$ buffer with both the 1650-1530 cm^{-1} and 1370-1330 cm^{-1} regions changing. We observed the shape transformation of the mode assigned to imidazole, the loss of the vibrational mode at 1533 cm^{-1}, and the growth of a mode at 1567 cm^{-1}. This region of the spectrum can have modes from a variety of bonds including C=N, C=O, O-N=O. The mode in the 1370-1330 cm^{-1} region changes from a small broad one to a sharp mode. The observed changes to the spectrum of Sustainion might originate from transformations of the imidazole ring leading to its loss due to nucleophilic OH^- attack or by electrochemical oxidation. Pellerite *et al.* reported similar changes to the IR spectrum of Sustainion soaked in 1 M KOH for 24 h without any applied potential.[37] In that case, the observed changes to the spectrum were later reversed by a soak in 1 N HCl and were attributed to the formation of a carboxylated zwitterion upon CO_2 addition, not permanent degradation by the ring opening.[37] We, however, do not believe that Sustainion under applied potential undergoes reversible changes in KOH or carbonate/bicarbonate buffer given the loss of nitrogen and C-N bonds observed by XPS. The ionomer films tested in borate buffer show fewer changes to the spectrum. The 1533 cm^{-1} mode disappears, but no new mode appears at 1567 cm^{-1}. There is a new vibrational mode at 1313 and 813 cm^{-1}. The mode at 1313 cm^{-1} might originate from the borate species present in the film but given the low amount of boron determined by XPS we conclude this is unlikely.

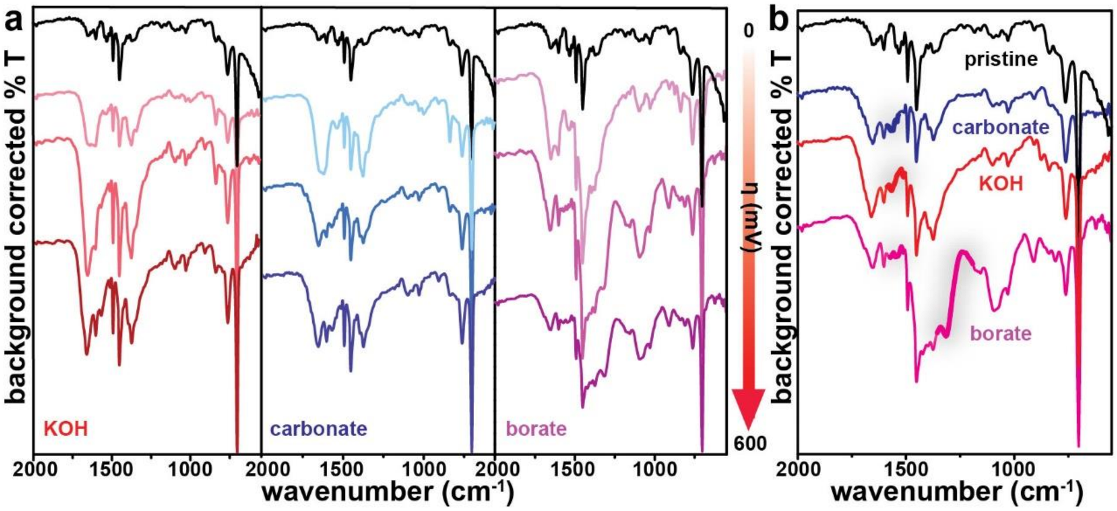

Figure 4.8. **Chemical changes to the structure of Sustainion probed by ATR-FTIR.** (a) ATR-FTIR spectra of Sustainion films collected after testing the films in 1.0 M KOH (red traces), 1 M K_2CO_3/$KHCO_3$ buffer pH 10 (blue traces), and 1 M borate buffer pH 8 (purple traces). Top to bottom: black trace is of pristine Sustainion film, then in order of increasing overpotential (η = 400, 500, and 600 mV). (b) ATR-FTIR spectra collected on Sustainion films tested at η = 600 mV in the three supporting electrolytes.

These studies suggest Sustainion is sensitive of the basicity of the electrolyte but might not be strongly affected by anions such as CO_3^{2-} or HCO_3^-. XPS showed considerable loss of the C-N bonds in both KOH and carbonate/bicarbonate buffer. ATR-FTIR data supports these results showing changes to the C=N imidazole mode that suggest the charge-carrying group is degrading. This process might be unaffected by the presence of CO_3^{2-} or HCO_3^- due to the high carbonate/bicarbonate conductivity reported for Sustainion. Fast conduction of the anions through the ionomer film during operation would facilitate the transfer of OH^- (and protons in the form of HCO_3^-) to (and away from) the electrode surface. These processes would decrease the pH gradient and provide sufficient OER reactants to avoid ionomer oxidation.

PiperION ATR-FTIR Analysis. The ATR-FTIR spectra of PiperION after electrochemistry in the three electrolytes is in Figure 4.9. Consistent with our XPS results, the most noticeable changes to the ATR-FTIR spectrum of PiperION are observed in $K_2CO_3/KHCO_3$ buffer (Figure 4.9, blue traces). The vibrational mode at 1630 cm^{-1} transforms into multiple modes at 1640, 1605, and 1558 cm^{-1}. The mode at 1558 cm^{-1} appears at η = 400 mV and the one at 1605 cm^{-1} by η = 600 mV. The mode at 1395 cm^{-1} converts into two modes by η = 600 mV. We, however, did not observe the appearance of a stretch or a bend consistent with a carboxylate formation which is a degradation product predicted by the electrochemical oxidation route. The changes to the 1640-1560 cm^{-1} region of the spectrum might result from a formation of new C=N or C=C bonds.

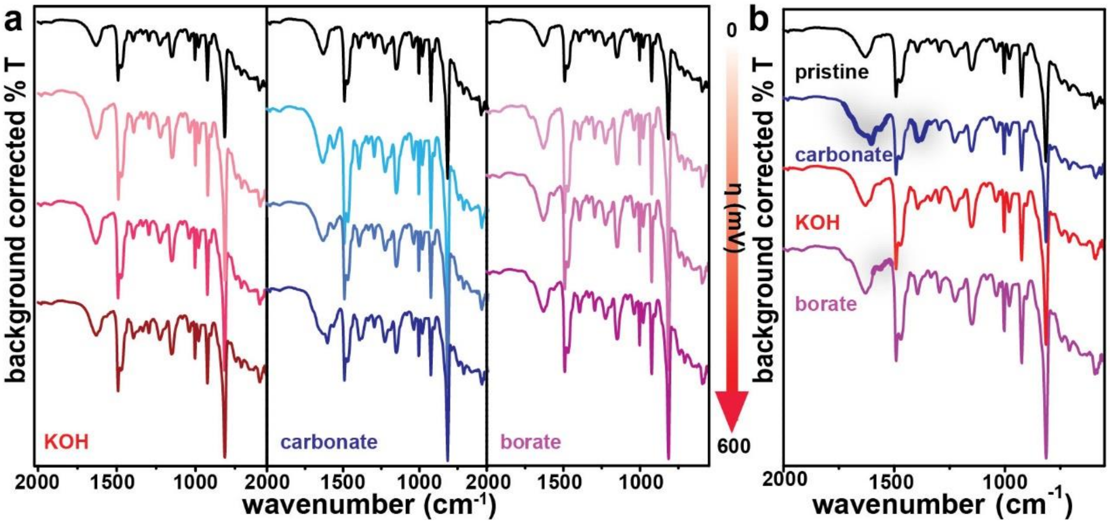

Figure 4.9. **Chemical changes to the structure of PiperION probed by ATR-FTIR on a diamond crystal.** (a) ATR-FTIR spectra of PiperION films collected after testing the films in 1.0 M KOH (red traces), 1 M $K_2CO_3/KHCO_3$ buffer pH 10 (blue traces), and 1 M borate buffer pH 8 (purple traces). Top to bottom: black trace is of pristine PiperION film, then in order of increasing overpotential (η = 400, 500, and 600 mV). (b) ATR-FTIR spectra collected on PiperION films tested at η = 600 mV in the three supporting electrolytes.

The PiperION film tested in KOH does not seem to undergo any structural changes as no new vibrational modes appeared in the ATR-FTIR spectrum. We also did not observe any chemical changes in KOH by XPS (except at η = 700 mV). The ATR-FTIR spectra of the film tested in borate buffer has a small change in the 1600-1500 cm^{-1}

region: a new mode appears at 1558 cm^{-1} similarly to the one we observed in $K_2CO_3/KHCO_3$ buffer. The mode becomes noticeable at η = 500 mV and might be the result of some changes to the structure of the ionomer.

PiperION did not show any signs of significant structural changes in KOH or borate buffer evident by QCM, XPS (until η = 700 mV), and ATR-FTIR. The stability of the ionomer, however, can be impacted by the presence of metal oxide catalyst undergoing OER in an electrolyzer. We showed that PiperION ionomer in direct contact with IrO_x powder at the anode of an AEMWE oxidizes substantially and loses headgroups.[14] In carbonate/bicarbonate buffer PiperION undergoes structural changes as suggested by our XPS and ATR-FTIR data. XPS showed N loss and film dissolution but without new peaks appearing in the C 1s spectra. ATR-FTIR spectra revealed several new modes growing and the existing modes changing shape. Based on the evidence presented by the surface characterization techniques, the polymer is undergoing dissolution (e.g., we find an increase in Pt/C ratio by XPS after electrochemistry). We, however, cannot be sure in the (electro)chemical mechanism because some of the degradation products might dissolve into the electrolyte and avoid detection.

Computational Studies of Ionomer Oxidative Stability. To help differentiate between chemical and electrochemical degradation routes for these polymers, we performed DFT calculations to computationally examine redox potentials (E_0) of the polymer structures and to predict where the oxidation is likely to occur within the polymer. The E_0 of the polymers can suggest which of the polymers is more likely to oxidize under applied potential. The identification of the fraction of the polymer that the E_0 corresponds to leads to better understanding of the degradation pathway.

Our calculations indicate that E_0 for the ionomers are: Sustainion (2.18 eV vs SHE *cis*, 2.33 eV vs SHE *trans*) > PiperION (1.78 eV vs SHE) > Aemion (1.46 eV vs SHE) (Figure 4.10). The range of values for Sustainion is attributed to the competing effects produced by π-stacking: the destabilization of the ground state and the stabilization of the spin density vie a multicenter single-electron bond. The latter was observed for the imidazolium-containing sidechain. Given the stabilization provided by the imidazole fragment, the phenyl ring in contact with it is less likely to be oxidized than the phenyl ring next to it without the charge-carrying group. However, the E_0 for this route is very high. The experimental data shows changes to the N 1s bonding environment or oxidation state which would not occur in the case of phenyl oxidation. A possible route for Sustainion degradation, given a high E_0 for phenyl oxidation, is the loss of the sidechains through the OH^- attack on the C connecting the phenyl and imidazole fragment or the imidazole ring leading to the loss of the sidechains. This mechanism is perhaps promoted by the applied potential as we see no evidence of Sustainion degrading in the supporting electrolytes without applied potential.

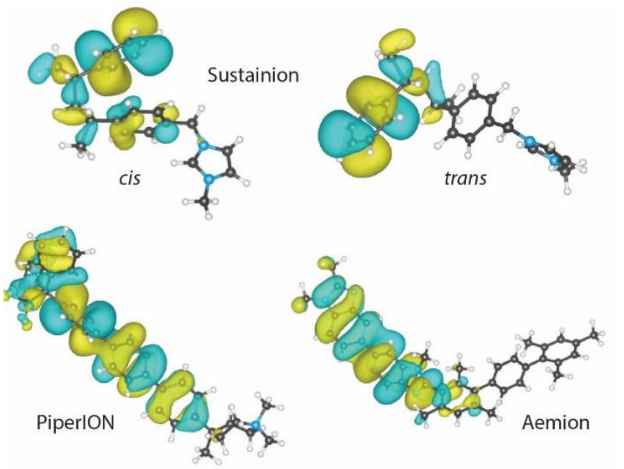

Figure 4.10. HOMO electronic occupation diagram calculated by DFT for the ionomer fragments indicated. The HOMO is, to a first approximation, the energetically most favorable site for oxidation to occur.

Within the PiperION structure the phenyl rings adjacent to the trifluoromethyl group help stabilize the HOMO by withdrawing electron density which decreases electron-electron repulsion. Oxidative attack is thus likely to affect the other phenyl rings in the backbone that are occupied by higher-energy electrons. The changes we observed experimentally are more-consistent with the attack on the charge-carrying groups given the changes to the shape of the N 1s spectrum and the absence of carboxylate-related C 1s peaks or vibrational modes. However, that does not rule out the electrochemical aromatic oxidation considering as degradation products may be in small amounts and/or dissolve into the electrolyte.

Because Aemion has the lowest E_0, it appears most likely to suffer from oxidative damage. Our calculations suggest that oxidizing any cationic motif is unlikely. The E_0 corresponds to the removal of an electron from the benzimidazole. The likeliest point of oxidative damage is the N in the benzimidazole that does not have a methyl group attached to it (Figure 4.1a**)**. The methyl groups on substituted phenyl and imidazolium rings add spin-stabilization. The imidazolium ring-opening is also proposed as the chemical degradation route. We suspect that the polymer degrades through cleavage of the imidazole ring with applied potential playing a role in the process. Aemion does not degrade in 1.0 M KOH without applied potential. Nor does it degrade in carbonate/bicarbonate solutions. Thus, the routes leading to the polymer damage might include an OH^- attack on the polarized bonds or a direct oxidation of the structure by the OER intermediates or the electrode surface.

Analyzing the Ionomer Stability in Acidic Environment. The higher degree of structural changes that Aemion and PiperION showed in 1 M carbonate/bicarbonate buffer compared to the other electrolytes suggested that the interactions of the HCO_3^-/CO_3^{2-} anions with the ionomer matrices play a role in the stability of the polymers during OER. Our two hypotheses in regard to the effect anions have on the ionomer were: (*i*) the development of a pH gradient with consecutive ionomer oxidation facilitated by a local pH drop at the electrode surface, and/or (*ii*) poor transport of OH^- to the electrode surface due to low carbonate/bicarbonate conductivity of Aemion and PiperION which leads to the ionomer oxidation reaction dominating. To determine if the low pH in addition to the applied potential was responsible for the observed structural changes, we tested the thin 0.16 wt. % ionomer films in 0.1 M $HClO_4$ (pH ~ 1) at η = 400 and 600 mV and analyzed them with XPS.

The stability of Aemion in acidic environment seems to be better than in carbonate/bicarbonate buffer (Figure C.6a shows XPS data and fitting). No film dissolution or appearance of new C or N peaks was observed at η = 400 mV. At η = 600 mV while no changes to the C 1s and N 1s were observed, the Pt/C ratio from XPS slightly increased signifying film dissolution. Aemion does not appear to be affected by the acidic pH while under applied potential and, thus, is likely not degrading in carbonate/bicarbonate buffer due to the local pH drop. Given that we observed some degree of dissolution in all four tested electrolytes, we hypothesize that ionomer oxidation facilitated by applied potential occurs in all cases but at a different rate. Testing Aemion in pH 1 acid showed its good stability in acidic conditions. Thus, we were left to conclude that the difference in OH^- vs CO_3^{2-}/HCO_3^- conductivities is causing Aemion to degrade in carbonate, perhaps due to the formation of a modest pH gradient and lack of OH^- to oxidize at the electrode surface.

The structural changes observed for Sustainion tested in acid resemble the results of the electrochemical testing in borate buffer (Figure C.6b). At η = 400 mV no dissolution was observed, but there was a small loss of the C-N bonds and a change to the shape of N 1s peak. At η = 600 mV film dissolution was identified and the loss of C-N bonds became more pronounced. However, the N 1s peak assigned to N^+ still dominated the spectra for all overpotentials. Sustainion sustained less damage in acidic environment than in base. Sustainion was apparently designed to operate in carbonate-containing environment. It degraded the most in the electrolytes of higher basicity, but only when potential was applied. Given the comparably higher E_0 estimated from DFT, we hypothesize that OH^- attack becomes more likely when the film is polarized by the electrode surface. It seems likely that the carbonate/bicarbonate conductivity of Sustainion is high enough to perhaps suppress larger pH gradients.

Interestingly, PiperION sustained significant damage in 0.1 M $HClO_4$ (Figure C.6c). At η = 400 mV no dissolution was observed, but a new high-energy peak appeared in the N 1s spectrum. At η = 600 mV the F/C ratio doubled, and the Pt/C ratio increased signifying film dissolution. N 1s peak remained at the same binding energy as in the pristine film but decreased in intensity. The C 1s spectrum gained several peaks at higher binding energy pointing to the formation of new C compounds. The amount of the film loss during electrochemical testing in acid is similar to the film loss observed in carbonate/bicarbonate buffer. Thus, for PiperION we hypothesize that its stability might depend on both the carbonate/bicarbonate conductivity and the local pH drop, as we see degradation occurring in both $HClO_4$ and carbonate/bicarbonate buffer. We also know from our previous work that PiperION is subject to oxidative degradation when used for a prolonged operation in pure-water AEMWE with IrO_x and that pH gradients are likely at high current denisites.[14]

Conclusion

In Chapter IV, we analyzed the effects of supporting electrolytes on the stability of anion-conducting ionomers under oxidizing potentials in the context of their application in alkaline membrane electrolyzers. The ionomers demonstrated different degrees of stability in KOH, $K_2CO_3/KHCO_3$ buffer, borate buffer, and $HClO_4$. Aemion degraded and dissolved in all four electrolytes, with damage to the chemical structure being the most pronounced in carbonate/bicarbonate buffer. The stability of Aemion seems to be affected by strongly interacting carbonate/bicarbonate anions that may prevent a rapid flux of OH^- to the electrode surface and allow ionomer oxidation. PiperION showed material loss in carbonate/bicarbonate buffer and in acidic conditions remaining stable in KOH and borate buffer. The low conductivity of carbonate/bicarbonate forms of PiperION might facilitate a pH gradient leading to the oxidative changes to the polymer due to the local pH drop or the absence of sufficient OH^- for OER in which case the relative polymer oxidation rate increases. Sustainion exhibited the same degree of degradation in KOH and carbonate/bicarbonate buffer and little observed degradation in borate buffer and $HClO_4$. The degradation for this ionomer appears to be triggered primarily by the applied potential but seems to be favored in electrolytes with higher OH^- concentration. We also acknowledge that the presence of OER catalysts can introduce additional degradation pathways (Figure C.7).[14]

Looking forward, gas chromatography coupled with mass spectrometry and nuclear magnetic resonance spectroscopy can be employed to analyze (dilute) soluble ionomer fragments to unravel the mechanisms of ionomer degradation. The analysis of post-mortem GDLs from pure-water fed AEMWE will also be key, as shown by our initial results.[14]

In sum, we demonstrated that a combination of characterization techniques can unravel some of the processes at the ionomer/catalyst interface. The three-electrode setup was a simple model system that mimics in many ways the anode of the AEMWE. This approach can be successfully employed to test the interactions of a variety of OER catalysts (PGM and non-PGM). Such experiments can be run in parallel with the AEMWE tests (with the GDLs being analyzed as well) to gain a comprehensive understanding of water electrolysis in a zero-gap configuration.

Bridge

In Chapter IV a better understanding of the polymer stability under applied potential in the presence of different anion was developed. The findings about the ionomer interactions with anions during electrolyzer operation are used in Chapter V to predict the possible challenges facing the large-scale implementation of AEMWE technology. The spectroscopic techniques and methods used in Chapter IV were employed to conduct the investigation described in Chapter VI. Chapters V and VI build upon this work by investigating the stability issues that depend on the identity of the oxygen-evolution-reaction catalyst.

CHAPTER V

OXYGEN ELECTROCATALYSIS ON MIXED-METAL OXIDE/OXYHYDROXIDES: FROM FUNDAMENTALS TO MEMBRANE ELECTROLYZER TECHNOLOGY

Chapter V contains co-authored materials previously published as *Acc. Mater. Res*. **2021**, *2* (7), 548–558 reproduced with permission. Copyright 2021 Accounts of Materials Research. Prof. Boettcher and I conceived of the project. I wrote the paper with assistance from Yingqing Ou, Quicheng Xu, Liam Twight, and Nathan Stovall. Prof. Boettcher provided editorial assistance.

Introduction

The ability of hydrogen to serve as a medium between chemical and electrical energy makes it an attractive alternative to carbon-based fuels for powering transportation of people and goods, heating buildings, producing fertilizers, refining metals, and making electricity with fuel cells.[1-2] Today most hydrogen is produced by steam-reforming of fossil fuels.[1] An alternative is water electrolysis – splitting of water into hydrogen and oxygen with electricity. Water splitting involves two half-reactions: the oxygen-evolution reaction at the anode (OER; in base: $4OH^- \rightarrow 2H_2O + 4e^- + O_2$, in acid: $2H_2O \rightarrow 4H^+ + O_2 + 4e^-$) and hydrogen evolution reaction at the cathode (HER; in base: $2H_2O + 2e^- \rightarrow H_2 + 2OH^-$, in acid: $2H^+ + 2e^- \rightarrow H_2$). Driving the OER results in a large overpotential (excess energy beyond the thermodynamic requirement) that decreases the efficiency of electrolyzers. Electrocatalysts capable of lowering the overpotential have been under investigation for nearly a century.

The oldest electrolyzer technology is alkaline water electrolysis (AWE). AWE is typically operated at ~ 80 °C in a concentrated basic liquid electrolyte (KOH or NaOH). Although the current densities are typically < 500 $mA\cdot cm^{-2}$, the low materials cost from the inexpensive (steel) cell components and non-PGM catalysts leads to a relatively low overall cost for hydrogen.[1] A newer technology, PEMWE, replaces liquid electrolyte with a solid, locally acidic, ionomer membrane.[3] Pure water is fed to a compressed stack allowing operation at > 2 $A\cdot cm^{-2}$ and yielding high-purity output hydrogen.[1, 3] The solid-polymer electrolyte reduces cross-over of hydrogen and oxygen gas, allowing thinner electrolytes with lower resistive losses and the direct electrochemical compression of the output hydrogen.[3] The acidic membrane, however, requires the use of PGM catalysts and expensive stack materials (e.g. Ti) because non-PGM catalysts corrode and dissolve.

AEMWE in principle can combine the advantages of AWE and PEMWE. The system uses the same compressed stack design as PEMWE but replaces the acidic membrane with a basic one enabling the use of non-PGM catalysts and cheaper stack materials.[1, 4] AEMWE is, however, at its early stage and has challenges to overcome before it can compete in efficiency and durability with PEMWE. The design of active and stable OER and HER catalysts is imperative for the development and commercialization of AEMWE systems.

Iron-containing Ni and Co-based catalysts have superior OER performance in base and AWE compared to other catalysts including PGMs.[5-7] The origin of their high performance has been subject to much discussion and a few key results follow. Friebel *et al*. reported Fe^{3+} as an active site in $Ni_{1-x}Fe_xOOH$ using a combination of *operando* X-ray absorption spectroscopy (XAS) and DFT calculations.[8] Gorlin *et al*. found that for $Ni_{1-x}Fe_xOOH$ with $x > 0.09$, Ni remains largely in +2 oxidation state during OER.[9] In contrast, Li *et al*. proposed that Fe^{3+} promotes the formation of Ni^{4+} that is responsible for the enhanced OER activity.[10] Smith *et al*. studied $Fe_{100-y}Co_yO_x$ and observed Co oxidation under OER conditions.[11] Gong *et al.* concluded that under-coordinated Fe^{3+} was an active site, despite Fe not being oxidized.[12] Hunter found evidence for Fe^{6+} and ferrate-like species in non-aqueous conditions.[13] Chen *et al*. found Fe^{4+} under active conditions with Mossbauer spectroscopy, but demonstrated that this species persisted after the applied potential was removed.[14] The Fe cation sites are also dynamic; dissolving and redepositing depending on the concentration of solution Fe^{3+}.[15]

Understanding of the mechanism of OER in basic conditions and the identity of active sites is important for designing better catalysts for both AWE and AEMWE. Additionally, the effects of Fe adsorption/desorption, catalyst restructuring, and its electrical conductivity should be accounted for when incorporating $Ni(Co)_{1-x}Fe_xOOH$ into traditional AWE or membrane-electrode-assembly (MEA) systems.

In Chapter V, we describe our efforts to identify and understand the active sites in Fe-doped Ni and Co (oxy)hydroxides. We aim to understand the mechanisms of Fe incorporation into the catalysts, the role played by Fe during OER, and how this understanding influences design principles for OER catalysts in electrolyzer technologies. Finally, we discuss research directions related to OER catalysts and electrolyzers relevant for high-performance non-PGM AEMWE.

Discussion

Intrinsic Activity Trends for Metal (Oxy)Hydroxides. The use of thick catalyst layers and ill-defined active surface areas, as well as differences in electrical conductivity and local surface structure has historically complicated the direct comparisons of intrinsic OER activity.[6, 8] A better comparison can be made if the catalysts were prepared as thin films (2-3 nm) supported on conductive supports that minimize ohmic and mass-transfer overpotentials and the amount of inactive (bulk) catalyst.[16] This thin-film configuration also allows *in-situ* mass monitoring using a quartz crystal microbalance (QCM) and calculation of lower-limit turnover frequencies (TOF, the number of O_2 molecules evolved per metal active site per second) based on the total number of metal cations. The use of TOFs is a good metric for the comparison of intrinsic catalytic activity. In alkaline media, IrO_x is ~10-fold less active than $Ni_{0.9}Fe_{0.1}O_x$ (TOFs = 0.009 ± 0.005 s^{-1} and 0.21 ± 0.03 s^{-1} at $\eta = 0.3$ V, respectively).[16] We compared the activities of many first-row transition metal oxides (NiO_x, CoO_x, $Ni_yCo_{1-y}O_x$, $Ni_{0.9}Fe_{0.1}O_x$, IrO_x, MnO_x, and FeO_x). We also analyzed if synergetic effects existed with two or more different metals. In the case of Co and Ni, we observed no synergy, in contradiction with previous trends reported.[17-18] Addition of Fe to Co or Ni improved the performance to different degrees suggesting different interactions of Fe with the matrices.[16, 18] X-ray photoelectron spectroscopy (XPS) showed the catalysts were converted into (oxy)hydroxide phases during operation in agreement with thermodynamics-based Pourbaix diagrams.[16, 19] CoO_xH_y and NiO_xH_y both form layered structures with octahedrally coordinated metal cations and small ordered domain sizes where the individual layers are noncovalently bonded and intercalated with ions and water.[19-20]

The electrical conductivity of the catalyst phases is important in designing high performance electrodes. For (oxy)hydroxides, the oxidation and protonation state of the material depends on applied potential, and therefore the conductivity is different than that measured from pressed catalyst-powder pellets. We measured thin-film conductivity as a function of applied potential using microfabricated interdigitated array (IDA) electrodes.[19, 21-22] We discovered that the conductivity varied with composition and applied potential. CoO_xH_y and NiO_xH_y were insulating when the cations were +2 and conductive when oxidized to nominally +3 or +4; a conversion that happens under OER conditions and that is (usually) reversible. The redox behavior of CoO_xH_y and NiO_xH_y provides another mechanism to measure the number of electrochemically accessible metal cations which can be done by integrating the pre-OER redox feature visible in the voltammetry. [23] Whether all these sites serve as active sites is an ongoing debate.[24-27]

XPS analysis of thin-film CoO_xH_y and NiO_xH_y catalysts revealed Fe impurities absorbed from the electrolyte even without intentional addition of Fe salts.[16, 19, 21] To observe the intrinsic activity, Fe impurities had to be removed. We produced Fe-free KOH by absorbing Fe species with $Ni(OH)_2$ and $Co(OH)_2$.[19] We note that these Fe-free electrolytes do contain residual $Co(OH)_2$ or $Ni(OH)_2$ that can be removed by filtration with a 0.1 μm polyethersulfone filter. The catalysts tested in Fe-free KOH did not show any traces of Fe incorporation by XPS.[19] We then reported the first intrinsic activity trend of first-row transition metals with rigorous exclusion of Fe-impurities. We accounted for the influence of the film thickness, conductivity, and underlying substrate interactions (Figure 5.1).[28-30] We discovered that, in the absence of Fe, NiO_xH_y was a terrible OER catalyst – three-orders-of-magnitude less active than $Ni(Fe)O_xH_y$.[19] CoO_xH_y shows higher activity than NiO_xH_y in the absence of Fe, but when Fe is added, $Ni(Fe)O_xH_y$ has a higher TOF than $Co(Fe)O_xH_y$ at all overpotentials.[21] The activity of FeO_xH_y was found to be strongly dependent on the film thickness and the support (see below).[28, 30-31] At this point, we proposed that Fe was an essential component of the active site in all the first-row transition-metal catalysts in alkaline conditions (with reasonably high activity) whether incorporated intentionally or from the electrolyte impurities.[28]

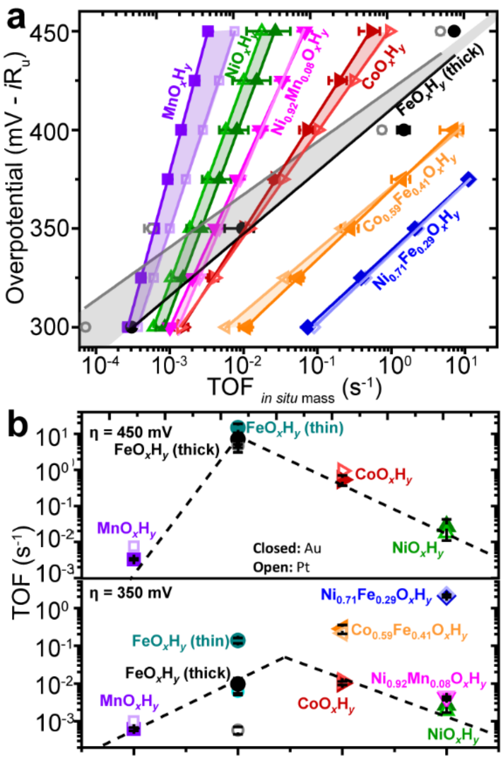

Figure 5.1. Activity trends for first-row transition metals. (a) Steady-state activity trends as a function of potential for first-row transition-metal (oxy)hydroxides on Au (solid) and Pt (open) quartz-crystal-microbalance electrodes. The TOFs reported are based on the total mass measured with the QCM assuming every metal cation is a possible active site. (b) The data plotted at η = 450 mV (top) and at η = 350 mV (bottom). Compositions in (b) are ordered based on atomic number of the host/primary cation. Lines and shading guide the eye. All the films had a loading of 8 to 12 μg·cm^{-2}, except for the thin FeO_xH_y which was 0.5−1.0 μg·cm^{-2}. Adapted from ref 30 with permission. Copyright 2015 American Chemical Society.

Understanding Fe-based Active Sites. To better understand how Fe-based OER catalysts function, we studied pure FeO_xH_y.[28] To do this, the instability of FeO_xH_y under alkaline OER conditions and its low electrical conductivity had to be addressed. FeO_xH_y films were prepared by three methods – electrodeposition,[19, 32] thermal decomposition of a spin-cast metal-nitrate films,[16] and thermal evaporation of Fe metal – and were probed by XPS after annealing in air and immersion in 1 M KOH.[30] Fe was oxidized to nominally FeOOH under these conditions regardless of preparation method. Using electrodeposited FeO_xH_y films, the dependence of OER activity on the substrate type (Au and Pt) and film thickness was investigated (correcting for dissolution via QCM measurements). At η =

350 mV, the OER current was insensitive to mass loading, but depended on the substrate identity with FeO_xH_y on Au much more active than on Pt (likely due to interaction of Fe and Au oxides under OER conditions).[31, 33] At $\eta = 450$ mV, the OER current was proportional to FeO_xH_y loading up to ~3 $\mu g \cdot cm^{-2}$ before increasing slower between 3 and 7.5 $\mu g \cdot cm^{-2}$ and remaining constant after 7.5 $\mu g \cdot cm^{-2}$. We concluded that only a thin layer of FeO_xH_y nearest to the electrode surface is active at $\eta = 350$ mV due to the low electrical conductivity of FeO_xH_y. At $\eta = 450$ mV, the thickness of the active layer increases because the electrical conductivity increases as the Fe accesses higher oxidation states.[30]

The comparison of the intrinsic activity of $Ni(Fe)O_xH_y$, $Co(Fe)O_xH_y$, and FeOOH was made by calculating TOF per electrochemically active Fe site (TOF_{Fe}) at $\eta = 350$ mV and 450 mV. To account for limited conductivity, we approximated the amount of "active" FeO_xH_y as that within a loading range such that < 1 mV of Ohmic drop occurs at 1 $mA \cdot cm^{-2}$ (0.1 $\mu g \cdot cm^{-2}$ at 350 mV and 5 $\mu g \cdot cm^{-2}$ at 450 mV). It was observed that at $\eta =$ 350 mV and 450 mV, $Ni_{0.75}Fe_{0.25}OOH$ had a higher TOF_{Fe} than $Co_{0.54}Fe_{0.46}OOH$ and FeO_xH_y /Au. This data suggested that the "host", and therefore local chemical environment of Fe, enhances the OER activity.[28]

We investigated how Fe was involved in OER using *operando* XAS. For this we studied $Co(Fe)O_xH_y$, which shares key features with $Ni(Fe)O_xH_y$. The OER activity of $Co(Fe)O_xH_y$ increases 100-fold with 40%-60% co-deposited Fe relative to Fe-free CoO_xH_y. Voltametric analysis shows an anodic shift in the $Co^{2+/3+}$ redox wave with increasing Fe content suggesting strong electronic coupling between Co and Fe.[21] The nominally $Co^{2+/3+}$ wave is, however, more negative than the nominally $Ni^{2+/3+}$ wave, even in the presence of large amounts of Fe. This is important, because it allowed us to resolve the local structure and oxidation states at both Fe and Co sites by XAS at potentials more positive of the Co wave (i.e. when the catalyst is in the relevant oxidized "active-state" but not yet evolving oxygen) and compare to more-positive potentials where substantial OER current is passing. Compared to previous studies,[8, 13-14] our work was important because we engineered porous catalyst structures as thin films where essentially all the Co and Fe sites were exposed to electrolyte.[7] The porous structure was achieved by an electrodeposition from a precursor salt solution via a cathodic reduction of NO_3^-.[7] The

XAS thus reported on changes to surface-active Co and Fe sites without large background signal from sites buried and not accessible to the electrolyte. In Co(Fe)O_xH_y, we found a 6% decrease in the Fe-O bond length and a small absorption-edge shift at OER potentials indicating partial oxidation of Fe relative to the pre-OER resting state (likely 3+).[7] Oxidation of Co was only observed in Fe-free CoO_xH_y consistent with Fe being a key species at the active site involved in stabilizing OER intermediates.[7]

Although NiO_xH_y is intrinsically less active than CoO_xH_y, Ni(Fe)O_xH_y is more-active than Co(Fe)O_xH_y. In NiO_xH_y a lower OER onset potential upon Fe incorporation is accompanied by a positive shift of the $Ni^{2+/3+}$ wave.[19] Others correlated the increased OER activity to this shift[34-35] and hypothesized that charge transfer from Ni^{2+} to the Lewis-acidic Fe^{3+} makes the Ni site more oxidizing and facilitates the oxidation of water into O_2.

We doped NiO_xH_y with Fe, Ti, Mn, La, and Ce cations and studied the correlation between the $Ni^{2+/3+}$ potential and OER activity.[36] Solution spin-casting and electrodeposition were used to prepare films with well-mixed cations and similar mass loading and morphology (Figure 5.2a-b).[36] Ce was the only cation besides Fe which enhanced the activity of NiO_xH_y (Figure 5.2c). During the initial voltammetry in rigorously “Fe-free” KOH solution, $Ni_{0.85}Ce_{0.15}O_xH_y$ and $Ni_{0.65}Ce_{0.35}O_xH_y$ exhibited activities ~ 8 and 4 times higher than pure NiO_xH_y, respectively. The increased activity of Ce-incorporated films declined during cycling. The O 1s XPS spectra of Ni(Ce)O_xH_y collected before and after extended cycling showed a change from a metal hydroxide to oxide. We interpreted this as phase-segregated cerium oxides forming that eliminated the more-active Ni-O(H)-Ce motifs.

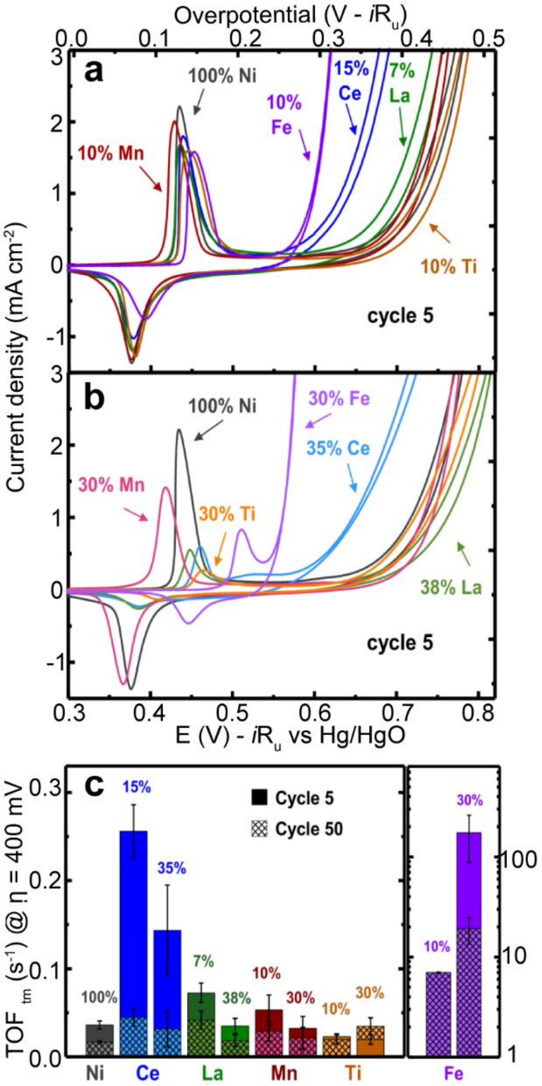

Figure 5.2. **Doping NiOH with other transition metals**. Cyclic voltammetry (cycle 5) of spin-cast $Ni_{1-z}M_zO_xH_y$ films, where M is the metal cation (Ce, La, Mn, Ti and Fe), at approximately (a) $z \approx 0.1$ and (b) $z \approx 0.3$ in Fe-free 1 M KOH at 20 $mV \cdot s^{-1}$. (c) OER TOF of spin-cast films at 400 mV overpotential at cycle 5 (solid) and cycle 50 (pattern) in Fe-free 1.0 M KOH from voltammetry data collected at 20 $mV \cdot s^{-1}$. TOF_{tm} are calculated assuming all metal cations are active (and thus are lower limits); the OER current is taken as the average of the forward and reverse scans. Adapted from ref 36 with permission. Copyright 2016 American Chemical Society.

The incorporation of Ti, Mn, or La cations into NiO_xH_y did not improve activity.[36] Ti and La shifted the Ni redox wave positive, but the OER activity remained the same as in the pure NiO_xH_y. The lack of activity enhancement accompanying the shift in $Ni^{2+/3+}$ redox peak potential indicates that there is no strong relationship between the two. In retrospect, this is perhaps not surprising as after the oxidation of the Ni/Co, the films are conductive with relatively delocalized electronic structures and additional applied potential will increase the oxidative driving force regardless of the initial $Ni^{2+/3+}$ wave position.[37-38] The unique role of Fe in enhancing the OER activity also supports the idea that Fe serves a critical role – likely bonding to intermediates – as a part of the "active site".

Modes of Fe Incorporation in Ni/Co (Oxy)Hydroxides. We three ways of incorporating Fe into Ni/Co (oxy)hydroxides: co-deposition, adsorption from electrolyte impurities, and adsorption from Fe-spiked electrolyte. We found that the activity enhancement relative to how much Fe is incorporated depended on the incorporation method – some Fe sites appear more active than others.[39] We cycled freshly electrodeposited NiO_xH_y film in Fe-spiked KOH (1 mM $Fe(NO_3)_3$). After the initial cycles, a dramatic increase in activity was observed, as evidenced by the > 100 mV decrease in onset potential (Figure 5.3a). Meanwhile, the Ni redox peak potential and average e^- per Ni, was largely unchanged.[39] After 100 cycles, the anodic peak potential ($E_{p,a}$) of NiO_xH_y shifted positive by ~30 mV. In contrast to the change in the $E_{p,a}$, the OER activity was only marginally improved after 100 cycles, even as Fe was incorporated up to 24%. This suggested that Fe species might initially be absorbed on the edge/defect sites where they drive fast water oxidation while having little influence on the Ni redox features whereas further Fe incorporation by cycling leads to (inactive) Fe sitting on "internal" sites within the 2D (oxy)hydroxide structure.

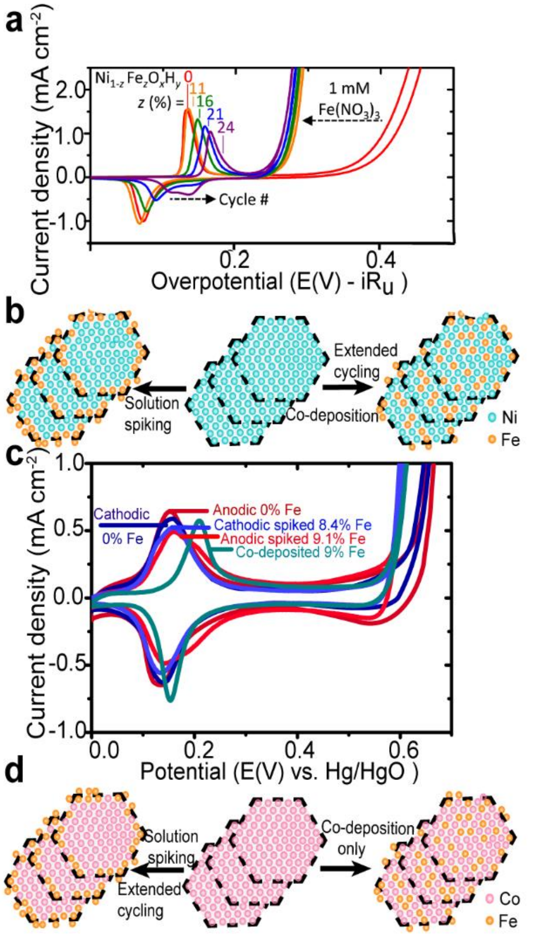

Figure 5.3. Modes of Fe incorporation. (a) CVs showing spiking 1 mM Fe^{3+} leads to 130-150 mV decrease in overpotential for NiO_xH_y in the first 2 cycles with much smaller decrease over the next 98 cycles. 24% Fe is incorporated into NiOOH compared to only ~9% in CoO_xH_y after 50 cycles (c). The extended cycling studies suggest that Fe permeates into the bulk of NiO_xH_y (b) but only accesses the surface of CoO_xH_y (d). Adapted from ref 39 and 15.

We compared the results to a co-electrodeposited $Ni(Fe)O_xH_y$ film and found for similar Fe content the co-deposited $Ni(Fe)O_xH_y$ shows a more-prominent positive shift of the Ni redox peak. We hypothesize that co-deposited $Ni(Fe)O_xH_y$ have Fe homogeneously distributed throughout the structure that strongly interacts with Ni, substantially affecting the average Ni redox properties. The fact that the OER activity of $Ni(Fe)O_xH_y$ appears not to depend on the "bulk" electronic structure and the $Ni^{2+/3+}$ redox peak potential suggests that it is the surface-bound, under-coordinated Fe sites that are responsible for the high OER activity. Chen *et al*. also proposed that due to the disordered structure of the deposited $Ni(Fe)O_xH_y$ there exists edge/defect sites which host Fe species and these Ni-O-Fe motifs are responsible for efficient water oxidation.[14] This proposal was based on the observation of long-lived Fe^{4+} sites in Mössbauer experiments that are evidently not highly OER active.

Similar to $Ni(Fe)O_xH_y$, incorporation of Fe into CoO_xH_y via cycling in Fe-spiked KOH results in enhanced OER activity.[15] However, Fe appears difficult to incorporate into the "bulk" structure of CoO_xH_y, as evidenced by the almost unchanged $E_{p,a}$ after extended cycling (Figure 5.3b). This result can be explained by the stronger Co-O, compared Ni-O, bond.[40] After cycling CoO_xH_y in Fe-spiked KOH, we transferred the $Co(Fe)O_xH_y$ to Fe-free KOH. With further cycling, a fast deactivation process was observed. Post-mortem XPS characterization showed a 60% decrease in the Fe content.[15] In comparison, co-deposited $Co(Fe)O_xH_y$ showed little activity loss when cycled in Fe-free KOH and XPS showed only ~10% Fe loss. These results suggest that dynamic Fe species are incorporated during cycling in Fe-spiked KOH. These Fe likely reside at surface edge/defect sites and thus easily dissolve in Fe-free electrolyte during OER when solution Fe is absent and hence cannot replenish the surface Fe sites. Fe in the co-deposited $Co(Fe)O_xH_y$ film is distributed throughout the film which prevents its rapid loss in Fe-free KOH.

We further applied electrochemical atomic force microscopy (EC-AFM) to study morphology dynamics during OER. We began with single-layer $Ni(OH)_2$ (SL-$Ni(OH)_2$) nanosheets synthesized hydrothermally and exfoliated.[41] In the absence of Fe, the SL-$Ni(OH)_2$ preserved its original hexagonal shape and smooth surface at the open-circuit voltage (OCV) in 0.1 M KOH (Figure 5.4a).[42] With an increase in potential to 1.41 V vs. RHE, which corresponds to the onset of Ni oxidation, the SL-$Ni(OH)_2$ roughened (Figure 5.4b). Further increases in potential lead to restructuring of the single nanosheets into nanoparticles (Figure 5.4c, d). The volume and surface area of the nanoparticles increased with cycling. Once the growth of the $Ni(OH)_2$ nanoparticles halted, we introduced 3 ppm of $Fe(NO_3)_3$ into the electrolyte (Figure 5.4g). The Fe spike caused a ~19% volume expansion after three CVs and Fe was observed to deposit inhomogeneously. After Fe in KOH was increased to 12 ppm, segregated FeOOH appeared to deposit (Figure 5.4h). The restructuring of the $Ni(OH)_2$ nanoparticles during

Fe incorporation might explain how Fe moves into the bulk during extended CV cycling. The morphology changes seem to be the result of a Ni dissolution/redeposition process.[42-43]

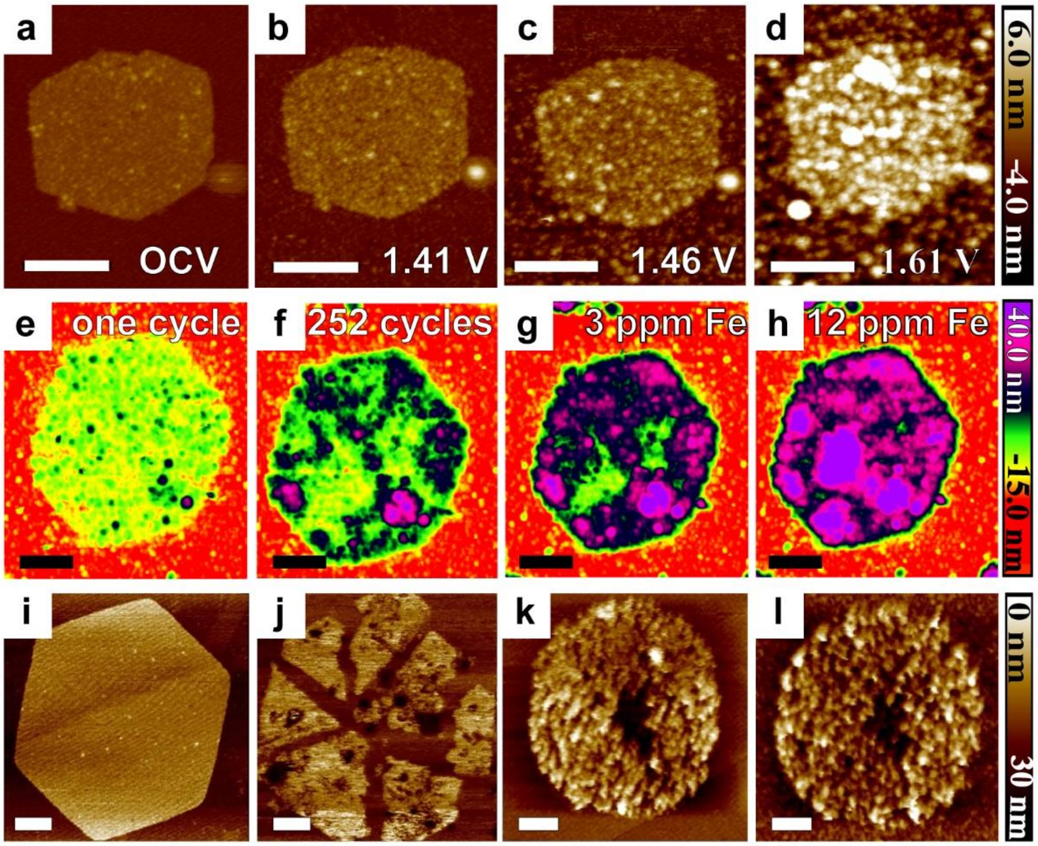

Figure 5.4. Ni and Co SL structural evolution upon Fe incorporation. AFM images of SL-Ni(OH)$_2$ in Fe-free KOH (a) at the open-circuit voltage, and then after the chronopotentiometry measurement (for 500 s) at (b) 1.41 V vs RHE, (c) 1.46 V vs RHE, and (d) 1.61 V vs RHE (scale bars = 200 nm), (e) after one LSV in 0.1 M KOH, (f) after 252 CV cycles, and in the presence of (g) 3 ppm Fe(NO$_3$)$_2$ and (h) 12 ppm Fe(NO$_3$)$_2$ after three CV cycles (scale bars = 200 nm). AFM topographical images of Ni$_{0.8}$Co$_{0.2}$O$_x$H$_y$ nanosheets (i) at the beginning and (j) after 200 CV cycles between 1 and 1.7 V vs. RHE in 0.1 M KOH (scale bars = 100 nm). SL-Co(OH)$_2$ nanosheets images under identical conditions (k) at the beginning and (l) after the electrochemical testing. Adapted from ref 42 and 43.

Co(OH)$_2$ nanosheets undergo less morphological changes under electrochemical conditions.[43] EC-AFM showed that Co-rich Ni$_{1-\delta}$Co$_{\delta}$O$_x$H$_y$ and CoO$_x$H$_y$ initially had a porous morphology and the higher porosity was likely able to reduce the mechanical stress originated from redox (Figure 5.4i-l). As a result, Co-rich $Ni_{1-\delta}Co_{\delta}O_xH_y$ exhibited higher electrochemical and mechanical stability consistent with our hypothesis that Fe absorbed from the electrolyte is difficult to incorporate into the bulk of CoO_xH_y.[15, 43]

Markovic and coworkers used scanning tunneling microscopy (STM) and ICP-MS techniques combined with isotope labelling to investigate the dynamic stability of Fe sites in transition-metal (oxy)hydroxide clusters.[44] STM revealed that the cluster height of Ni (oxy)hydroxide on Pt(111) slightly increased when the electrode was immersed in Fe-spiked KOH solution, suggesting that Fe was adsorbed on the surface. The dynamic Fe exchange at the catalyst-electrolyte interface was monitored by isotopic labelling starting with ^{56}Fe on the electrode and ^{57}Fe in the electrolyte. ^{56}Fe dissolved during chronoamperometry, while ^{57}Fe in electrolyte deposited onto the electrode surface. The system eventually reaches a dissolution-redeposition steady state. During activity tests in Fe-spiked electrolyte, OER performance improved. When measured in Fe-free KOH, the OER performance degraded, consistent with our results above. The sum of these studies indicates that the high OER activity of Fe-MO_xH_y can only be maintained in the presence of Fe in the electrolyte, supporting the view that the dynamic Fe exchange underlies the stability/performance of these catalysts.

We further studied how more-complex compositions behave in an effort to increase intrinsic activity/stability as well as better understand mechanism. For example, others reported that mixed Ni-Co-Fe (oxy)hydroxides are more active than NiFe systems,[45-46] although explanations for the activity trends differed and the measurements were not performed in a way where reliable intrinsic activities could be confirmed. We considered several reasons why addition of Co might enhance activity of Ni(Fe)O_xH_y: 1) the onset of CoO_xH_y electrical conductivity is at lower overpotentials so active sites might become electrochemically accessible at more negative potentials; 2) CoO_xH_y may uptake more Fe than NiO_xH_y before Fe phase segregates so addition of Co might allow formation of more Fe active sites, 3) the electronic interaction of Fe, Ni and Co might yield more-optimal intermediate binding energies. For some more-complex compositions, morphological changes can increase the active-Fe-site density due to leaching during OER, as likely observed for Cr-containing Ni-Fe (oxy)hydroxides.[47-48]

We first evaluated the OER activity of Ni(Co)O_xH_y with the rigorous exclusion of Fe impurities.[18] Generally a single redox wave was observed for the mixed-metal system that shifted negatively with increasing Co. This data suggests a strong electronic interaction between homogeneously mixed Ni and Co cations. The most-active binary composition was only two-fold more active compared to the parent compounds. We then examined the ternary Ni(Co,Fe)O_xH_y and found that the best composition was only ~1.5 times more active than Ni(Fe)O_xH_y on a per-metal-cation TOF basis.[18] The OER activity for pure and Fe-containing binary Ni/Co compounds does not correlate with the position or size of the redox waves which instead correlate with "bulk" composition of the system.

Towards Advanced Electrolysis: Ni and Co-based Catalysts in AEMWE. AEMWEs in principle allow for the use of earth-abundant OER catalysts over IrO_2 required for commercial PEMWE.[1, 49-50] While the AEM provides a locally basic environment, the feed is often pure water and a detailed chemical understanding of the activity and durability of OER catalysts in these conditions is missing.

We compared the performance of first-row transition metal (oxy)hydroxide/oxide catalysts in three-electrode alkaline electrolytes and AEMWE in pure water.[49] The best OER catalyst in alkaline electrolyte, $NiFeO_xH_y$, performed poorly in AEMWE. However, we found a correlation between the electrical conductivity of the catalyst, measured *ex-situ*, and the performance of the electrolyzers (Figure 5.5). $NiCoO_x$, $NiCoO_x$:Fe, and $NiCoFeO_x$ with high intrinsic electronic conductivity show smaller cell voltages at 0.2 $A\cdot cm^{-2}$, better than IrO_x. $NiFeO_xH_y$ shows the lowest *ex-situ* conductivity (6.3×10^{-9} $S\cdot cm^{-1}$) and highest cell voltage.[49] In the absence of the liquid electrolyte, we hypothesize that the bulk of $NiFeO_xH_y$ cannot convert to a conductive oxidized form which prevents high activity.

Work in liquid electrolyte shows that absorbed Fe participates in a dissolution-redeposition equilibrium and is an essential component of the active site.[44] In a typical AEMWE system with pure-water feed, dissolved Fe would enter the neutral water flow where its solubility is much higher than in alkaline conditions. This phenomenon might explain why the $NiCoO_x$:Fe (with Fe mainly adsorbed on the surface) degraded quicker than the NiCoFeO$_x$ (prepared by co-precipitation of Ni, Co, and Fe) during our AEMWE stability test.

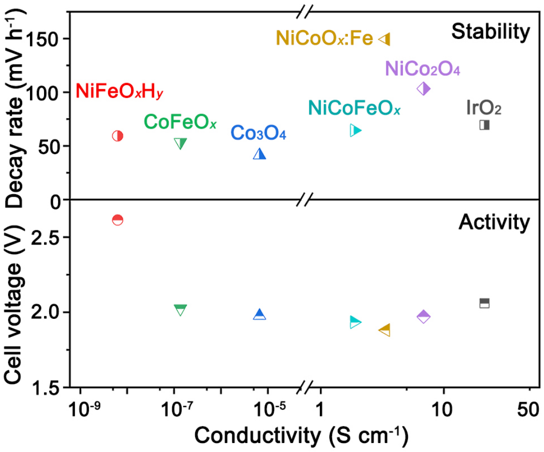

Figure 5.5. Activity and stability dependance on conductivity. The electrical conductivity, activity, and degradation rate in pure-water AEMWE at 0.2 A·cm^{-2} of a series of the first-row transition metal (oxy)hydroxide/oxide catalyst powders. Adapted from ref 49.

In lab-scale, three-electrode experiments a thin catalyst layer is deposited on conductive electrodes in 1 M KOH with rapid stirring to enhance mass transport. The KOH permeates the porous catalyst assembly in ways the solid ionomer cannot. Three electrode conditions thus do not account for the bottlenecks of the MEA including catalyst utilization, mass-transport limitations (water and gas), and ionic (OH$^-$) and electrical conductivity. Thus, lab-scale results obtained via alkaline electrolyte cells are often more promising than those measured in an AEMWE.[51]

Kim *et al*. showed high performance for Ni-Fe-based nanofoam OER catalyst in pure water (2.7 A·cm^{-2} at 1.8 V, 85 °C) using a highly basic ammonium-enriched ionomer, but the performance decayed rapidly (1.3 mV·h^{-1} at 200 mA·cm^{-2} and 60 °C) which was attributed to oxidation of the ionomer but also may be due to flushing of residual KOH from the system (Figure 5.6 blue trace).[50] Yan and co-workers demonstrated that by growing Fe$_x$Ni$_y$OOH directly on a compressed Ni foam one avoids the use of Ti or stainless-steel gas diffusion layers (GDL) altogether, improves access to the active sites through the pores in the foam, and reduces the catalyst loss during operation in pure water (1020 mA·cm^{-2} at 1.8 V, 80 °C; 0.56 mV·h^{-1} for > 160 h at 200 mA·cm^{-2}) (Figure 6, red trace).[52] Good initial AEMWE performance is evidently achievable with non-PGM catalysts in pure water, but stability remains a serious issue that can only be solved by understanding and controlling the ionomer and catalyst chemistry during OER.

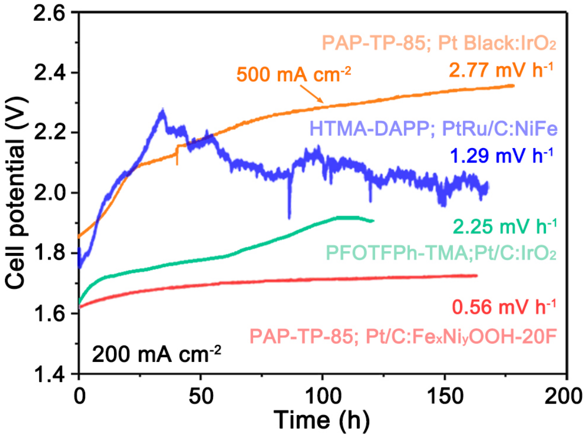

Figure 5.6. A summary of AEMWE performance in pure water at 200 mA·cm^{-2} (except orange trace, 500 mA·cm^{-2}). Catalysts, membrane materials, and degradation rates are identified for each trace. Adapted from ref 50, 52, 54, and 55.

We used a reference electrode with an AEMWE stack to measure the impedance and polarization responses of the anode and cathode separately.[53] This technique is valuable in pinpointing the source of performance loss, particularly when using impure water feeds.[2] We also developed easily adoptable procedures for MEA fabrication and a baseline for AEMWE performance in pure water with all commercial components (0.67 mV·h^{-1} after break-in at 500 mA·cm^{-2}, 55 °C): PiperION PAP-TP-85 ionomer/membrane, steel GDL, and IrO_2 anode and Pt cathode (Figure 5.6 orange trace).[54] Soni *et al* further showed promising durability with a trimethylammonium-modified poly(fluorene-alttetrafluorophenylene)s membrane and ionomer **(**Figure 5.6 green trace**)**.[55]

Possible Effects of Dynamic Fe Sites on Membrane Stability. Most AEMWE tests use PGM catalysts or basic liquid electrolytes that minimize catalyst instability.[56-57] Substantial *in situ* and post-operation chemical analysis is usually lacking. Fe enhances the OER activity of Co and Ni-based catalysts when absorbed on the surface or substituting Ni or Co sites.[15, 44, 58] The maintenance of high activity is contingent upon sufficient Fe in the electrolyte[44, 58] such that the rate of Fe deposition equals that of dissolution.[44] The presence of Fe cations in the water feed will likely have detrimental effect on durability, for example due to Fenton processes with hydrogen peroxide.[2] Hydrogen peroxide can be formed by gas mixing in the stack.[3] Degradation can be avoided by preventing gas crossover which requires more-selective AEMs. Fe cations travelling through the membrane from the anode will also deposit on the cathode causing HER activity loss or may accumulate in the membrane and precipitate. Post-operation chemical analysis of the membrane (EDX, XPS, NMR), catalyst structure at the anode and cathode (XRD, SEM, XPS), as well as *in situ* ICP-MS analysis of the outgoing water flow appears needed to detect catalyst leaching and redistribution.

One strategy to reduce Fe leaching may be to incorporate it within the catalysts bulk structure. However, the preferential leaching of Fe compared to Ni in highly basic conditions and elevated temperatures in such devices will have to be addressed.[59-60] Improvement of stability can be achieved through novel synthetic methods and taking advantage of the catalyst/support interactions.[61] The MEA configuration, though, might help to prevent the loss of dissolved species and favor their redeposition at the anode while a more-selective AEM will slow the crossover of the those species to the cathode.[2] At the cathode, adjusting the water flow and current densities along with selecting an HER catalyst with a crystal structure different from the precipitating/depositing species may minimize deactivation.[2]

Catalyst Utilization. Unlike catalyst immersed in KOH, the catalyst embedded in an ionomer pressed against the solid-ionomer membrane has a limited supply of OH^- that must travel through the membrane and ionomer/catalyst network.[49, 51] The catalyst powders are usually spray-coated on a porous transport layer (PTL). Good electrical contact to the PTL is crucial for Ni and Co-based catalysts that have lower intrinsic electrical conductivity than IrO_2. Hegge *et al*. demonstrated that utilization can be improved by maximizing the catalyst porosity and electrical contact using nanofibers.[62] The phase transformation and surface reconstructions observed during OER for Ni-based transition-metal (oxy)hydroxides also present challenges. In a MEA, the ionomer and the membrane are responsible for carrying OH^-. Dynamically changing catalyst/membrane and catalyst/ionomer interfaces might cause interruptions in the OH^- transport chain, which, along with limited electrical conductivity in poorly integrated catalyst/PTL configurations, might result in high ohmic losses.

pH Changes at the Anode/Membrane Interface. Operating AEMWE with a pure water feed at high current densities will affect the pH at the anode. Holdcroft *et al.* visualized the transport of OH^- through an AEM from cathode to anode during electrolysis demonstrating that the interface between the anode and the membrane remains less basic than the rest of the membrane due to the fast consumption of OH^-.[4] Non-PGM transition-metal oxides dissolve faster at lower pH which presents a durability challenge for PGM-free AEMWE.[3] Another source of acidification at the anode is ionomer oxidation. Yu Seung Kim *et al.* studied the acidification of phenyl-containing AEMs by phenol formation and showed how it leads to performance loss in AEMFCs.[63] Membrane acidification might be decreased by replacing the phenyl groups in the backbone with more oxidatively stable components and minimizing their adsorption onto the catalyst surface[50] or by tuning the phenyl adsorption energy.[63]

It is still, however, not clear what the pH is at the catalyst surface during operating AEMWE in pure water or with a supporting electrolyte. Means of measuring the pH at these nanoscale interfaces would be useful as would non-PGM OER catalysts with wider pH stability. Co and Ni-based catalysts corrode and dissolve at acidic pH,[64] although Co oxides appear more pH-stable than Ni ones. Fe, Ni, and Co might be paired with more-acid-stable elements like Sb or Ti to improve durabilty.[65]

Conclusion

Despite decades of work, there remains substantial need to further understand and control the OER reaction in alkaline conditions – particularly in the context of the dynamic Fe sites in AWE and AEMWE systems. Based on our work, and that of many others around the world, we have learned the following lessons: 1) crystalline metal oxides that are capable of driving OER at relatively low overpotential are structurally dynamic in alkaline, oxidizing conditions, favoring hydrated disordered (oxy)hydroxide phases during operation, 2) minimizing electrical-conductivity and mass-transport limitations are essential for fundamental activity measurements and for engineering high performance in practical electrodes, 3) dynamic adsorption or incorporation of Fe is essential for the highest-activity catalysts as Fe is a key component of the OER active site and very likely directly bonding with intermediates, 4) bulk materials properties, either of oxides themselves or even of the active (oxy)hydroxide phases (such as the Co/Ni redox potential, e_g orbital filling, covalency, etc.), are not simply correlated with the OER activity. Local electronic and structural descriptors are probably needed to rationalize OER activity.

We suspect these lessons are universally applicable to OER catalysts in alkaline conditions. It is established that phosphide- and sulfide-based OER catalysts serve only as precursors to the (oxy)hydroxide phases discussed above[66] and we have not been able to observe high catalytic OER activity from *any material* in the rigorous absence of Fe. Further, Binninger and coworkers argue that all metal oxides are unstable under OER conditions.[67] This appears particularly true for high-activity perovskite oxides, such as $Ba_{0.5}Sr_{0.5}Co_{0.8}Fe_{0.2}O_3$ (BSCF) which was identified as a material with high OER activity on the basis of molecular orbital principles[68] (assuming retention of the as-prepared crystalline morphology during OER). Later, it was discovered that surface reconstruction and cation leaching leads to Co(Fe)OOH shells.[69-70] Epitaxial [001]-oriented $LaNiO_3$ single crystals rearrange to (oxy)hydroxides when Ni-terminated (but not when La-terminated and largely OER-inactive).[71] $La_{1-x}Sr_xCoO_3$ formed a thin CoOOH layer that absorbs Fe which was most pronounced for the higher Sr-substituted species.[72] The chemical tunability, high activity, and structural dynamicity of perovskite oxides makes them a rich system for further study of surface-absorbed Fe. All these dynamic processes should be accounted for in AWE and AEMWE systems in order to design for optimal performance and durability. Much work remains.

Bridge

Chapter V summarized the knowledge we have of the dynamic changes happening to non-platinum-group-metal catalysts and their potential for being implemented into zero-gap electrolyzers. Chapter VI builds upon that by discussing the performance trends and catalyst-dependent degradation pathways of several widely used non-platinum-group-metal catalysts in an AEMWE.

CHAPTER VI

ANODE CATALYSTS IN ANION-EXCHANGE-MEMBRANE ELECTROLYSIS WITHOUT SUPPORTING ELECTROLYTE: CONDUCTIVITY, DYNAMICS, AND IONOMER DEGRADATION

Chapter VI contains co-authored unpublished material that was submitted to *Advanced Materials*. Prof. Boettcher, Grace Lindquist, and I conceived of the project. Grace Lindquist and I collected experimental data with assistance from Nathan Stovall, Sarah Beaudoin, Willow Thompson, and Kevin Fabrizio. Prof. Hutchison and Prof. Boettcher assisted with data interpretation. Grace Lindquist and I wrote the manuscript with editorial assistance from Prof. Hutchison and Prof. Boettcher.

Introduction

Water electrolysis powered by renewable energy produces green H_2 fuel, which is probably essential for a 100% renewable energy economy.[1] Of the low-temperature water electrolysis technologies, alkaline water electrolysis (AWE) is the most mature. AWE operates in hot liquid alkaline electrolyte (~80 °C, ~5 M KOH) with two electrodes separated by a porous diaphragm. It provides high efficiency and uses earth-abundant non-platinum-group-metal (PGM) materials, but is affected in performance and capital expense due to gas crossover through the porous separator and shunt currents through the electrolyte flow paths.[2] Proton-exchange-membrane (PEM) electrolyzers use a thin (~20-50 μm) cation-selective solid ionomer membrane that reduces gas crossover, enables operating at higher currents (> 2 A cm^{-2}), and eliminates shunt currents with a pure-water feed.[3] However, the locally-acidic environment created by the PEM requires expensive PGM catalyst materials. Anion-exchange-membrane (AEM) electrolyzers are a developing technology that combines the benefits of AWE and PEM, ideally operating in water with no supporting liquid electrolyte under differential pressure and providing a locally-alkaline environment for non-PGM catalysts and materials.[2b]

To date, AEM water electrolyzers (AEMWEs) do not have comparable performance or durability to PEM or AWE electrolyzers.[2a, 3] To compensate, most AEMWEs use soluble supporting electrolyte, commonly carbonate or hydroxide, to improve conductivity and increase apparent durability.[4] The use of supporting electrolyte, however, has practical implications that complicate system design as discussed above and masks underlying degradation phenomena that are important to understand and prevent.[5] Understanding the factors that control performance and durability in the absence of supporting electrolyte is therefore an important immediate goal.

In terms of oxygen evolution reaction (OER) catalysis, most AEMWE testing is conducted with expensive IrO_2 because it is stable and active.[6] Ni-Fe oxyhydroxides have the lowest overpotential and highest per-cation turnover frequency in three-electrode studies,[7] but their performance and durability is generally poor in pure-water membrane-electrode-assembly (MEA) configurations, which we have attributed to difficulties in oxidizing the bulk of the catalyst to its active state without soluble electrolyte.[6c] Recently, non-PGM catalysts have shown more-promising performance and durability in MEA configurations, but appear to require either supporting electrolyte[8] or complex electrode and/or catalyst design and preparation,[9] for example with the Ni/Fe catalyst supported on a high-surface area Ni foam, that may not be easily translated to commercial-scale devices.[4e, 10] These studies are often further complicated by membrane and ionomer instability that causes degradation independent of catalyst identity. Very few studies investigate the catalyst-level phenomenon that result in the improved durability over traditional nanoparticle catalyst layers in industrially-relevant MEA conditions. Recent developments in AEM ionomer and MEA preparation and assembly have improved AEMWE durability,[6a, 6b, 10a] making it possible to better isolate the role of metal-oxide catalysts in system degradation.

In Chapter VI, we study five Ni-, Co-, and Fe-oxide-based nanoparticle anode catalysts and compare them to commercial nanoparticle IrO_2 in pure-water AEMWE to understand the fundamental factors controlling the performance and durability of non-PGM materials in commercially relevant designs. Using *operando* analysis and post-operation materials characterization, particularly by x-ray photoelectron spectroscopy of the catalyst layer, we observe multiple processes contributing simultaneously to degradation. We show the differences in anode-catalyst dynamic transformations occurring during operation and the effects this behavior has on device performance. In addition, we show that the introduction of trace soluble Fe species during device operation accelerates degradation. Finally, we demonstrate a device using a Co_3O_4 anode with comparable performance and durability to IrO_2 at high current density, proving a viable route for non-PGM operation at scales where IrO_2 may not be viable due to scarcity.

Experimental

Catalyst Dispersions and GDL Coating. Pt black (high surface area, Fuel Cell Store) nanoparticles were used as the cathode catalyst for all trials. Co_3O_4 (99.5%, 30-50nm), NiO (99.5%, 15-35 nm), $NiCoO_2$ (99.9%, 20 nm), $NiFe_2O_4$ (99.99%, 20 nm), $Ni_{0.5}Co_{0.5}Fe_2O_4$ (99.995%, 40 nm, US Research Nanomaterials), and IrO_2 (core/shell Ir/IrO_x, Fuel Cell Store) nanoparticles were used at the anode. Cathode and anode electrodes were prepared identically by spray-coating using a previously published method.[6a] Catalyst inks were prepared by mixing the catalyst powder (100 mg), water (0.5 g), isopropyl alcohol (1.7 g), and 5 wt% TP-85 (Versogen) ionomer (200 mg). Catalyst inks were sonicated for 1 h to disperse before spray coating using an airbrush (Testors, Aztek A2203). Pt black was sprayed onto carbon paper (Toray 090, Fuel Cell Store) and anode catalysts were sprayed onto a woven stainless-steel mesh (25AL3, Bekaert). A catalyst loading between 2.2 and 2.5 $mg \cdot cm^{-2}$ was determined by mass difference.

Membrane Conditioning. PAP-TP-85 membranes (40 μm, Versogen) were conditioned according to manufacturer instructions. The membranes were soaked in 0.5 M KOH for 24 h, replacing the solution with fresh KOH after 1 h. Membranes were stored in 0.5 M KOH when not in use.

MEA Assembly and Hardware Operation. GDLs were cut to 1 cm^2 and assembled in the electrolyzer according to previously published procedure.[6a] A water tank filled with 18.2 $M\Omega \cdot cm$ provided water to the cathode and anode at 125 $mL \cdot min^{-1}$.[6a] The anode water flow was recirculated in the system while the cathode water flow was degassed in a chemical hood then recirculated back into the water tank. Temperature of the water was maintained such that the temperature in the electrolyzer cell was 57 ± 1 C° and was monitored with a thermocouple inserted into the anode and cathode cell hardware plates. The temperature difference between anode and cathode was maintained to less than ± 1 C°.

Applied Current Testing Conditions. All tests were conducted under chronopotentiometric conditions unless otherwise indicated. The MEA was conditioned by stepping the current from 100 $mA \cdot cm^{-2}$ to 1 $A \cdot cm^{-2}$ in 100 mA intervals, holding for 2 min at each step. Impedance spectra were then collected from 500 kHz to 200 mHz at 50 $mA \cdot cm^{-2}$. Then, the cell was held at 1 V to observe the steady-state electrolysis current decay to zero, confirming there were no pinholes or shunt pathways present. The cell was brought back to 1 $A \cdot cm^{-2}$ for 2 min to stabilize. The potential was then recorded, and the current was decreased in 100 $mA \cdot cm^{-2}$ steps until reaching 100 $mA \cdot cm^{-2}$, then further decreased to 50 $mA \cdot cm^{-2}$ and lastly 10 $mA \cdot cm^{-2}$, measuring the potential for 10 s at each step to collect the JV curve. The cell was held at 500 $mA \cdot cm^{-2}$ for stability measurements. During 20 h stability testing, impedance data, as described above, was collected after 1 h, 3 h, 8 h, and 20 h. For the 40 h and 200 h tests, impedance was collected only at the start and end of durability testing. After analysis, the cells were disassembled, and the ionomer and membrane were converted to the Cl^- counter anion form by submerging the MEA in 3 M NaCl solution for at least 30 min (to prevent OH^- attack induced by drying the ionomer). The materials were then rinsed thoroughly with 18.2 MΩ·cm water for 30 s and dried in air.

Applied Voltage Testing Conditions. To test the performance of $NiFe_2O_4$ at a lower voltage, the cell was tested under chronoamperometric conditions. For this, the MEA was conditioned by stepping the voltage from 1.7 to 1.9 V in 50 mV steps. Impedance spectra were collected over the same frequency range at 1.6 V. The cell was then stepped down from 1.9 to 1.6 V in 50 mV steps held at 10 s to record the JV curve. Durability testing was conducted at 1.8 V. Impedance data of the same conditions was collected at the same time points as the chronopotentiometric testing for consistency. The MEA was disassembled and converted to Cl^- counter ion as described above.

Fe Spike Test. An MEA with a Co_3O_4 anode was prepared and conditioned according to the above procedure, but water was flowed to the anode and cathode with separate water pumps. The anode was flowed at 75 $mL\cdot min^{-1}$ and the cathode 75 $mL\cdot min^{-1}$, which was the highest flow rate possible before high back pressure caused the water line to detach from the pump. Durability testing was operated at 500 $mA\cdot cm^{-2}$. When the degradation rate stabilized to below 1 $mV\cdot h^{-1}$, the inlet line for the anode pump was moved to a 1 ppm Fe^{3+} solution (0.19 mM $Fe(NO_3)_3\cdot 9\ H_2O$ (ACS reagent grade ≥98%, Sigma)). The solution was held at the same temperature as the water tank to maintain a constant hardware temperature. Current was held at 500 $mA\cdot cm^{-2}$ during this time and durability testing was continued for an additional 28 h. The MEA was disassembled and converted to Cl^- counter ion as described above.

Catalyst Conductivity Measurements. The catalyst powders (~200 mg) were pressed between two stainless steel disks inset in a plastic holder (Figure D.1) (see Appendix D for all figures). An aluminum bar was placed above and below the disks to make electric contact, which were connected to a potentiostat using copper wire. Plastic sheets were placed above and below the aluminum to prevent short-circuit through the metal press. The powders were compressed to 23,000 psi. The thickness of the powder was measured by measuring the distance between the top and bottom of the steel disks using a digital micrometer and subtracting the thickness of the disks with no catalyst powder. Polarization curves were collected from -1 to 1 V at 1 $V\cdot s^{-1}$ (Figure D.2). The contact resistance was measured by the same method with no catalyst between the two disks. For the blank and IrO_2 measurements the range was adjusted to -0.02 to 0.02 V at 10 $mV\cdot s^{-1}$ to prevent current overload (Figure D.3). The measurement for IrO_2 matched that of the contact resistance, and thus a value is not reported for this catalyst. For all other catalysts the resistance was obtained from a linear fit of the obtained current-voltage curve. The contact resistance was subtracted before calculating conductivity according to $\sigma = l/(RA)$, where σ is electrical conductivity in $S\cdot cm^{-1}$, l is the thickness of the catalyst powder in cm, R is the measured resistance in Ω, and A is the disk surface area in cm^2.

BET Surface Area Measurements. Nitrogen (N_2) adsorption/desorption isotherms were measured using a Micromeritics ASAP 2020 surface area analyzer at 77 K. Specific surface areas (S_{BET}) of the samples were calculated using the Brunauer-Emmett-Teller

(BET) method, and pore widths and pore volumes (V_p) were calculated using the Barrett, Joyner, and Halenda (BJH) adsorption curves. Samples were suspended in isopropyl alcohol and dried at room temperature under vacuum for 12 h. Samples were then activated at 393 K (Co_3O_4, $NiFe_2O_4$, $Ni_{0.5}Co_{0.5}Fe_2O_4$, $NiCoO_2$, and IrO_2) or 423 K (NiO) for at least 24 h to remove the solvent and trapped gas. Activation was considered complete when the outgassing rate fell below 2.5 μtorr$\cdot$min^{-1}. The sample mass was calculated by the difference in mass between the empty sample tube and the loaded sample tube post-activation.

Catalyst Testing on Quartz-Crystal Electrodes in KOH. The catalyst inks were prepared by mixing metal-oxide nanopowders (100 mg), 18.2 MΩ·cm water (0.5 g), isopropanol (1.7 g), and 5 wt. % of PiperION ionomer (200 mg) in ethanol. The inks were spin-coated onto 5 MHz Au/Ti quartz crystals (Fil-Tech) at 3000 rpm and dried at 80 °C to obtain the loading of ~ 22 $\mu g_{MO}\cdot cm^{-2}$ (not including the mass of the ionomer, 10 wt. %). The cyclic voltammetry (CV) plots were collected in 1 M KOH with the working electrodes connected to the QCM controller (Stanford Research Systems QCM200). Potentials in three-electrode modes were measured versus a 1 M KOH Hg/HgO reference electrode (CH Instruments). High-purity N_2 was bubbled during the experiment. All electrochemical data was corrected for uncompensated series resistance (R_u), which was determined by equating R_u to the minimum total impedance in the frequency regime between 10 and 50 kHz, where the capacitive and inductive impedances are negligible, and the phase angle was near zero.

XPS Analysis of Pristine and Post-Mortem GDLs. X-ray photoelectron spectroscopy measurements were performed on an ESCALAB 250 (ThermoScientific) using Al Kα monochromated (20 eV pass energy, 500 μm spot size) and non-monochromated Mg Kα (400 W, 75 eV pass energy) flood sources. The use of the Mg source is critical in discerning Fe in the samples as typical Al sources exhibit overlap of the Fe 2p peaks with Ni and Co Auger LMM features. The samples were charge-neutralized via an in-lens electron source. Spectra were analyzed via the ThermoScientific Avantage 5.99 software. The binding energies were calibrated to the C 1s signal at 284.8 eV.

The catalyst powders that do not contain Fe were analyzed as sprayed inks on stainless-steel GDLs prior and after the AEMWE operation with the ionomer ion-exchanged to Cl^- form. To avoid signal contribution from the Fe-rich stainless-steel, the metal ratios in the Fe-containing catalysts were analyzed separately from GDLs. To obtain the metal ratios in pristine catalysts, the powders were analyzed on a piece of carbon tape. To assess the changes to the metal ratios after WE operation, the GDLs were sonicated in ethanol to remove the catalyst layer. The lose powder was collected, dried, and analyzed on a piece of carbon tape. The C 1s, N 1s, and F 1s spectra for Fe-containing catalysts were obtained with the inks on GDLs similarly to the other catalysts.

Results and Discussion

AEMWE Performance and Durability. AEMWE devices were constructed for each catalyst following published procedures[6a] and described in detail in the Experimental section. Catalysts were dispersed in an ink of isopropyl alcohol, water, and ionomer and sprayed onto gas-diffusion-layer (GDL) substrates. Commercial nanopowders (IrO_2, Co_3O_4, NiO, $NiCoO_2$, $NiFe_2O_4$, and $Ni_{0.5}Co_{0.5}Fe_2O_4$) were used as anode catalysts (Table 6.1) and Pt black as the cathode catalyst.

Table 6.1. Anode catalyst properties

Catalyst	**Diameter (nm)**	**Surface Area ($m^2 \cdot g^{-1}$)**	**σ ($mS \cdot cm^{-1}$)**
IrO_2	5-10	14	metallic*
Co_3O_4	30-50	28	23
NiO	15-35	32	1.1
$NiCoO_2$	20	20	0.55
$Ni_{0.5}Co_{0.5}Fe_2O_4$	40	58	0.0006
$NiFe_2O_4$	20	70	0.0075

*measurement indistinguishable from contact resistance

Anode catalysts were sprayed onto a stainless-steel woven mesh and cathode catalysts on Toray-090 carbon paper. The loading for all catalysts was between 2.2 and 2.7 $mg \cdot cm^{-2}$ with 10% by weight ionomer content. A thin layer (2-5 wt% relative to catalyst loading) of ionomer was sprayed on top of the catalyst layer. The MEAs were constructed using a 40-μm-thick PiperION TP-85 membrane and compressed with a torque on the assembly bolts of 5.6 N·m. Water was flowed to the anode and cathode using a pump flowing at 125 mL·min^{-1} until the hardware temperature equilibrated to 57 °C. The cell was conditioned prior to data collection as described in the Experimental section.

First, the performance and durability of each catalyst was assessed during pure-water electrolyzer operation. IrO_2 out-performed all other catalysts by ~ 100 mV at 10 mA·cm^{-2} (Figure 6.1a) (see Appendix D for all figures). At such a low current density, ohmic and mass-transport losses should be minimal, and performance is largely dominated by the OER overpotential. As current density increases the performance more closely compares to the next best catalysts, Co_3O_4 and NiO, which are within 50 mV of IrO_2 at 1 A·cm^{-2}. All mixed-metal catalysts displayed worse performance. To further investigate the origin of this performance trend, GEIS was conducted at 50 mA·cm^{-2} immediately after cell conditioning (Figure 6.1b). The data was fit to a Randle's circuit with constant phase elements (Figure 6.1b inset). All cells show comparable series resistance values, and thus the performance discrepancies are not attributed to differences in materials/cell assembly conditions, for example, poor contact between the catalyst layer and membrane or differences in ink dispersion quality. The trend in low-frequency resistance, assigned to charge-transfer phenomena, agrees with the voltage trend observed at 50 mA·cm^{-2}, as expected. IrO_2 and Co_3O_4 also showed the best durability over 20 h, stabilizing to a degradation rate of 2.6 mV·h^{-1}and 1.8 mV·h^{-1}, respectively (Figure 6.1c). While NiO showed similar performance, an initial rapid degradation was observed before the electrolyzer stabilized to a degradation rate of 6.4 mV·h^{-1} at ~200 mV higher voltage than IrO_2 and Co_3O_4. Fe-containing catalysts showed exceptionally high degradation rates, with $NiFe_2O_4$ surpassing 5 V after only ~4 h. Although Ni-Fe-oxide-based catalysts outperform IrO_2 in alkaline three-electrode-cell tests,[7a, 7c] in a pure-water MEA with a catalyst/ionomer environment the trend in performance appears reversed.

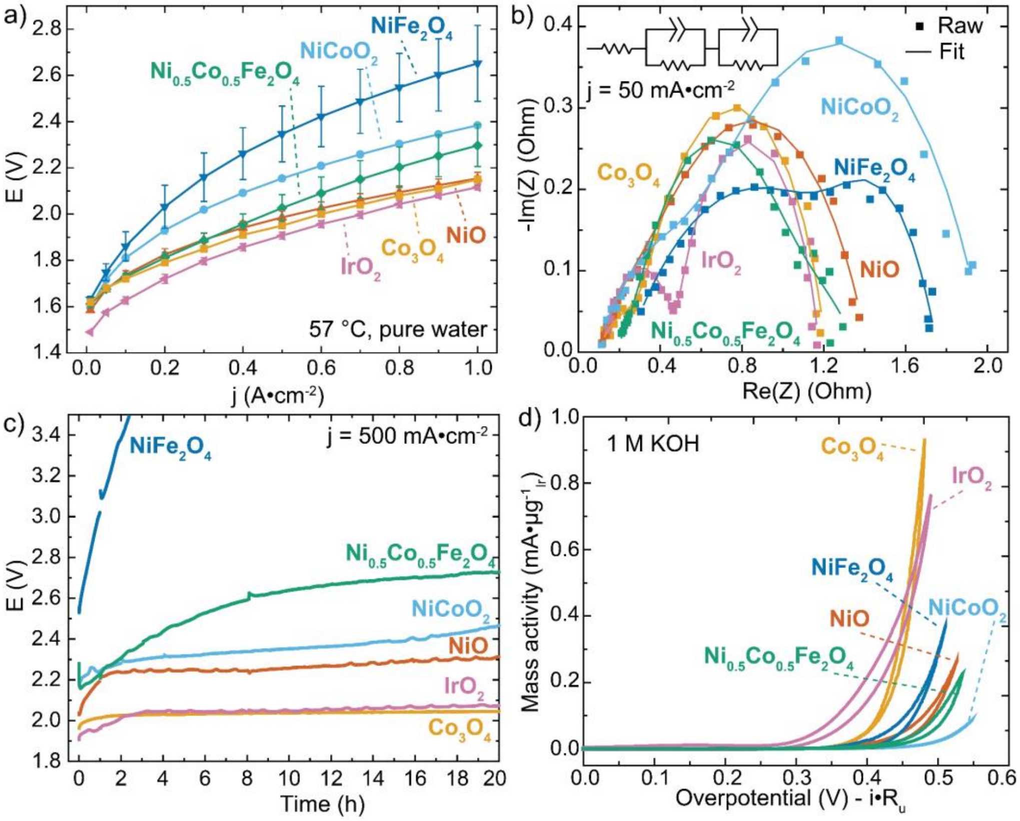

Figure 6.1. Electrochemical performance. a) Polarization curves of anode catalysts tested. All experiments were conducted in pure water at 57 °C. A stainless-steel woven substrate with the indicated catalyst was used as the anode GDL and Pt black catalyst on Toray carbon paper was used as the cathode GDL. The error bars represent the standard deviation from three independently fabricated cells. b) Galvanostatic electrochemical impedance spectroscopy (GEIS, at 50 mA·cm^{-2}) for each catalyst tested in the pure-water MEA. The inset shows the equivalent circuit used for data fitting. c) Durability testing for each catalyst held at 500 mA·cm^{-2} for 20 h at 57 °C. d) Cyclic voltammetry for catalysts embedded in anion-exchange ionomer (10 wt. %) tested in 1 M KOH on Au/Ti quartz-crystal-microbalance electrodes.

We tested the same inks used to coat GDLs (catalyst inks with 10 wt. % ionomer) on quartz-crystal electrodes in 1 M KOH (Figure 6.1d) to identify differences between MEA and soluble electrolyte environments for catalysis. IrO_2 and Co_3O_4 still outperform the Ni/Fe-oxide catalysts. In our previous studies we used less-crystalline Ni/Fe-oxide thin films that converted to the $3^+/4^+$ oxyhydroxide state rapidly during operation, leading to dramatically increased activity.[7a, 7c] The Ni/Fe nanopowdered catalysts used for the MEA configuration might not easily convert to the more-active phase due to low electronic conductivity and in the MEA, lack of soluble electrolyte. Thus, the activity trend observed in prior thin-film studies cannot be directly translated to an ionomer environment in an MEA configuration.

The conductivity of the anode layer has significant impact on AEMWE performance.[11] The electrical conductivity of each catalyst was measured by pressing each catalyst powder between two stainless steel disks under 23,000 psi and collecting a polarization curve. Catalyst performance at 1 A·cm^{-2} follows electrical conductivity (Figure 6.2), indicating that the worst-performing catalysts suffer from limited available active sites due to a poor electron transport through the catalyst layer. A similar experiment was conducted with all Co-based anode catalysts measuring electronic conductivity in a catalyst/ionomer layer as opposed to pressed powders and a similar trend was observed (Figure D.4 and Supplemental Methods in Appendix D). The ionomer environment, in combination with low-conductivity catalyst, may impede the conversion of the Ni-Fe-oxide catalysts into the more active (oxy)hydroxide form that is more conductive and would ensure better electrical conductivity between the catalyst particles and the GDL.

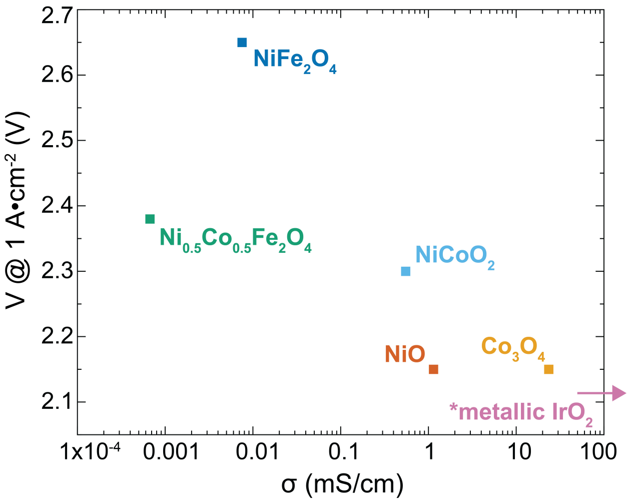

Figure 6.2. Electrical conductivity of non-PGM catalysts. Conductivity was measured by compressing the powders into a pellet (23,000 psi) and measuring electrical resistance while under compression from the slope of a polarization curve. The resistance measured for IrO_2 pellet was comparable to the contact/wire resistance, and thus IrO_2 is simply labeled as metallic (Figure D.3).

Several important points are evident from these data. *i)* IrO_2 and Co_3O_4, the most electronically-conductive of the catalysts tested, have superior performance in the pure-water-fed system, *ii*) the least-conductive, Fe-based catalysts, which have been shown to be superior for alkaline OER kinetics,[7a, 7c] perform the worst, and *iii)* mixed-metal and Fe-containing catalysts show significantly worse stability than single-metal, non-Fe-based catalysts. Such performance and durability trends could be attributed to the instability of the catalyst (through leaching or restructuring), ionomer, mechanical issues, or some combination of all. To investigate this, the compressed AEMWE cells were disassembled and the anode GDLs analyzed with x-ray photoelectron spectroscopy (XPS). Upon disassembly the solid membrane is pulled away from the GDL exposing the leftover catalyst powder embedded in the ionomer directly in contact with the catalyst.

Ionomer Degradation. The ionomer binder directly in contact with the catalyst layer oxidizes under operating potentials at the anode with IrO_2.[6a, 12] However, the mechanism by which this oxidation occurs is poorly understood.[6a, 13] Oxidation could be occurring directly at the catalyst/ionomer surface or chemically through reactivity with OER intermediates or other reactive oxygen species formed, for example, through radical reactivity.[14] These degradation phenomena may or may not depend on catalyst type. Others have suggested that degradation rates correlate with ionomer/catalyst interaction strength,[15] and the adsorption energies of ionomer functional groups to the catalyst surface are expected to vary for different oxide catalysts. If degradation is occurring by chemical reactivity with OER intermediates, degradation may depend on catalyst activity and OER mechanism. Furthermore, AEM ionomers will oxidize at sufficiently high voltage regardless of catalyst/electrode surface,[12] thus degradation may only depend on device operating voltage.

The extent of the ionomer oxidation by the six catalysts was assessed by XPS. The chemical structure of the ionomer and membrane used is in Figure 6.3a. The C 1s, N 1s, and F 1s spectra were collected on the pristine ink and port-mortem GDLs after 20 h of operating at 500 $mA \cdot cm^{-2}$ (Figure 6.3b). The changes to the shape and binding energy of the peaks are indicative of oxidative changes under applied potential and, in some cases, dissolution. Despite similar performance, IrO_2 and Co_3O_4 appear to interact with the surrounding ionomer differently. During operation with Co_3O_4 at the anode, the XP spectra of the ionomer does not change substantially. The N 1s peak that represents the charge-carrying groups in PiperION retains its position and shape. The XP spectra of the ionomer interacting with IrO_2, on the other hand, undergoes significant chemical changes. A new high-binding-energy peak emerges at 288.4 eV after 20 h of operation and the N 1s peak vanishes. The F 1s peak also diminishes.

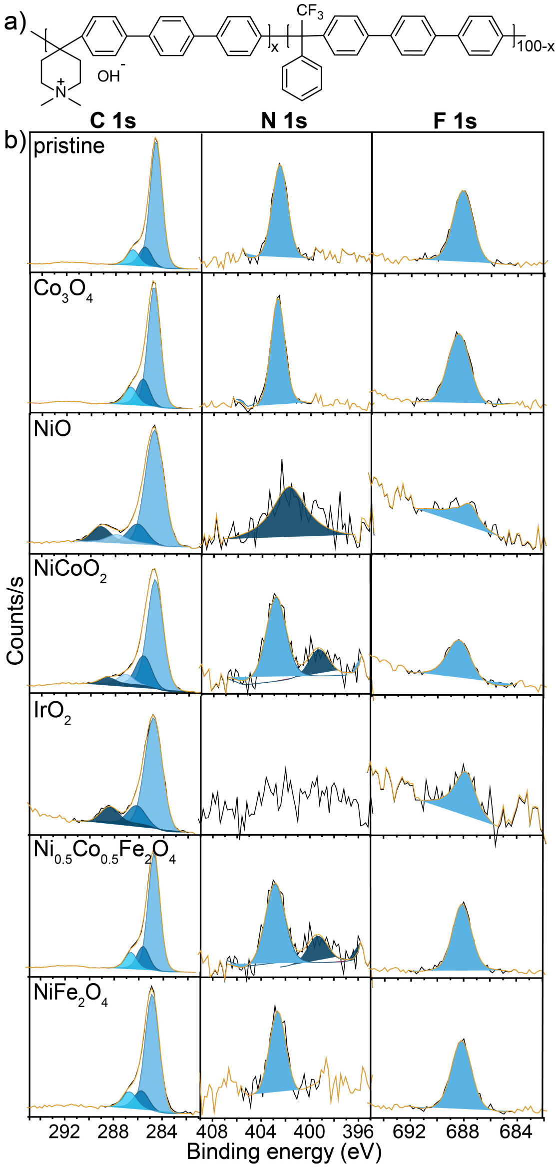

Figure 6.3. **Catalyst-dependent ionomer degradation.** a) Chemical structure of the membrane/ionomer used in this study (PiperION by Versogen, PAP-TP-85); b) XP spectra of C 1s, N 1s, and F 1s peaks collected on the pristine anode GDLs with the catalyst inks sprayed on (top) and the post-mortem GDLs after 20 h of operating at 500 mA·cm^{-2} in pure water.

As 20 h is a short durability test, the Co_3O_4 catalyst was operated for 250 h (Figure 6.4). The performance is similar to what has been previously observed for IrO_2 with both MEA's stabilizing to degradation rates < 1 mV·h^{-1} after 150 h.[6a] XPS analysis of the ionomer in the 250-hour Co_3O_4 electrolyzer run shows significant changes in the C 1s region (Figure 6.4 inset), comparable to that of IrO_2 after a long-term operation[6a]. Hence, the ionomer does oxidize during operation with Co_3O_4 but at a slower rate than with IrO_2. The variability in ionomer oxidation rates at short time scales may be explained by the difference in the catalysts' electronic conductivity. Catalyst surfaces are known to facilitate ionomer degradation, either through the polymer interactions with OER intermediates or by direct oxidation through functional groups adsorbing onto the catalyst surface.[14b, 15-16] A more electrically-conductive catalyst could oxidize the ionomer faster due to lower ohmic voltage losses through the percolative electronic transport pathways in the catalyst, while a less-conductive catalysts might only be able to oxidize the ionomer closer to the GDL where electronic ohmic losses are small and high oxidizing potentials remain available.

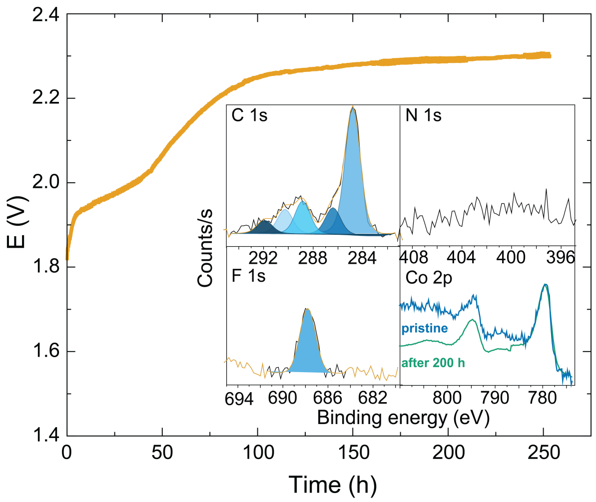

Figure 6.4. Extended durability testing of AEMWE with Co_3O_4 anode catalyst. Cell was operated for 250 h at 500 mA·cm^{-2} in pure water at 57 °C. A Pt-black catalyst on Toray carbon paper was used as the cathode. Inset shows XP spectra of ionomer (C 1s, N 1s, and F 1s) and catalyst (Co 2p) after operation, illustrating severe oxidative damage and loss of N-containing cationic groups.

The next two most-stable catalysts, NiO and $NiCoO_2$, also facilitate ionomer degradation: new high-energy peaks appear in the C 1s spectra; N 1s shifts in energy and diminishes; F 1s also decreases in intensity (Figure 6.3b). This could be attributed to the ionomer degradation due to the higher operating voltage but the XPS of the two worst-performing catalysts, $NiFe_2O_4$ and $Ni_{0.5}Co_{0.5}Fe_2O_4$, showed less changes to the ionomer structure than for NiO and $NiCoO_2$ despite operating at a higher cell voltage (Figure 6.3b). Changes are only observed in the N 1s peaks suggesting the ionomer dissolution or changes to the chemical structure of the charge-carrying groups. But these changes are minimal compared to what is observed with the better performing catalysts like IrO_2 or NiO. The XPS analysis of the GDLs is performed on multiple spots to obtain an averaged picture of the ionomer structure. The $NiFe_2O_4$ GDL showed minor changes to the carbon peak in some of the analyzed spots, but the majority of the spectra showed no change. We hypothesize that the ionomer oxidation by these poor AEMWE anode catalysts is limited by their low electronic conductivity and that only the catalyst sites near the GDL are available for ionomer oxidation. Thus, ionomer oxidation may not be the primary degradation pathway for the Fe-based catalysts. To test this, the $NiFe_2O_4$ catalyst was operated at a constant voltage rather than current. Even when held at 1.8 V, lower than the operating voltage of the best-performing catalyst, the activity of the system degraded rapidly, passing only a few mA of current by the end of the 20 h operation (Figure D.5). The C 1s and N 1s spectra of the ionomer in contact with the catalyst show small changes compared to the pristine material (inset in Figure D.5). Therefore, the changes in the catalyst structure were also considered.

Catalyst Restructuring and Leaching. Non-PGM OER catalysts are known to structurally evolve under operating conditions.[7a, 7b] Co, Ni, and Fe oxides, for example, oxidize during OER typically converting to more-active and electrically conductive layered oxyhydroxides.[7c] These catalysts also have dynamic Fe sites that dissolve and re-deposit that are responsible for the superior OER activity.[17] For Ni-Fe and Co-Fe oxyhydroxide catalysts leaching of the metals has been reported.[17a] Fe was measured to dissolve at higher rates than Ni or Co in Fe/Ni and Fe/Co oxides/oxyhydroxides, with Ni dissolution products being the least soluble.[17a] These catalysts may also uptake additional ions present in trace amounts in electrolyte.

To assess restructuring and leaching in the mixed-metal non-PGM catalyst powders during electrolysis, we measured the metal ratios before and after operation (Figure 6.5a). The ratios determined by XPS are reflective of the surface composition and do not correspond to the overall composition of the nanopowders. For $NiCoO_2$, the initial surface ratio of Co/Ni found by XPS was 0.22 ± 0.02. This ratio decreased to 0.15 ± 0.03 after operation, suggesting that the catalyst is restructuring and/or leaching, forming a Ni-rich surface. The Fe/Ni ratio in $NiFe_2O_4$ increased from the initial 0.54 ± 0.02 to 1.1 ± 0.07 indicating the formation of an Fe-rich top layer. This is likely due to Fe leaching, followed by redeposition on the surface of the catalyst owing to Fe not being able to exit the electrolyzer by passing through the solid membrane. The Fe/Ni ratio in $Ni_{0.5}Co_{0.5}Fe_2O_4$, however, showed the opposite trend, decreasing from 2.9 ± 0.02 to 1.8 ± 0.09, but this change was accompanied by a decrease in the Co/Ni ratio (1.0 ± 0.05 to 0.52 ± 0.04) suggesting the formation of a Ni-rich surface. Such composition on the surface is likely the result of Ni restructuring and covering Co and Fe. As Co is known to be stable during OER [17b, 18], Co leaching is unlikely.

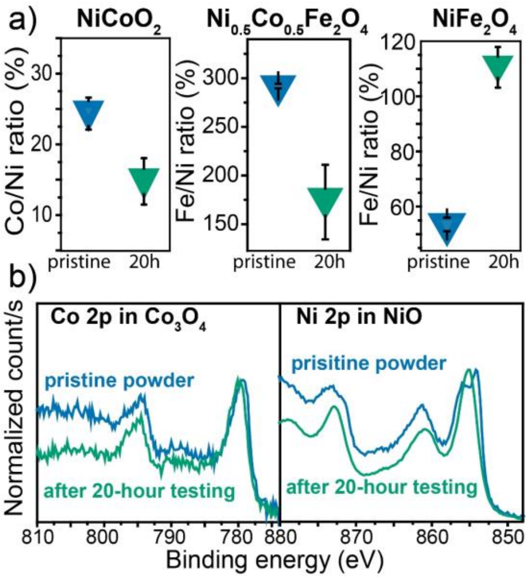

Figure 6.5. **Comparison of non-PGM catalyst structure pre- and post-operation.** a) The change in metal ratios of mixed-metal catalysts determined by XPS and b) XPS spectra of Co 2p in Co_3O_4 and Ni 2p in NiO. All catalysts were operated for 20 h of at 500 mA·cm^{-2}.

For the monometallic oxides (NiO and Co_3O_4) we studied changes in the shape and energy of the metal peaks (Figure 6.5b). The Co 2p peak remained unchanged after 20 h of water electrolysis. The shape of the peak is consistent with Co_3O_4.[19] Co_3O_4 is known to form a sub-nanometer amorphous shell during OER, otherwise maintaining crystallinity,[20] and a small extent of oxidation may be occurring that is not detected by XPS. The Ni 2p peak shifted to higher binding energy and changed its shape consistent with the transition from NiO to NiOOH.[19] $Ni(OH)_2$ significantly restructures under OER conditions compared to $Co(OH)_2$ that maintains its initial morphology.[18, 21] The change in oxidation state and structure might be accompanied by $Ni^{2+/3+}$ leaching/redeposition. The changes to the catalyst structure likely explain the observed degradation behavior. Catalyst/ionomer interactions influence electrolyzer performance and durability.[16, 22] Structural evolution and cation leaching/redeposition likely disrupts the catalyst/ionomer interfaces. For example, as NiO dynamically restructures to form more disordered NiOOH, the physical proximity of the ionomer and catalyst likely decreases, increasing *iR* or decreasing ionic conductivity, leading to higher voltages without observing significant ionomer oxidation by XPS. Any leaching of the metal cations and their consequent redeposition on the electrode surface could further disrupt the catalyst/ionomer network. The lack of restructuring and leaching/redeposition under OER conditions likely contributes to the better durability of Co_3O_4.

Role of Dynamic Fe Species. Leached ions also can participate in chemical reactions with the ionomer leading to chemical changes (e.g. Fenton-type oxidation reactions).[23] Fe is particularly dynamic, and thus the role of soluble Fe ions was further investigated. Since we observed a formation of an Fe-rich surface on the GDL tested with $NiFe_2O_4$, we focused on that catalyst to pinpoint the role the Fe ions play in electrolyzer performance. We hypothesized that Fe leaches and redeposits onto the anode during operation forming an amorphous blocking layer that is disruptive to the catalyst/ionomer network decreasing ionic conductivity.

To probe the role of soluble Fe species, we intentionally added soluble Fe to the water feed. An MEA with a Co_3O_4 anode was operated for ~ 10 h to stabilize, then 1 ppm Fe^{3+} was flown to the anode while pure water was maintained at the cathode from a separate pump and water reservoir (Figure 6.6). The Fe increased the degradation rate to ~4 mV h^{-1}. The run was carried out for 40 h, during which the degradation continued at this constant rate. XPS shows large changes to the C 1s and N 1s spectra. The performance of Co_3O_4 tested for 40 h in the absence of Fe (Figure 6.6, gold) did not degrade as rapidly. However, the XPS analysis of the ionomer at the anode after the 40-h Fe-free run shows nearly identical changes to the C 1s and N 1s peaks (Figure 6.6 inset). As discussed above, Co_3O_4 oxidizes the ionomer but at a slower rate compared to IrO_2 (Figure 6.4). One might attribute this new degradation to soluble Fe species crossing the AEM to the cathode where it could block active sites on Pt or otherwise facilitate cathodic degradation, but Fe was not detected on the cathode GDL post-operation by XPS (Figure D.6). Thus, it appears the introduction of Fe is accelerating the degradation in the anode. Soluble Fe ions likely deposit on the anode catalyst surface disrupting the ionic conductivity of the catalyst/ionomer network.

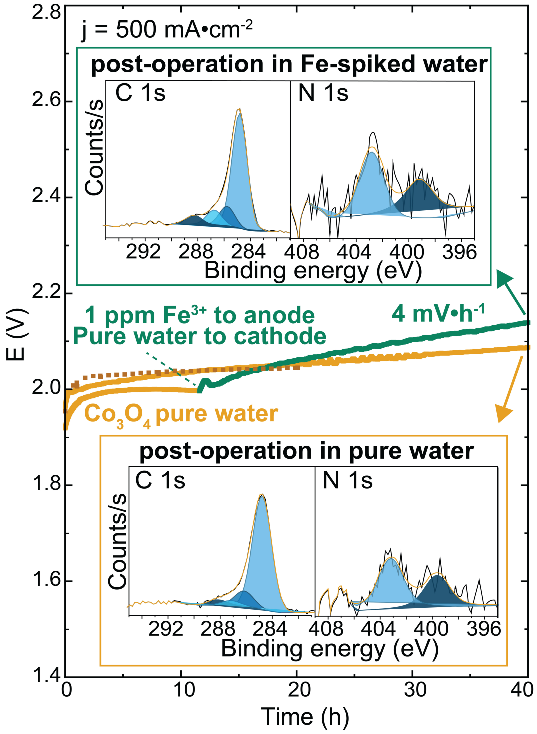

Figure 6.6. **Effect of soluble Fe on AEM durability.** Durability testing of Co_3O_4 spiked with a solution of $Fe(NO_3)_3$: Co_3O_4 was operated in pure water until stabilizing (yellow), after which the anode inlet was moved to a solution of 1 ppm Fe^{3+} (green trace). The 20 h Co_3O_4 run is shown in darker yellow dashed line for reference. Inset: XP spectra of the anode GDL post-Fe spike (top) and pure water (bottom) operation.

Conclusion

We have discovered critical catalyst processes that dramatically affect the performance and stability of AEMWE devices key for scalable H_2 production (summarized in Figure 6.7). The experimental results indicate that conductive IrO_2 provides more active sites to oxidize the ionomer, as opposed to mixed Ni/Fe/Co catalysts that show a lower extent of oxidation by XPS due to much lower electrical conductivity. IrO_2 is sufficiently conductive, so any Ir sites in contact with the ionomer network are active, leading to rapid ionomer degradation throughout the catalyst layer. Co_3O_4, while less electrically-conductive, appears conductive enough to maintain sufficient activity throughout the catalyst layer. Improved performance is likely possible by further improving the electrical properties. The OER on Co_3O_4 likely converts the particle surface to CoOOH, but the depth of conversion is sufficiently thin as to not disrupt the catalyst/ionomer interface. The ionomer still oxidatively degrades throughout the catalyst layer but at a slower rate than for IrO_2. XPS shows NiO converts to NiOOH phase, and our evidence suggests that changes to ionomer/catalyst interface associated with this transition contribute to faster degradation. The low electronic conductivity of $NiCoO_2$, $Ni_{0.5}Co_{0.5}Fe_2O_4$, and $NiFe_2O_4$ confines OER to the region in direct contact with the stainless-steel support. As the ionomer oxidizes, ionic conductivity to this region decreases. Ionically accessible catalyst sites are now further from the GDL, but low electronic conductivity limits reactivity of these sites creating a resistive layer leading to voltage increases. $NiCoO_2$ and $Ni_{0.5}Co_{0.5}Fe_2O_4$ show a Ni-rich surface after operation and $NiFe_2O_4$ shows an Fe-rich surface after operation. Changes to the ionomer/catalyst interface associated with this rearrangement likely result in changes to surface contact and charge-transfer resistance. For $NiCoO_2$, as Co is known to be very stable during operation[17b, 18], we hypothesize Ni ions are leaching/redepositing from the catalyst, possibly due to a lower local pH environment created by the reduced OH^- conductivity to the region. The Fe-rich surface for $NiFe_2O_4$ is likely due to dominant Fe leaching/redeposition. For $Ni_{0.5}Co_{0.5}Fe_2O_4$ both Ni and Fe are likely leaching. For all catalysts, leached ions can wash away decreasing activity or create voids in the ionomer network disrupting the ionic connectivity and physical coupling between ionomer and catalysts. Ions that then redeposit on the catalyst likely change ionomer/catalyst interactions reducing ionic conductivity or blocking active sites. In solution, those ions may also accelerate existing or introduce additional ionomer degradation mechanisms. Multiple degradation modes are likely occurring simultaneously with the Ni-Fe-oxides contributing to their rapid failure during device operation.

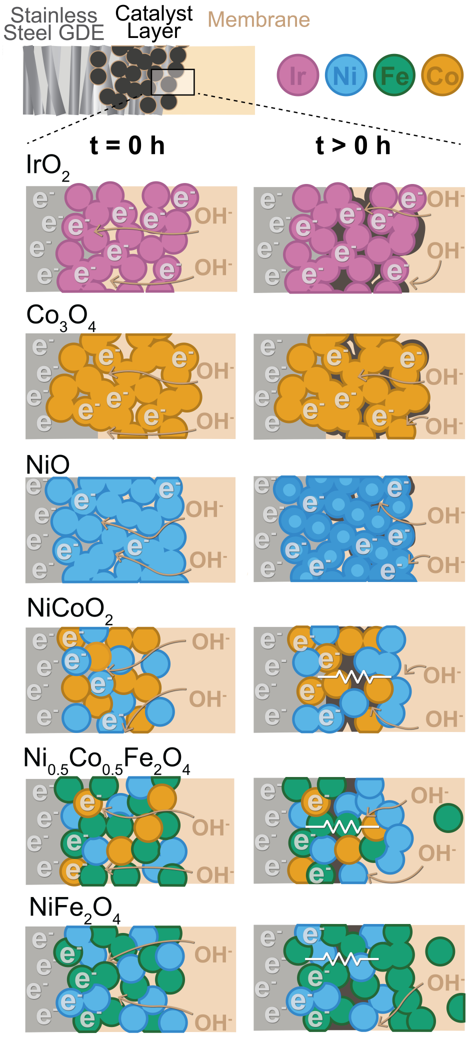

Figure 6.7. **Summary of possible anode degradation processes.** The left panel shows the catalyst starting state and right after extended operation. Pristine ionomer is shown in tan; degraded ionomer regions are dark brown. IrO_2 (pink) degrades the ionomer throughout the catalyst layer but has sufficient electronic conductivity to still access ionically conductive regions. Co_3O_4 (gold) also degrades the ionomer but at a slower rate and has sufficient electrical conductivity to maintain some activity throughout the catalyst layer. NiO (light blue) converts to the electrically conductive NiOOH phase (dark blue), increasing electronic conductivity but disrupting the catalyst/ionomer interaction. $NiCoO_2$ (blue and gold), $Ni_{0.5}Co_{0.5}Fe_2O_4$ (blue, gold, and green), and $NiFe_2O_4$ (blue and green) have low electronic conductivity. Ionomer degradation decreases ionic pathways to the catalyst creating a resistive zone.

Understanding the behavior of non-PGM catalysts in industrially relevant (nominally) pure-water-fed AEMWE devices is critical to inform design for advanced electrolyzer technology. In this chapter, we isolate anode catalyst processes from overall device performance and report the first chemical insight into catalyst characteristics and processes driving system degradation. Analyzing the performance and stability of five non-PGM anode catalysts in comparison with a baseline IrO_2 catalyst in a pure-water-fed AEM electrolyzer, we reveal that high electronic conductivity of the catalyst results in a better voltage performance but faster ionomer oxidation. We also discover a variety of degradation processes occurring for each catalyst. The main sources of degradation stem from catalyst restructuring and ionomer oxidation under OER-relevant conditions—the structural stability, coupled with good electrical conductivity and OER activity, of IrO_2 and Co_3O_4 are the reasons for their superior durability. We have thus begun, for the first time, to isolate ionomer degradation from catalysts phenomena during operation in an MEA configuration and simultaneously provided fundamental insight into non-PGM catalyst operation in industrially-relevant configurations and conditions. Our approach also uses a simple, scalable GDL preparation method and commercially available catalyst to show Co_3O_4 is a viable option for developing non-PGM-based AEM electrolyzers, which is essential for the AEMWE to grow into a competitive future technology.

APPENDIX A

CHAPTER II SUPPORTING INFORMATION

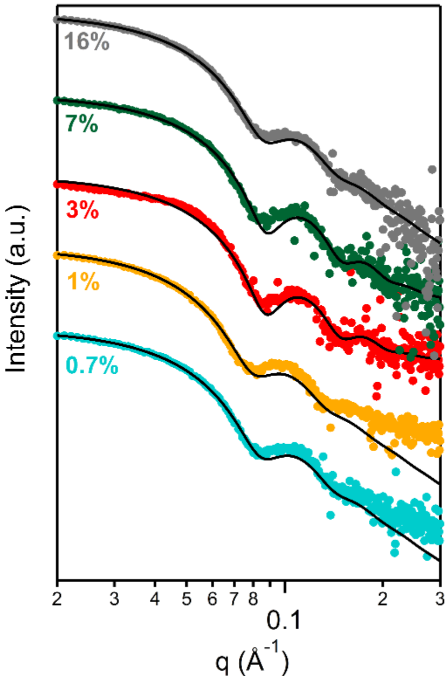

Figure A.1. SAXS data for the homogeneously-doped ITO nanocrystals used in this study (from top to bottom: 16%, 7%, 3%, 1%, and 0.7% Sn-doping). The colored dots represent the raw SAXS data and the black lines represent fits to those data. Modelled sizes can be found in Table 2.1.

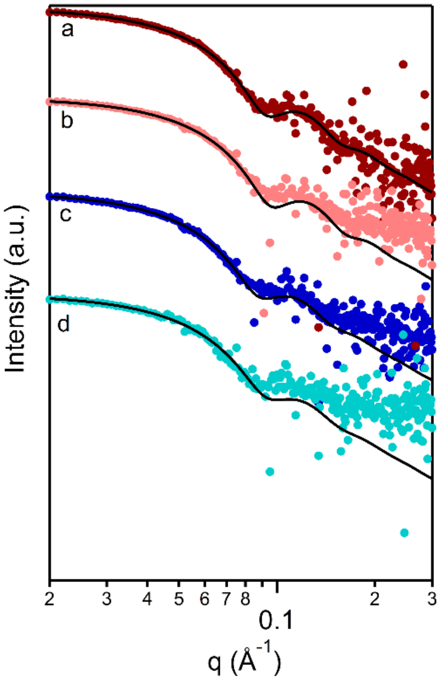

Figure A.2. SAXS data for the ITO/In_2O_3 core/shell nanocrystals used in this study. For each of these, we synthesized an ITO core, performed SAXS analysis of the cores, then added a thin In_2O_3 shell and performed SAXS again. This plot shows the scattering patterns for the core/shells nanocrystals a) and c) compared to the cores alone b) and d). a) 12% ITO core with a thin In_2O_3 shell, b) 12% ITO core with no shell, c) 0.4% ITO core with a thin In_2O_3 shell, and d) 0.4% ITO core with no shell. The colored dots represent the raw SAXS data and the black lines represent fits to those data. Modelled sizes can be found in Table 2.1.

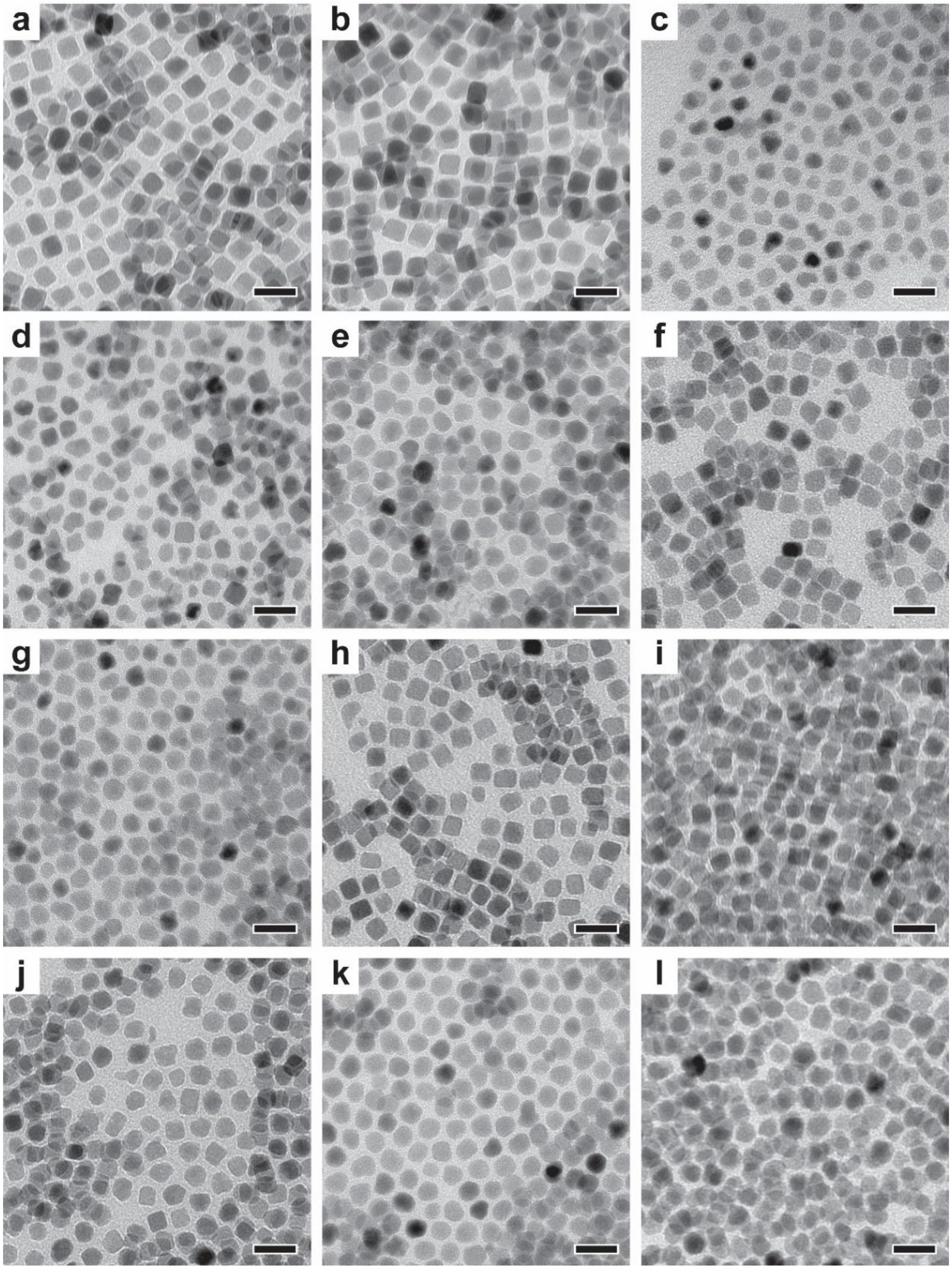

Figure A.3. TEM images from all samples listed in Table 1, including homogeneously-doped ITO nanocrystals a) 0.7%, b) 1%, c) 3%, d) 7%, e) 16% Sn metal percent; ITO cores f) 0.4%, g) 12% Sn metal percent with sub-nanometer In_2O_3 shells; and ITO cores with thicker In_2O_3 shells h) 1.5%, i) 3%, j) 5%, k) 10%, and l) 16% Sn metal percent. All scale bars are 20 nm.

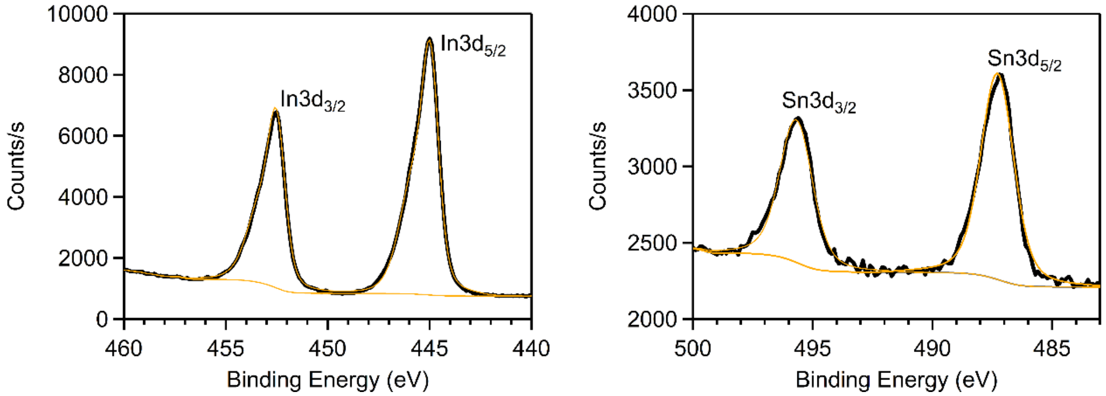

Figure A.4. Representative XPS data used to calculate Sn:In content. These spectra show the In and Sn 3d regions for the 16% homogeneously doped ITO nanocrystals as an example. In both spectra, the black lines represent the raw data and the yellow lines represent the overall fits to the data. Sn content can be found in Table 2.1.

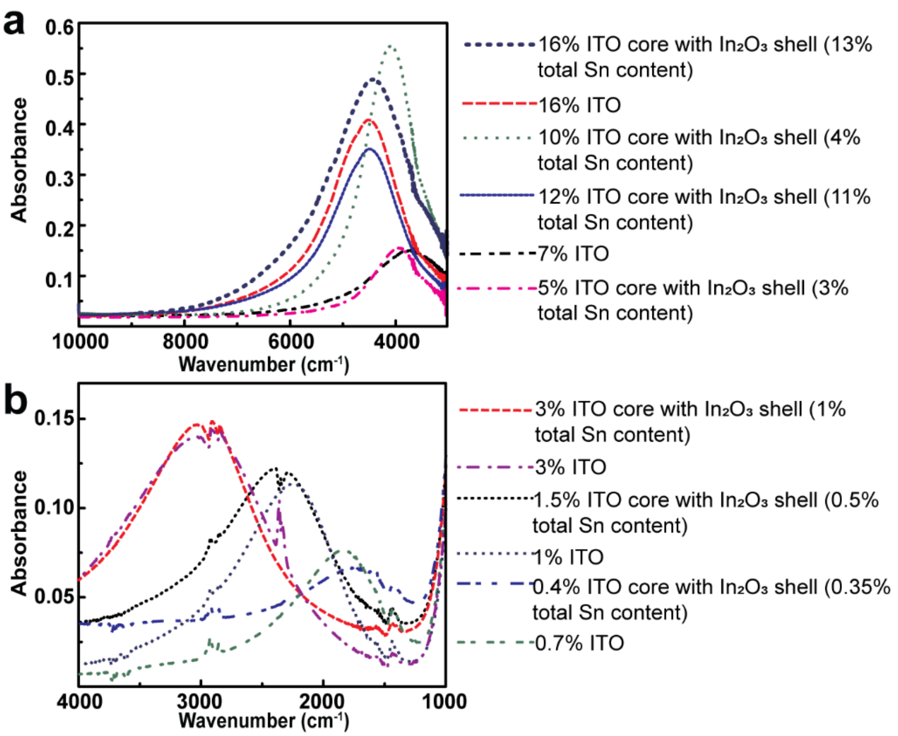

Figure A.5. a) Raw non-normalized absorbance data for ITO thin films that possess the LSPR in the wavelength range covered by the UV/Vis-NIR spectrometer; b) Raw non-normalized absorbance data for ITO nanocrystal films with low doping level collected using IR spectrometer.

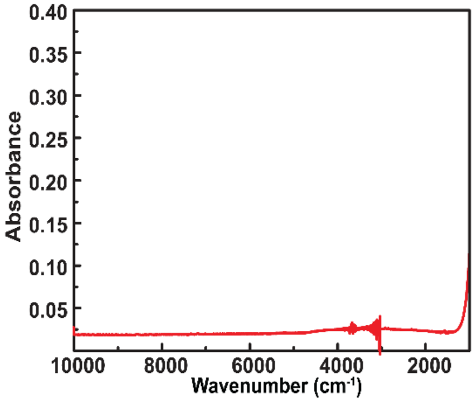

Figure A.6. Absorbance of CaF_2 used as a substrate for measuring the absorbance of ITO nanocrystal films.

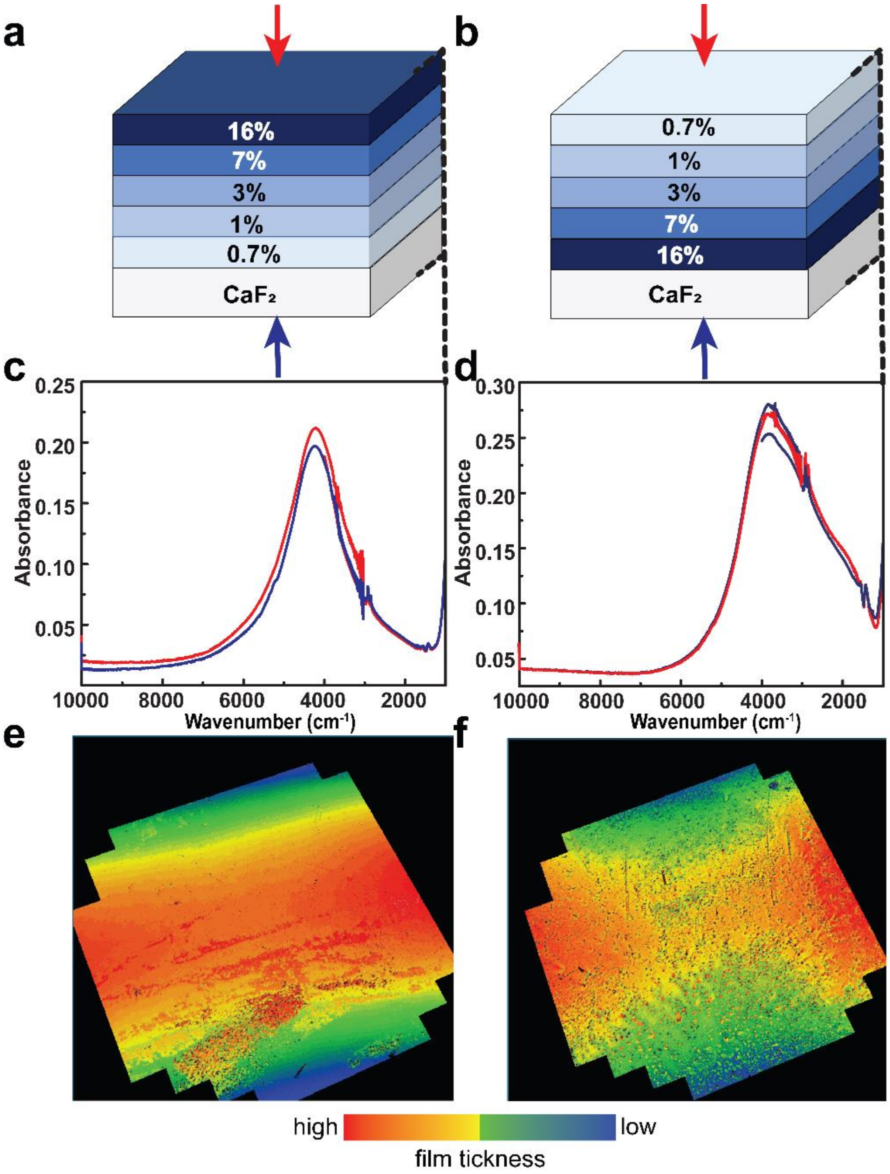

Figure A.7. To investigate if the beam direction changed the shape and energy of the combined optical response in the multilayered films, the absorbance spectra for the samples with the geometries a) and b) were collected from two directions indicated by the arrows. c) and d) show the corresponding absorbance spectra for the multilayered samples. The colors of the spectra match the colors of the arrows showing from what direction the spectra were collected. e) and f) show the ellipsometry data collected for each sample. The data were collected on a CaF_2 substrate one-inch diameter. The depicted plots correspond to a 10.82 x 10.55 mm area in the middle of the substrate.

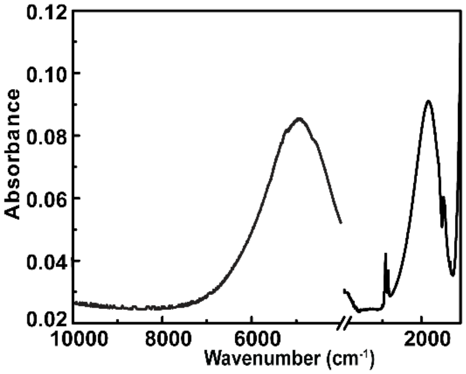

Figure A.8. Raw non-normalized absorbance spectrum of the film designed for the narrow band-stop filter. The break in the x-axis (4,000-3,900 cm^{-1}) is inserted to avoid the instrumental noise at the edge of the detector range. The absorbance data from the FTIR spectrometer was lowered to the same base as the data from the UV/Vis spectrometer to allow intensity comparison.

APPENDIX B

CHAPTER III SUPPORTING INFORMATION

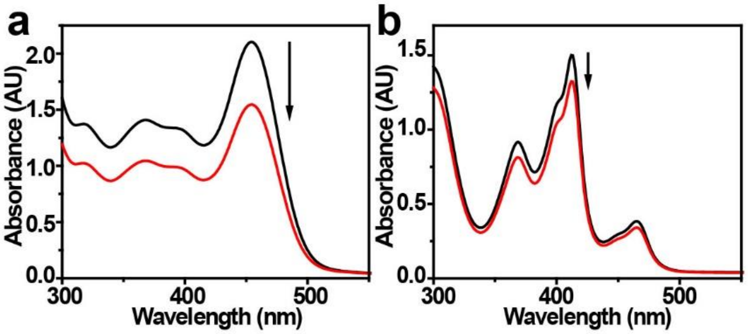

Figure B.1. The change in intensity of the UV-vis spectrum of $[(COD)IrCl]_2$ after reacting with ATO nanoparticles in air-free conditions in (a) toluene and (b) acetonitrile. No changes to the shapes of the spectra were observed.

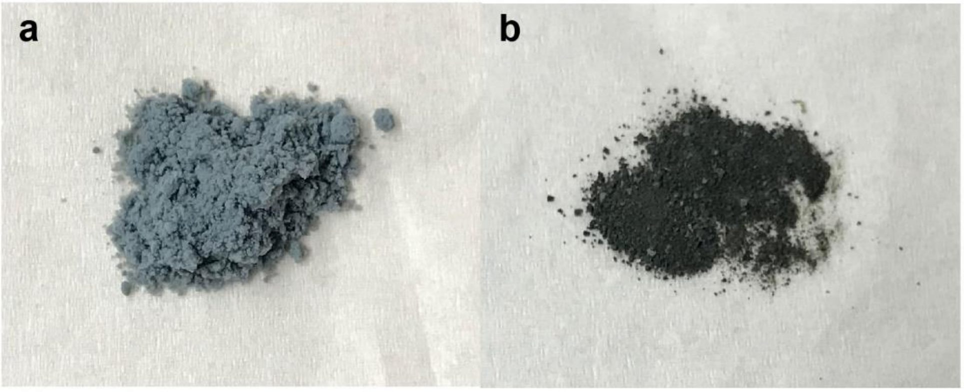

Figure B.2. ATO nanopowder before (a) and after (b) reacting with the $[(COD)IrCl]_2$ solution.

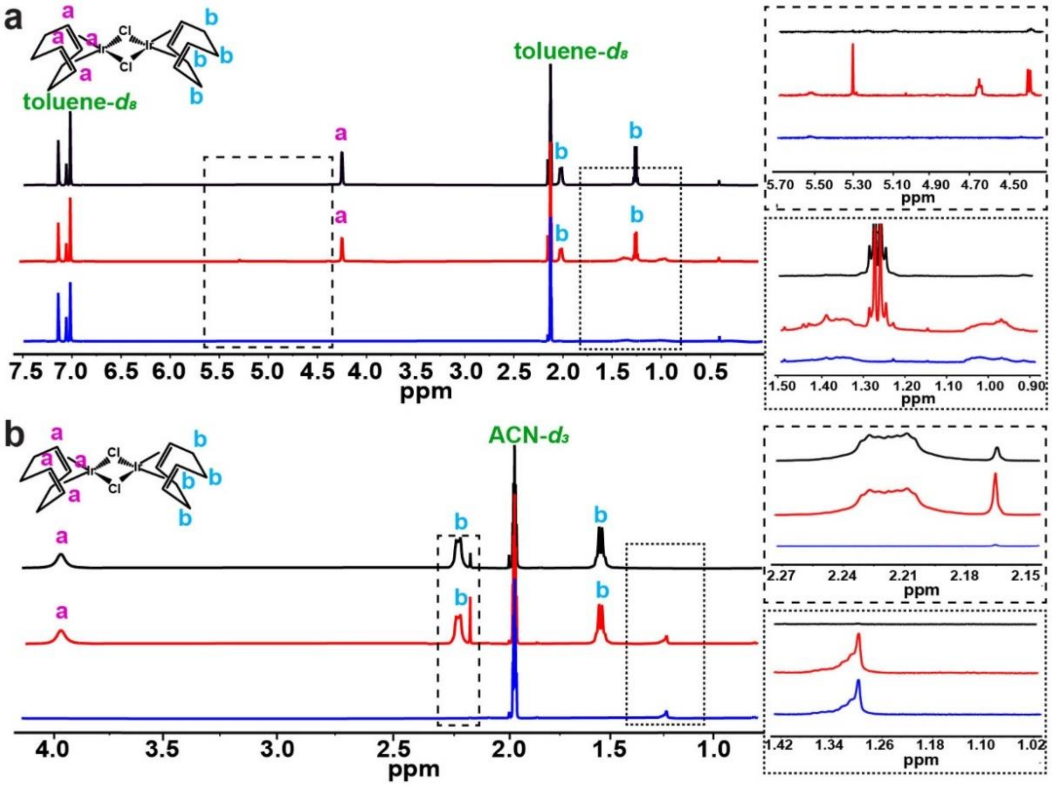

Figure B.3. By NMR [(COD)IrCl]$_2$ adheres to ATO mostly intact. Reactions of ATO nanopowder with [(COD)IrCl]$_2$ in (a) toluene-d_8 and (b) ACN-d_3 were monitored with ^{1}H NMR. In black: fresh [(COD)IrCl]$_2$ solution in the analyzed solvent. In red: [(COD)IrCl]$_2$ solution after reacting with ATO for 5 h in air-free conditions. In blue: deuterated solvents after being in contact with ATO for 5 h with no [(COD)IrCl]$_2$ added. Inset (a): in the dashed box, peaks at 5.3, 4.7, and 4.4 ppm arising in the spectrum after ATO powder reacts with [(COD)IrCl]$_2$; in the dotted box, broad peaks at 1.0 - 1.5 ppm appearing after ATO is added with and without [(COD)IrCl]$_2$ being added. Inset (b): in the dashed box, a peak at 2.16 ppm that is present in the spectrum of the fresh [(COD)IrCl]$_2$ solution increases in intensity as the solution reacts with ATO; in the dotted box, a broad peak at 1.25 - 1.34 ppm is present in the spectra of the samples with ATO nanopowder.

The nanoparticles were left to react with [(COD)IrCl]$_2$ for 5 h. To account for any contributions to the spectra from ATO nanoparticles or impurities absorbed on ATO, the nanoparticles were soaked in toluene-d_8 and ACN-d_3 without [(COD)IrCl]$_2$ for 5 h and a ^{1}H NMR spectrum of the solvents were recorded. The ^{1}H NMR spectrum of fresh [(COD)IrCl]$_2$ in toluene-d_8 shows a doublet at 4.25 ppm; a multiplet at 2.02 ppm; and a doublet at 1.26 ppm. The hydrogens on the outer edges of the COD ligands produce two peaks due to occupying endo and exo positions. After reaction with ATO, two broad peaks in the 1.0 - 1.5 ppm range (Figure B.3a, inset in the dashed box) and several small peaks in the 4.5 – 5.5 ppm range and at 2.2 ppm appear (Figure B.3a, inset in the dotted box). The broad peaks at 1.0 - 1.5 ppm were also observed in spectra collected after ATO nanoparticles were soaked in toluene-*d_8* for 5 h without $[(COD)IrCl]_2$ (Figure B.3a, blue trace) and are thus tentatively assigned to ATO particles remaining in solution after passing through the 0.1 μm filter. The small peaks from 2.2 – 5 ppm may be from free COD released after binding of $[(COD)IrCl]_2$ to the ATO. Free COD produces an NMR spectrum with peaks at 5.6 and 2.3 ppm in a 1:2 ratio. Two of the small peaks appearing after the reaction with ATO are at similar shifts but are 2:1 in integrated intensity (5.3 and 2.2 ppm, respectively). Thus, they are not free COD in solution, but may be other minor reaction biproducts. The ^{1}H NMR analysis of $[(COD)IrCl]_2$ after reacting with ATO nanoparticles in ACN-*d_3* similarly shows no new peaks with only small peak at 2.16 ppm from water contamination and the same broad peak at 1.25-1.34 ppm from remaining ATO nanoparticles (Figure B.3b). Given the lack of significant changes to the NMR spectrum of $[(COD)IrCl]_2$ after the reaction with ATO in either solvent (apart from a decrease in the peak intensities as some as $[(COD)IrCl]_2$ is absorbed on the ATO), we conclude that $[(COD)IrCl]_2$ attaches to the surface of the ATO nanoparticles in toluene largely intact. Because of the finer control over the Ir loading, in further studies we synthesized Ir-functionalized catalyst in toluene at 100 °C.

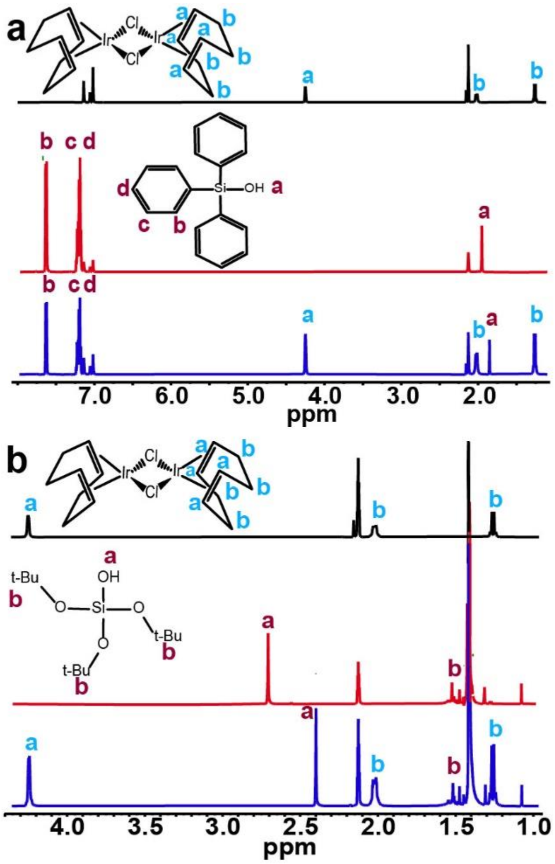

Figure B4. No OH/[(COD)IrCl]$_2$ binding observed by NMR. Top panel (a and b): ^{1}H NMR spectrum of [(COD)IrCl]$_2$ in toluene-*d*$_8$. Middle panel: ^{1}H NMR spectrum of (a) TPS and (b) TBS in toluene-*d*$_8$. Bottom panel: ^{1}H NMR spectrum of the mixed solution of [(COD)IrCl]$_2$ and (a) TPS and (b) TBS after being stirred in the glovebox at 100 °C for 1 hour.

Our initial hypothesis was that [(COD)IrCl]$_2$ might attach to metal oxide surfaces via reaction with surface hydroxyl. We thus studied attachment to triphenyl silanol (TPS) so that we could monitor if [(COD)IrCl]$_2$ binds to the OH group by NMR. A stock solution of 4 mM [(COD)IrCl]$_2$ was prepared and mixed with a solution of TPS in toluene-*d*$_8$. After 1 h an ^{1}H NMR spectrum of the mixed solution was recorded (Figure SB.4a). The NMR spectrum of the mixture (Figure B.4a, bottom panel) shows a 0.12 ppm shift in the energy of the hydroxyl hydrogen. Such a shift is too small to signify binding. Other peaks belonging to TPS and [(COD)IrCl]$_2$ remain in their initial positions which would be unlikely if binding indeed was happening. We repeated the experiment changing the relative amounts of the [(COD)IrCl]$_2$ and TPS and observed that the H on the hydroxyl group shifts by different amounts depending on the concentrations of the components and that the rest of the peaks remain in their initial positions. We concluded that the shift observed in the position of the hydroxyl H is concentration-dependent and does not signify binding of the two compounds.

We also tried tris(*tert*-butoxy)silanol (TBS) that has a more acidic H in the hydroxyl group (Figure B.4b). The shift observed for the hydroxyl hydrogen was 0.31 ppm. The rest of the peaks remained in the initial position. Adjusting the concentrations of the two solutions produced different shifts of the same hydrogen, but no other shifts were observed. We concluded that $[(COD)IrCl]_2$ does not bind to the surface of metal-oxide support but rather is attracted by electrostatic interactions.

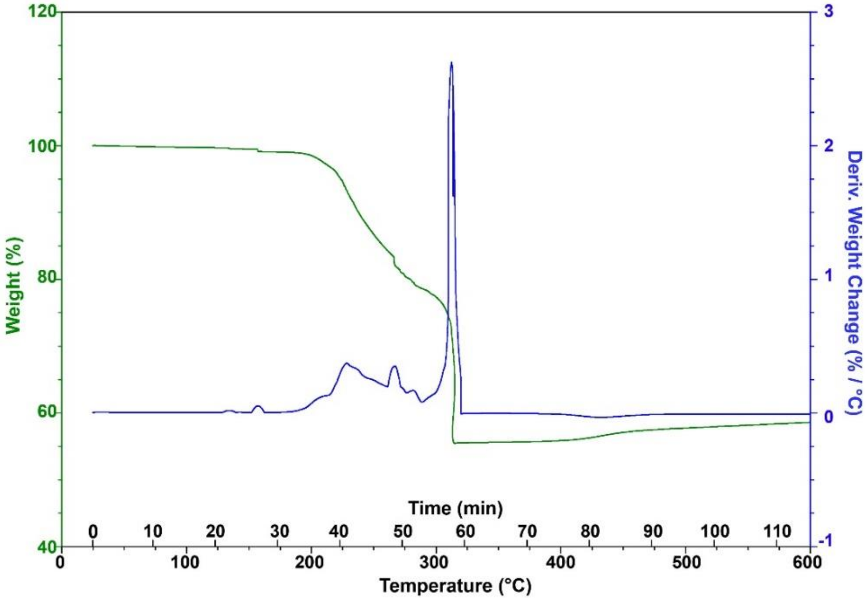

Figure B.5. Thermogravimetric analysis of 10 mg of $[(COD)IrCl]_2$ from room temperature to 600°C at the rate of 5°C/minute.

Table B.1. XPS data summary for the Ir-functionalized FTO and ATO samples pristine and tested in 0.1 M $HClO_4$ (EC). All tested electrodes were annealed at 350 °C after reacting with Ir precursor. Ir 4f fitting was done with keeping 4f7 and 4f5 FWHM the same for any given sample.

Sample	Binding energy (eV)			
	Ir 4f7 (1)	Ir 4f7 (2)	Ir 4f7 (3)	Ti 2p
1S-ATO not annealed	62.0	--	--	--
1S-FTO not annealed	62.1	--	--	--
1S-FTO prisitine	62.1	63.5	--	--
1S-FTO (EC)	62.2	--	--	--
3S-FTO pristine	62.4	63.6	64.8	--
3S-FTO (EC)	62.1	63.4	64.6	--
1S-FTO-5-TiO_2 pristine	61.8	63.4	--	458.5
1S-FTO-5-TiO_2 (EC)	62.1	63.5	--	458.9
3S-FTO-2-TiO_2 pristine	62.1	63.7	65.4	458.9
3S-FTO-2-TiO_2 (EC)	62.9	64.0	65.2	--
3S-FTO-5-TiO_2 pristine	61.7	63.0	64.3	458.5
3S-FTO-5-TiO_2 (EC)	62.2	63.4	64.6	458.6
3S-FTO-20-TiO_2 pristine	61.7	63.1	--	458.4
3S-FTO-20-TiO_2 (EC)	61.9	63.0	64.2	458.6
3S-FTO-2-TiO_2 (400 °C) pristine	62.9	64.6	66.1	459.1
3S-FTO-2-TiO_2 (400 °C) (EC)	62.5	63.8	65.1	458.9
3S-FTO-5-TiO_2 (400 °C) pristine	62.0	63.2	64.4	458.1
3S-FTO-5-TiO_2 (400 °C) (EC)	62.1	63.3	64.6	458.5
3S-FTO-20-TiO_2 (400 °C) pristine	61.8	62.9	64.0	458.3
3S-FTO-20-TiO_2 (400 °C) (EC)	61.9	63.1	64.3	458.6
1S-ATO pristine	62.4	63.5	--	--
1S-ATO on FTO electrode pristine	63.2	64.6	--	--
1S-ATO on FTO electrode (EC)	62.6	64.4	--	--
1S-ATO-5-TiO_2 pristine	62.4	63.2	--	459.0
1S-ATO-5-TiO_2 on FTO electrode pristine	62.8	64.0	--	459.0

Table B.1 continued

Sample	Binding energy (eV)			
	Ir 4f7 (1)	Ir 4f7 (2)	Ir 4f7 (3)	Ti 2p
1S-ATO-5-TiO_2 on FTO electrode (EC)	62.8	64.0	--	459.0
3S-ATO pristine	62.2	63.5	--	--
3S-ATO on FTO electrode pristine	62.8	64.5	--	--
3S-ATO on FTO electrode (EC)	62.3	63.3	64.7	--
3S-ATO-5-TiO_2 pristine	62.2	63.5	--	458.9
3S-ATO-5-TiO_2 on FTO electrode pristine	62.4	64.1	--	458.8
3S-ATO-5-TiO_2 on FTO electrode (EC)	62.1	64.1	--	458.5

Table B.2. The summary of the Ir:Sn and Ti:Sn on Ir-FTO and Ir-ATO sample before and after electrochemical (EC) testing.

Sample	Ir:Sn (atom. %)		Ti:Sn (atom. %)	
	before EC	after EC	before EC	after EC
1S-FTO	5.7 ± 0.3	3.9 ± 1.1		
3S-FTO	38.5 ± 5.7	56.3 ± 0.7		
1S-FTO-5-TiO_2	15.2 ± 2.0	5.5 ± 0.5	14.7 ± 0.4	9.1± 1.4
3S-FTO-5-TiO_2	110.9 ± 9.3	76.6 ± 2.4	77.8 ± 3.8	10.4 ± 1.1
3S-FTO-2-TiO_2	102.7 ± 30.3	49.5 ± 26.9	22.8 ± 2.3	0
3S-FTO-20-TiO_2	42.3 ± 2.1	113.7 ± 14.2	181.9 ± 11.1	142.7 ± 12.2
3S-FTO-2-TiO_2 (400 ℃)	74.7 ± 4.7	46.5 ± 18.6	14.5 ± 2.7	3.3 ± 0.7
3S-FTO-5-TiO_2 (400 ℃)	44.9 ± 4.6	80.0 ± 12.0	36.9 ± 1.3	36.1 ± 2.9
3S-FTO-20-TiO_2 (400 ℃)	46.9 ± 2.0	79.8 ± 6.3	114.3 ± 7.9	156.9 ± 8.3
1S-ATO	7.2 ± 0.1	6.4 ± 0.1		
3S-ATO	12.3 ± 0.7	12.9 ± 1.0		
1S-ATO-5-TiO_2	6.7 ± 0.2	6.8 ± 0.3	3.0 ± 0.1	2.7 ± 0.3
3S-ATO-5-TiO_2	20.6 ± 0.1	5.1 ± 0.5	15.3 ± 1.7	2.2 ± 0.2

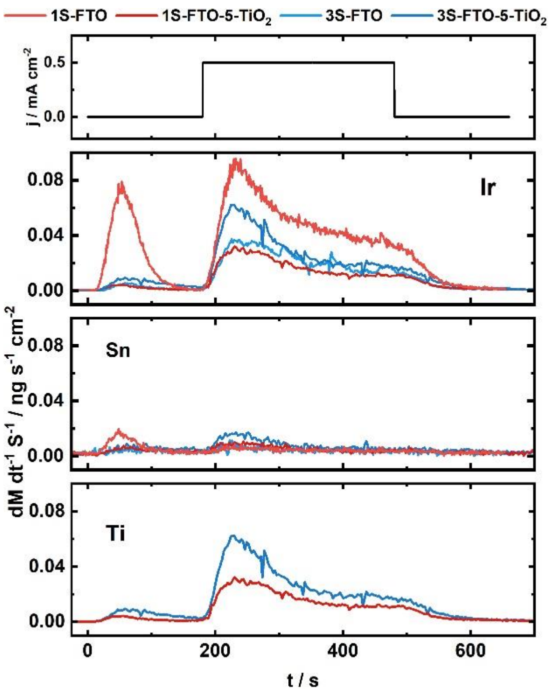

Figure B.6. Dissolution profiles of Ir, Sn and Ti for 1S-FTO, 3S-FTO, 1S-FTO-5-TiO2 and 3S-FTO-5-TiO2 catalysts during initial contact at OCP and galvanostatic hold at 0.5 mA·cm^{-2}.

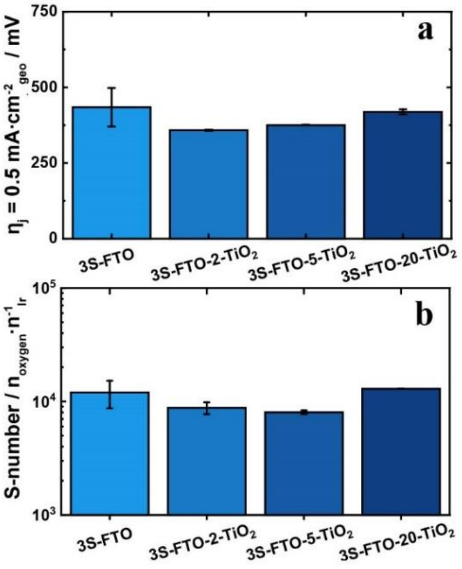

Figure B.7. a) Compilation of oxygen evolution reaction overpotentials (η) for the different Ir-based catalysts measured at geometric current densities of 0.5 mA·cm^{-2}. Overpotential values presented on the figure were taken at the end of the chronopotentiometry measurements, where samples reached steady-state operation. b) S-numbers of different Ir-based catalysts prepared in this work. S-numbers values are calculated from a galvanostatic hold at 0.5 mA·cm^{-2}.

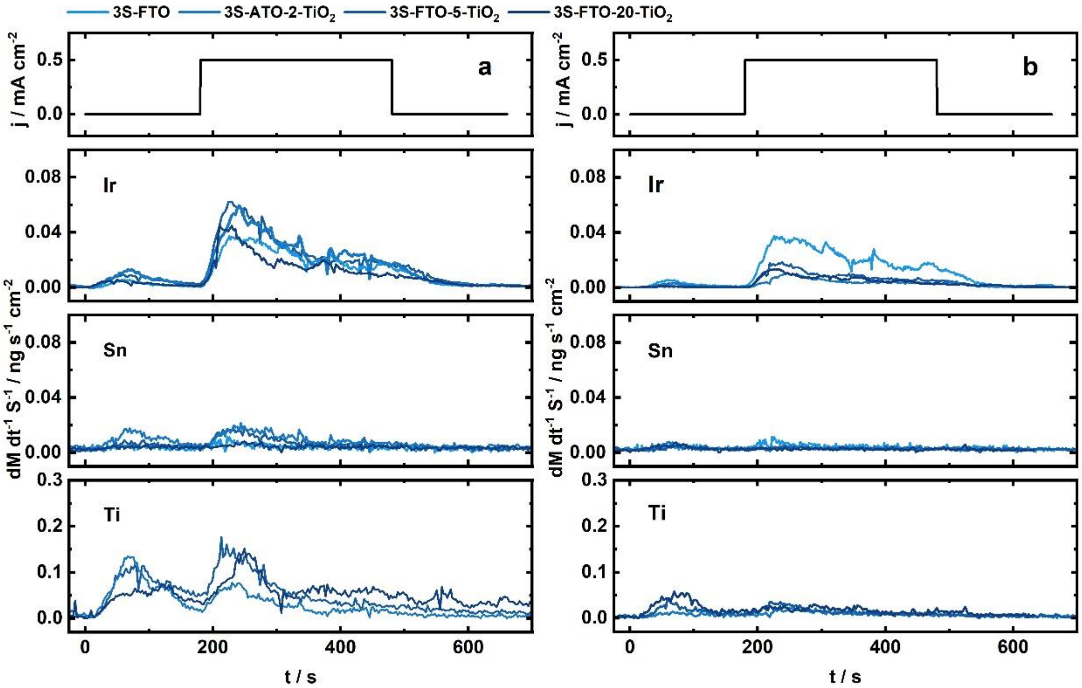

Figure B.8. Dissolution profiles of Ir, Sn and Ti for a) 3S-FTO, 3S-FTO-2-TiO$_2$, 3S-FTO-5-TiO$_2$, 3S-FTO-20-TiO$_2$ and b) 3S-FTO, 3S-FTO-2-TiO$_2$ (400 °C), 3S-FTO-5-TiO$_2$ (400 °C), 3S-FTO-20-TiO$_2$ (400 °C) catalysts during initial contact at OCP and galvanostatic hold at 0.5 mA·cm^{-2}.

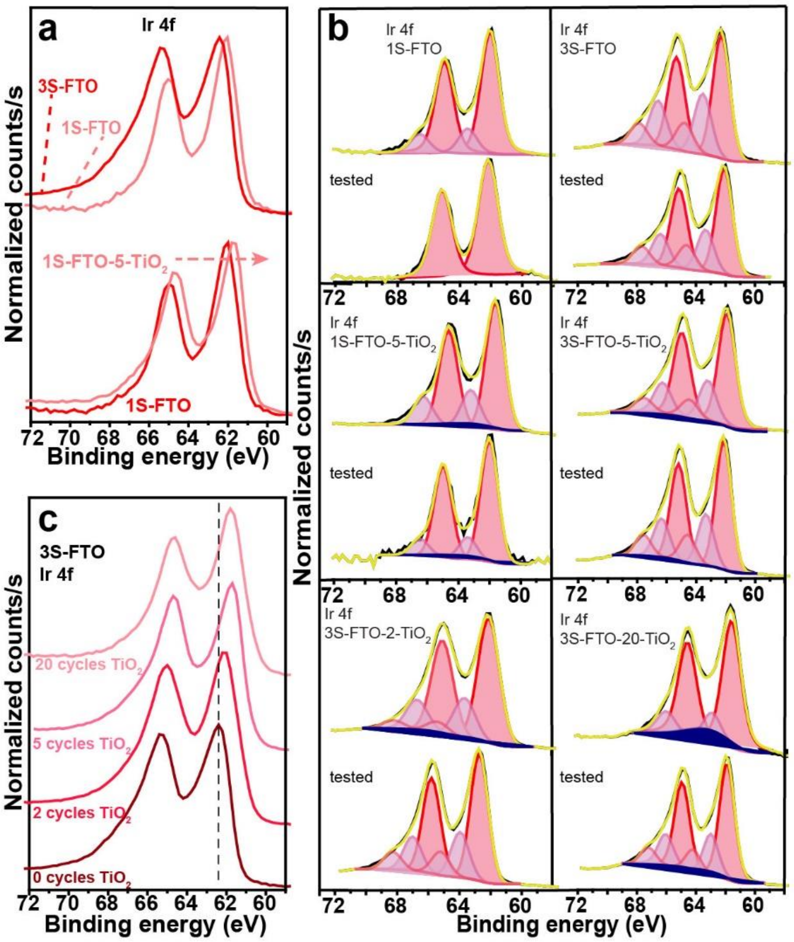

Figure B.9. XPS analysis of Ir-functionalized FTO substrates. a) Ir 4f spectra of 1S-FTO vs 3S-FTO and 1S-FTO vs 1S-FTO vs 1S-FTO-5-TiO_2. The high binding energy edge of the 3S-FTO spectrum has a raised background originating from inelastic electron scattering resulting from ejecting electrons travelling through layers of material. The Ir 4f peak (1S-FTO) shifts to lower binding energy upon TiO_2 addition. b) XP spectra of Ir 4f peak before and after a 0.5 mA·cm^{-2} hold in 0.1 M $HClO_4$. Ti 3s peak in shown in dark blue. c) The binding energy of Ir 4f (3S-FTO) shifts to lower values as the number of TiO_2 cycles increases.

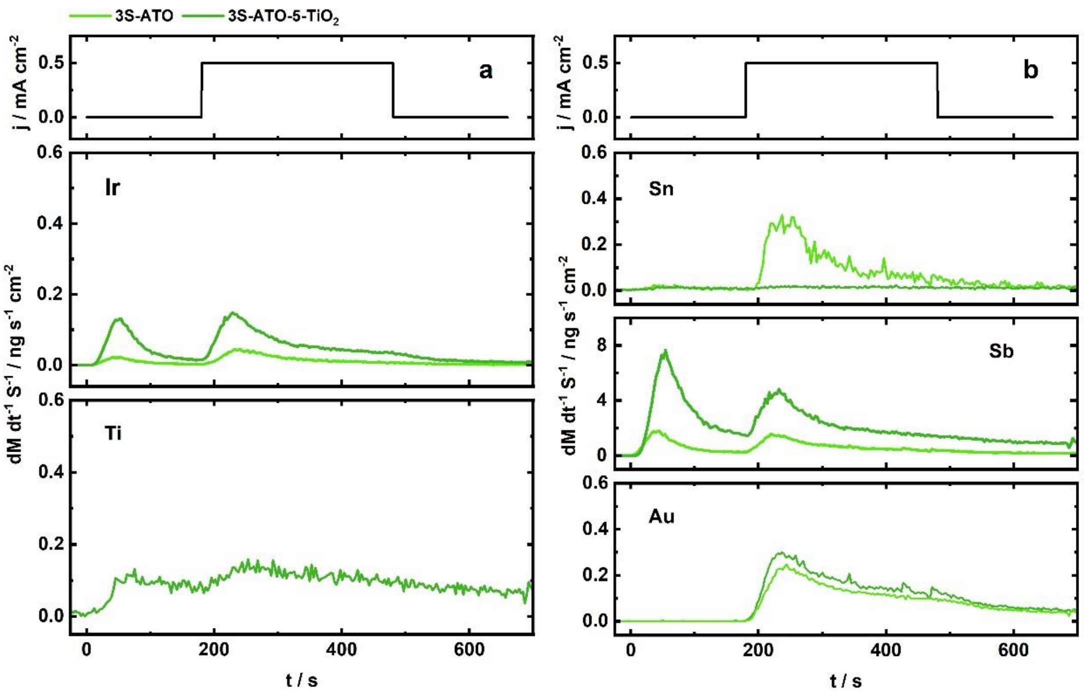

Figure B.10. Dissolution profiles of a) Ir, Ti and b) Sn, Sb, Au for samples 3S-ATO and 3S-ATO-5-TiO_2 catalysts during initial contact at OCP and galvanostatic hold at 0.5 mA·cm^{-2}.

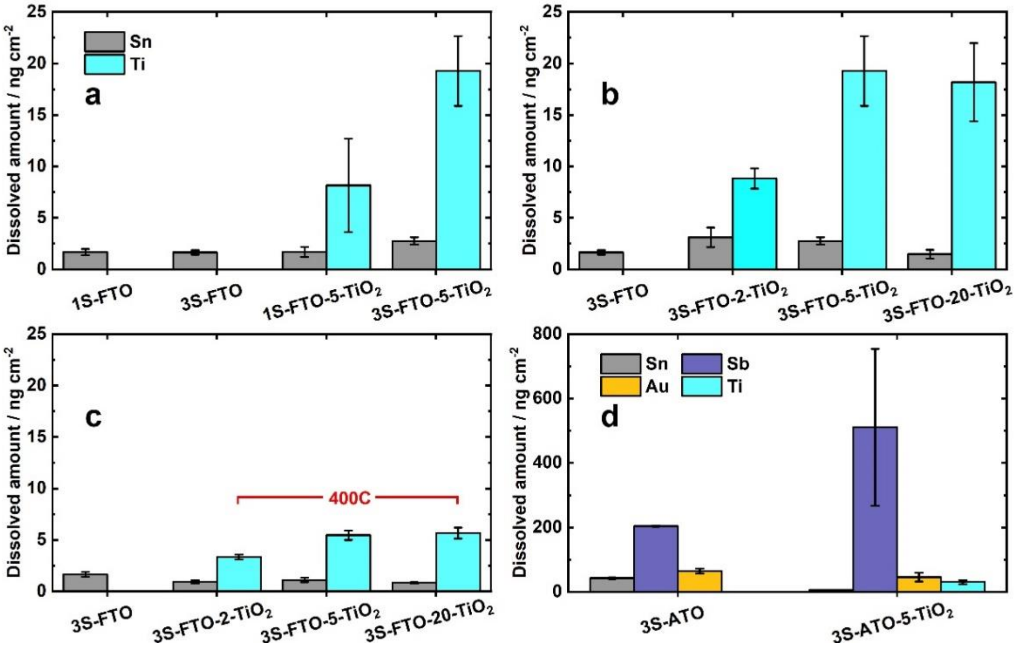

Figure B.11. Amount of dissolved metal for a) 1S-FTO, 3S-FTO, 1S-FTO-5-TiO_2, 3S-FTO-5-TiO_2 b) 3S-FTO, 3S-FTO-2-TiO_2, 3S-FTO-5-TiO_2, 3S-FTO-20-TiO_2, c) 3S-FTO, 3S-FTO-2-TiO_2 (400 ℃), 3S-FTO-5-TiO_2 (400 ℃), 3S-FTO-20-TiO_2 (400 ℃) and d) 3S-ATO and 3S-ATO-5-TiO_2 catalysts during galvanostatic hold at 0.5 mA·cm^{-2}.

Table B.3. The thickness of TiO_2 layer after ALD deposition of 2, 5, and 20 cycles at selected temperatures measured on a witness Si wafer.

T (℃)	# of cycles	thickness of SiO_2 (nm)	thickness of TiO_2 (nm)	MSE (nm^2)
150	2	3.0	0.14	0.049
150	5	3.2	0.36	0.049
150	20	2.8	1.18	0.028
250	5	2.9	0.23	0.044

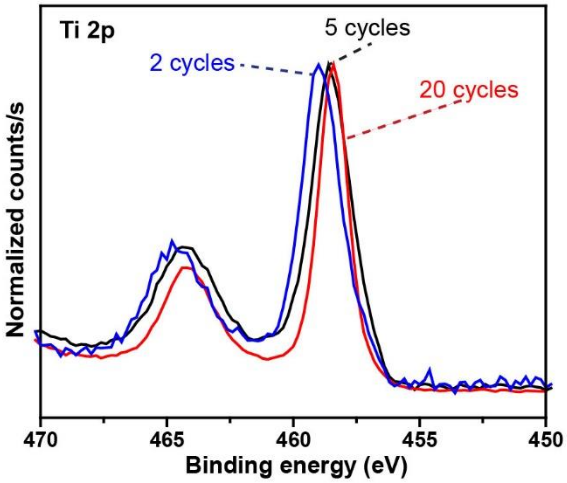

Figure B.12. XP spectra of Ti 2p taken on pristine 3S-FTO substrates after depositing 2, 5, and 20 cycles of TiO_2 by ALD. The binding energy of Ti 2p in the pristine 1S-FTO-5-TiO_2 and 3S-FTO-5-TiO_2 is consistent with Ti (IV) (458.6 ± 0.2 eV).[1]

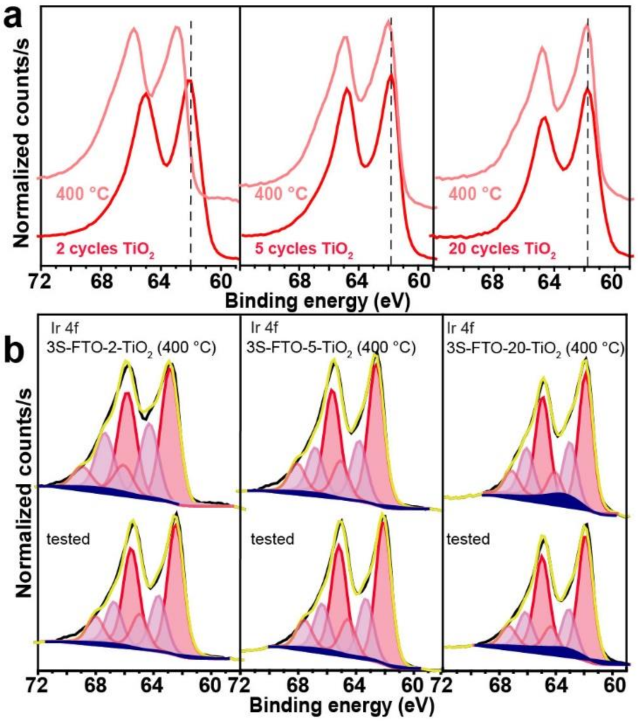

Figure B.13. XPS analysis of the post-ALD annealed Ir-FTO samples. a) The binding energy of Ir 4f for the post-ALD annealed samples shifted up for 3S-FTO-2-TiO$_2$ and 3S-FTO-5-TiO$_2$ but remained the same for 3S-FTO-20-TiO$_2$. b) Ir 4f peaks with fits for pristine and tested post-ALD annealed samples. The XPS analysis shows almost an eV shift to higher binding energy of Ir 4f upon 400 °C annealing for 3S-FTO-2-TiO$_2$. The shift is much smaller for 3S-FTO-5-TiO$_2$ (~0.3 eV for Ir 4f); almost no shift in energy for 3S-FTO-20-TiO$_2$. The shift might originate from new bond formation between Ir and Ti. However, the energy of Ti 2p does not change after annealing regardless of TiO$_2$ thickness.

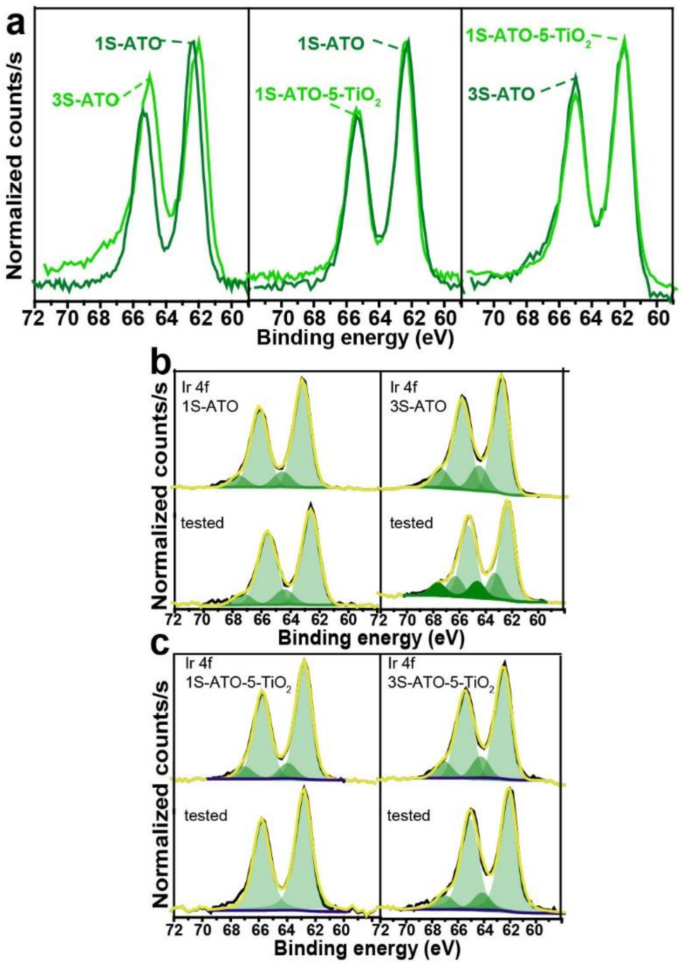

Figure B.14. XPS analysis of Ir-functionalized ATO. a) Ir 4f spectra for ATO nanopowder after 1 and 3 soaks in Ir precursor solution and after ALD deposition of 5 cycles of TiO_2. b,c) Fitted Ir 4f spectra taken on the electrodes before and after electrochemical testing. The proximity of Ir-ATO to the FTO electrode resulted in Ir 4f shifting to higher binding energy. XPS analysis was carried out on pristine powders dispersed on FTO as well. Almost no Ir was lost during testing of 1S-ATO and 1S-ATO-5-TiO_2 with the loss of TiO_2 observed for the TiO_2-protected sample (Table B.2). The 3S-ATO samples also loses very little Ir consistent with ICP-MS results. The 3S-ATO protected by TiO_2, however, loses significant amount of Ir while being more active towards OER than 3S-ATO (Figure B.10). Ti dissolution is also observed (Figure B.11d).

APPENDIX C

CHAPTER IV SUPPORTING INFORMATION

Table C.1. Measured thicknesses of the ionomer films.

Ionomer	wt. %	Calculated from film mass (QCM) and density (nm)	Measured by profilometer (nm)
Aemion	5	348 ± 14	335 ± 29
Sustainion	5	341 ± 6	300 ± 26
PiperION	5	473 ± 25	425 ± 37
Aemion	0.16	17.7 ± 1.4	-
Sustainion	0.16	8.8 ± 1.1	-
PiperION	0.16	11.7 ± 1.4	-

Table C.2. The size (pm), hydration energy (kJ/mol), number of water molecules in the hydrations shell, and the geometry of the anions used in the current study.[1-2]

Anion	Size (pm)	Hydration energy (kJ/mol)	Number of water molecules in the hydration shell	Geometry
OH^-	133	-430	3	Linear
CO_3^{2-}	178	-1315	4	Trigonal planar
HCO_3^-	158	-335	2	Trigonal planar
H_3BO_3	-	Small*	4	Trigonal planar (w/respect to B)

* DFT calculations predict weak H-bonding[1]

Table C.3. XPS data summary for the ionomer films tested in the three supporting electrolytes under various applied potentials.

	Electro-lyte	**Overpotential (mV)**	**C1**	**C2**	**C3**	**C4**	**C5**	**N1**	**N2**	**N3**	**F**
Aemion	Initial	0	284.8	286.2	287.4			398.3	400.0	401.4	
	KOH	400	284.8	286.3	287.4			398.6	400.6	401.7	
		500	284.8	286.3	287.7			398.3	400.1	401.5	
		600	284.8	286.2	287.4			398.4	400.6	401.5	
		700	284.8	286.4	287.7			398.2	400.4	401.7	
	Carbonate	400	284.8	286.3	287.4			398.3	399.9	401.3	
		500	284.8	286.3	287.8			398.0	399.4	401.3	
		600	284.8	286.2	288.2			398.4	400.3		
		700	284.8	286.2	287.7	288.8			399.1		
	Borate	400	284.8	286.2	287.4			397.3	399.8	401.3	
		500	284.8	286.2	287.4			398.5	400.6	401.6	
		600	284.8	286.3	287.4			398.6	400.1	401.6	
		700	284.8	286.4	287.9			398.7	400.2	401.5	
Sustainion	Initial	0	284.8	285.9	286.9			399.7		401.5	
	KOH	400	284.8	285.9	286.9			398.2	400.0	401.6	
		500	284.8	286.4	287.2	287.9		398.3	399.9	401.6	
		600	284.8	286.3	287.4			398.7	400.1	401.6	
		700	284.8	286.4	287.8			398.1	399.9	401.6	
	Carbonate	400	284.8	286.2	287.4			398.2	400.2	401.6	
		500	284.8	286.2	287.4			397.7	399.8	401.4	
		600	284.8	286.2				398.0	399.9	401.6	
		700	284.8	286.2	288.9			398.4	400.0	401.1	
	Borate	400	284.8	285.9	286.9			398.0	400.0	401.5	
		500	284.8	285.9	286.8			398.2	400.1	401.6	
		600	284.8	285.7	286.7			398.3	399.9	401.5	
		700	284.8	285.9	286.7			398.1	399.9	401.6	
PiperION	Initial	0	284.8	285.9	286.7					402.7	688.7
	KOH	400	284.8	285.9	286.7					402.8	688.2
		500	284.8	285.8	286.8					402.6	688.2
		600	284.8	285.7	286.7					402.8	688.3
		700	284.8	285.8	286.7					402.8	688.2
	Carbonate	400	284.8	285.7	286.7			398.0	400.0	402.7	688.4
		500	284.8	285.7	286.7					402.9	688.3
		600	284.8	285.9	287.2					402.7	688.1
		700	284.8	285.9	286.7			398.3			688.2
	Borate	400	284.8	285.7	286.7					402.7	688.2
		500	284.8	285.7	286.7					402.8	688.3
		600	284.8	285.8	286.7					402.8	688.3
		700	284.8	285.9	286.7	287.7	288.8			402.6	688.0

Table C.4. Conductivities of Aemion, Sustainion, and PiperION membranes in OH^-, HCO_3^-, and CO_3^{2-} forms summarized from references. We hypothesize that the trends measured on thick membranes will translate to thin ionomer films and ionomer-catalyst composites in the anode reaction zone of an electrolyzer.

Membrane	Conductivity (σ; mS/cm) of AEMs with different counter-ions at room temperature			From manufacturer's datasheet (OH^-)	References
	OH^-	HCO_3^-	CO_3^{2-}		
Aemion (HMT-PMBI)	10.0	3.8	2.0	> 80 (for AF1-HNN8-50-X; temperature not specified)	Wright, A. G. *et al. Energy Environ. Sci.* **2016**, *9* (6), 2130-2142.
Sustainion (X24)	64	24	-	111 (Sustainion-X37; 50 °C); 130 (Sustainion-X37; 70 °C)	Liu, Z. *et al. J. Electrochem. Soc.* **2018**, *165* (15), J3371-J3377.
PiperION (PAP-TP-85)	58	6	5	150 (PiperION-A; at 80 °C)	Luo, X. *et al. J. Membr. Sci.* **2020**, 598, 117680.

Processing of the ionomer solutions into thin films and preparing them for electrochemical analysis

The manufacturers of every solid anion-exchange membrane suggest specific preconditioning of their solid membrane for optimal performance. The solid membranes are usually several microns thick and require prolonged soaking in the suggested solutions to ion-exchange the membrane for the anions that will not have a negative effect on the AEMWE operation. The liquid versions of the solid AEMs, ionomers, that are mixed with the catalyst powders and spray-coated onto GDLs or the membrane itself are commonly simply dried but not soaked in any solution before or after drying. In our study of the ionomer thin films, we treated the films very similarly to the processing of the solid membranes suggested by the manufacturers of the ionomers/membranes. We do not believe that preconditioning of the thin films is as important as it is for the thicker solid membranes, but we still did our best to exclude any potential damage to the ionomer films structures from processing.

Aemion ionomer solution in ethanol comes in a mixed Cl^-/I^- form. Cl^- readily exchanges for OH^- but I^- does not, which later can cause performance loss in the electrolyzer. The current preconditioning procedure suggested by Ionomr is to soak the membrane in 3 M KOH to facilitate a full ion-exchange. Another way to get rid of I^- is to soak the Cl^-/I^- membrane in 1 M NaCl and then soak it in 1 M KOH. Given that we used very thin ionomer films, we simplified this procedure to the 1 M NaCl soak after the spin-coated film is dried. We have compared the stability of the Aemion films that were only soaked in NaCl to the films that were soaked in NaCl and then in KOH. We did not observe differences (see Figure C.2). We also analyzed if ion-exchanging the films back into Cl^- after electrochemical testing before drying would decrease the observed degradation (Figure C.3). The films were soaked in 1 M NaCl immediately after electrochemical testing in 1 M KOH and 1 M carbonate/bicarbonate buffer at η = 500 mV, then rinsed, and dried. We observed very similar changes to the structures of the tested films: dissolution and changes to the N 1s peak shape.

Sustainion thin films were soaked in 1 M KOH for one hour (as suggested by Dioxide Materials) after spin-coating and drying on a hot plate at 80°C. To ensure that drying in OH^- form did not affect our results, we tested Sustainion films at η = 500 mV in 1 M KOH and 1 M carbonate/bicarbonate buffer again, but this time we soaked the films in KOH right before electrochemical testing and in 1 M NaCl immediately after testing and before drying. Figure C.4a shows that the structure loses the C-N component in the C 1s spectra when tested in 1 M carbonate/bicarbonate buffer regardless of the preconditioning method. The shape of the N 1s peak changes to decrease the contribution from the N^+ component for both methods. The XPS of the films tested in KOH (Figure C.4b) shows a similar decrease of the N/C ratio from 6 to 3-4% for both conditioning methods along with the change in the N 1s peak shape. The C-N component loss in the C 1s spectrum of the Cl^--exchanged films was less pronounced than in the films dried in the OH^- form, but the peaks representing the C-N bonds shifted by 0.5 eV similarly to the films treated with the KOH soak.

PiperION ionomer solution comes in HCO_3^- form. For the solid membrane it is recommended to soak the membrane in 0.5 M NaOH before use. In addition, PiperION is susceptible to degradation via Hoffman Elimination if dried in the hydroxyl form (as water is removed, the hydration shell of the hydroxide ion is reduced increasing its nucleophilicity; bicarbonate could also degrade into hydroxide and CO_2 at elevated temperatures, e. g. > 80°C) (see Figure 4.3 for the hypothesized chemical and electrochemical degradation routes for PiperION). To prevent degradation induced by drying, the ionomer films were soaked in 1 M HCl (three-minute soak for the films < 10 nm and five-minute soak for the films spin-coated from the 5 wt. % solution) to quench any residual KOH and convert the ionomer counter-ion to Cl^-: the form that can be dried without triggering Hoffman Elimination. This procedure was suggested by Versogen to the authors. The data shown in this manuscript for PiperION was collected by conducting an HCl soak each time before the films were dried. We did not follow the HCl soak with the NaOH soak for our < 10 nm films. See Figure C.3 for the XPS data collected for the PiperION films tested in 1 M K_2CO_3/$KHCO_3$ buffer pH 10 that were treated with HCl and NaOH before electrochemical testing. The thicker PiperION films spin-coated from 5 wt. % ionomer solution were soaked in 1 M HCl for five minutes before annealing and also soaked in 0.5 M NaOH for 30 minutes immediately before they were tested electrochemically without additional drying.

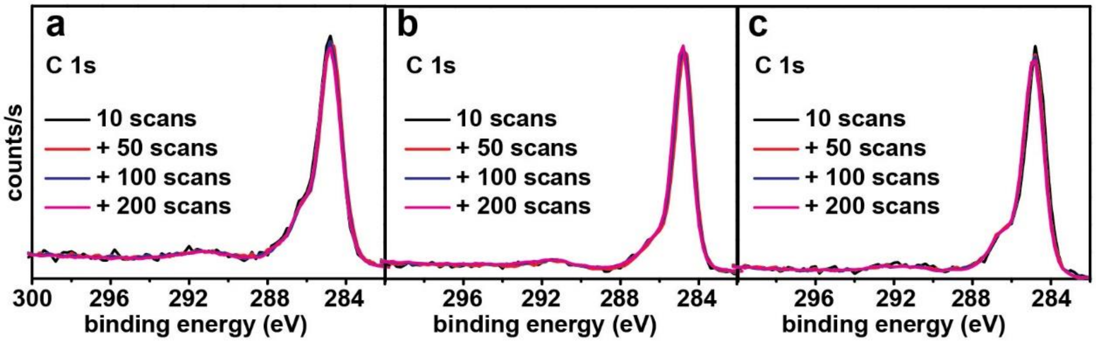

Figure C.1. XPS spectra of C1s for a) Aemion, b) Sustainion, and c) PiperION thin films spin-coated from 0.16 wt. % solutions on Pt substrates. The scans are taken on the same spot to determine if there is any damage to the films by the beam. The total number of scans on each spot is 360 at the pass energy of 20 eV. The average number of scans used for the film analysis presented in this paper was ~300.

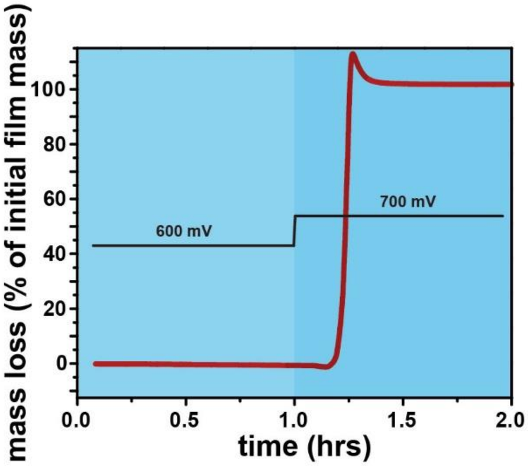

Figure C.2. The mass loss for Aemion film that was preconditioned in 1 M NaCl for one hour after spin-coating and drying, then in 1 M KOH for 30 minutes prior to testing in 1 M K_2CO_3/$KHCO_3$ buffer pH 10. After holding the film at open circuit voltage for 15 minutes, η = 600 mV and then 700 mV were applied for one hour each. The film completely came off the QC at η = 700 mV. Aemion film that we tested in 1 M K_2CO_3/$KHCO_3$ buffer pH 10 after preconditioning it only in NaCl behaved identically. Thus, we believe our process of preconditioning Aemion ionomer films did not have a negative effect on their stability.

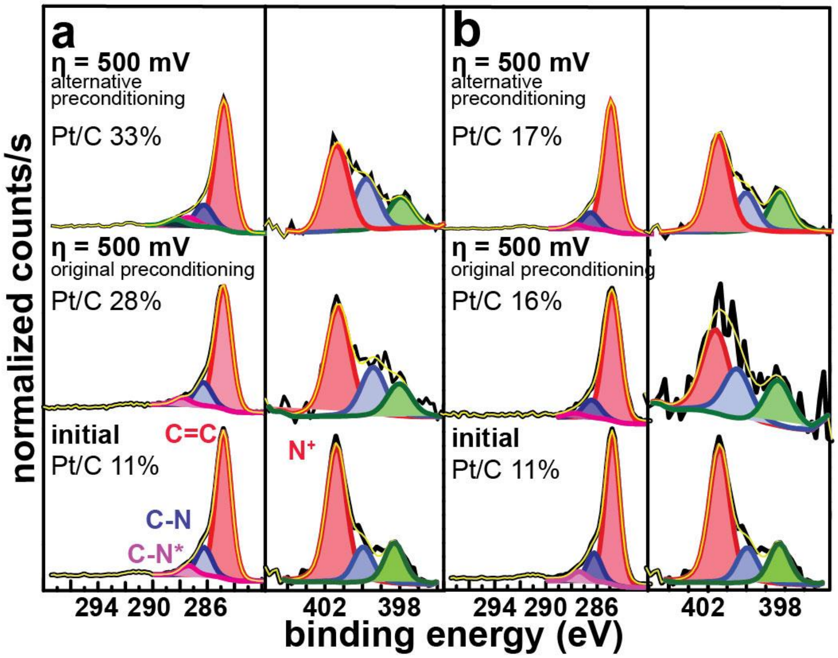

Figure C.3. XPS of Aemion films tested at η = 500 mV in a) pH 10, 1 M carbonate/bicarbonate buffer and b) 1 M KOH. Similar changes to the film structure were observed after two methods of preconditioning: the films were observed to dissolve, and the N 1s peak changed shape with the N^+ component decreasing in intensity.

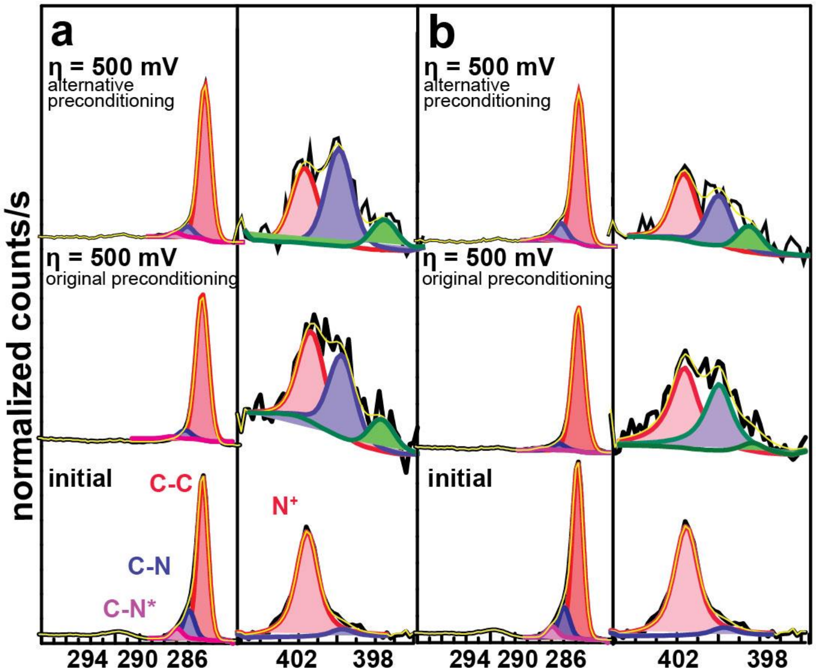

Figure C.4. XPS of Sustainion films tested at η = 500 mV in a) pH 10, 1 M carbonate/bicarbonate buffer and b) 1 M KOH after being preconditioned using two different methods.

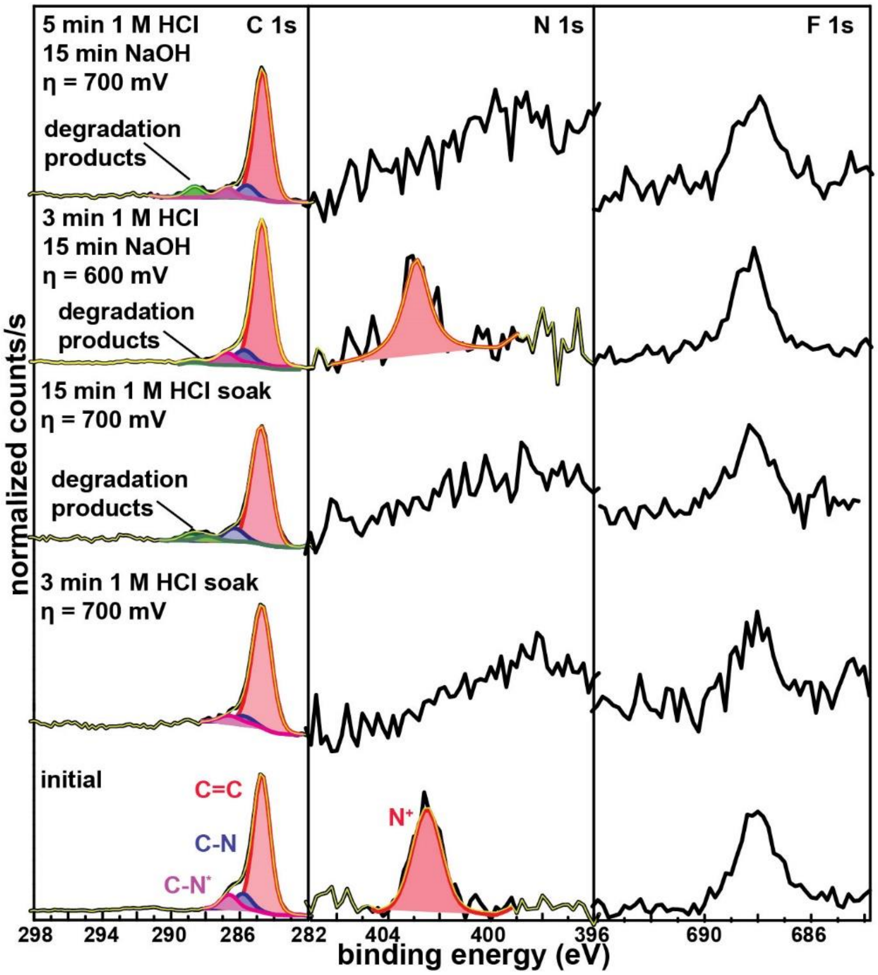

Figure C.5. Bottom panel: C 1s, N 1s, and F 1s XP spectra of a pristine PiperION film. Second and third panel from the bottom compares XPS of PiperION thin films tested at η = 700 mV in 1 M K_2CO_3/$KHCO_3$ buffer pH 10 after a three-minute and a fifteen-minute HCl soaks. The same degree of film loss and N 1s peak change was observed. Top two panels: XPS of PiperION thin films tested in 1 M K_2CO_3/$KHCO_3$ buffer pH 10 at η = 600 and 700 mV after a three-minute soak in 1 M HCl and a fifteen-minute soak in 0.5 M NaOH. The films degraded similarly to the films that were not soaked in 0.5 M NaOH prior to testing.

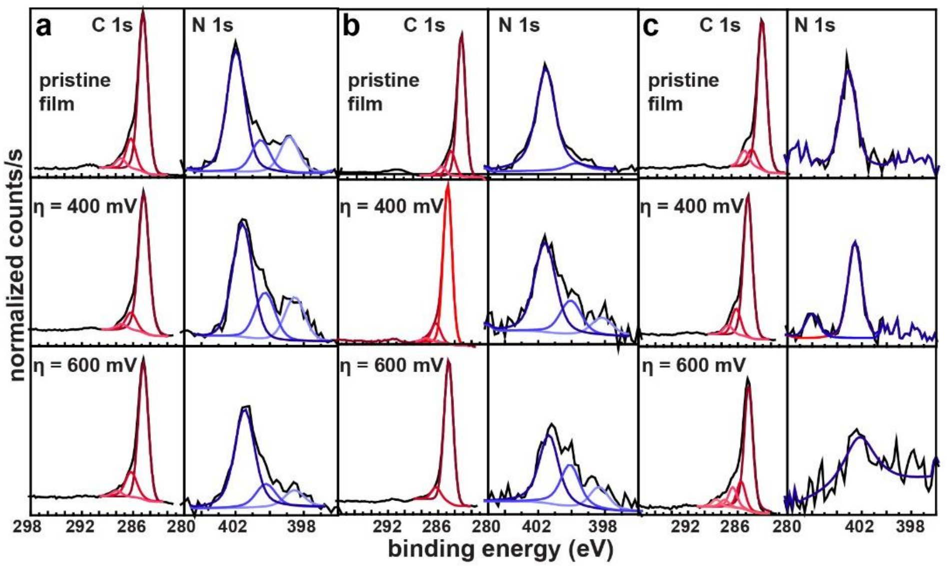

Figure C.6. C 1s and N 1s XP spectra of ionomer films tested in 0.1 M $HClO_4$ at η = 400 and 600 mV for (a) Aemion, (b) Sustainion, and (c) PiperION.

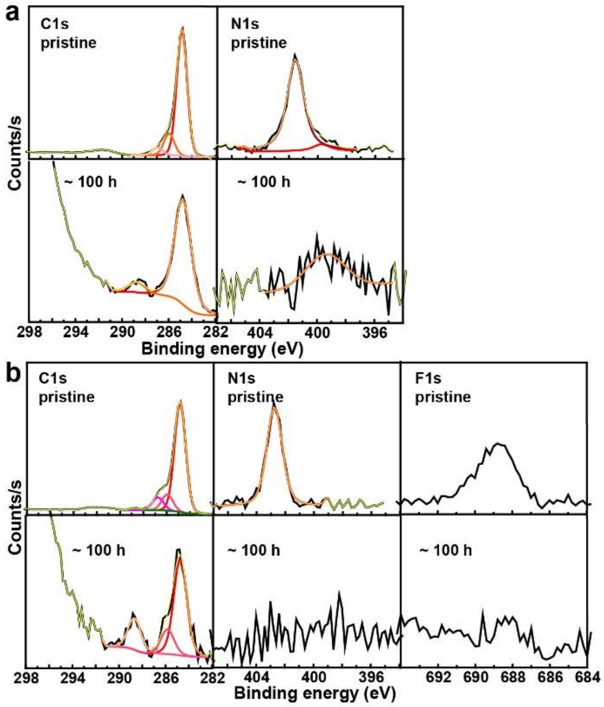

Figure C.7. XP spectra collected from the anode GDLs run in a pure-water-fed AEMWE for ~ 100 h at 0.5 $A\cdot cm^2$ with IrO_2 and a) Sustainion or b) PiperION ionomers. Ionomers sustained significant damage.

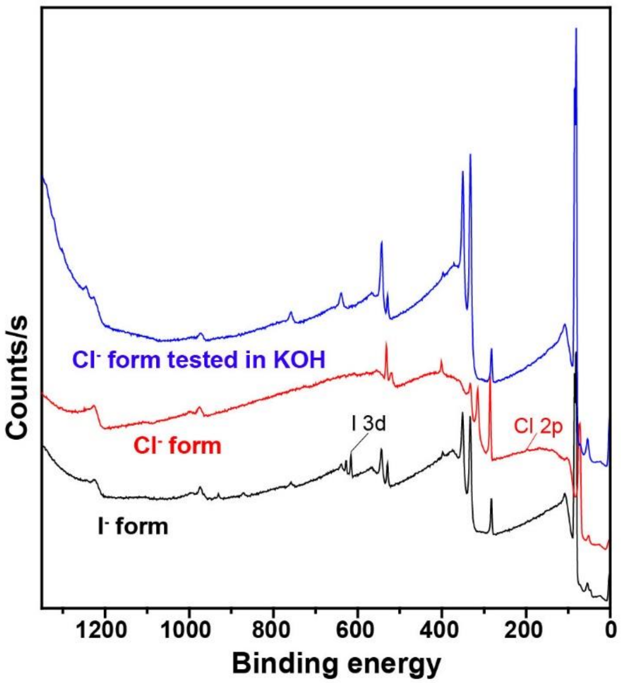

Figure C.8. Survey XP spectra of Aemion films spin-coated from ionomer solution in EtOH (black), ion-exchanged in 1 M NaCl for 1 h (red), and tested in 1 M KOH after being ion-exchanged in 1 M NaCl (blue). I^- seems to leave the film during ion-exchange process. Once the film is tested in KOH, Cl^- exchanges for OH^-.

APPENDIX D

CHAPTER VI SUPPORTING INFORMATION

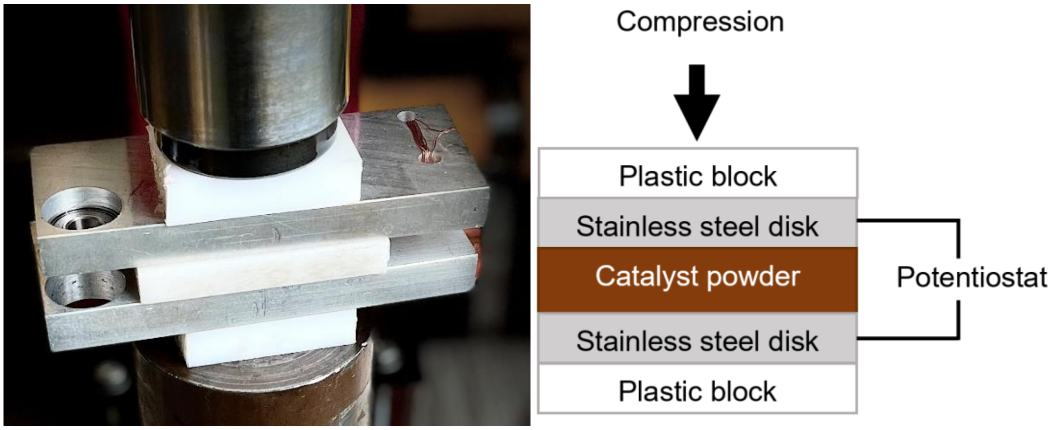

Figure D.1. Conductivity measurement experimental setup.

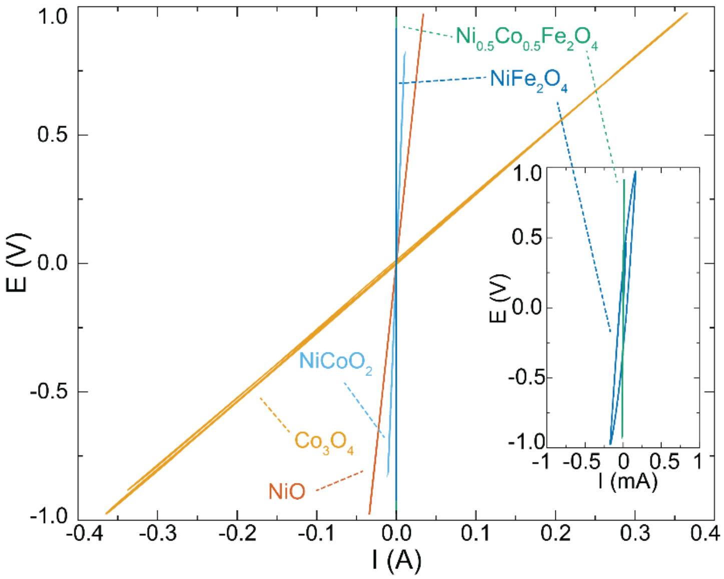

Figure D.2. Cyclic voltammetry plots of measured catalyst powders.

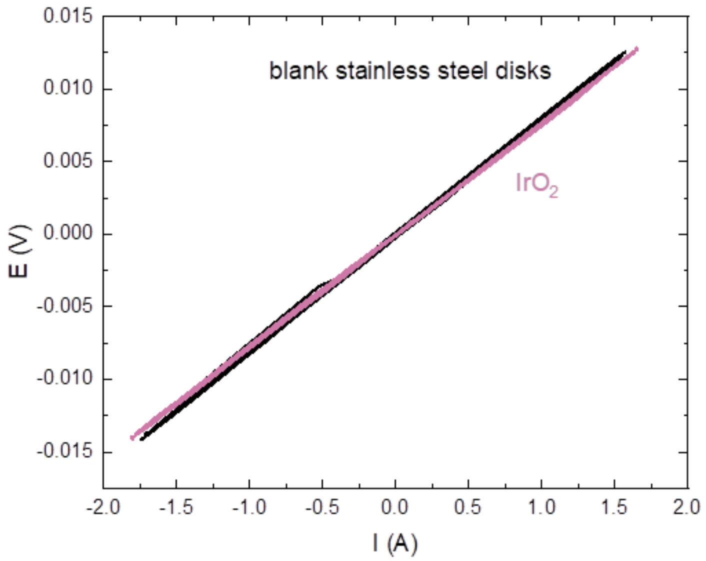

Figure D.3. Conductivity measurement of IrO_2 compared to the contact resistance measured between the two stainless steel disks.

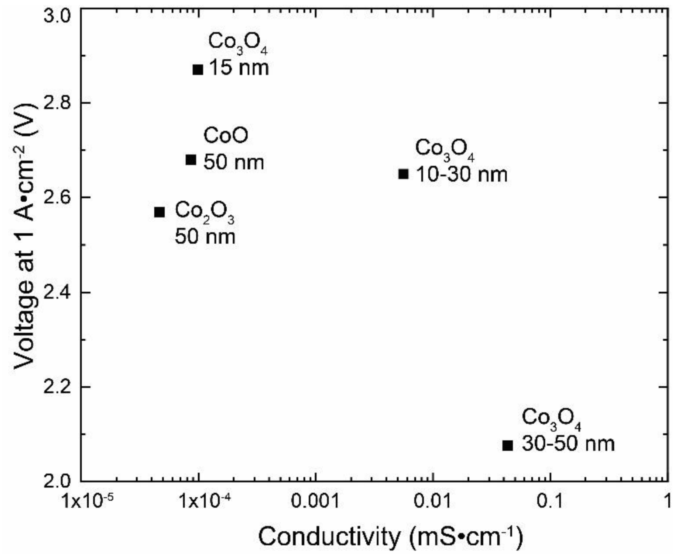

Figure D.4. Effect of catalyst layer conductivity on voltage performance for various Co-based anode catalysts. The indicated catalyst was sprayed in an ink with ionomer onto a glass slide and dried at 80 °C.

It should be noted, the conductivity in Figure D.4 is significantly lower than that in Figure 6.2. The conductivity in Figure D.4 is a measurement of the uncompressed catalyst layer sprayed onto a glass slide, while the conductivity measurements in Figure 6.2 are of the catalyst powder only.

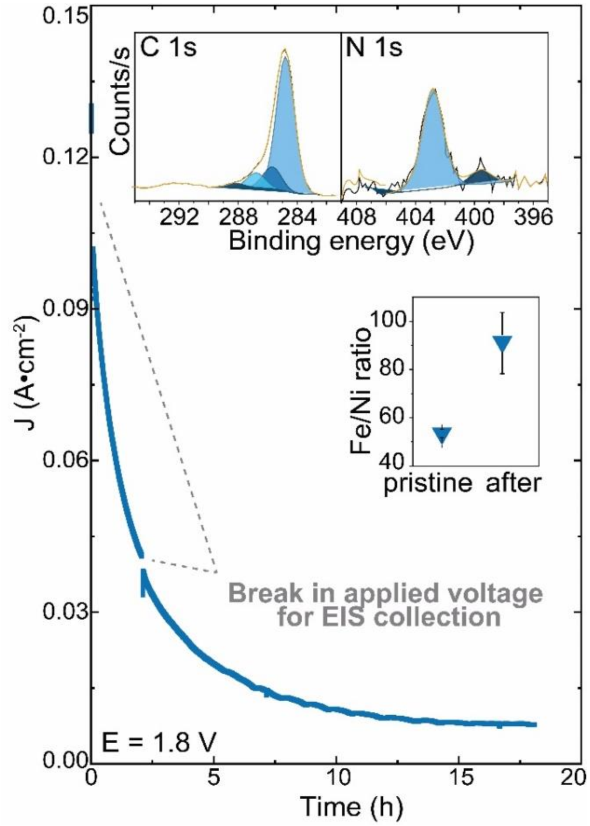

Figure D.5. Chronoamperometric durability testing of $NiFe_2O_4$ catalyst. $NiFe_2O_4$ was operated at 1.8 V with pure water at 57 °C. A stainless steel woven substrate was used as the anode GDL and Pt Black catalyst on Toray carbon paper was used as the cathode. The Fe/Ni ratio increases from 0.54 ± 0.2 to 0.91 ± 0.11 following the trend observed for the 20-hour electrolyzer run held at 500 $mA\cdot cm^2$ where the Fe/Ni ratio increased to 1.1 ± 0.07 (Figure 6.5a).

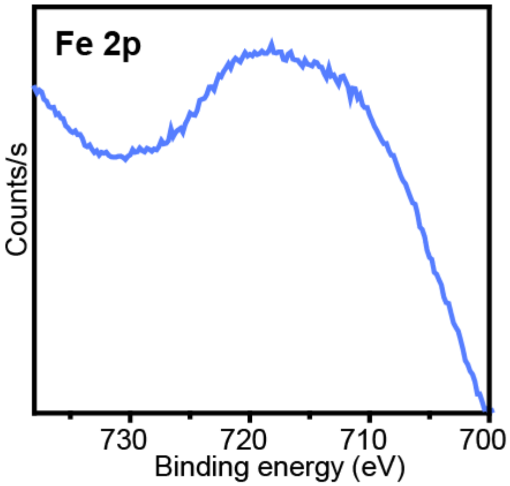

Figure D.6. Fe XPS data of the cathode GDL surface post Fe-spike experiment. No Fe is detected indicating the observed degradation is not due to Fe crossing the membrane to the cathode.

Supplemental Materials and Methods

Catalyst Dispersions and Electrolyzer Operation. Co_3O_4 (99.9%, 15 nm), Co_3O_4 (99%, 10-30 nm), Co_3O_4 (>99.5%, 30-50 nm), Co_2O_3 (50 nm, US Nano) and CoO (50 nm, US Nano) nanoparticles were used at the anode. Cathode and anode inks were prepared identically to all experiments described in the main text. For every 100 mg of catalyst, 0.5 g of water, 1.7 g of IPA and 200 mg of 5 wt % TP-85 (Versogen) ionomer was added. Catalyst inks were sonicated for 1 h to disperse. GDL coating and MEA testing was conducted identical to electrolyzer experiments in the main text.

Catalyst Layer Conductivity Measurements. Catalyst inks were sprayed on glass slides with a hand spray gun in a manner identical to GDL coating and dried at 80 °C. A polarization curve was measured using a source meter and the slope fit to obtain electrical resistance. Catalyst layer thickness was determined using a stylus profilometer. Electrical conductivity was calculated as described in the main text materials and methods.

REFERENCES CITED

CHAPTER II

(1) Cai, L.; Xu, H.; Chu, D. Compact Liquid Crystal Based Tunable Band-Stop Filter with an Ultra-Wide Stopband by Using Wave Interference Technique. *Int. J. Antennas Propag*. **2017**, *2017*, 1-11.

(2) Chen, Z.; Li, H.; Li, B.; He, Z.; Xu, H.; Zheng, M.; Zhao, M. Tunable Ultra-Wide Band-Stop Filter Based on Single-Stub Plasmonic-Waveguide System. *Appl. Phys. Express* **2016**, *9*, 1-4.

(3) Li, H. J.; Zhai, X.; Wujiaihemaiti, R.; Wang, L. L.; Li, X. F. Tunable Optical Filters and Multichannel Switches Based on MIM Plasmonic Nanodisk Resonators Inset a Silver Bar. *Phys. Scr.* **2015**, *90*, 1-6.

(4) Zhang, Z.; Yang, J.; He, X.; Han, Y.; Zhang, J.; Huang, J.; Chen, D. Plasmonic Filter and Demultiplexer Based on Square Ring Resonator. *Appl. Sci.* **2018**, *8*, 1-10.

(5) Wang, G.; Lu, H.; Liu, X.; Mao, D.; Duan, L. Tunable Multi-Channel Wavelength Demultiplexer Based on MIM Plasmonic Nanodisk Resonators at Telecommunication Regime. *Opt. Express* **2011**, *19*, 3513-3518.

(6) Nguyen-Huu, N.; Lo, Y. L. Tailoring the Optical Transmission Spectra of Double-Layered Compound Metallic Gratings. *IEEE Photonics J.* **2013**, *5*, 2700108, 1-9.

(7) Fleischman, D.; Sweatlock, L. A.; Murakami, H.; Atwater, H. Hyper-Selective Plasmonic Color Filters. *Opt. Express* **2017**, *25*, 27386-27395.

(8) Kyoung, J.; Hwang, S. W. Configurable Plasmonic Band-Pass Filters Operating under the Addition Rule. *ACS Photonics* **2016**, *3*, 819–827.

(9) Cheng, C.; Chen, J.; Wu, Q. Y.; Ren, F. F.; Xu, J.; Fan, Y. X.; Wang, H. T. Controllable Electromagnetic Transmission Based on Dual-Metallic Grating Structures Composed of Subwavelength Slits. *Appl. Phys. Lett.* **2007**, *91*, 1-3.

(10) Tanzid, M.; Sobhani, A.; DeSantis, C. J.; Cui, Y.; Hogan, N. J.; Samaniego, A.; Veeraraghavan, A.; Halas, N. J. Imaging through Plasmonic Nanoparticles. *Proc. Natl. Acad. Sci. U.S.A.* **2016**, *113*, 5558–5563.

(11) Noginov, M. A.; Gu, L.; Livenere, J.; Zhu, G.; Pradhan, A. K.; Mundle, R.; Bahoura, M.; Barnakov, Y. A.; Podolskiy, V. A. Transparent Conductive Oxides: Plasmonic Materials for Telecom Wavelengths. *Appl. Phys. Lett.* **2011**, *99*, 1-3.

(12) Lu, H.; Liu, X.; Mao, D.; Wang, L.; Gong, Y. Tunable Band-Pass Plasmonic Waveguide Filters with Nanodisk Resonators. *Opt. Express* **2010**, *18*, 17922-17927.

(13) Lu, H.; Liu, X.; Wang, G.; Mao, D. Tunable High-Channel-Count Bandpass Plasmonic Filters Based on an Analogue of Electromagnetically Induced Transparency. *Nanotechnology* **2012**, *23*, 1-6.

(14) Guo, Q.; Yao, Y.; Luo, Z. C.; Qin, Z.; Xie, G.; Liu, M.; Kang, J.; Zhang, S.; Bi, G.; Liu, X.; et al. Universal Near-Infrared and Mid-Infrared Optical Modulation for Ultrafast Pulse Generation Enabled by Colloidal Plasmonic Semiconductor Nanocrystals. *ACS Nano* **2016**, *10*, 9463–9469.

(15) Kriegel, I.; Scotognella, F. Tunable Light Filtering by a Bragg Mirror/Heavily Doped Semiconducting Nanocrystal Composite. *Beilstein J. Nanotechnol.* **2015**, *6*, 193–200.

(16) Lounis, S. D.; Runnerstrom, E. L.; Llordés, A.; Milliron, D. J. Defect Chemistry and Plasmon Physics of Colloidal Metal Oxide Nanocrystals. *J. Phys. Chem. Lett*. **2014**, *5*, 1564–1574.

(17) Agrawal, A.; Johns, R. W.; Milliron, D. J. Control of Localized Surface Plasmon Resonances in Metal Oxide Nanocrystals Keynote Topic. *Annu. Rev. Mater. Res.* **2017**, *47*, 1-31.

(18) Tandon, B.; Ghosh, S.; Milliron, D. J. Dopant Selection Strategy for High-Quality Factor Localized Surface Plasmon Resonance from Doped Metal Oxide Nanocrystals. *Chem. Mater.* **2019**, *31*, 7752–7760.

(19) Mortimer, R. J., Rosseinsky, D. R., Monk, P. M. S., *Electrochromic Materials and Devices*; Wiley-VCH Verlag GmbH & Co. KGaA: Weinheim, Germany, **2015**, 3-33.

(20) Kanehara, M.; Koike, H.; Yoshinaga, T.; Teranishi, T. Indium Tin Oxide Nanoparticles with Compositionally Tunable Surface Plasmon Resonance Frequencies in the Near-IR Region. *J. Am. Chem. Soc.* **2009**, *131*, 17736–17737.

(21) Lounis, S. D.; Runnerstrom, E. L.; Bergerud, A.; Nordlund, D.; Milliron, D. J. Influence of Dopant Distribution on the Plasmonic Properties of Indium Tin Oxide Nanocrystals. *J. Am. Chem. Soc.* **2014**, *136*, 7110–7116.

(22) Wang, Y.; Runnerstrom, E. L.; Milliron, D. J. Switchable Materials for Smart Windows. *Annu. Rev. Chem. Biomol. Eng.* **2016**, *7*, 283–304.

(23) Kasani, S.; Curtin, K.; Wu, N. A Review of 2D and 3D Plasmonic Nanostructure Array Patterns: Fabrication, Light Management and Sensing Applications. *Nanophotonics* **2019**, *8*, 2065-2089.

(24) Ghobadi, A.; Hajian, H.; Soydan, M. C.; Butun, B.; Ozbay, E. Lithography-Free Planar Band-Pass Reflective Color Filter Using A Series Connection of Cavities. *Sci. Rep.* **2019**, *9*, 1-11.

(25) Freeman, R. G.; Hommer, M. B.; Grabar, K. C.; Jackson, M. A.; Natan, M. J. Ag-Clad Au Nanoparticles: Novel Aggregation, Optical, and Surface-Enhanced Raman Scattering Properties. *J. Phys. Chem.* **1996**, *100*, 718–724.

(26) Navarro Ab, J. R. G.; Werts, M. H. V. Resonant Light Scattering Spectroscopy of Gold, Silver and Gold-Silver Alloy Nanoparticles and Optical Detection in Microfluidic Channels. *Analyst* **2013**, *138*, 583-592.

(27) Liao, H.; Lu, W.; Yu, S.; Wen, W.; Wong, G. K. L. Optical Characteristics of Gold Nanoparticle-Doped Multilayer Thin Film. *J. Opt. Soc. Am. B* **2005**, *22*, 1923-1926.

(28) Jun Liu, Y.; Bing Zheng, Y.; Liou, J.; Chiang, I.-K.; Choon Khoo, I.; Jun Huang, T. All-Optical Modulation of Localized Surface Plasmon Coupling in a Hybrid System Composed of Photoswitchable Gratings and Au Nanodisk Arrays. *J. Phys. Chem. C* **2011**, *115*, 7717–7722.

(29) Stanley, R. Plasmonics in the Mid-Infrared. *Nat. Photonics* **2012**, 6, 409–411.

(30) Hartland, G. Designing Plasmon Resonances. *J. Phys. Chem. Lett.* **2014**, *5*, 1583–1584.

(31) Kovalenko, M. V.; Manna, L.; Cabot, A.; Hens, Z.; Talapin, D. V.; Kagan, C. R.; Klimov, V. I.; Rogach, A. L.; Reiss, P.; Milliron, D. J.; et al. Prospects of Nanoscience with Nanocrystals. *ACS Nano* **2015**, *9*, 1012–1057.

(32) Zhao, Y.; Pan, H.; Lou, Y.; Qiu, X.; Zhu, J.; Burda, C. Plasmonic $Cu_{2-x}S$ Nanocrystals: Optical and Structural Properties of Copper-Deficient Copper(I) Sulfides. *J. Am. Chem. Soc.* **2009**, *131*, 4253–4261.

(33) Tandon, B.; Yadav, A.; Khurana, D.; Reddy, P.; Santra, P. K.; Nag, A. Size-Induced Enhancement of Carrier Density, LSPR Quality Factor, and Carrier Mobility in Cr−Sn Doped In_2O_3 Nanocrystals. *Chem. Mater.* **2017**, *29*, 9360-9368.

(34) Crockett, B. M.; Jansons, A. W.; Koskela, K. M.; Johnson, D. W.; Hutchison, J. E. Radial Dopant Placement for Tuning Plasmonic Properties in Metal Oxide Nanocrystals. *ACS Nano* **2017**, *11*, 7719–7728.

(35) Jansons, A. W.; Koskela, K. M.; Crockett, B. M.; Hutchison, J. E. Transition Metal-Doped Metal Oxide Nanocrystals: Efficient Substitutional Doping through a Continuous Growth Process. *Chem. Mater.* **2017**, *29*, 8167–8176.

(36) Jansons, A. W.; Hutchison, J. E. Continuous Growth of Metal Oxide Nanocrystals: Enhanced Control of Nanocrystal Size and Radial Dopant Distribution. *ACS Nano* **2016**, *10*, 6942–6951.

(37) Ilavsky, J.; Jemian, P. R. Irena: Tool Suite for Modeling and Analysis of Small-Angle Scattering. *J. Appl. Crystallogr.* **2009**, *42*, 347–353.

(38) Runnerstrom, E. L.; Bergerud, A.; Agrawal, A.; Johns, R. W.; Dahlman, C. J.; Singh, A.; Selbach, S. M.; Milliron, D. J. Defect Engineering in Plasmonic Metal Oxide Nanocrystals. *Nano Lett.* **2016**, *16*, 3390–3398.

(39) Ito, D.; Yokoyama, S.; Zaikova, T.; Masuko, K.; Hutchison, J. E. Synthesis of Ligand-Stabilized Metal Oxide Nanocrystals and Epitaxial Core/Shell Nanocrystals via a Lower- Temperature Esterification Process. *ACS Nano* **2014**, *8,* 64–75.

(40) Crockett, B. M.; Jansons, A. W.; Koskela, K. M.; Sharps, M. C.; Johnson, D. W.; Hutchison, J. E. Influence of Nanocrystal Size on the Optoelectronic Properties of Thin, Solution-Cast Sn-Doped In_2O_3 Films. *Chem. Mater.* **2019**, *31*, 3370–3380.

(41) Fang, H.; Hegde, M.; Yin, P.; Radovanovic, P. V. Tuning Plasmon Resonance of In_2O_3 Nanocrystals throughout the Mid-Infrared Region by Competition between Electron Activation and Trapping. *Chem. Mater.* **2017**, *29*, 4970–4979.

(42) Malitson, I. H. A Redetermination of Some Optical Properties of Calcium Fluoride. *Appl. Opt.* **1963**, *2*, 1103-1107.

(43) König, T. A. F.; Ledin, P. A.; Kerszulis, J.; Mahmoud, M. A.; El-Sayed, M. A.; Reynolds, J. R.; Tsukruk, V. V. Electrically Tunable Plasmonic Behavior of Nanocube-Polymer Nanomaterials Induced by a Redox-Active Electrochromic Polymer. *ACS Nano* **2014**, *8*, 6182–6192.

(44) Rycenga, M.; Camargo, P. H. C.; Li, W.; Moran, C. H.; Xia, Y. Understanding the SERS Effects of Single Silver Nanoparticles and Their Dimers, One at a Time. *J. Phys. Chem. Lett.* **2010**, *1*, 696–703.

(45) Jiang, C.; Markutsya, S.; Tsukruk, V. V. Collective and Individual Plasmon Resonances in Nanoparticle Films Obtained by Spin-Assisted Layer-by-Layer Assembly. *Langmuir* **2004**, *20*, 882–890.

(46) Mahmoud, M. A.; Chamanzar, M.; Adibi, A.; El-Sayed, M. A. Effect of the Dielectric Constant of the Surrounding Medium and the Substrate on the Surface Plasmon Resonance Spectrum and Sensitivity Factors of Highly Symmetric Systems: Silver Nanocubes. *J. Am. Chem. Soc.* **2012**, *134*, 6434–6442.

(47) R. Daniel, J.; McCarthy, L. A.; Ringe, E.; Boudreau, D. Enhanced Control of Plasmonic Properties of Silver-Gold Hollow Nanoparticles via a Reduction-Assisted Galvanic Replacement Approach. *RSC Adv.* **2019**, *9*, 389–396.

(48) Lu, H.; Liu, X.; Wang, L.; Gong, Y.; Mao, D. Ultrafast All-Optical Switching in Nanoplasmonic Waveguide with Kerr Nonlinear Resonator. *Opt. Express* **2011**, *19*, 2910-2915.

(49) Hendrickson, J. R.; Vangala, S.; Dass, C.; Gibson, R.; Goldsmith, J.; Leedy, K.; Walker, D. E.; Cleary, J. W.; Kim, W.; Guo, J. Coupling of Epsilon-Near-Zero Mode to Gap Plasmon Mode for Flat-Top Wideband Perfect Light Absorption. *ACS Photonics* **2018**, *5*, 776–781.

(50) Yang, L.; Zhou, Y. J.; Zhang, C.; Xiao, Q. X. Compact Wideband Plasmonic Filter with Flat-Top Transmission Response Based on Corrugated Metal-Insulator-Metal Ring Resonator. *Sci. Rep.* **2017**, *7*, 1–10.

(51) Hu, X. L.; Sun, L. B.; Wu, Q. J.; Wang, L. S.; Bai, S. A.; Li, Q.; Yang, S. M.; Tai, R. Z.; Mohr, M.; Fecht, H. J.; et al. Broad Band Optical Band-Reject Filters in Near-Infrared Regime Utilizing Bilayer Ag Metasurface. *J. Appl. Phys.* **2017**, *121*, 1-6.

(52) Bhachu, D. S.; Scanlon, D. O.; Sankar, G.; Veal, T. D.; Egdell, R. G.; Cibin, G.; Dent, A. J.; Knapp, C. E.; Carmalt, C. J.; Parkin, I. P. Origin of High Mobility in Molybdenum-Doped Indium Oxide. *Chem. Mater.* **2015**, *27*, 2788–2796.

(53) Zandi, O.; Agrawal, A.; Shearer, A. B.; Reimnitz, L. C.; Dahlman, C. J.; Staller, C. M.; Milliron, D. J. Impacts of Surface Depletion on the Plasmonic Properties of Doped Semiconductor Nanocrystals. *Nat. Mater.* **2018**, *17*, 710-717.

CHAPTER III

(1) Mayyas, A. T.; Ruth, M. F.; Pivovar, B. S.; Bender, G.; Wipke, K. B. *Manufacturing Cost Analysis for Proton Exchange Membrane Water Electrolyzers*; NREL/TP-6A20-72740 National Renewable Energy Lab, Golden, CO 2019.

(2) *Path to Hydrogen Competitiveness: A Cost Perspective*; Hydrogen Council: 2020.

(3) Ayers, K.; Danilovic, N.; Ouimet, R.; Carmo, M.; Pivovar, B.; Bornstein, M. Perspectives on Low-Temperature Electrolysis and Potential for Renewable Hydrogen at Scale. *Annu. Rev. Chem. Biomol. Eng.* **2019**, 219-241.

(4) Carmo, M.; Fritz, D. L.; Mergel, J.; Stolten, D. A Comprehensive Review on PEM Water Electrolysis. *Int. J. Hydrog. Energy* **2013,** *38* (12), 4901-4934.

(5) Reier, T.; Nong, H. N.; Teschner, D.; Schlögl, R.; Strasser, P. Electrocatalytic Oxygen Evolution Reaction in Acidic Environments – Reaction Mechanisms and Catalysts. *Adv. Energy Mater.* **2016,** *7* (1).

(6) Rozain, C.; Mayousse, E.; Guillet, N.; Millet, P. Influence of Iridium Oxide Loadings on the Performance of PEM Water Electrolysis Cells: Part I–Pure IrO_2-Based Anodes. *Appl. Catal.* **2016,** *182,* 153-160.

(7) Shiva Kumar, S.; Himabindu, V. Hydrogen Production by PEM Water Electrolysis – A Review. *Mater. Sci. Energy Technol.* **2019,** *2* (3), 442-454.

(8) Vincent, I.; Bessarabov, D. Low Cost Hydrogen Production by Anion Exchange Membrane Electrolysis: A Review. *Renew. Sust. Energ. Rev.* **2018,** *81*, 1690-1704.

(9) Kwasny, M. T.; Tew, G. N. Expanding Metal Cation Options in Polymeric Anion Exchange Membranes. *J. Mater. Chem.* **2017,** *5* (4), 1400-1405.

(10) Miller, H. A.; Bouzek, K.; Hnat, J.; Loos, S.; Bernäcker, C. I.; Weißgärber, T.; Röntzsch, L.; Meier-Haack, J. Green Hydrogen from Anion Exchange Membrane Water Electrolysis: A Review of Recent Developments in Critical Materials and Operating Conditions. *Sustain. Energy Fuels* **2020,** *4* (5), 2114-2133.

(11) Bernt, M.; Hartig-Weiß, A.; Tovini, M. F.; El-Sayed, H. A.; Schramm, C.; Schröter, J.; Gebauer, C.; Gasteiger, H. A. Current Challenges in Catalyst Development for PEM Water Electrolyzers. *Chem. Ing. Tech.* **2020,** *92* (1-2), 31-39.

(12) Ayers, K. The Potential of Proton Exchange Membrane–Based Electrolysis Technology. *Curr. Opin. Electrochem.* **2019,** *18*, 9-15.

(13) Rodríguez-García, B.; Reyes-Carmona, Á.; Jiménez-Morales, I.; Blasco-Ahicart, M.; Cavaliere, S.; Dupont, M.; Jone, D.; Rozière, J.; Galán-Mascarós, J. R.; Jaouen, F. Cobalt Hexacyanoferrate Supported on Sb-Doped SnO_2 as a Non-Noble Catalyst for Oxygen Evolution in Acidic Medium. *R. Soc. Chem.* **2017**, 589-597.

(14) Yang, X., Li, H., Lu, A. -Y., Min, S., Idriss, Z., Hedhili, N. M., Huang, K. -W., Idriss, H., and Li, L. -J. Highly Acid-Durable Carbon Coated Co_3O_4 Nanoarrays as Efficient Oxygen Evolution Electrocatalysts. *Nano Energy* **2016,** *25*, 42-50.

(15) Li, A.; Ooka, H.; Bonnet, N.; Hayashi, T.; Sun, Y.; Jiang, Q.; Li, C.; Han, H.; Nakamura, R. Stable Potential Windows for Long-Term Electrocatalysis by Manganese Oxides Under Acidic Conditions. *Angew. Chem. Int. Ed.* **2019,** *58* (15).

(16) Blasco-Ahicart, M.; Soriano-López, J.; Carbó, J. J.; Poblet, J. M.; Galan-Mascaros, J. R. Polyoxometalate Electrocatalysts Based on Earth-Abundant Metals for Efficient Water Oxidation in Acidic Media. *Nat. Chem.* **2018,** *10* (1), 24-30.

(17) Hartig-Weiss, A.; Miller, M.; Beyer, H.; Schmitt, A.; Siebel, A.; Freiberg, A. T. S.; Gasteiger, H. A.; El-Sayed, H. A. Iridium Oxide Catalyst Supported on Antimony-Doped Tin Oxide for High Oxygen Evolution Reaction Activity in Acidic Media. *ACS Appl. Nano Mater.* **2020,** *3* (3), 2185-2196.

(18) Oakton, E.; Lebedev, D.; Povia, M.; Abbott, D. F.; Fabbri, E.; Fedorov, A.; Nachtegaal, M.; Copéret, C.; Schmidt, T. J. IrO_2-TiO_2: A High-Surface-Area, Active, and Stable Electrocatalyst for the Oxygen Evolution Reaction. *ACS Catal.* **2017,** *7* (4), 2346-2352.

(19) Oh, H.-S.; Nong, H. N.; Reier, T.; Bergmann, A.; Gliech, M.; Ferreira de Araújo, J.; Willinger, E.; Schlögl, R.; Teschner, D.; Strasser, P. Electrochemical Catalyst–Support Effects and Their Stabilizing Role for IrO_x Nanoparticle Catalysts during the Oxygen Evolution Reaction. *J. Am. Chem. Soc.* **2016,** *138* (38), 12552-12563.

(20) Saveleva, V. A.; Wang, L.; Kasian, O.; Batuk, M.; Hadermann, J.; Gallet, J. J.; Bournel, F.; Alonso-Vante, N.; Ozouf, G.; Beauger, C.; Mayrhofer, K. J. J.; Cherevko, S.; Gago, A. S.; Friedrich, K. A.; Zafeiratos, S.; Savinova, E. R. Insight into the Mechanisms of High Activity and Stability of Iridium Supported on Antimony-Doped Tin Oxide Aerogel for Anodes of Proton Exchange Membrane Water Electrolyzers. *ACS Catal.* **2020,** *10* (4), 2508-2516.

(21) Finke, C. E.; Omelchenko, S. T.; Jasper, J. T.; Lichterman, M. F.; Read, C. G.; Lewis, N. S.; Hoffmann, M. R. Enhancing the Activity of Oxygen-Evolution and Chlorine-Evolution Electrocatalysts by Atomic Layer Deposition of TiO_2. *Energy Environ. Sci.* **2019,** *12* (1), 358-365.

(22) Kasian, O.; Li, T.; Mingers, A. M.; Schweinar, K.; Savan, A.; Ludwig, A.; Mayrhofer, K. Stabilization of an Iridium Oxygen Evolution Catalyst by Titanium Oxides. *J. Phys. Energy* **2021,** *3* (3), 034006.

(23) Pham, C. V.; Bühler, M.; Knöppel, J.; Bierling, M.; Seeberger, D.; Escalera-López, D.; Mayrhofer, K. J. J.; Cherevko, S.; Thiele, S. IrO_2 Coated TiO_2 Core-Shell Microparticles Advance Performance of Low Loading Proton Exchange Membrane Water Electrolyzers. *Appl. Catal.* **2020,** *269*, 118762.

(24) Oener, S. Z.; Foster, M. J.; Boettcher, S. W. Accelerating Water Dissociation in Bipolar Membranes and for Electrocatalysis. *Science* **2020,** *369* (6507), 1099.

(25) Chen, Q.; Thimsen, E. Highly Conductive Sb–SnO_2 Nanocrystals Synthesized by Dual Nonthermal Plasmas. *ACS Appl. Mater.* **2020,** *12* (22), 25168-25177.

(26) Conti, T. G.; Chiquito, A. J.; Da Silva, R. O.; Longo, E.; Leite, E. R. Electrical Properties of Highly Conducting SnO_2:Sb Nanocrystals Synthesized Using a Nonaqueous Sol–Gel Method. *J. Am. Ceram. Soc.* **2010,** *93* (11), 3862-3866.

(27) Fukano, T.; Motohiro, T. Low-Temperature Growth of Highly Crystallized Transparent Conductive Fluorine-Doped Tin Oxide Films by Intermittent Spray Pyrolysis Deposition. *Sol. Energy Mater Sol. Cells* **2004,** *82* (4), 567-575.

(28) Asadzadeh, M.; Tajabadi, F.; Dastan, D.; Sangpour, P.; Shi, Z.; Taghavinia, N. Facile Deposition of Porous Fluorine Doped Tin Oxide by Dr. Blade Method for Capacitive Applications. *Ceram. Int.* **2021,** *47* (4), 5487-5494.

(29) Geiger, S.; Kasian, O.; Mingers, A. M.; Mayrhofer, K. J. J.; Cherevko, S. Stability Limits of Tin-Based Electrocatalyst Supports. *Sci. Rep.* **2017,** *7* (1), 4595.

(30) Nong, H. N.; Oh, H.-S.; Reier, T.; Willinger, E.; Willinger, M.-G.; Petkov, V.; Teschner, D.; Strasser, P. Oxide-Supported $IrNiO_x$ Core–Shell Particles as Efficient, Cost-Effective, and Stable Catalysts for Electrochemical Water Splitting. *Angew. Chem. Int. Ed.* **2015,** *54* (10), 2975-2979.

(31) Lagadec, M. F.; Grimaud, A. Water Electrolysers with Closed and Open Electrochemical Systems. *Nat. Mater.* **2020,** *19* (11), 1140-1150.

(32) Lindquist, G. A.; Xu, Q.; Oener, S. Z.; Boettcher, S. W. Membrane Electrolyzers for Impure-Water Splitting. *Joule* **2020,** *4* (12), 2549-2561.

(33) Sheehan, S. W.; Thomsen, J. M.; Hintermair, U.; Crabtree, R. H.; Brudvig, G. W.; Schmuttenmaer, C. A. A Molecular Catalyst for Water Oxidation That Binds to Metal Oxide Surfaces. *Nat. Commun.* **2015,** *6* (1), 6469.

(34) Ledendecker, M.; Geiger, S.; Hengge, K.; Lim, J.; Cherevko, S.; Mingers, A. M.; Göhl, D.; Fortunato, G. V.; Jalalpoor, D.; Schüth, F.; Scheu, C.; Mayrhofer, K. J. J. Towards Maximized Utilization of Iridium for the Acidic Oxygen Evolution Reaction. *Nano Res.* **2019,** *12* (9), 2275-2280.

(35) Geiger, S.; Kasian, O.; Ledendecker, M.; Pizzutilo, E.; Mingers, A. M.; Fu, W. T.; Diaz-Morales, O.; Li, Z.; Oellers, T.; Fruchter, L.; Ludwig, A.; Mayrhofer, K. J. J.; Koper, M. T. M.; Cherevko, S. The Stability Number as a Metric for Electrocatalyst Stability Benchmarking. *Nat. Catal.* **2018,** *1* (7), 508-515.

(36) Cherevko, S.; Topalov, A. A.; Zeradjanin, A. R.; Katsounaros, I.; Mayrhofer, K. J. J. Gold Dissolution: Towards Understanding of Noble Metal Corrosion. *RSC Adv.* **2013,** *3* (37), 16516-16527.

(37) Klemm, S. O.; Topalov, A. A.; Laska, C. A.; Mayrhofer, K. J. J. Coupling of a High Throughput Microelectrochemical Cell with Online Multielemental Trace Analysis by ICP-MS. *Electrochem. Commun.* **2011,** *13* (12), 1533-1535.

(38) Klemm, S. O.; Karschin, A.; Schuppert, A. K.; Topalov, A. A.; Mingers, A. M.; Katsounaros, I.; Mayrhofer, K. J. J. Time and Potential Resolved Dissolution Analysis of Rhodium Using a Microelectrochemical Flow Cell Coupled to an ICP-MS. *J. Electroanal. Chem.* **2012,** *677-680*, 50-55.

(39) Oh, H.-S.; Nong, H. N.; Strasser, P. Preparation of Mesoporous Sb-, F-, and In-Doped SnO_2 Bulk Powder with High Surface Area for Use as Catalyst Supports in Electrolytic Cells. *Adv. Funct. Mater.* **2015,** *25* (7), 1074-1081.

(40) Fernando, N. K.; Cairns, A. B.; Murray, C. A.; Thompson, A. L.; Dickerson, J. L.; Garman, E. F.; Ahmed, N.; Ratcliff, L. E.; Regoutz, A. Structural and Electronic Effects of X-ray Irradiation on Prototypical $[M(COD)Cl]_2$ Catalysts. *J. Phys. Chem.* **2021,** *125* (34), 7473-7488.

(41) Jeong, S.; Lee, J.-Y.; Lee, S. S.; Choi, Y.; Ryu, B.-H. Impact of Metal Salt Precursor on Low-Temperature Annealed Solution-Derived Ga-doped In_2O_3 Semiconductor for Thin-Film Transistors. *J. Phys. Chem.* **2011,** *115* (23), 11773-11780.

(42) George, S. M. Atomic Layer Deposition: An Overview. *Chem. Rev.* **2010,** *110* (1), 111-131.

(43) Kasian, O.; Geiger, S.; Mayrhofer, K. J. J.; Cherevko, S. Electrochemical On-line ICP-MS in Electrocatalysis Research. *The Chemical Record* **2019,** *19* (10), 2130-2142.

(44) Kasian, O.; Grote, J.-P.; Geiger, S.; Cherevko, S.; Mayrhofer, K. J. J. The Common Intermediates of Oxygen Evolution and Dissolution Reactions during Water Electrolysis on Iridium. *Angew. Chem. Int. Ed.* **2018,** *57* (9), 2488-2491.

(45) Chang, S. H.; Connell, J. G.; Danilovic, N.; Subbaraman, R.; Chang, K.-C.; Stamenkovic, V. R.; Markovic, N. M. Activity–Stability Relationship in the Surface Electrochemistry of the Oxygen Evolution Reaction. *Faraday Discuss.* **2014,** *176* (0), 125-133.

(46) Danilovic, N.; Subbaraman, R.; Chang, K. C.; Chang, S. H.; Kang, Y. J.; Snyder, J.; Paulikas, A. P.; Strmcnik, D.; Kim, Y. T.; Myers, D.; Stamenkovic, V. R.; Markovic, N. M. Activity-Stability Trends for the Oxygen Evolution Reaction on Monometallic Oxides in Acidic Environments. *J. Phys. Chem. Lett.* **2014,** *5* (14), 2474–2478.

(47) Geiger, S.; Kasian, O.; Shrestha, B. R.; Mingers, A. M.; Mayrhofer, K. J. J.; Cherevko, S. Activity and Stability of Electrochemically and Thermally Treated Iridium for the Oxygen Evolution Reaction. *J. Electrochem. Soc.* **2016,** *163* (11), F3132-F3138.

(48) Lin, C. P.; Chen, H.; Nakaruk, A.; Koshy, P.; Sorrell, C. C. Effect of Annealing Temperature on the Photocatalytic Activity of TiO_2 Thin Films. *Energy Procedia* **2013,** *34*, 627-636.

(49) Kriegel, H.; Kollmann, J.; Raudsepp, R.; Klassen, T.; Schieda, M. Chemical and Photoelectrochemical Instability of Amorphous TiO_2 Layers Quantified by Spectroscopic Ellipsometry. *J. Mater. Chem.* **2020,** *8* (35), 18173-18179.

CHAPTER IV

(1) Pivovar, B.; Rustagi, N.; Satyapal, S. Hydrogen at Scale (H_2@Scale): Key to a Clean, Economic, and Sustainable Energy System. *Electrochem. Soc. Interface* **2018,** *27* (1), 47-52.

(2) Ayers, K.; Danilovic, N.; Ouimet, R.; Carmo, M.; Pivovar, B.; Bornstein, M. Perspectives on Low-Temperature Electrolysis and Potential for Renewable Hydrogen at Scale. *Annu. Rev. Chem. Biomol. Eng.* **2019,** *10* (1), 219-239.

(3) Yang, C.; Wang, S.; Ma, W.; Jiang, L.; Sun, G. Highly Alkaline Stable N1-alkyl Substituted 2-methylimidazolium Functionalized Alkaline Anion Exchange Membranes. *J. Mater. Chem.* **2015,** *3* (16), 8559-8565.

(4) Vincent, I.; Bessarabov, D. Low Cost Hydrogen Production by Anion Exchange Membrane Eelectrolysis: A Review. *Renew. Sust. Energ. Rev.* **2018,** *81*, 1690-1704.

(5) Mustain, W. E.; Chatenet, M.; Page, M.; Kim, Y. S. Durability Challenges of Anion Exchange Membrane Fuel Cells. *Energy Environ. Sci.* **2020,** *13* (9), 2805-2838.

(6) Li, D.; Motz, A. R.; Bae, C.; Fujimoto, C.; Yang, G.; Zhang, F.-Y.; Ayers, K. E.; Kim, Y. S. Durability of Anion Exchange Membrane Water Electrolyzers. *Energy Environ. Sci.* **2021,** 14, 3393-3419.

(7) Li, D.; Park, E. J.; Zhu, W.; Shi, Q.; Zhou, Y.; Tian, H.; Lin, Y.; Serov, A.; Zulevi, B.; Baca, E. D.; Fujimoto, C.; Chung, H. T.; Kim, Y. S. Highly Quaternized Polystyrene Ionomers for High Performance Anion Exchange Membrane Water Electrolysers. *Nat. Energy* **2020,** *5* (5), 378-385.

(8) Xu, D.; Stevens, M. B.; Cosby, M. R.; Oener, S. Z.; Smith, A. M.; Enman, L. J.; Ayers, K. E.; Capuano, C. B.; Renner, J. N.; Danilovic, N.; Li, Y.; Wang, H.; Zhang, Q.; Boettcher, S. W. Earth-Abundant Oxygen Electrocatalysts for Alkaline Anion-Exchange-Membrane Water Electrolysis: Effects of Catalyst Conductivity and Comparison with Performance in Three-Electrode Cells. *ACS Catal.* **2019,** *9* (1), 7-15.

(9) Xiao, J.; Oliveira, A. M.; Wang, L.; Zhao, Y.; Wang, T.; Wang, J.; Setzler, B. P.; Yan, Y. Water-Fed Hydroxide Exchange Membrane Electrolyzer Enabled by a Fluoride-Incorporated Nickel–Iron Oxyhydroxide Oxygen Evolution Electrode. *ACS Catal.* **2021,** *11* (1), 264-270.

(10) Mališ, J.; Mazúr, P.; Paidar, M.; Bystron, T.; Bouzek, K. Nafion 117 Stability under Conditions of PEM Water Electrolysis at Elevated Temperature and Pressure. *Int. J. Hydrog. Energy* **2016,** *41* (4), 2177-2188.

(11) Miller, H. A.; Bouzek, K.; Hnat, J.; Loos, S.; Bernäcker, C. I.; Weißgärber, T.; Röntzsch, L.; Meier-Haack, J. Green Hydrogen from Anion Exchange Membrane Water Electrolysis: A Review of Recent Developments in Critical Materials and Operating Conditions. *Sustain. Energy Fuels* **2020,** *4* (5), 2114-2133.

(12) Stanislaw, L. N.; Gerhardt, M. R.; Weber, A. Z. Modeling Electrolyte Composition Effects on Anion-Exchange-Membrane Water Electrolyzer Performance. *ECS Trans.* **2019,** *92* (8), 767-779.

(13) Vincent, I.; Kruger, A.; Bessarabov, D. Development of Efficient Membrane Electrode Assembly for Low Cost Hydrogen Production by Anion Exchange Membrane Electrolysis. *Int. J. Hydrog. Energy* **2017,** *42* (16), 10752-10761.

(14) Lindquist, G. A.; Oener, S. Z.; Krivina, R.; Motz, A. R.; Keane, A.; Capuano, C.; Ayers, K. E.; Boettcher, S. W. Performance and Durability of Pure-Water-Fed Anion Exchange Membrane Electrolyzers Using Baseline Materials and Operation. *ACS Appl. Mater. Interfaces* **2021**, *13* (44), 51917-51924.

(15) Borup, R.; Meyers, J.; Pivovar, B.; Kim, Y. S.; Mukundan, R.; Garland, N.; Myers, D.; Wilson, M.; Garzon, F.; Wood, D.; Zelenay, P.; More, K.; Stroh, K.; Zawodzinski, T.; Boncella, J.; McGrath, J. E.; Inaba, M.; Miyatake, K.; Hori, M.; Ota, K.; Ogumi, Z.; Miyata, S.; Nishikata, A.; Siroma, Z.; Uchimoto, Y.; Yasuda, K.; Kimijima, K.-i.; Iwashita, N. Scientific Aspects of Polymer Electrolyte Fuel Cell Durability and Degradation. *Chem. Rev.* **2007,** *107* (10), 3904-3951.

(16) Li, D.; Matanovic, I.; Lee, A. S.; Park, E. J.; Fujimoto, C.; Chung, H. T.; Kim, Y. S. Phenyl Oxidation Impacts the Durability of Alkaline Membrane Water Electrolyzer. *ACS Appl. Mater. Interfaces* **2019,** *11* (10), 9696-9701.

(17) Park, E. J.; Maurya, S.; Hibbs, M. R.; Fujimoto, C. H.; Kreuer, K.-D.; Kim, Y. S. Alkaline Stability of Quaternized Diels–Alder Polyphenylenes. *Macromolecules* **2019,** *52* (14), 5419-5428.

(18) Fan, J.; Willdorf-Cohen, S.; Schibli, E. M.; Paula, Z.; Li, W.; Skalski, T. J. G.; Sergeenko, A. T.; Hohenadel, A.; Frisken, B. J.; Magliocca, E.; Mustain, W. E.; Diesendruck, C. E.; Dekel, D. R.; Holdcroft, S. Poly(bis-arylimidazoliums) Possessing High Hydroxide Ion Exchange Capacity and High Alkaline Stability. *Nat. Commun.* **2019,** *10* (1), 2306.

(19) Tao, H. B.; Xu, Y.; Huang, X.; Chen, J.; Pei, L.; Zhang, J.; Chen, J. G.; Liu, B. A General Method to Probe Oxygen Evolution Intermediates at Operating Conditions. *Joule* **2019,** *3* (6), 1498-1509.

(20) Cao, X.; Novitski, D.; Holdcroft, S. Visualization of Hydroxide Ion Formation upon Electrolytic Water Splitting in an Anion Exchange Membrane. *ACS Mater. Lett.* **2019,** *1* (3), 362-366.

(21) Wright, A. G.; Fan, J.; Britton, B.; Weissbach, T.; Lee, H.-F.; Kitching, E. A.; Peckham, T. J.; Holdcroft, S. Hexamethyl-p-terphenyl Poly(benzimidazolium): A Universal Hydroxide-Conducting Polymer for Energy Conversion Devices. *Energy Environ. Sci.* **2016,** *9* (6), 2130-2142.

(22) Kaczur, J. J.; Yang, H.; Liu, Z.; Sajjad, S. D.; Masel, R. I. Carbon Dioxide and Water Electrolysis Using New Alkaline Stable Anion Membranes. *Front. Chem.* **2018,** *6*, 263.

(23) Wang, J.; Zhao, Y.; Setzler, B. P.; Rojas-Carbonell, S.; Ben Yehuda, C.; Amel, A.; Page, M.; Wang, L.; Hu, K.; Shi, L.; Gottesfeld, S.; Xu, B.; Yan, Y. Poly(aryl piperidinium) Membranes and Ionomers for Hydroxide Exchange Membrane Fuel Cells. *Nat. Energy* **2019,** *4* (5), 392-398.

(24) Sauerbrey, G. Z. Use of Quartz Vibration for Weighing Thin Films on a Microbalance. *Phys. A: Hadrons Nucl.* **1959,** *155* (2), 206-222.

(25) Winget, P.; Weber, E. J.; Cramer, C. J.; Truhlar, D. G. Computational Electrochemistry: Aqueous One-Electron Oxidation Potentials for Substituted Anilines. *Phys. Chem. Chem.* **2000,** *2* (6), 1231-1239.

(26) Epsztein, R.; Shaulsky, E.; Qin, M.; Elimelech, M. Activation Behavior for Ion Permeation in Ion-Exchange Membranes: Role of Ion Dehydration in Selective Transport. *J. Membr. Sci.* **2019,** *580*, 316-326.

(27) Koch, S.; Heizmann, P. A.; Kilian, S. K.; Britton, B.; Holdcroft, S.; Breitwieser, M.; Vierrath, S. The Effect of Ionomer Content in Catalyst Layers in Anion-Exchange Membrane Water Electrolyzers Prepared with Reinforced Membranes (Aemion+™). *J. Mater. Chem. A* **2021,** *9* (28), 15744-15754.

(28) Duffin, A. M.; Schwartz, C. P.; England, A. H.; Uejio, J. S.; Prendergast, D.; Saykally, R. J. pH-Dependent X-ray Absorption Spectra of Aqueous Boron Oxides. *J. Chem. Phys.* **2011,** *134* (15), 154503.

(29) Zhou, Y.; Yamaguchi, T.; Zhang, W.; Ikeda, K.; Yoshida, K.; Zhu, F.; Liu, H. The Structural Elucidation of Aqueous H_3BO_3 Solutions by DFT and Neutron Scattering Studies. *Phys. Chem. Chem.* **2020,** *22* (30), 17160-17170.

(30) Luo, X.; Kushner, D. I.; Li, J.; Park, E. J.; Kim, Y. S.; Kusoglu, A. Anion Exchange Ionomers: Impact of Chemistry on Thin-Film Properties. *Adv. Funct. Mater.* **2021,** *31* (20), 2008778.

(31) Moulder, J. F.; Stickle, W. F.; E.'Sobol, P.; Bomben, K. D. *Handbook of X-ray photoelectron spectroscopy*. Perkin-Elmer Corporation, **1992**, 252-253.

(32) Li, D.; Motz, A. R.; Bae, C.; Fujimoto, C.; Yang, G.; Zhang, F.-Y.; Ayers, K. E.; Kim, Y. S. Durability of Anion Exchange Membrane Water Electrolyzers. *Energy Environ. Sci.* **2021,** *14*, 3393-3419.

(33) Thomas, O. D.; Soo, K. J. W. Y.; Peckham, T. J.; Kulkarni, M. P.; Holdcroft, S. A Stable Hydroxide-Conducting Polymer. *J. Am. Chem. Soc.* **2012,** *134* (26), 10753-10756.

(34) Lindquist, G. A.; Xu, Q.; Oener, S. Z.; Boettcher, S. W. Membrane Electrolyzers for Impure-Water Splitting. *Joule* **2020,** *4* (12), 2549-2561.

(35) Hübner, G.; Roduner, E. EPR Investigation of $HO^{\cdot}$ Radical Initiated Degradation Reactions of Sulfonated Aromatics as Model Compounds for Fuel Cell Proton Conducting Membranes. *J. Mater. Chem.* **1999,** *9* (2), 409-418.

(36) Kiessling, A.; Fornaciari, J. C.; Anderson, G.; Peng, X.; Gerstmayr, A.; Gerhardt, M. R.; McKinney, S.; Serov, A.; Kim, Y. S.; Zulevi, B.; Weber, A. Z.; Danilovic, N. Influence of Supporting Electrolyte on Hydroxide Exchange Membrane Water Electrolysis Performance: Anolyte. *J. Electrochem. Soc.* **2021,** *168* (8), 084512.

(37) Pellerite, M.; Kaplun, M.; Hartmann-Thompson, C.; Lewinski, K. A.; Kunz, N.; Gregar, T.; Baetzold, J.; Lutz, D.; Quast, M.; Liu, Z.; Yang, H.; Sajjad, S. D.; Gao, Y.; Masel, R. Imidazolium-Functionalized Polymer Membranes for Fuel Cells and Electrolyzers. *ECS Trans.* **2017,** *80* (8), 945-956.

(38) Liu, Z.; Yang, H.; Kutz, R.; Masel, R. I. CO_2 Electrolysis to CO and O_2 at High Selectivity, Stability and Efficiency Using Sustainion Membranes. *J. Electrochem. Soc.* **2018,** *165* (15), J3371-J3377.

(39) Luo, X.; Rojas-Carbonell, S.; Yan, Y.; Kusoglu, A. Structure-Transport Relationships of Poly(aryl piperidinium) Anion-Exchange Membranes: Effect of Anions and Hydration. *J. Membr. Sci.* **2020,** *598*, 117680.

(40) Endrődi, B.; Kecsenovity, E.; Samu, A.; Halmágyi, T.; Rojas-Carbonell, S.; Wang, L.; Yan, Y.; Janáky, C. High Carbonate Ion Conductance of a Robust PiperION Membrane Allows Industrial Current Density and Conversion in a Zero-Gap Carbon Dioxide Electrolyzer Cell. *Energy Environ. Sci.* **2020,** *13* (11), 4098-4105.

(41) Gabla, J. J.; Mistry, S. R.; Maheria, K. C. An Efficient Green Protocol for the Synthesis of Tetra-Substituted Imidazoles Catalyzed by Zeolite BEA: Effect of Surface Acidity and Polarity of Zeolite. *Catal. Sci. Technol.* **2017,** *7* (21), 5154-5167.

(42) Thavamani, S.; Amaladhas, T. Encapsulation of Cu(II), Ni(II) and V(IV) - Imidazole Complexes in Fly Ash Zeolite, Characterisation and Catalytic Activity towards Hydroxylation of Phenol. *J. Mater. Environ. Sci.* **2016,** *7*, 2314-2327.

CHAPTER V

(1) Ayers, K.; Danilovic, N.; Ouimet, R.; Carmo, M.; Pivovar, B.; Bornstein, M. Perspectives on Low-Temperature Electrolysis and Potential for Renewable Hydrogen at Scale. *Annu. Rev. Chem. Biomol. Eng.* **2019,** *10* (1), 219-239.

(2) Lindquist, G. A.; Xu, Q.; Oener, S. Z.; Boettcher, S. W. Membrane Electrolyzers for Impure-Water Splitting. *Joule* **2020,** *4* (12), 2549-2561.

(3) Reier, T.; Nong, H. N.; Teschner, D.; Schlögl, R.; Strasser, P. Electrocatalytic Oxygen Evolution Reaction in Acidic Environments – Reaction Mechanisms and Catalysts. *Adv. Energy Mater.* **2017,** *7* (1), 1601275.

(4) Cao, X.; Novitski, D.; Holdcroft, S. Visualization of Hydroxide Ion Formation upon Electrolytic Water Splitting in an Anion Exchange Membrane. *ACS Mater. Lett.* **2019,** *1* (3), 362-366.

(5) Trasatti, S.; Petrii, O. A. Real Surface Area Measurements in Electrochemistry. *J. Electroanal. Chem.* **1992,** *327* (1), 353-376.

(6) Matsumoto, Y.; Sato, E. Electrocatalytic Properties of Transition Metal Oxides for Oxygen Evolution Reaction. *Mater. Chem. Phys.* **1986,** *14* (5), 397-426.

(7) Enman, L. J.; Stevens, M. B.; Dahan, M. H.; Nellist, M. R.; Toroker, M. C.; Boettcher, S. W. Operando X-ray Absorption Spectroscopy Shows Iron Oxidation is Concurrent with Oxygen Evolution in Cobalt-Iron (Oxy)hydroxide Electrocatalysts. *Angew. Chem. Int. Ed.* **2018,** *57*, 12840-12844.

(8) Friebel, D.; Louie, M. W.; Bajdich, M.; Sanwald, K. E.; Cai, Y.; Wise, A. M.; Cheng, M.-J.; Sokaras, D.; Weng, T.-C.; Alonso-Mori, R.; Davis, R. C.; Bargar, J. R.; Nørskov, J. K.; Nilsson, A.; Bell, A. T. Identification of Highly Active Fe Sites in (Ni,Fe)OOH for Electrocatalytic Water Splitting. *J. Am. Chem. Soc.* **2015,** *137* (3), 1305-1313.

(9) Görlin, M.; Chernev, P.; Ferreira de Araújo, J.; Reier, T.; Dresp, S.; Paul, B.; Krähnert, R.; Dau, H.; Strasser, P. Oxygen Evolution Reaction Dynamics, Faradaic Charge Efficiency, and the Active Metal Redox States of Ni–Fe Oxide Water Splitting Electrocatalysts. *J. Am. Chem. Soc.* **2016,** *138* (17), 5603-5614.

(10) Li, N.; Bediako, D. K.; Hadt, R. G.; Hayes, D.; Kempa, T. J.; von Cube, F.; Bell, D. C.; Chen, L. X.; Nocera, D. G. Influence of Iron Doping on Tetravalent Nickel Content in Catalytic Oxygen Evolving Films. *Proc. Nat. Acad. Sci.* **2017,** *114* (7), 1486-1491.

(11) Smith, R. D. L.; Pasquini, C.; Loos, S.; Chernev, P.; Klingan, K.; Kubella, P.; Mohammadi, M. R.; Gonzalez-Flores, D.; Dau, H. Spectroscopic Identification of Active Sites for the Oxygen Evolution Reaction on Iron-Cobalt Oxides. *Nat. Commun.* **2017,** *8* (1), 2022.

(12) Gong, L.; Chng, X. Y. E.; Du, Y.; Xi, S.; Yeo, B. S. Enhanced Catalysis of the Electrochemical Oxygen Evolution Reaction by Iron(III) Ions Adsorbed on Amorphous Cobalt Oxide. *ACS Catal.* **2018,** *8* (2), 807-814.

(13) Hunter, B. M.; Thompson, N. B.; Müller, A. M.; Rossman, G. R.; Hill, M. G.; Winkler, J. R.; Gray, H. B. Trapping an Iron(VI) Water-Splitting Intermediate in Nonaqueous Media. *Joule* **2018,** *2* (4), 747-763.

(14) Chen, J. Y.; Dang, L.; Liang, H.; Bi, W.; Gerken, J. B.; Jin, S.; Alp, E. E.; Stahl, S. S. Operando Analysis of NiFe and Fe Oxyhydroxide Electrocatalysts for Water Oxidation: Detection of Fe^{4+} by Mossbauer Spectroscopy. *J. Am. Chem. Soc.* **2015,** *137* (48), 15090-15093.

(15) Zhang, T.; Nellist, M. R.; Enman, L. J.; Xiang, J.; Boettcher, S. W. Modes of Fe Incorporation in Co-Fe (Oxy)hydroxide Oxygen Evolution Electrocatalysts. *ChemSusChem* **2019,** *12* (9), 2015-2021.

(16) Trotochaud, L.; Ranney, J. K.; Williams, K. N.; Boettcher, S. W. Solution-Cast Metal Oxide Thin Film Electrocatalysts for Oxygen Evolution. *J. Am. Chem. Soc.* **2012,** *134* (41), 17253-17261.

(17) Wu, J.; Ren, Z.; Du, S.; Kong, L.; Liu, B.; Xi, W.; Zhu, J.; Fu, H. A Highly Active Oxygen Evolution Electrocatalyst: Ultrathin CoNi Double Hydroxide/CoO Nanosheets Synthesized via Interface-Directed Assembly. *Nano Res.* **2016,** *9*, 713-725.

(18) Stevens, M. B.; Enman, L. J.; Korkus, E. H.; Zaffran, J.; Trang, C. D. M.; Asbury, J.; Kast, M. G.; Toroker, M. C.; Boettcher, S. W. Ternary Ni-Co-Fe Oxyhydroxide Oxygen Evolution Catalysts: Intrinsic Activity Trends, Electrical Conductivity, and Electronic Band Structure. *Nano Res.* **2019,** *12,* 2288-2295.

(19) Trotochaud, L.; Young, S. L.; Ranney, J. K.; Boettcher, S. W. Nickel-Iron Oxyhydroxide Oxygen-Evolution Electrocatalysts: the Role of Intentional and Incidental Iron Incorporation. *J. Am. Chem. Soc.* **2014,** *136* (18), 6744-6753.

(20) Batchellor, A. S.; Kwon, G.; Laskowski, F. A. L.; Tiede, D. M.; Boettcher, S. W. Domain Structures of Ni and NiFe (Oxy)Hydroxide Oxygen-Evolution Catalysts from X-ray Pair Distribution Function Analysis. *J. Phys. Chem. C* . **2017,** *121* (45), 25421-25429.

(21) Burke, M. S.; Kast, M. G.; Trotochaud, L.; Smith, A. M.; Boettcher, S. W. Cobalt-Iron (Oxy)hydroxide Oxygen Evolution Electrocatalysts: The Role of Structure and Composition on Activity, Stability, and Mechanism. *J. Am. Chem. Soc.* **2015,** *137* (10), 3638-3648.

(22) Smith, A. M.; Trotochaud, L.; Burke, M. S.; Boettcher, S. W. Contributions to Activity Enhancement via Fe Incorporation in Ni-(Oxy)hydroxide/Borate Catalysts for Near-Neutral pH Oxygen Evolution. *Chem. Commun.* **2015,** *51* (25), 5261-5263.

(23) Stevens, M. B.; Enman, L. J.; Batchellor, A. S.; Cosby, M. R.; Vise, A. E.; Trang, C. D. M.; Boettcher, S. W. Measurement Techniques for the Study of Thin Film Heterogeneous Water Oxidation Electrocatalysts. *Chem. Mater.* **2017,** *29* (1), 120-140.

(24) Lee, S.; Banjac, K.; Lingenfelder, M.; Hu, X. Oxygen Isotope Labeling Experiments Reveal Different Reaction Sites for the Oxygen Evolution Reaction on Nickel and Nickel Iron Oxides. *Angew. Chem. Int. Ed.* **2019,** *58* (30), 10295-10299.

(25) Roy, C.; Sebok, B.; Scott, S. B.; Fiordaliso, E. M.; Sørensen, J. E.; Bodin, A.; Trimarco, D. B.; Damsgaard, C. D.; Vesborg, P. C. K.; Hansen, O.; Stephens, I. E. L.; Kibsgaard, J.; Chorkendorff, I. Impact of Nanoparticle Size and Lattice Oxygen on Water Oxidation on $NiFeO_xH_y$. *Nat. Catal.* **2018,** *1* (11), 820-829.

(26) Ferreira de Araújo, J.; Dionigi, F.; Merzdorf, T.; Oh, H.-S.; Strasser, P. Evidence of Mars-Van-Krevelen Mechanism in the Electrochemical Oxygen Evolution on Ni-Based Catalysts. *Angew. Chem. Int. Ed.* **2021,** 60, 2-10.

(27) Moysiadou, A.; Lee, S.; Hsu, C.-S.; Chen, H. M.; Hu, X. Mechanism of Oxygen Evolution Catalyzed by Cobalt Oxyhydroxide: Cobalt Superoxide Species as a Key Intermediate and Dioxygen Release as a Rate-Determining Step. *J. Am. Chem. Soc.* **2020,** *142* (27), 11901-11914.

(28) Zou, S.; Burke, M. S.; Kast, M. G.; Fan, J.; Danilovic, N.; Boettcher, S. W. Fe (Oxy)hydroxide Oxygen Evolution Reaction Electrocatalysis: Intrinsic Activity and the Roles of Electrical Conductivity, Substrate, and Dissolution. *Chem. Mater.* **2015,** *27* (23), 8011-8020.

(29) Batchellor, A. S.; Boettcher, S. W. Pulse-Electrodeposited Ni–Fe (Oxy)hydroxide Oxygen Evolution Electrocatalysts with High Geometric and Intrinsic Activities at Large Mass Loadings. *ACS Catal.* **2015,** *5* (11), 6680-6689.

(30) Burke, M. S.; Zou, S.; Enman, L. J.; Kellon, J. E.; Gabor, C. A.; Pledger, E.; Boettcher, S. W. Revised Oxygen Evolution Reaction Activity Trends for First-Row Transition-Metal (Oxy)hydroxides in Alkaline Media. *J. Phys. Chem. Lett.* **2015,** *6* (18), 3737-3742.

(31) Enman, L. J.; Vise, A. E.; Burke Stevens, M.; Boettcher, S. W. Effects of Metal Electrode Support on the Catalytic Activity of Fe(oxy)hydroxide for the Oxygen Evolution Reaction in Alkaline Media. *ChemPhysChem* **2019,** *20* (22), 3089-3095.

(32) Corrigan, D. A. The Catalysis of the Oxygen Evolution Reaction by Iron Impurities in Thin Film Nickel Oxide Electrodes. *J. Electrochem. Soc.* **1987,** *134* (2), 377-384.

(33) Klaus, S.; Trotochaud, L.; Cheng, M.-J.; Head-Gordon, M.; Bell, A. T. Experimental and Computational Evidence of Highly Active Fe Impurity Sites on the Surface of Oxidized Au for the Electrocatalytic Oxidation of Water in Basic Media. *ChemElectroChem* **2016,** *3* (1), 66-73.

(34) Haber, J. A.; Xiang, C.; Guevarra, D.; Jung, S.; Jin, J.; Gregoire, J. M. High-Throughput Mapping of the Electrochemical Properties of (Ni-Fe-Co-Ce)O_x Oxygen-Evolution Catalysts. *ChemElectroChem* **2014,** *1* (3), 524-528.

(35) Louie, M. W.; Bell, A. T. An Investigation of Thin-Film Ni-Fe Oxide Catalysts for the Electrochemical Evolution of Oxygen. *J. Am. Chem. Soc.* **2013,** *135* (33), 12329-37.

(36) Enman, L. J.; Burke, M. S.; Batchellor, A. S.; Boettcher, S. W. Effects of Intentionally Incorporated Metal Cations on the Oxygen Evolution Electrocatalytic Activity of Nickel (Oxy)hydroxide in Alkaline Media. *ACS Catal.* **2016,** *6* (4), 2416-2423.

(37) Boettcher, S. W.; Surendranath, Y. Heterogeneous Electrocatalysis Goes Chemical. *Nat. Catal.* **2021,** *4* (1), 4-5.

(38) Nong, H. N.; Falling, L. J.; Bergmann, A.; Klingenhof, M.; Tran, H. P.; Spöri, C.; Mom, R.; Timoshenko, J.; Zichittella, G.; Knop-Gericke, A.; Piccinin, S.; Pérez-Ramírez, J.; Cuenya, B. R.; Schlögl, R.; Strasser, P.; Teschner, D.; Jones, T. E. Key Role of Chemistry Versus Bias in Electrocatalytic Oxygen Evolution. *Nature* **2020,** *587* (7834), 408-413.

(39) Stevens, M. B.; Trang, C. D. M.; Enman, L. J.; Deng, J.; Boettcher, S. W. Reactive Fe-Sites in Ni/Fe (Oxy)hydroxide Are Responsible for Exceptional Oxygen Electrocatalysis Activity. *J. Am. Chem. Soc.* **2017,** *139* (33), 11361-11364.

(40) Subbaraman, R.; Tripkovic, D.; Chang, K. C.; Strmcnik, D.; Paulikas, A. P.; Hirunsit, P.; Chan, M.; Greeley, J.; Stamenkovic, V.; Markovic, N. M. Trends in Activity for the Water Electrolyser Reactions on 3d M(Ni,Co,Fe,Mn) Hydr(oxy)oxide Catalysts. *Nat. Mater.* **2012,** *11* (6), 550-557.

(41) Ida, S.; Shiga, D.; Koinuma, M.; Matsumoto, Y. Synthesis of Hexagonal Nickel Hydroxide Nanosheets by Exfoliation of Layered Nickel Hydroxide Intercalated with Dodecyl Sulfate Ions. *J. Am. Chem. Soc.* **2008,** *130* (43), 14038-14039.

(42) Deng, J.; Nellist, M. R.; Stevens, M. B.; Dette, C.; Wang, Y.; Boettcher, S. W. Morphology Dynamics of Single-Layered $Ni(OH)_2$/NiOOH Nanosheets and Subsequent Fe Incorporation Studied by *in Situ* Electrochemical Atomic Force Microscopy. *Nano Lett.* **2017,** *17* (11), 6922-6926.

(43) Dette, C.; Hurst, M. R.; Deng, J.; Nellist, M. R.; Boettcher, S. W. Structural Evolution of Metal (Oxy)hydroxide Nanosheets during the Oxygen Evolution Reaction. *ACS Appl. Mater. Interfaces* **2019,** *11* (6), 5590-5594.

(44) Chung, D. Y.; Lopes, P. P.; Farinazzo Bergamo Dias Martins, P.; He, H.; Kawaguchi, T.; Zapol, P.; You, H.; Tripkovic, D.; Strmcnik, D.; Zhu, Y.; Seifert, S.; Lee, S.; Stamenkovic, V. R.; Markovic, N. M. Dynamic Stability of Active Sites in Hydr(oxy)oxides for the Oxygen Evolution Reaction. *Nat. Energy* **2020,** *5* (3), 222-230.

(45) Bates, M. K.; Qingying, J.; Doan, H.; Liang, W.; Mukerjee, S. Charge-Transfer Effects in Ni-Fe and Ni-Fe-Co Mixed-Metal Oxides for the Alkaline Oxygen Evolution Reaction. *ACS Catal.* **2016,** *6*, 155-161.

(46) Dong, C.; Han, L.; Zhang, C.; Zhang, Z. Scalable Dealloying Route to Mesoporous Ternary CoNiFe Layered Double Hydroxides for Efficient Oxygen Evolution. *ACS Sustain. Chem. Eng.* **2018,** *6*, 16096-16104.

(47) Xu, D.; Stevens, M. B.; Rui, Y.; DeLuca, G.; Boettcher, S. W.; Reichmanis, E.; Li, Y.; Zhang, Q.; Wang, H. The Role of Cr Doping in NiFe Oxide/(Oxy)hydroxide Electrocatalysts for Oxygen Evolution. *Electrochim. Acta* **2018,** *265*, 10-18.

(48) Yang, Y.; Dang, L.; Shearer, M. J.; Sheng, H.; Li, W.; Chen, J.; Xiao, P.; Zhang, Y.; Hamers, R. J.; Jin, S. Highly Active Trimetallic NiFeCr Layered Double Hydroxide Electrocatalysts for Oxygen Evolution Reaction. *Adv. Energy Mater.* **2018,** *8* (15), 1703189.

(49) Xu, D.; Stevens, M. B.; Cosby, M. R.; Oener, S. Z.; Smith, A. M.; Enman, L. J.; Ayers, K. E.; Capuano, C. B.; Renner, J. N.; Danilovic, N.; Li, Y.; Wang, H.; Zhang, Q.; Boettcher, S. W. Earth-Abundant Oxygen Electrocatalysts for Alkaline Anion-Exchange-Membrane Water Electrolysis: Effects of Catalyst Conductivity and Comparison with Performance in Three-Electrode Cells. *ACS Catal.* **2019,** *9* (1), 7-15.

(50) Li, D.; Park, E. J.; Zhu, W.; Shi, Q.; Zhou, Y.; Tian, H.; Lin, Y.; Serov, A.; Zulevi, B.; Baca, E. D.; Fujimoto, C.; Chung, H. T.; Kim, Y. S. Highly Quaternized Polystyrene Ionomers for High Performance Anion Exchange Membrane Water Electrolysers. *Nat. Energy* **2020,** *5* (5), 378-385.

(51) Lagadec, M. F.; Grimaud, A. Water Electrolysers with Closed and Open Electrochemical Systems. *Nat. Mater.* **2020,** *19* (11), 1140-1150.

(52) Xiao, J.; Oliveira, A. M.; Wang, L.; Zhao, Y.; Wang, T.; Wang, J.; Setzler, B. P.; Yan, Y. Water-Fed Hydroxide Exchange Membrane Electrolyzer Enabled by a Fluoride-Incorporated Nickel–Iron Oxyhydroxide Oxygen Evolution Electrode. *ACS Catal.* **2021,** *11* (1), 264-270.

(53) Xu, Q.; Oener, S. Z.; Lindquist, G.; Jiang, H.; Li, C.; Boettcher, S. W. Integrated Reference Electrodes in Anion-Exchange-Membrane Electrolyzers: Impact of Stainless-Steel Gas-Diffusion Layers and Internal Mechanical Pressure. *ACS Energy Lett.* **2020**, 305-312.

(54) Lindquist, G. A.; Oener, S. Z.; Motz, A. A.; Keane, A.; Capuano, C.; Ayers, K. E.; Boettcher, S. W. Preparation of Baseline Membrane-Electrode-Assemblies for Stable, High-Performance Anion-Exchange-Membrane Electrolysis in Pure Water. *ACS Appl. Mater. Interfaces* **2021**, *13* (44), 51917–51924.

(55) Soni, R.; Miyanishi, S.; Kuroki, H.; Yamaguchi, T. Pure Water Solid Alkaline Water Electrolyzer Using Fully Aromatic and High-Molecular-Weight Poly(fluorene-alt-tetrafluorophenylene)-trimethyl Ammonium Anion Exchange Membranes and Ionomers. *ACS Appl. Energy Mater.* **2021,** *4* (2), 1053-1058.

(56) Carbone, A.; Zignani, S. C.; Gatto, I.; Trocino, S.; Aricò, A. S. Assessment of the FAA3-50 Polymer Electrolyte in Combination with a $NiMn_2O_4$ Anode Catalyst for Anion Exchange Membrane Water Electrolysis. *Int. J. Hydrog. Energy* **2020,** *45* (16), 9285-9292.

(57) Faid, A. Y.; Xie, L.; Barnett, A. O.; Seland, F.; Kirk, D.; Sunde, S. Effect of Anion Exchange Ionomer Content on Electrode Performance in AEM Water Electrolysis. *Int. J. Hydrog. Energy* **2020,** *45* (53), 28272-28284.

(58) Farhat, R.; Dhainy, J.; Halaoui, L. I. OER Catalysis at Activated and Codeposited NiFe-Oxo/Hydroxide Thin Films Is Due to Postdeposition Surface-Fe and Is Not Sustainable without Fe in Solution. *ACS Catal.* **2020,** *10* (1), 20-35.

(59) Etzi Coller Pascuzzi, M.; Man, A. J. W.; Goryachev, A.; Hofmann, J. P.; Hensen, E. J. M. Investigation of the Stability of NiFe-(Oxy)hydroxide Anodes in Alkaline Water Electrolysis under Industrially Relevant Conditions. *Catal. Sci. Technol.* **2020,** *10* (16), 5593-5601.

(60) Xie, L.; Kirk, D. W. Nickel Catalyst Migration in an Anion Exchange Membrane Fuel Cell. *Electrochim. Acta* **2020,** *364*, 137091.

(61) Dresp, S.; Luo, F.; Schmack, R.; Kühl, S.; Gliech, M.; Strasser, P. An efficient Bifunctional Two-Component Catalyst for Oxygen Reduction and Oxygen Evolution in Reversible Fuel Cells, Electrolyzers and Rechargeable Air Electrodes. *Energy Environ. Sci.* **2016,** *9* (6), 2020-2024.

(62) Hegge, F.; Lombeck, F.; Cruz Ortiz, E.; Bohn, L.; von Holst, M.; Kroschel, M.; Hübner, J.; Breitwieser, M.; Strasser, P.; Vierrath, S. Efficient and Stable Low Iridium Loaded Anodes for PEM Water Electrolysis Made Possible by Nanofiber Interlayers. *ACS Appl. Energy Mater.* **2020,** *3* (9), 8276-8284.

(63) Maurya, S.; Lee, A. S.; Li, D.; Park, E. J.; Leonard, D. P.; Noh, S.; Bae, C.; Kim, Y. S. On the Origin of Permanent Performance Loss of Anion Exchange Membrane Fuel Cells: Electrochemical Oxidation of Phenyl Group. *J. Power Sources* **2019,** *436*, 226866.

(64) Mondschein, J. S.; Callejas, J. F.; Read, C. G.; Chen, J. Y. C.; Holder, C. F.; Badding, C. K.; Schaak, R. E. Crystalline Cobalt Oxide Films for Sustained Electrocatalytic Oxygen Evolution under Strongly Acidic Conditions. *Chem. Mater.* **2017,** *29* (3), 950-957.

(65) Wang, Z.; Zheng, Y.-R.; Chorkendorff, I.; Nørskov, J. K. Acid-Stable Oxides for Oxygen Electrocatalysis. *ACS Energy Lett.* **2020,** *5* (9), 2905-2908.

(66) Jin, S. Are Metal Chalcogenides, Nitrides, and Phosphides Oxygen Evolution Catalysts or Bifunctional Catalysts? *ACS Energy Lett.* **2017,** *2* (8), 1937-1938.

(67) Binninger, T.; Mohamed, R.; Waltar, K.; Fabbri, E.; Levecque, P.; Kotz, R.; Schmidt, T. J. Thermodynamic Explanation of the Universal Correlation between Oxygen Evolution Activity and Corrosion of Oxide Catalysts. *Nat. Sci. Rep.* **2015,** *5* (12167).

(68) Suntivich, J.; May, K. J.; Gasteiger, H. A.; Goodenough, J. B.; Shao-Horn, Y. A Perovskite Oxide Optimized for Oxygen Evolution Catalysis from Molecular Orbital Principles. *Science* **2011,** *334*, 1383-1385.

(69) May, K. J.; Carlton, C. E.; Stoerzinger, K. A.; Risch, M.; Suntivich, J.; Lee, Y.-L.; Grimaud, A.; Shao-Horn, Y. Influence of Oxygen Evolution during Water Oxidation on the Surface of Perovskite Oxide Catalysts. *J. Phys. Chem. Lett.* **2012,** *3*, 3264-3270.

(70) Risch, M.; Grimaud, A.; May, K. J.; Stoerzinger, K. A.; Chen, T. J.; Mansour, A. N.; Shao-Horn, Y. Structural Changes of Cobalt-Based Perovskites upon Water Oxidation Investigate by EXAFS. *J. Phys. Chem. C.* **2013,** *117*, 8628 - 8635.

(71) Baeumer, C.; Li, J.; Lu, Q.; Liang, A. Y.-L.; Jin, L.; Martins, H. P.; Duchon, T.; Glos, M.; Gericke, S. M.; Wohlgemuth, M. A.; Giesen, M.; Penn, E. E.; Dittmann, R.; Gunkel, F.; Waser, R.; Bajdich, M.; Nemsak, S.; Mefford, J. T.; Chueh, W. C. Tuning Electrochemically Driven Surface Transformations in Atomically Flat $LaNiO_3$ Thin Films for Water Electrolysis. *Nat. Mater.* **2021**, 20, 674-682.

(72) Lopes, P. P.; Chung, D. Y.; Rui, X.; Zheng, H.; He, H.; Martins, P. F. B. D.; Strmcnik, D.; Stamenkovic, V. R.; Zapol, P.; Mitchell, J. F.; Klie, R. F.; Markovic, N. M. Dynamically Stable Active Sites from Surface Evolution of Perovskite Materials during the Oxygen Evolution Reaction. *J. Am. Chem. Soc.* **2021**, *143* (7), 2741-2750.

CHAPTER VI

[1] a)B. Pivovar, N. Rustagi, S. Satyapal, *Electrochem. Soc. Interface* **2018**, 27, 47; b)G. W. Crabtree, M. S. Dresselhaus, M. V. Buchanan, *Phys. Today* **2004**, 57, 39.

[2] a)K. Ayers, N. Danilovic, R. Ouimet, M. Carmo, B. Pivovar, M. Bornstein, *Annu. Rev. Chem. Biomol. Eng.* **2019**, 10, 219; b)K. Zeng, D. Zhang, *Prog. Energy Combust. Sci.* **2010**, 36, 307.

[3] M. Carmo, D. L. Fritz, J. Mergel, D. Stolten, *Int. J. Hydrog. Energy* **2013**, 38, 4901.

[4] a)A. Carbone, S. C. Zignani, I. Gatto, S. Trocino, A. S. Aricò, *Int. J. Hydrog. Energy* **2020**, 45, 9285; b)A. Y. Faid, L. Xie, A. O. Barnett, F. Seland, D. Kirk, S. Sunde, *Int. J. Hydrog. Energy* **2020**, 45, 28272; c)P. Chen, X. Hu, *Adv. Energy Mater.* **2020**, 10, 2002285; d)H. Koshikawa, H. Murase, T. Hayashi, K. Nakajima, H. Mashiko, S. Shiraishi, Y. Tsuji, *ACS Catal.* **2020**, 10, 1886; e)D. Li, E. J. Park, W. Zhu, Q. Shi, Y. Zhou, H. Tian, Y. Lin, A. Serov, B. Zulevi, E. D. Baca, C. Fujimoto, H. T. Chung, Y. S. Kim, *Nat. Energy* **2020**, 5, 378; f)N. Hassan, Y. Zheng, P. Kohl, W. E. Mustain, *J. Electrochem. Soc.* **2022**.

[5] A. Kiessling, J. C. Fornaciari, G. Anderson, X. Peng, A. Gerstmayr, M. R. Gerhardt, S. McKinney, A. Serov, Y. S. Kim, B. Zulevi, A. Z. Weber, N. Danilovic, *J. Electrochem. Soc.* **2021**, 168, 084512.

[6] a)G. A. Lindquist, S. Z. Oener, R. Krivina, A. R. Motz, A. Keane, C. Capuano, K. E. Ayers, S. W. Boettcher, *ACS Appl. Mater. Interfaces* **2021**, 13, 51917; b)R. Soni, S. Miyanishi, H. Kuroki, T. Yamaguchi, *ACS Appl. Energy Mater.* **2021**, 4, 1053; c)D. Xu, M. B. Stevens, M. R. Cosby, S. Z. Oener, A. M. Smith, L. J. Enman, K. E. Ayers, C. B. Capuano, J. N. Renner, N. Danilovic, Y. Li, H. Wang, Q. Zhang, S. W. Boettcher, *ACS Catal.* **2019**, 9, 7.

[7] a)M. B. Stevens, L. J. Enman, E. H. Korkus, J. Zaffran, C. D. M. Trang, J. Asbury, M. G. Kast, M. C. Toroker, S. W. Boettcher, *Nano Research* **2019**, 12, 2288; b)M. B. Stevens, C. D. M. Trang, L. J. Enman, J. Deng, S. W. Boettcher, *J. Am. Chem. Soc.* **2017**, 139, 11361; c)L. Trotochaud, S. L. Young, J. K. Ranney, S. W. Boettcher, *J. Am. Chem. Soc.* **2014**, 136, 6744.

[8] L. Wang, V. A. Saveleva, M. J. Eslamibidgoli, D. Antipin, C. Bouillet, I. Biswas, A. S. Gago, S. S. Hosseiny, P. Gazdzicki, M. H. Eikerling, E. R. Savinova, K. A. Friedrich, *ACS Appl. Energy Mater.* **2022**, 5, 2221.

[9] B. Mayerhöfer, F. D. Speck, M. Hegelheimer, M. Bierling, D. Abbas, D. McLaughlin, S. Cherevko, S. Thiele, R. Peach, *Int. J. Hydrog. Energy* **2022**, 47, 4304.

[10] a)J. Xiao, A. M. Oliveira, L. Wang, Y. Zhao, T. Wang, J. Wang, B. P. Setzler, Y. Yan, *ACS Catal.* **2021**, 11, 264; b)J. Yang, M. J. Jang, X. Zeng, Y. S. Park, J. Lee, S. M. Choi, Y. Yin, *Electrochem. Commun.* **2021**, 131, 107118.

[11] N. U. Hassan, M. Mandal, B. Zulevi, P. A. Kohl, W. E. Mustain, *Electrochim. Acta* **2022**, 409, 140001.

[12] R. A. Krivina, G. A. Lindquist, M. C. Yang, A. K. Cook, C. H. Hendon, A. R. Motz, C. Capuano, K. E. Ayers, J. E. Hutchison, S. W. Boettcher, *ACS Appl. Mater. Interfaces* **2022**.

[13] a)D. Li, A. R. Motz, C. Bae, C. Fujimoto, G. Yang, F.-Y. Zhang, K. E. Ayers, Y. S. Kim, *Energy Environ. Sci.* **2021**, 14, 3393; b)I. Martens, L. G. A. Melo, M. M. West, D. P. Wilkinson, D. Bizzotto, A. P. Hitchcock, *ACS Catal.* **2020**, 10, 8285.

[14] a)H. B. Tao, Y. Xu, X. Huang, J. Chen, L. Pei, J. Zhang, J. G. Chen, B. Liu, *Joule* **2019**, 3, 1498; b)G. Hübner, E. Roduner, *J. Mater. Chem.* **1999**, 9, 409.

[15] J. Wang, Y. Zhao, B. P. Setzler, S. Rojas-Carbonell, C. Ben Yehuda, A. Amel, M. Page, L. Wang, K. Hu, L. Shi, S. Gottesfeld, B. Xu, Y. Yan, *Nat. Energy* **2019**, 4, 392.

[16] S. A. Berlinger, B. D. McCloskey, A. Z. Weber, *ACS Energy Lett.* **2021**, 6, 2275.

[17] a)D. Y. Chung, P. P. Lopes, P. Farinazzo Bergamo Dias Martins, H. He, T. Kawaguchi, P. Zapol, H. You, D. Tripkovic, D. Strmcnik, Y. Zhu, S. Seifert, S. Lee, V. R. Stamenkovic, N. M. Markovic, *Nat. Energy* **2020**, 5, 222; b)T. Zhang, M. R. Nellist, L. J. Enman, J. Xiang, S. W. Boettcher, *ChemSusChem* **2019**, 12, 2015.

[18] C. Dette, M. R. Hurst, J. Deng, M. R. Nellist, S. W. Boettcher, *ACS Appl. Mater. Interfaces* **2019**, 11, 5590.

[19] M. C. Biesinger, L. W. M. Lau, A. R. Gerson, R. S. C. Smart, *Phys. Chem. Chem. Phys.* **2012**, 14, 2434.

[20] a)A. Bergmann, E. Martinez-Moreno, D. Teschner, P. Chernev, M. Gliech, J. F. de Araújo, T. Reier, H. Dau, P. Strasser, *Nat. Commun.* **2015**, 6, 8625; b)T. Wiegmann, I. Pacheco, F. Reikowski, J. Stettner, C. Qiu, M. Bouvier, M. Bertram, F. Faisal, O. Brummel, J. Libuda, J. Drnec, P. Allongue, F. Maroun, O. M. Magnussen, *ACS Catal.* **2022**, 3256.

[21] J. Deng, M. R. Nellist, M. B. Stevens, C. Dette, Y. Wang, S. W. Boettcher, *Nano Lett.* **2017**, 17, 6922.

[22] a)R. Jinnouchi, K. Kudo, K. Kodama, N. Kitano, T. Suzuki, S. Minami, K. Shinozaki, N. Hasegawa, A. Shinohara, *Nat. Commun.* **2021**, 12, 4956; b)C. Santoro, A. Lavacchi, P. Mustarelli, V. Di Noto, L. Elbaz, D. R. Dekel, F. Jaouen, *ChemSusChem*, e202200027.

[23] a)G. A. Lindquist, Q. Xu, S. Z. Oener, S. W. Boettcher, *Joule* **2020**, 4, 2549; b)H.-F. Lu, H.-F. Chen, C.-L. Kao, I. Chao, H.-Y. Chen, *Phys. Chem. Chem. Phys.* **2018**, 20, 22890.

APPENDIX B

(1) Biesinger, M. C.; Payne, B. P.; Grosvenor, A. P.; Lau, L. W. M.; Gerson, A. R.; Smart, R. S. C. Resolving Surface Chemical States in XPS Analysis of First Row Transition Metals, Oxides and Hydroxides: Cr, Mn, Fe, Co and Ni. *Appl. Surf. Sci.* **2011,** *257* (7), 2717-2730.

APPENDIX C

(1) Duffin, A. M.; Schwartz, C. P.; England, A. H.; Uejio, J. S.; Prendergast, D.; Saykally, R. J. pH-dependent X-ray Absorption Spectra of Aqueous Boron Oxides. *J. Chem. Phys.* **2011,** *134* (15), 154503.

(2) Marcus, Y. Thermodynamics of Solvation of Ions. Part 5.—Gibbs free energy of hydration at 298.15 K. *J. Chem. Soc. Faraday Trans.* **1991,** *87* (18), 2995-2999.